

# Spatiotemporal brain dynamics induced by propofol and ketamine in humans



**Marco Samuel Fabuš**

St John's College  
University of Oxford

A thesis submitted for the degree of  
*Doctor of Philosophy*

Trinity 2023

*For my parents*

# Acknowledgements

It is said that it takes a village to raise a doctoral student, and I have found this to be true. There are many people and communities without whom this thesis would not exist. I would like to extend my deepest gratitude to these – though doing it full justice would take many, many hours.

First, I have much to thank for to my supervisors:

To Dr Katie Warnaby, for taking a walk with me on 31 May 2019 and changing my life. For showing me that physicists have a place in Neuroscience, for always being there with advice and kindness, and for guiding my research whilst giving me unprecedented freedom for exploration at the same time. I still can't believe you manage to run a research group and a pub at the same time.

To Prof Mark Woolrich, for always having a scarily high density of useful comments combined with incredible creativity and humanity.

To Prof Rupert McShane, for welcoming me into the world of Psychiatry, devoting time to our study, and providing a unique clinical perspective on my work.

To all the colleagues in the three groups I've had the privilege to be a part of:

To the Anaesthesia Neuroimaging Group (Minh, Di, James, Jostein, Saad, and everyone else) for all our fun group meetings, and to Prof Jamie Sleight for all his advice and insights into consciousness and anaesthesia.

To the OHBA Analysis Group (Mats, Chet, Richard, Ollie, and so many more!) for inducting me into the ways of Hidden Markov Models, and especially to Prof Andrew Quinn, who showed me what gold-standard neuroscience methods research looks like.

To the Oxford Ketamine Clinic (Sara, Tim, Alex, and all the nursing and administrative colleagues), and especially to Dr Dan Casey for all the work on our study and all the discussions about Psychiatry and Medicine.

To my family: mami, tati, Medy, Mely, babika, and everyone else, for always being there, for unconditional and unwavering support, and for making me feel I always have a home to come back to. To my parents especially, for valuing education and believing in me, and to my late grandfather Miroslav for sparking in me a love of science.

To my friends, who have been there for many rounds of my info dumping, frustration, and elation: First and foremost to Meg, my joy and best friend, who was there for every day of this doctorate and grew together with me through our best and worst. To Joe, for all our Wednesday dinners and ranting about academia. To Caitlin, for our catch-ups and updates through all these years. To Kenneth, for all our consciousness conversations and for building the community around OPS and welcoming me into it. To friends of OPS (Elin, Sam, Eva, Scarlett, George, and many others), for exploring the world in unique ways and inspiring new research ideas. To Ana, for all the beautiful nature photos (especially during lockdown!). To my Slovak friends (Vilo, Sely, Matej, Mišo, Peťo, and many more), for all the jokes that do not translate into English.

To the funders who made this work possible whilst keeping me housed and fed: the Wellcome Centre for Integrative Neuroimaging studentship, St John's College, Nuffield Department of Clinical Neurosciences, Department of Psychiatry, and the Guarantors of Brain.

To all the patients and volunteers who are represented in this thesis – you are making a better world possible and I wish you nothing but kindness.

To everyone who supported me on my graduate medicine application journey – may I one day thank you by reducing suffering in this world.

To the University of Michigan research group for collecting the original healthy volunteer ketamine data and sharing it for the analyses in this thesis, as well as to colleagues in the Oxford Anaesthesia Neuroimaging group for collecting the original propofol dataset.

The joy and gratitude I feel when reflecting on the last few years is difficult to put into words. This thesis belongs to all those who shaped me, supported me, and gave me the space to be curious.

Thank you.

# Author Contributions & Publications

I declare that all work in this thesis was carried out by myself, except where otherwise indicated here, or acknowledged via citation.

Figure 1.1 has been reproduced from Hight et al. *Can J Anesth.* 2022 with permission. Supplementary Figure 2.1 was created by Dr Di Zang and is reproduced with permission. Furthermore, this thesis has resulted in several publications, some of which have been adapted for this thesis. In all of these, I conceptualised the relevant methods and the study, performed the analyses, interpreted the results, produced the figures, and wrote the relevant text. My co-authors assisted with supervision, results interpretation, funding acquisition, and manuscript editing, and agree with inclusion of this material in the thesis. Specifically:

## Chapter 2

A preliminary account of the work linking SWAS to GABA<sub>A</sub> receptors was reported at the AAGBI Annual 2022 Congress, with the abstract published in *Anaesthesia*:

Fabus MS, Woolrich MW, Warnaby CE. Regional anaesthetic brain susceptibility to propofol is linked with local GABA<sub>A</sub> receptor density. *Anaesthesia.* 2022; 77: 6–44

These results were also discussed in my winning submission for the 2022 Royal Society of Medicine (Anaesthesia Section) student essay prize, “*Differing susceptibility to propofol anaesthesia across the brain: time to move beyond frontal electroencephalogram monitoring?*”.

The results comparing SWAS with BIS have been accepted as an abstract for the Euroanaesthesia 2023 conference, to be published in the *European Journal of Anaesthesiology*:

Fabus MS, Tran MC, Warnaby CE. Comparison of the bispectral index and slow-wave activity in propofol anaesthesia. *ESAIC 2023 conference abstract.*

Finally, for more context on the meaning and uses of complexity in anaesthesia, please also see a paper of mine with Prof Jamie Sleight and Prof Duan Li:

Li D, Fabus MS, Sleight JW. Brain complexities and anesthesia: Their meaning and measurement. *Anesthesiology.* 2022;137(3):290-302.

In that article, I contributed sections on spatiotemporal complexity, the effect of signal properties on Lempel-Ziv complexity, and alongside my co-authors edited and reviewed the final manuscript.

### Chapter 3

This chapter is adapted from my first-author publication currently under review in *Anesthesiology*:

Fabus MS, Sleight JW, Warnaby CE. Effect of propofol on heart rate and its coupling to cortical slow waves in humans. *Under review*.

### Chapter 4

The methodological and validation parts of this chapter are adapted from my existing first-author publication:

Fabus MS, Quinn AJ, Warnaby CE, Woolrich MW. Automatic decomposition of electrophysiological data into distinct nonsinusoidal oscillatory modes. *Journal of Neurophysiology*. 2021;126(5):1670-84.

Prof Quinn helped develop the methodology and implement it into the EMD-Python toolbox. The application of itEMD to propofol anaesthesia has been published as a conference abstract from the International Anesthesia Research Society (IARS) Annual 2021 Meeting:

Fabus MS, Quinn AJ, Woolrich MW, Warnaby CE. Three distinct low-frequency (< 4Hz) traveling wave types in volunteer propofol anaesthesia revealed by empirical mode decomposition. *Anesthesia & Analgesia*. 2021;132(5S).

Finally, in spectral analyses of non-sinusoidal oscillations, harmonics are present in the power spectrum. These can affect connectivity measures and their analysis remains controversial. I undertook a theoretical study of waveform shape, providing a rigorous definition of what a harmonic is and validating it on simulations and Local Field Potentials (LFPs). This work is not included in this thesis for brevity but has been published before in full:

Fabus MS, Woolrich MW, Warnaby CW, Quinn AJ. Understanding harmonic structures through instantaneous frequency. *IEEE Open Journal of Signal Processing*. 2022;3:320-34.



Marco Samuel Fabus MPhys  
Oxford, 19/05/2023

# Abstract

Human brain dynamics are radically altered under the influence of anaesthetics. However, despite their widespread clinical use, the whole-brain mechanisms by which anaesthetics alter consciousness are still not fully understood and clinical translation of existing insights is limited. This thesis presents several lines of investigation aimed to improve our understanding of spatiotemporal brain states under the anaesthetics propofol and ketamine.

First, slow-wave activity saturation (SWAS) was studied across the brain and in relation to existing depth of anaesthesia markers. Local propofol concentration needed to achieve SWAS in healthy volunteers correlated with GABA<sub>A</sub> receptor density (Spearman  $\rho=-0.69$ ,  $P=0.0018$ ), providing more evidence for the importance of the neurophysiological state of SWAS. The average Bispectral Index at SWAS across volunteers was  $49\pm 4$ , but its value varied significantly over time.

Second, relevant cortico-cardiac interactions were studied. A slow propofol infusion increased heart rate in a dose-dependent manner (increase of  $+4.2\pm 1.5$  bpm/ $(\mu\text{gml}^{-1})$ ,  $P<0.001$ ). Individual cortical slow waves were coupled to the heartbeat ( $P<0.001$ ), with heartbeat incidence peaking about 450ms before slow-wave onset. A ketamine case study showed decreased amplitude of heartbeat-evoked potentials, suggesting impaired interoceptive signalling may have a part in dissociative phenomenology.

Third, novel methodology was developed, validated, and applied throughout the thesis. Iterated Masking Empirical Mode Decomposition was used to identify three types of low-frequency propofol waves with different spatiotemporal maps and dose-responses. Hidden Markov Modelling of propofol showed a shift to anterior alpha states and a reduced switching rate ( $P<0.01$ ); with ketamine states exhibiting low alpha power and decreased connectivity became more prominent ( $P<0.001$ ).

Fourth, the potential of translating electroencephalographic markers from high- to low-density montages was studied. Posterior montages were best at capturing the reduced state switching under propofol. A patient study of antidepressant ketamine treatment demonstrated reduced temporal lobe alpha and theta power were associated with dissociation ( $P=0.0109$ ).

# Table of Contents

Acknowledgements .....	iii
Author Contributions & Publications .....	v
Abstract .....	vii
Table of Contents .....	viii
List of Figures .....	xiv
List of Tables .....	xvii
List of Abbreviations .....	xviii
<b>1 Background .....</b>	<b>1</b>
1.1 General anaesthesia and its effects on physiology .....	1
1.1.1 General overview .....	1
1.1.2 GABAergic anaesthetics and propofol .....	5
1.1.3 NMDA-acting anaesthetics and ketamine .....	6
1.1.4 Beyond hypnotics: opioids and muscle relaxants .....	9
1.2 Electroencephalography and its uses in anaesthesia monitoring .....	10
1.2.1 General and historical overview .....	10
1.2.2 EEG changes under general anaesthesia .....	13
1.2.3 Slow-wave saturation .....	17
1.2.4 Autonomic nervous system and cortico-cardiac interactions .....	17
1.3 Thesis outline .....	18
<b>2 Neurobiology of slow-wave saturation and its relationship with existing anaesthetic markers .....</b>	<b>22</b>
2.1 Introduction .....	22
2.2 Materials and Methods .....	27
2.2.1 Data .....	27
2.2.2 Slow-wave activity saturation analysis .....	28



2.2.3	Lempel-Ziv Complexity analysis .....	28
2.2.4	Topographical relationship of complexity and slow-wave saturation ....	29
2.2.5	Linking SWAS and LZW to local gamma-aminobutyric acid receptor density.....	30
2.2.6	Comparison of SWAS with the Bispectral Index (BIS) .....	30
2.3	Results.....	31
2.3.1	Slow-wave activity saturation (SWAS) across brain regions.....	31
2.3.2	Topographical relationship of complexity and slow-wave saturation ....	34
2.3.3	Links with local gamma-aminobutyric acid receptor density .....	35
2.3.4	Comparison with the Bispectral Index (BIS) .....	37
2.4	Discussion.....	40
2.4.1	SWAS across the cortex.....	40
2.4.2	Brain complexity and slow waves .....	42
2.4.3	Slow waves and the Bispectral Index .....	43
2.4.4	Limitations of the study.....	44
<b>3</b>	<b>Effect of propofol on heart rate and its coupling to cortical slow waves in humans .....</b>	<b>46</b>
3.1	Introduction .....	46
3.2	Materials and methods.....	48
3.2.1	Data collection.....	48
3.2.2	Data pre-processing.....	48
3.2.3	Time-series ECG analysis.....	49
3.3.4	Heart rate variability ECG analysis.....	49
3.3.5	Slow-wave analysis.....	50
3.3.6	Cortico-cardiac coupling analysis.....	50
3.3.7	Clinical dataset analysis .....	52
3.3.8	Statistical analyses.....	53
3.3	Results.....	54

3.3.1	Time-series ECG analysis.....	54
3.3.2	Heart rate variability analysis .....	55
3.3.3	Slow-wave analysis.....	57
3.3.4	Cortico-cardiac coupling.....	58
3.3.5	Clinical dataset analysis.....	62
3.4	Discussion.....	64
3.4.1	Propofol and the heart rate.....	64
3.4.2	Propofol and heart rate variability.....	65
3.4.3	Propofol and ECG morphology .....	66
3.4.4	Cortico-cardiac coupling in propofol .....	66
<b>4</b>	<b>Automatic decomposition of electrophysiological data into distinct non-sinusoidal oscillatory modes .....</b>	<b>71</b>
4.1	Introduction .....	71
4.2	Methods .....	75
4.2.1	Empirical Mode Decomposition (EMD) Algorithms .....	75
4.2.2	Simulations.....	80
4.2.3	Validation using Experimental Data .....	84
4.2.4	Application of itEMD to human propofol electroencephalography (EEG) data.....	87
4.2.5	Data and Code Availability.....	89
4.3	Results.....	90
4.3.1	Simulations.....	90
4.3.2	Validation in experimental datasets.....	101
4.3.3	Application to human propofol anaesthesia EEG data .....	105
4.4	Discussion.....	112
4.4.1	Limitations of itEMD.....	113
4.4.2	Three distinct low-frequency modes in propofol anaesthesia .....	115
4.4.3	Limitations of the propofol analysis.....	116

<b>5</b>	<b>Spatiotemporal brain states in propofol anaesthesia.....</b>	<b>119</b>
5.1	Introduction .....	119
5.2	Materials and Methods.....	121
5.2.1	Data Acquisition and Pre-processing.....	121
5.2.2	Hidden Markov Modelling .....	122
5.2.6	EXG-HMM .....	125
5.2.7	Low-density HMM translation .....	125
5.3	Results.....	126
5.3.1	32-channel EEG-HMM .....	126
5.3.2	EXG-HMM.....	133
5.3.3	Low-density HMM translation .....	137
5.4	Discussion.....	140
5.4.1	Spatiotemporal brain states in propofol-mediated unconsciousness..	140
5.4.2	Combined heart-brain states .....	142
5.4.3	Low-density EEG.....	143
5.4.4	Limitations .....	144
<b>6</b>	<b>Neural correlates of ketamine dissociation in healthy volunteers .....</b>	<b>146</b>
6.1	Introduction .....	146
6.1.1	Psychedelics as novel antidepressants .....	146
6.1.2	Ketamine dissociation.....	148
6.1.3	Chapter overview .....	149
6.2	Materials and Methods.....	151
6.2.1	Data collection .....	151
6.2.2	Signal pre-processing.....	152
6.2.3	Source reconstruction.....	154
6.2.4	Hidden Markov Modelling .....	154
6.2.5	Receptor fingerprinting .....	156

6.3	Results .....	157
6.3.1	Whole-brain ketamine-associated network states .....	157
6.3.2	Distinct baseline and ketamine state transitions .....	161
6.3.3	Brain states associated with dissociative phenomenology .....	163
6.3.4	Receptor fingerprinting of dynamic brain states.....	165
6.3.5	State appearance in low-density EEG.....	167
6.3.6	Case study of heartbeat-evoked potentials under ketamine .....	169
6.4	Discussion.....	172
6.4.1	Hidden Markov Modelling of ketamine in healthy volunteers .....	172
6.4.2	Receptor fingerprinting .....	176
6.4.3	Limitations .....	177
<b>7</b>	<b>Ketamine dissociation in patients with treatment-resistant depression..</b>	<b>180</b>
7.1	Introduction .....	180
7.2	Material and Methods.....	181
7.2.1	Study protocol.....	181
7.2.2	Study population .....	184
7.2.3	Data pre-processing .....	186
7.2.4	Data analysis .....	186
7.2.5	Statistical analyses .....	187
7.3	Results .....	188
7.3.1	Pre-infusion measurements and Set & Setting scales .....	188
7.3.2	Post-infusion dissociation scales .....	191
7.3.3	Photoplethysmography (PPG) results .....	194
7.3.4	Electroencephalography (EEG) results .....	195
7.3.5	Longitudinal case study.....	198
7.4	Discussion.....	201
7.4.1	Translating EEG markers of dissociation into the clinic .....	201

7.4.2	Notes on feasibility of routine brain-based ketamine monitoring.....	202
7.4.2	Limitations .....	203
<b>8</b>	<b>Concluding remarks .....</b>	<b>205</b>
8.1	Spatiotemporal brain states identified by data-driven methods.....	205
8.2	Translational aspects of EEG analyses.....	208
8.3	Cardiac influences on brain states .....	211
<b>9</b>	<b>Appendices.....</b>	<b>215</b>
	Appendix 1: Supplementary Figures to Chapter 2 .....	215
	Appendix 2: Supplementary Figures to Chapter 3 .....	217
9.2.1	Understanding cortico-cardiac coupling .....	221
	Appendix 3: Supplementary Figures to Chapter 4 .....	224
	Appendix 4: Supplementary Figures to Chapter 5 .....	225
	Appendix 5: Supplementary Figures to Chapter 6 .....	233
	Appendix 6: Supplementary Figures to Chapter 7 .....	239
	Appendix 7: Questionnaires for the ketamine study.....	240
9.7.1	Set & Setting Questionnaire .....	240
9.7.2	Subjective noise & light levels .....	241
9.7.3	5D-ASC questionnaire.....	242
9.7.4	CADSS-6.....	244
9.7.5	Open-ended questions .....	245
9.7.6	Demographic questionnaire.....	246
<b>10</b>	<b>References.....</b>	<b>247</b>

# List of Figures

Figure 1.1: Classical frontal anaesthetic EEG responses.....	15
Figure 2.1: Slow-wave activity saturation sigmoid modelling.....	32
Figure 2.2: Local slow-wave parameter topography.....	33
Figure 2.3: Spatial differences in SWAS correlate with GABA <sub>A</sub> receptor density .....	36
Figure 2.4: Bispectral Index (BIS) and Slow-wave power (SWP). .....	38
Figure 2.5: Variability of BIS during 10 minutes at SWAS .....	39
Figure 2.6: BIS at SWAS against P <sub>SWAS</sub> . .....	39
Figure 3.1: Propofol increased HR and changed ECG shape in healthy volunteers	55
Figure 3.2: Propofol decreased parasympathetic activity in healthy volunteers .....	56
Figure 3.3: Propofol slow-wave activity increase tracked HR increase. ....	57
Figure 3.4: Single-subject low-frequency cortico-cardiac coupling. ....	59
Figure 3.5: Group-level cortico-cardiac coupling in healthy volunteers. ....	60
Figure 3.6: Multivariate extension of the analysis.....	61
Figure 4.1: Limitations of EMD. ....	79
Figure 4.2: Iterated Masking EMD (itEMD) on simulated data. ....	91
Figure 4.3: Influence of noise on EMD performance in simulated data. ....	94
Figure 4.4: Influence of frequency distortion on EMD performance. ....	96
Figure 4.5: Example 2s of sifting results in simulated data.....	98
Figure 4.6: Influence of signal sparsity on EMD performance in simulated data. ...	100
Figure 4.7: Rat hippocampal LFP results. ....	102
Figure 4.8: Human MEG occipital alpha results. ....	104
Figure 4.9: Iterated EMD sift results in propofol anaesthesia. ....	106

Figure 4.10: Trough-based wave analysis results. ....	108
Figure 4.11: Wave topography in trough-based analysis. ....	110
Figure 5.1: Z-scored power maps of propofol EEG-HMM states.....	126
Figure 5.2: State fractional occupancies across time in the EEG-HMM model. ....	128
Figure 5.3: State power spectra and model switching rates. ....	129
Figure 5.4: State associations with behavioural responsiveness and SWAS. ....	131
Figure 5.5: Transition probability matrices.....	132
Figure 5.6: Z-scored power maps of propofol EXG-HMM states.....	134
Figure 5.7: State fractional occupancies across time in the EEG-HMM model. ....	135
Figure 5.8: Further properties of the EXG-HMM model.....	136
Figure 5.9: Spearman correlations between state switching rates in the full and low-density models. ....	138
Figure 5.10: Best bipolar montages for optimising various criteria. ....	139
Figure 6.1: Overview of the ketamine HMM study methodology. ....	153
Figure 6.2: Brain states during a sub-anaesthetic ketamine infusion. ....	158
Figure 6.3: Alternative views of broadband state activity.....	159
Figure 6.4: Connectivity in ketamine HMM states. ....	161
Figure 6.5: Ketamine HMM state transitions and modules. ....	162
Figure 6.6: Brain states associated with disembodiment scores. ....	164
Figure 6.7: Receptor fingerprinting of ketamine HMM states. ....	166
Figure 6.8: HMM state power spectra in a simulated low-density montage.....	168
Figure 6.9: Case study of changing heartbeat-evoked potentials under ketamine. ....	171
Figure 7.1: Example ketamine clinic treatment bay. ....	183
Figure 7.2: Light and noise questionnaire responses and objective measurements. ....	189

Figure 7.3: Set & Setting questionnaire responses. ....	190
Figure 7.4: Dissociation scales responses. ....	192
Figure 7.5: Correlation P-values for dissociation items. ....	193
Figure 7.6: Group-mean pulse rate during infusions. ....	194
Figure 7.7: EEG spectral results for the OHFT study. ....	196
Figure 7.8: Temporal alpha asymmetry results. ....	198
Figure 7.9: EEG spectral results in a longitudinal case study.....	200



# List of Tables

Table 3.1: GLM coefficients for HR in the clinical study. ....	63
Table 7.1: OHFT study demographics.....	185
Table 7.2: Light and noise questionnaire responses. ....	189
Table 7.3: RM-ANOVA P-values and effect sizes for EEG frequency bands. ....	197
Table 7.4: GLM modelling of the subjective dissociation report. ....	197
Table 7.5: Set & Settings responses in a longitudinal case study. ....	199
Table 7.6: Dissociation scores in a longitudinal case study.....	199

# List of Abbreviations

5D-ASC	5-dimensional Altered States of Consciousness
5HT	5-hydroxytryptamine (serotonin)
AAGBI	Association of Anaesthetists of Great Britain and Ireland
ANOVA	Analysis of variance
ASA	American Society of Anesthesiologists
AW-IFM	Amplitude-weighted instantaneous frequency mean
BIS	Bispectral Index
CADSS	Clinician-Administered Dissociative States Scale
CamCAN	Cambridge Centre for Ageing Neuroscience
CB1	Cannabinoid receptor type 1
CRCNS	Collaborative Research in Computational Neuroscience
C <sub>SWAS</sub>	Concentration at slow-wave saturation
DAT	Dopamine transporter
DMN	Default mode network
ECG	Electrocardiography
ECoG	Electrocorticography
EEG	Electroencephalography
EEMD	Ensemble empirical mode decomposition
EMD	Empirical Mode Decomposition
EMG	Electromyography
EOG	Electrooculography
ESC	Effect-site concentration (estimated)

EXG	EEG / EEG
FD	Frequency distortion
FDA	Food and Drug Administration
FDR	False discovery rate
FMRI	Functional magnetic resonance imaging
FMRIB	Oxford Centre for Functional MRI of the Brain
FO	Fractional occupancy
FSL	FMRIB Software Library
GABA	Gamma-aminobutyric acid
GLM	General linear model
HCN	Hyperpolarization-activated cyclic nucleotide
HCP	Human Connectome Project
HEP	Heartbeat-evoked potential
HHT	Hilbert-Huang transform
HMM	Hidden Markov Model
HR	Heart rate
HRV	Heart rate variability
IA	Instantaneous amplitude
ICA	Independent component analysis
IF	Instantaneous frequency
IMF	Intrinsic mode function
IRAS	Integrated Research Application System
itEMD	Iterated masking empirical mode decomposition
LCMV	Linear-constraint minimum-variance

LFP	Local field potential
LOBR	Loss of behavioural response
LSD	Lysergic acid diethylamide
LZW	Lempel-Ziv-Welch
MDMA	3,4-Methylenedioxymethamphetamine
MEG	Magnetoencephalography
MNE	Montreal Neurological Institute
MOR	Mu-opioid receptor
MRI	Magnetic resonance imaging
mTOR	Mechanistic target of rapamycin
NAP	National Audit Project
NET	Norepinephrine transporter
NICE	National Institute for Health and Care Excellence
NMBD	Neuromuscular blocking drugs
NMDA	N-methyl-D-aspartate
NREM	Non-rapid eye movement
OHBA	Oxford Centre for Human Brain Activity
OHFT	Oxford Health Foundation Trust
OSL	OHBA Software Library
PCI	Perturbation complexity index
PMSI	Pseudo-Mode Splitting Index
PPG	Photoplethysmography
$P_{SWAS}$	Power at slow-wave saturation
PTSD	Post-traumatic stress disorder

REC	Research Ethics Committee
RM-ANOVA	Repeated measures analysis of variance
RMSSD	Root-mean-square successive difference
ROBR	Return of behavioural response
RS	R-wave to slow wave time interval
RWA	R-wave amplitude
SH <sub>P</sub>	Proportional Shannon entropy
SWA	Slow-wave activity
SWAS	Slow-wave activity saturation
TCI	Target-controlled infusion
TDE	Time-delay embedding
TIVA	Total intravenous anaesthesia
TRD	Treatment-resistant depression
VACHT	Vesicular acetylcholine transporter
VAS	Visual analogue scale
WIN	Wellcome Centre for Integrative Neuroimaging

# 1 Background

This thesis aims to improve our understanding of the brain under the influence of the general anaesthetics. Specifically, this is done by studying brain states as captured by non-invasive neurophysiological imaging in humans during propofol and ketamine administration. Along the way, the thesis is developed with three key themes present. Firstly, there is a focus on analyses that may support future clinical translation, for instance by comparing results to current clinical practice or by studying the same effects in both volunteers and patients. Secondly, novel data-driven methodology is developed and applied to gain new insights. Finally, combined heart-brain effects are considered in order to highlight the complex physiological feedback loops in the human body. This chapter provides a broad (yet brief) overview of general anaesthesia before narrowing down to propofol and ketamine, as well as introduces some of the relevant methodology and thesis structure.

## 1.1 General anaesthesia and its effects on physiology

### 1.1.1 General overview

Millions of general anaesthetics are administered every year in the United Kingdom (UK) and beyond, enabling safe and life-changing surgical procedures<sup>1</sup>. From James Young Simpson and John Snow first pioneering the use of chloroform in the UK in the 1840s<sup>2</sup>, anaesthesia has grown to be the largest hospital specialty in the UK,

comprising a diverse and highly innovative specialty<sup>i</sup>. Modern anaesthetic practice uses multiple concomitant drugs (i.e. balanced general anaesthesia) to achieve the anaesthetic triad: unconsciousness, analgesia, and muscle relaxation<sup>5</sup>. Local and regional anaesthesia, whilst also essential in clinical practice, are beyond the scope of this thesis. In practice, substantial heterogeneity exists between different types of procedures, patient populations, and preferences between anaesthetists. Broadly, the anaesthetic process can be subdivided into three parts: induction (i.e. achieving initial loss of patient consciousness and securing their airway), maintenance (i.e. ensuring continued anaesthesia adequate for any surgical stimuli present), and emergence (i.e. waking the patient up at the end of surgery).

Despite leaps in clinical practice, the brain mechanisms underlying the effects of general anaesthetics have remained elusive for over a century since their introduction into clinical practice, and a complete explanation of anaesthetic loss of consciousness is still yet to be formulated. This remains a problem for patient safety, particularly when muscle relaxants are used and in the context of the rising use of total intravenous anaesthesia, which presents an increased risk of accidental patient awareness<sup>6</sup>. Intraoperative vital sign monitoring has grown in sophistication, allowing precise delivery of drug concentrations and volumes. However, even though the brain is the likely seat of consciousness and the main hypnotic effect-site, until recently the use of brain-based depth of anaesthesia monitoring has been rare. In 2013, their use was reported in only 2.8% in a large sample UK estimate<sup>1</sup>, though recent data published in March 2023 as part of the 7<sup>th</sup> National Audit Project (NAP7) shows an increase to

---

<sup>i</sup> Interestingly, on top of being voted the “greatest doctor of all time” by Hospital Doctor magazine in 2003, John Snow was also part of the Temperance movement and a vegetarian, avoiding all animal products in his diet<sup>3,4</sup>.

19%<sup>7</sup>. The use of brain-based monitoring devices has been hindered in part because they are based on population-derived indices, are susceptible to muscle and motion artifacts, and are unreliable for some drugs (e.g. ketamine<sup>8</sup>). A clear need for better markers and monitors of adequate depth of anaesthesia therefore exists. Under-anaesthesia can lead to accidental patient awareness during surgery and surgical pain, which can lead to negative postoperative outcomes including post-traumatic stress disorder (PTSD)<sup>9</sup>. Accidental awareness under general anaesthesia is rare (estimated overall around 1 in 20,000 anaesthetics in NAP5<sup>1</sup>), but the rate of PTSD in patients after an accidental awareness episode is approximately 15%<sup>9,10</sup>. The low incidence of awareness is in part because anaesthetists tend to administer higher hypnotic doses to minimise the risk of awareness. However, the negative brain consequences of over-anaesthesia are also being increasingly recognised, particularly in vulnerable groups such as the elderly and those in development<sup>11</sup>. These postoperative cognitive disorders mainly include postoperative delirium (POD) and postoperative cognitive dysfunction (POCD), with for example POD incidence in patients over age 60 after major surgery between 20%-50%<sup>12</sup>, and overall POCD incidence estimated between 10%-18%<sup>13,14</sup>.

A surprisingly wide variety of drugs can affect a patient's consciousness level. The following three sections will outline the known mechanisms of action of the most common hypnotic drugs (often simply referred to as anaesthetics), analgesics, and muscle relaxants (paralytics). Anaesthetics can be categorised based on their main target binding site. Broadly, it is thought that to achieve hypnotic effects, most commonly used anaesthetics either potentiate inhibitory  $\gamma$ -aminobutyric acid type A (GABA<sub>A</sub>) channels or antagonise N-methyl-D-aspartate (NMDA) channels. Other classes of hypnotic agents exist, e.g.  $\alpha_2$ -adrenergic receptor agonists such as



dexmedetomidine. For many drugs, the ultimate mechanism likely goes beyond NMDA/GABA<sub>A</sub> and may also involve constitutively active potassium channels (e.g. two-pore-domain TREK-1<sup>15</sup>) or hyperpolarisation-activated currents ( $I_h$  produced by activation of hyperpolarization-activated cyclic nucleotide-gated potassium channel 1, HCN-1<sup>16</sup>). Anaesthetics, particularly the volatile hypnotics, are thus highly promiscuous in their binding targets. However, in this simplified framework, anaesthetics exerting GABAergic action include the intravenous anaesthetics etomidate, propofol, and barbiturates, as well as inhalational anaesthetics such as sevoflurane, halothane, isoflurane, and desflurane<sup>17</sup>. NMDA agonist hypnotics include phencyclidine, ketamine, nitrous oxide, and elemental xenon. As typical examples of these classes and due to their wide-spread clinical use, propofol and ketamine are studied most in this thesis, and thus presented in more detail below.

Finally, anaesthesia shares commonalities with non-rapid eye movement sleep. In particular, hypnotic anaesthetic action originates in part from action on endogenous neural circuits involved in sleep-wake control<sup>18,19</sup>. This includes effects on subcortical regions involved in arousal control of the conscious level, such as the activation of sleep-promoting centres (e.g. the GABAergic ventrolateral preoptic nucleus, VLPO, of the hypothalamus) and depression of arousal-promoting sites (e.g. the noradrenergic locus coeruleus and cholinergic neurons of the basal forebrain). Broadly, it is thought anaesthetics may affect either the top-down thalamocortical mechanisms, or the above bottom-up arousal networks. However, the full description is likely more nuanced, as cortical regions (in particular the medial prefrontal cortex, mPFC) have been found to constitute an important part of the endogenous arousal network as well<sup>22</sup>.

### 1.1.2 GABAergic anaesthetics and propofol

GABA<sub>A</sub> receptors are ligand-gated ion channels that are ubiquitous in the human brain. GABA binding to the receptor causes a conformational change and increased permeability to anions (mainly chloride ions). This causes membrane hyperpolarisation and neuronal inhibition, making GABA<sub>A</sub> receptors the main inhibitory receptors in the human brain. Each GABA<sub>A</sub> receptor is a pentameric complex composed of subunits that determine its pharmacological properties. Subunit composition, e.g.  $\alpha$ ,  $\beta$ , and  $\gamma$  in a ratio of 2:2:1, differs across the brain and determines sensitivity to anaesthetics and their different behavioural endpoints including memory loss, sedation, and hypnosis<sup>20</sup>.

Propofol (2,6-diisopropylphenol) is the most common anaesthetic induction drug<sup>21</sup>. First approved in the 1980s, its favourable kinetics and side effect profile have made propofol the intravenous anaesthetic of choice for most practitioners. It is a highly lipid-soluble drug prepared as an oil-water emulsion. Its pharmacokinetic properties are detailed in Chapter 4. Briefly, it exhibits rapid plasma clearance, with emergence after a typical 2mg/kg bolus induction dose usually occurring within 8 to 10 minutes<sup>21</sup>. This efficient plasma clearance makes it suitable for use as a continuous intravenous infusion, often as part of total intravenous anaesthesia (TIVA). Such systems most often utilise a mathematical three-compartment model to guide target-controlled infusions (TCI)<sup>22</sup>. Brain effect-site concentrations vary between sedation and deep anaesthesia in the therapeutic range of roughly 1.5-5 $\mu$ g/ml.

In terms of autonomic effects, anaesthetic doses of propofol produce a large decrease in arterial blood pressure with significant vasodilatation and disruption of the baroreflex<sup>23</sup>. Propofol is also a respiratory depressant and it reduces upper airway

reflexes. It shows antiemetic activity, potentially because of its effects on 5HT<sub>3</sub> receptors<sup>21</sup>.

Hypnotic effects of propofol in the central nervous system (CNS) are largely a result of potentiating GABAergic inhibition which leads to neuronal hyperpolarisation. Hypnotic effects appear dependent on propofol binding to the  $\beta$  subunits of the GABA<sub>A</sub> receptor<sup>24,25</sup>. Propofol slows the decay rate of inhibitory synaptic currents by prolonging the opening of GABA<sub>A</sub> channels and allowing greater influx of Cl<sup>-</sup> ions into a cell<sup>26</sup>. It also enhances extrasynaptic tonic inhibition caused by GABA<sub>A</sub> receptors outside the synapse being continuously activated by ambient GABA<sup>27,28</sup>. Different aspects of propofol effects – e.g. memory blockade, loss of consciousness, depression of reflexes – may be due to these phasic (synaptic) and tonic (extrasynaptic) changes, with consciousness loss perhaps preferentially due to tonic inhibition enhancement in specific areas<sup>29</sup>.

On the network-level, functional neuroimaging studies (e.g. positron emission tomography (PET), functional magnetic resonance imaging (fMRI) and electroencephalography (EEG)) of propofol have revealed reduced activity in key regions likely to play a part in supporting consciousness, including the thalamus and precuneus<sup>30,31</sup>, as well as reduced information processing capacity in the default mode network<sup>32,33</sup> and impaired frontoparietal connectivity<sup>34</sup>. This is further discussed in Chapter 2 and Chapter 5.

### 1.1.3 NMDA-acting anaesthetics and ketamine

NMDA receptors are a subclass of ion-permeable glutamate receptors and the major excitatory neurotransmitter receptors in the human brain. They are permeable to Na<sup>+</sup>,

K<sup>+</sup>, and Ca<sup>2+</sup> ions when activated. However, at resting membrane potential and lower, the channel is blocked by a Mg<sup>2+</sup> ion. Membrane depolarisation repels the magnesium ion and allows ion flux. Activation of NMDA receptors requires both glutamate and glycine / D-serine binding. Each NMDA receptor is a complex made of four subunits of three types: GluN1, GluN2, and GluN3. As with GABA<sub>A</sub> receptors above, subunit composition varies between cell types and determines pharmacological properties of the receptor<sup>35</sup>.

Ketamine (RS-2-(2-Chlorophenyl)-2-(methylamino)cyclohexanone) is a phencyclidine derivative first used in humans in 1964<sup>36</sup>. It is a remarkably unique substance that, depending on the dose, produces analgesic, antidepressant, psychedelic, or anaesthetic effects. It is partially water-soluble and highly lipid-soluble, leading to rapid onset of effects and distribution. High clearance results in a short elimination half-life of approximately 2-3 hours with hepatic metabolism into norketamine and hydroxynorketamine before changing to water-soluble molecules excreted in urine. Ketamine is a racemic mixture of two stereoisomers, R (rectus) – ketamine and S (sinister) – ketamine. Of these, S-ketamine is more potent and shows faster clearance and recovery. Efficient clearance allows for continuous ketamine infusions, with target effect site concentrations in a therapeutic range of 0.5-2.2µg/ml. A typical induction bolus of 2mg/kg produces about 10 minutes of surgical anaesthesia<sup>21</sup>.

Unlike most anaesthetics, anaesthetic doses of ketamine do not produce significant respiratory depression and preserve airway reflexes. Ketamine also increases arterial blood pressure, heart rate, and skeletal muscle tone, likely by central sympathetic stimulation. Undesirable tachycardia and hypertension can be blunted by coadministration of benzodiazepines. It does not show antiemetic properties and may worsen nausea<sup>37</sup>. The preservation of airway tone, analgesic properties, and

increased sympathetic activity during ketamine anaesthesia make it particularly useful for emergency settings and in rural areas of developing countries. However, undesirable emergence reactions in about 20% of patients limit its use<sup>38</sup>. These include vivid dreams, hallucinations, and out-of-body experiences, which can cause fear and confusion. These psychomimetic effects in sub-anaesthetic doses (typically <1mg/kg) have however found uses in psychiatric settings and are discussed together with antidepressant effects in Chapters 6 and 7.

Ketamine is classically considered a non-competitive NMDA antagonist, but its pharmacological profile is complex. Apart from NMDA, it also acts on opioid and monoaminergic receptors<sup>39</sup>. The full molecular mechanism behind ketamine hypnosis is likely complex. This can be seen when ketamine is compared to other NMDA antagonists with low anaesthetic potency, such as memantine and MK-801. Differences in NMDA subtype potency (e.g. GluN2A/B vs GluN2C) and off-rate (i.e. being able to escape the channel before closing) may explain some of the discrepancies, but action at other receptors (e.g. HCN1) is likely involved<sup>40</sup>.

At the network level, ketamine shows differences and similarities to GABAergic anaesthetics. Similar to propofol anaesthesia, at doses past loss of responsiveness, dysfunction in communication between cortical areas captured by resting state fMRI connectivity is seen (e.g. fronto-parietally within the default mode network)<sup>41</sup>, with loss of EEG-derived fronto-parietal connectivity<sup>34</sup>. Unlike propofol, the repertoire of brain states remains similar to disconnected conscious states such as dreams and hallucinations, perhaps due to preserved cross-modal sensory transfer<sup>34,41,42</sup>. Brain states underlying ketamine effects are discussed in more detail in Chapter 6.

#### 1.1.4 Beyond hypnotics: opioids and muscle relaxants

A full review of the mechanisms underlying pain, analgesia, and neuromuscular blockade is beyond the scope of this thesis, and has been done elsewhere<sup>43</sup>.

Briefly, whilst their role in anaesthesia is coming under scrutiny due to the opioid epidemic<sup>44</sup>, opioids still form a key part of most perioperative analgesia plans. By acting as spinal and brain  $\mu$ -opioid agonists, opioids inhibit ascending transmission of nociceptive signals, exert an antinociceptive effect, and alter central affective responses to pain. A wide variety of synthetic and natural opioids are present in clinical practice and include short-acting (remifentanyl, alfentanyl), intermediate-acting (sufentanyl, fentanyl) and long-acting (morphine, oxycodone, codeine) opioids. They act synergistically with hypnotics and reduce hypnotic drug requirements<sup>45</sup>. However, reduction in anaesthetic concentrations is not complete and opioids are not complete anaesthetics. Side effects include bradycardia, respiratory depression, post-operative nausea and vomiting, development of tolerance, and opioid-induced hyperalgesia<sup>46</sup>.

Neuromuscular blockade to achieve skeletal muscle relaxation forms a key part of safe anaesthetic practice enabling tracheal intubation and optimal surgical conditions. Since introduction of succinylcholine in 1952, a variety of muscle relaxants have been introduced into clinical practice. Neuromuscular blocking drugs (NMBDs) exert their paralytic effect by blocking transmission of nerve impulses at the neuromuscular junction. They can be classed into two main groups, depolarising NMBDs that mimic acetylcholine (e.g. succinylcholine) and nondepolarizing NMBDs that interfere with cholinergic action (e.g. pancuronium, rocuronium, cisatracurium).

## 1.2 Electroencephalography and its uses in anaesthesia monitoring

Due to its ability to capture brain activity non-invasively with excellent temporal and moderate spatial resolution, as well as its potential for clinical translation, electroencephalography data was chosen as the main modality for this thesis. This technique and some common output metrics are introduced in this section.

### 1.2.1 General and historical overview

Localisation of mental faculties in the brain was already by accepted by some classical physicians including Hippocrates and Galen. However, for centuries, functional localisation was erroneously linked to the ventricles<sup>47</sup>. Even as human understanding of anatomy progressed, *in vivo* human neurophysiology lagged behind, largely due to a lack of non-invasive imaging techniques.

The electroencephalogram (EEG) was one of the first tools to dramatically change this. Neural communication in the brain happens through small ionic electrical currents that lead to measurable (albeit small, on the order of  $\mu\text{V}$ ) differences in electric potential on the scalp. Once it was understood that not only is the 'seat of the soul' in the brain, but also that it communicates and organises electrically, *the electric brain* was born<sup>48</sup>.

The typical historical narrative of EEG and its use during anaesthesia goes as follows. First, in 1875, Richard Caton noted electrical activity in monkey and rabbit brains<sup>49</sup>. Half a century later, after decades of trying unsuccessfully, Hans Berger first recorded electrical activity from a human brain in 1924 (published in 1929<sup>50</sup>) and coined the term 'EEG'. His findings were not taken seriously until Adrian and Matthews replicated

his findings in 1934<sup>51</sup>. Shortly after, EEG research expanded into different pathological and pharmacological conditions. In 1937, Gibbs, Gibbs, and Lennox were the first to suggest EEG could be useful during monitoring of surgical anaesthesia<sup>52</sup>, but early systems were too cumbersome to use clinically. It wasn't until 1996 that the first widespread commercial EEG depth of anaesthesia monitor, the proprietary Bispectral Index (BIS™) was approved in the United States<sup>53</sup>. Since then, several other monitors have appeared (e.g. Narcotrend<sup>54</sup>, GE Entropy<sup>55</sup>) although their use remains limited. This is in part due to the monitors not tracking certain anaesthetics (e.g. ketamine, nitrous oxide)<sup>8</sup> accurately, and research into individualised brain-based anaesthetic markers is ongoing.

The above account is richer than it may seem. Hans Berger's motivations were partly pseudoscientific, as he had a belief in telepathic communication stemming from a traumatic horse fall where his sister supposedly felt he was in a bad condition despite being far away<sup>56</sup>. Berger was described by others as introverted and anxious in social situations<sup>ii</sup>. Whilst it was Gibbs, Gibbs, and Lennox (1937) who first suggested its use as part of surgical anaesthesia monitoring, it was Berger who first recorded EEG during human anaesthesia, first with chloroform and then with hexobarbital in 1933<sup>60</sup>, with Grey Walter recording ether and nitrous oxide EEG in 1936<sup>61,iii</sup>. The first automatic

---

<sup>ii</sup> Berger's historical record may meet key modern diagnostic criteria for autistic spectrum disorder. He showed persistent deficits in social communication ("avoidant of social contact, found it difficult to communicate with staff and patients alike"<sup>57</sup>) and restricted / repetitive patterns of behaviour ("his days resembled one another like two drops of water"<sup>56</sup>). Not enough is known about his childhood to confirm this, but he also suffered from conditions significantly more common in autistic adults without intellectual disability (congestive heart failure and severe depression leading to his suicide in 1941)<sup>58</sup>. It should also be noted he collaborated with the Nazi regime, though he was not a party member<sup>59</sup>.

<sup>iii</sup> Erna Leonhardt Gibbs was in fact another interesting character, obtaining the 1958 Woman of the Year from the American Woman's Association as a result "the most comprehensive study ever made by a single individual in specialized brain research"<sup>62</sup>.



control of anaesthesia through EEG was proposed in 1950<sup>63,64</sup>, though, as mentioned, EEG did not gain in clinical prominence until the 2000s.

Electroencephalography offers a unique view into the brain. Simultaneous action of millions of neurons is associated with synchronous postsynaptic currents that can be volume-conducted to the scalp, producing the observed EEG signals. In theory, it can offer a very high (kilohertz) temporal resolution that captures direct neuronal communication, unlike functional magnetic resonance imaging and related techniques that rely on the (slower) blood flow or metabolic response. Furthermore, unlike magnetoencephalography, it can be used in freely-moving subjects in rooms without shielding and is relatively inexpensive.

However, like all other brain recording methods, EEG comes with significant limitations. Intrinsically, it is biased towards synchronised cells, and the signal thus likely represents the activity of less than 5% of active neurons, possibly much less<sup>65</sup>. Furthermore, due to volume conduction, spatial resolution of EEG is poor, at best a few centimetres. Because of the small magnitude of brain signals, EEG is also susceptible to a large number of artifacts; chiefly ocular potentials and muscle noise from the frontalis and temporalis muscles, but also the skin potentials, cardiac potentials, and external electric fields (e.g. 50Hz mains noise or a surgical diathermy). Experiments with paralysed but awake subjects have demonstrated that the EEG signal above ~30Hz is dominated by muscle noise<sup>66,67</sup>. Quality of the EEG recording can be improved by various pre-processing methods including band-pass filtering (typically 0.5-30Hz), removing gross movement artifacts, and performing pre-processing with blind source separation techniques (chiefly independent component analysis, ICA) to remove eyeblink, cardiac, and muscle artifacts<sup>68</sup>.

Apart from analysing the EEG in the time domain, a standard frequency domain approach is to divide the signal into canonical frequency bands. These include the slow and delta bands (<4Hz), theta (4-8Hz), alpha (8-13Hz), beta (14-30Hz), and gamma (>30Hz), though specific frequency limits vary between studies<sup>65</sup>. This analysis can be extended into the spectrogram, where power in each frequency bin is examined over time. Higher-order analyses exist, such as looking at cross-frequency coupling or measures of statistic dependence, also known as functional connectivity. These include measures of phase coherence, such as the phase locking value or phase lag index, which are motivated by the theoretical efficiency of using coherent signals for communication in the brain<sup>69</sup>.

### 1.2.2 EEG changes under general anaesthesia

Pharmacological alterations of EEG are in general complex and depend on the drug combination, dose, and cortical location studied. However, for GABAergic anaesthetics, there exists a set of common dose-dependent frontal EEG patterns displayed in the majority of patients – though with significant between-patient variability (Figure 1.1)<sup>70,71</sup>.

First, at mild sedation levels, paradoxical excitation of the EEG can be observed, characterised by beta activity around 12-20Hz. As the patient loses responsiveness, the EEG slows and shows frontal alpha-spindles around 8-12Hz. This anteriorisation of the EEG was first described in 1977<sup>72</sup> and is one of the reasons why frontal EEG monitoring is not only convenient, but potentially useful. After loss of responsiveness, slow / delta waves (<4Hz) become more prominent. This alpha-delta pattern was already identified by the early pioneers mentioned above<sup>52,60</sup>, with the slow (<1Hz)

oscillation studied by Steriade and colleagues<sup>73</sup>. At deep anaesthetic concentrations, burst-suppression occurs, leading to periods of EEG suppression (low amplitude <5 $\mu$ V for seconds to minutes) and bursts of high-amplitude activity lasting a few seconds. At even deeper concentrations, the EEG becomes continuously suppressed until it becomes isoelectric. Burst-suppressed and isoelectric traces are pathological patterns also seen in hypoxic injury and severe hypothermia<sup>74</sup>. Burst-suppression may be reflective of metabolic conditions<sup>75</sup> and may occur in a limited cortical region<sup>76</sup> with asynchronous bursts<sup>77</sup>. Intra-operative burst-suppression has been associated with a higher incidence of postoperative delirium<sup>78</sup>. However, it is not clear whether this association is causal, or simply reflective of underlying patient vulnerability<sup>79</sup>.

The slow/delta-spindle pattern observable on the EEG is generated by the thalamocortical system<sup>80,81</sup>. Slow waves measured on the scalp are characterised by a large numbers of neurons switching between UP states of high activity and DOWN states of relative silence<sup>73</sup>. The slow oscillation can persist after thalamic lesions and can be generated in isolated *in vitro* cortical slices, so it was initially thought to be cortically generated<sup>82</sup>. However, more recently, an essential contribution of the thalamus to *in vivo* slow oscillations has been revealed<sup>83</sup>, likely particularly important in initiating UP states and determining the oscillation frequency<sup>84</sup>. Cortical slow waves have been shown to be travelling waves on the scalp, predominantly in the anterior to posterior direction<sup>85,86</sup>. Spindles are generated thalamically and travel to the cortex anteriorly, forming loops between GABAergic thalamic reticular neurons and thalamocortical neurons. With thalamocortical neurons hyperpolarised, sensory information gating at the thalamus becomes disrupted<sup>87</sup>.

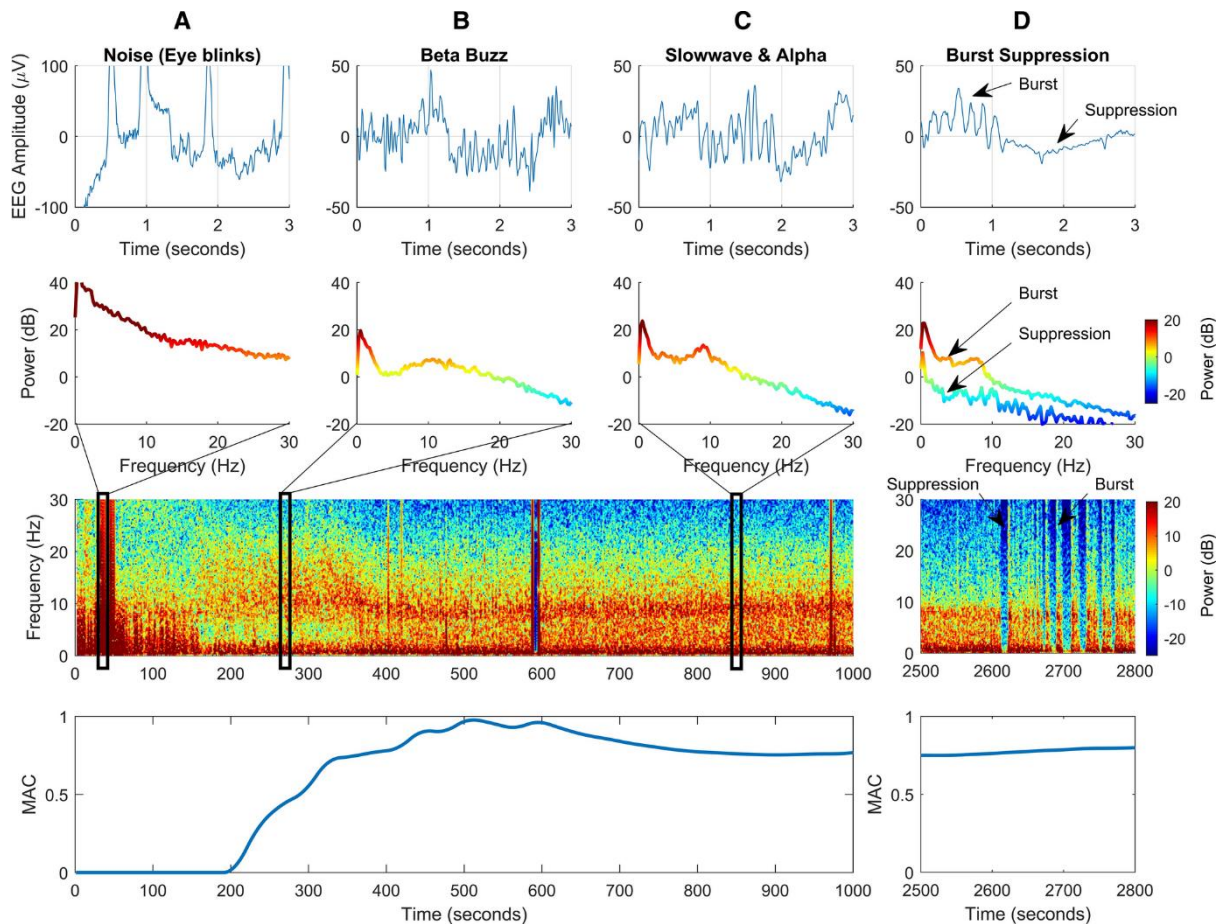


**Figure 1.1: Classical frontal anaesthetic EEG responses.** Shown are the raw EEG (row 1), power spectra (row 2), spectrogram (row 3), and volatile anaesthetic concentration (row 4). With increasing concentrations, the pattern transitions from noise (A) to paradoxical beta activity (B), slow/alpha rhythm (C), and burst suppression (D). This figure has been reproduced with permission from Figure 2 in <sup>71</sup> (licence 5536531205123).

The above patterns hold for commonly used hypnotic drugs, and they form the basis for current commercially available proprietary depth of anaesthesia indices<sup>88</sup>. However, care must be taken in real-world anaesthetic scenarios. Firstly, dissociative anaesthetics including ketamine and nitrous oxide can have an EEG dominated by increased high-frequency activity, likely driven by corticothalamic depolarisation, with decreased alpha oscillations<sup>89</sup>. They can produce slow waves, but sometimes in unusual ways, such as transient delta increase on introduction of nitrous oxide<sup>90</sup>.

Secondly, coadministration of opioids and other drugs can further complicate EEG interpretation. Depending on the level of surgically induced noxious stimulation, opioids may restore the alpha oscillation and modestly increase slow waves, or conversely decrease the EEG power<sup>71,91</sup>. Brainstem arousal modulators including atropine, scopolamine, or dexmedetomidine can also increase delta activity, even in absence of unconsciousness<sup>92</sup>. Neuromuscular blockade can decrease muscle artifacts in the EEG and can be falsely interpreted as decreased gamma power<sup>66</sup>. Thirdly, EEG patterns change throughout development and aging, with a broad trend to lower slow-wave power in older adults, and certain disorders result in high delta power even whilst awake<sup>93</sup>. Fourthly, induction and emergence from anaesthesia are not symmetric, and hysteresis (neural inertia) may be present<sup>94,95</sup>. These factors can result in misleadingly high or low values of proprietary EEG-derived depth of anaesthesia indices and present a challenge for titrating anaesthesia to the EEG<sup>96</sup>.

Novel analyses that move beyond analysing the power spectrum in anaesthesia are being increasingly studied in an attempt to unify distinct drug patterns that all lead to clinical loss of consciousness. These include examining the 'noise' in the EEG, i.e. background aperiodic activity (also termed fractal activity or pink / brown noise), which may reflect overall balance of cortical inhibition and excitation<sup>97</sup>. Other approaches focus on studying complexity of the EEG, based on theories of consciousness that suggest specific forms of information processing with sufficient complexity are necessary to maintain consciousness<sup>98–100</sup>. A potential advantage of such theoretically motivated formulations of consciousness is the ability to extend them to different imaging modalities and conditions including sleep, disorders of consciousness, and altered states of consciousness<sup>32,101,102</sup>.

### 1.2.3 Slow-wave saturation

For a variety of anaesthetics including propofol, halogenated ethers, and ketamine, it has been shown that slow-wave activity in the EEG (SWA; typically 0.5-1.5Hz) not only increases with increased anaesthetic concentration, but saturates and forms a plateau past the point of loss of behavioural responsiveness but prior to peak anaesthetic concentration (slow-wave activity saturation, SWAS)<sup>94,103</sup>.

Existing studies demonstrate the exciting potential of SWAS as an anaesthetic endpoint, but several key areas of ongoing investigation remain. These include fundamental scientific questions about how SWAS relates to underlying receptor neurobiology, as well as practical investigations into how SWAS compares with existing depth of anaesthesia indices and whether surgery at SWAS is feasible and improves clinical outcomes.

### 1.2.4 Autonomic nervous system and cortico-cardiac interactions

Human neurophysiology is a complex concert that extends beyond the brain, one full of recurrent loops and both top-down and bottom-up interactions<sup>104</sup>. The autonomic nervous system is traditionally responsible for involuntary activities essential to survival including cardiovascular and gastrointestinal homeostasis<sup>105</sup>. Managing autonomic responses is a key part of anaesthetic management aiming to avoid deleterious effects and is routinely carried out as part of monitoring the heart rate and blood pressure. The autonomic nervous system is sub-divided into two major branches, the sympathetic (“fight or flight”) nervous system and the parasympathetic (“rest and digest”) nervous system. Direct effects of propofol and ketamine on autonomic

responses were described above and are discussed further in Chapter 3 and Chapter 6; here a brief overview of the system is given.

The sympathetic nervous system originates from thoracolumbar regions of the spine. It activates in presence of a challenge to increase the heart rate, arterial pressure, and cardiac output, with blood diverted from viscera to skeletal muscle. Endogenously, this is achieved chiefly through action of norepinephrine, epinephrine, and dopamine action on  $\alpha$ - and  $\beta$ -adrenergic receptors at the target organ synapse.

The parasympathetic nervous system originates in the midbrain, medulla oblongata, and sacral part of the spine. Here, the target organs possess muscarinic acetylcholine receptors, and muscarinic antagonists can thus also be deployed to increase heart rate (anticholinergics including atropine and scopolamine). Most descending parasympathetic traffic is mediated by the vagus nerve (cranial nerve X). It supplies the heart, respiratory tract, liver, and most of the gastrointestinal system. Curiously, contemporary estimates indicate that 70%-90% of vagal fibres are visceral afferents<sup>106</sup>. Through ascending vagal pathways, visceral signals have an important role in shaping our conscious experience, including interoception and emotional processing<sup>107</sup>. Complex interactions, beyond just top-down control, between peripheral and central physiology have been recognized, with e.g. heart-brain interactions altered under anaesthesia<sup>108,109</sup>.

## 1.3 Thesis outline

There are various ways to define a 'brain state' under the influence of general anaesthetics. Broadly, this thesis uses a recent definition by Greene et al, who define a brain state as brain state as "a pattern of brain activity or functional coupling that

emerges from, and has consequences for, physiology and/or behaviour”<sup>110</sup>. In the first few chapters, the focus is on the state of slow-wave activity saturation. Current EEG-based anaesthetic monitors have been shown to inadequately identify patients who are conscious during surgery<sup>111–113</sup>. This may be due to monitoring of only frontal activity, particularly in light of some theories postulating a posterior ‘hot zone’ necessary for consciousness<sup>114–116</sup>, with different dose-dependent frontal / parietal behaviour observed<sup>117</sup>. Slow-wave activity saturation may indicate individualised perception loss, but it is not known how SWAS unfolds across the cortex. Furthermore, individual slow waves may be linked to low states of cortical complexity, potentially having a causal role in disrupting information flow under anaesthesia<sup>118,119</sup>. In Chapter 2, I examine slow-wave activity saturation across the cortex, linking it to local GABA<sub>A</sub> receptor density. I further study the relationship between SWAS and other proposed anaesthetic indices, the clinically used Bispectral Index and the well-researched Lempel-Ziv-Welch complexity.

Next, the heart shall appear for the first time, challenging how we should think about a ‘brain’ state. In sleep, slow waves have been linked to individual heart beats<sup>120</sup>. In Chapter 3, I show this is also the case in propofol anaesthesia. Furthermore, the controversial effect of propofol on heart rate and autonomic activity is studied, leading to a hypothesis of a common brainstem generator.

Slow waves are known to be highly non-sinusoidal<sup>121</sup>. This means standard Fourier-based analysis may miss important morphological features, such as those that change with aging<sup>122</sup>. In Chapter 4, I develop and validate a new method to decompose oscillatory modes, iterated masking empirical mode decomposition (itEMD). Applying it to propofol EEG suggests three low-frequency oscillators may be present, linking it to multiple types of slow waves proposed in sleep<sup>123–125</sup>.



Traditionally, brain activity has been seen as continuously unfolding. However, recently, it has been shown brain activity can be represented as switching between discrete states that can be found using techniques such as Hidden Markov Models<sup>126,127</sup>. These states have been shown to have physiological relevance, including in sleep<sup>128</sup> and ketamine anaesthesia<sup>129</sup>. In Chapter 5, I apply Hidden Markov Modelling (HMM) to study state switching during propofol anaesthesia. I then explore data-driven heart-brain HMM states. Finally, I push the HMM methodology to test simulated low-density EEG montages that would be easier to use in clinical settings.

Finally, we turn to ketamine. It has been proposed that the acute dissociative ketamine state may mediate its antidepressant effects<sup>130</sup>, but this remains controversial<sup>131,132</sup>. In addition, ketamine administration in psychiatric settings is currently most often done without any monitoring of the brain. In Chapter 6, I examine the neurobiology underlying sub-anaesthetic ketamine dissociation and find HMM brain states underlying dissociative phenomenology, as well as consider how these translate to low-density EEG montages. Building on this, in Chapter 7 I present results from an observational clinical study of EEG recorded during routine ketamine treatment of depression, which I devised and ran in collaboration with Oxford Health Foundation Trust.

In the final chapter, I explore recurrent themes in the thesis and synthesise my results with existing literature and clinical practice. I consider limitations and future directions of the work, as well as its significance for the wider project of explaining the neural mechanisms of anaesthetics and using this to improve anaesthetic patient care.



# **2 Neurobiology of slow-wave saturation and its relationship with existing anaesthetic markers**

## **2.1 Introduction**

Several commercially available EEG-based depth of anaesthesia monitors exist. These include the Bispectral Index (BIS, Covidien, Mansfield, MA, USA), Entropy module (GE Healthcare, Medical Diagnostics, Amersham, UK), and Narcotrend monitor (MonitorTechnik, Bad Bramstedt, Germany). Their proprietary software differs, but broadly they track the reduction in higher EEG frequencies and increases in low-frequency activity<sup>88</sup>.

However, the currently available depth of anaesthesia monitors may not be better than traditional vital sign monitoring at preventing accidental awareness<sup>133</sup>. Their use remains limited, with only about 2.8% of general anaesthetics in the UK being monitored with processed EEG in 2013<sup>1</sup>, rising to 19% in 2023<sup>7</sup>. This rise may be in part due to 2012 National Institute for Health and Care Excellence (NICE) and 2018 guidelines from the Association of Anaesthetists (AAGBI) recommending the use of EEG monitoring in at-risk patients and in all cases of total intravenous anaesthesia (TIVA)<sup>134</sup>. A recent survey of predominantly European anaesthetists showed that hypnotic monitoring is considered important and appetite for such monitoring is present, but a lack of knowledge of relevant algorithms exists<sup>135</sup>.

Next-generation individualised EEG signatures of adequate hypnosis and loss of perception are needed. Slow-wave activity saturation (SWAS) is being investigated as one such potential marker<sup>31,94</sup>. At SWAS, sensory processing revealed by functional MRI was found to be severely impaired, suggesting that SWAS may represent an individualised loss of perception marker<sup>31,136</sup>. Slow-wave activity saturation is characterized by two key parameters; firstly, power at SWAS ( $P_{SWAS}$ ), which correlates with grey matter volume and decreases with age<sup>31,94</sup> suggesting it is reflective of the number of neurons undergoing a slow oscillation, and secondly, the hypnotic concentration at SWAS ( $C_{SWAS}$ ). In a large routinely collected clinical dataset with  $N=393$  individuals induced into general anaesthesia, SWAS was identified in 92% of patients, with failed fitting largely attributable to artefacts or insufficient anaesthetic doses. These patients received a variety of co-induction agents including paralytics and opioids, suggesting SWAS is potentially a robust clinical target for anaesthesia titration. However, in order to support clinical translation of SWAS, more needs to be known about its neurobiological basis and relationship with existing depth of anaesthesia measures. For instance, frontal monitoring has been shown inadequate at recognising covert consciousness<sup>111</sup>, which could be due to relevant features not being frontal<sup>114</sup>.

The BIS monitor is the most widely used clinically<sup>137</sup>. It aims to capture anaesthetic depth with a single parameter, the Bispectral Index, a number ranging from 0 to 100 with 40-60 considered adequate anaesthetic depth. Due to the popularity and use in existing research and clinical practice of this index, it was chosen here for a comparison with SWAS. The exact Bispectral Index algorithm remains proprietary, but insights into its workings have been made. The BIS index is the weighted sum of three parameters: the 'Beta ratio', quantifying relative loss of high-frequency power, the

‘Synch-Fast-Slow’, measuring relative increase in delta power, and the ‘Suppression Ratio’, which tracks the percentage of time for which the EEG is suppressed at high anaesthetic doses<sup>88</sup>. Importantly, the BIS algorithm was recently reverse-engineered into an open-source implementation that was virtually indistinguishable compared to the native BIS values when applied to real anaesthetic EEG data<sup>138</sup>. This implementation suggests the BIS is largely dependent on the relative high- to low-frequency power, without computation of the bispectrum being necessary.

The dependence on high-frequency activity makes the BIS index especially susceptible to electromyographic (EMG) muscle noise. In a rare study of volunteers (anaesthetists) undergoing awake paralysis with rocuronium or suxamethonium, the BIS decreased to <60 (suggesting adequate anaesthesia), sometimes for several minutes, despite no changes to awareness<sup>96</sup>. This is concerning, as cases of accidental awareness can be most traumatic and difficult to recognise during uses of neuromuscular blockade drugs<sup>1</sup>. As BIS is based on population averages and not a scientifically sound hypnotic end-point, BIS also increases with age, further complicating its interpretation<sup>139</sup>.

Brain complexity has also been linked to conscious processing and awareness, with decreased global complexity observed across a range of unconscious states including anaesthesia, sleep, and coma<sup>98,99</sup>. Measures of brain complexity that reliably track consciousness are under development and include the validated perturbation complexity index (PCI)<sup>102</sup>. Using such measures clinically to monitor possible covert states of consciousness in coma and anaesthesia remains a key translational goal of both neuroscience and anaesthesiology<sup>140–142</sup>. Electrically, as outlined in Chapter 1, brain activity under propofol is characterized by large-scale cortical oscillations between up states of neuronal firing and down states of relative neuronal silence. Such

oscillations give rise to low-frequency (~1Hz) slow waves observable on spontaneous EEG<sup>73</sup>. These slow oscillations (and down states in particular) are associated with low complexity states, and may play a causal role in disrupting complexity<sup>117,118,143</sup>.

Lempel-Ziv complexity is a measure of data compressibility and relates to the number of non-redundant patterns in the signal<sup>144,145</sup>. It has emerged as a leading method to track brain complexity across different states of consciousness, either using changes in brain activity evoked by stimulation<sup>99,102</sup> or in the spontaneous EEG<sup>146</sup>. Changes in Lempel-Ziv complexity have also been shown across different vigilance states in sleep<sup>147</sup> and between hemispheres in patients where only half the brain is anaesthetized<sup>148</sup>. Lempel-Ziv complexity varies between brain regions during light sedation, with frontal areas having the largest increases in complexity<sup>149</sup>. This spatial organisation of complexity thus likely has important implications for clinical monitoring as well as for our understanding of brain complexity structures that support consciousness.

In this chapter, I investigated aspects of SWAS relevant for clinical translation. SWAS is defined in terms of the drug concentration ( $C_{\text{SWAS}}$ ) required to achieve SWAS, and the slow wave power when held at this EEG endpoint ( $P_{\text{SWAS}}$ ). However, it is unknown how these SWAS parameters vary across different brain regions; this may have important implications for optimal depth of anaesthesia monitoring. Using a dataset of an ultra-slow propofol infusion in healthy volunteers published previously<sup>31</sup>, I examined how SWAS varies spatially. A preliminary analysis of SWAS across the scalp was undertaken during my MPhys project, focusing on hysteresis modelling<sup>150</sup>. Here, that analysis was re-done to correct for minor hypnotic dosing errors and extended as outlined below.

I was interested if spatial variation of SWAS was linked to underlying anaesthetic receptor targets. Propofol, the most commonly used agent for surgical anaesthesia induction, is a key example of a hypnotic drug acting on gamma-aminobutyric acid A (GABA<sub>A</sub>) receptors and was chosen as the model for this chapter. GABA<sub>A</sub> receptors are heterogeneously distributed throughout the brain<sup>151–153</sup>. Thus, I hypothesised potential topographical differences in slow-wave parameters would be explicable by differing local GABA<sub>A</sub> receptor density, the main receptor target for propofol. Regional metabolic reductions caused by propofol are significantly linked to local *ex vivo* collected GABA receptor density measurements<sup>154</sup>. Recently, a quantitative *in vivo* high-resolution atlas of local GABA<sub>A</sub> receptor density was developed using [<sup>11</sup>C]flumazenil Positron Emission Tomography (PET)<sup>155</sup>. These GABA<sub>A</sub> binding values have been used to model brain dynamics extracted from functional magnetic resonance imaging (fMRI) in propofol anaesthesia<sup>156</sup> and disorders of consciousness<sup>157</sup>, suggesting differences in regional GABA<sub>A</sub> expression are important for explaining propofol's effects on the brain. I combined the results from this *in vivo* atlas with a recent EEG-MRI co-localisation study<sup>158</sup> to compute a scalp projection of GABA<sub>A</sub> receptor density in cortical regions corresponding to the standard 10-20 EEG montage, enabling for a test of my hypothesis by direct comparison with SWAS metrics across the scalp.

Finally, to investigate SWAS in relation to known depth of anaesthesia measures, I compared it to the two important metrics introduced above. First, as slow oscillations may mediate low complexity states, I compared SWAS with brain complexity (quantified by Lempel-Ziv-Welch complexity). Second, due to its prevalence and understanding by clinicians, I compared SWAS with the Bispectral Index (BIS).

## 2.2 Materials and Methods

### 2.2.1 Data

*Data collection:* This dataset came from the original SWAS study where an ultra-slow propofol infusion was administered in healthy volunteers<sup>31</sup>. A local Research Ethics Committee approved the original experiment and subsequent reanalyses of the data. The data were acquired using a 32-electrode EEG cap (BrainCap MR, Easycap GmbH) at 5kHz sampling rate referenced to FCz (standard 10-20 system). This was collected in N=16 healthy subjects (8 female) during intravenous induction of propofol up to an estimated effect-site concentration of 4 µg/ml. Electrode impedances were kept under 5kΩ. The experiment was separated into 4 main periods: 10 minutes awake, 48 minutes induction, 10 minutes peak anaesthesia and 48 minutes emergence. For details, see the original publication<sup>31</sup>. There were two key behavioural endpoints: the time when the participant lost (LOBR) and recovered behavioural responsiveness (ROBR) to a cognitive auditory word task. Time when the subject achieved slow-wave activity saturation ( $T_{\text{SWAS}}$ )<sup>94</sup> was also calculated, as detailed in the slow wave activity saturation analysis section below.

*Data pre-processing:* EEG data pre-processing was carried out with BrainVision Analyzer version 2.1 (BrainProduct GmbH), custom written MATLAB code (MATLAB 2020a, Math Works Inc.), and the EEGLAB (v2019.1) analysis toolbox. The EEG data were re-referenced to the common average of signals from all EEG channels, leaving 31 independent channels. Bad channel rejection was performed by Dr Di Zang to remove channels with excessive noise or bridging (mean 0.25 channels per subject, range 0-3). All data were down-sampled to 250Hz and band-pass filtered using a phase-preserving third order Butterworth filter (0.5 to 90Hz).



### 2.2.2 Slow-wave activity saturation analysis

To compare changes in complexity and slow-wave power, I analysed the pre-processed broadband EEG data from induction (48 minutes) of each subject. Slow-wave power (0.5-1.5Hz) was calculated using the short-time Fourier Transform spectrogram (4 second windows, 3 second overlap as per previous work<sup>94</sup>). A 4-parameter sigmoid curve (Equation 1; SWA = slow-wave activity;  $x$  = propofol concentration in  $\mu\text{g/ml}$ ;  $r$ ,  $s$ ,  $t$ ,  $u$  are constants)<sup>94</sup> was fitted to the power trace of each electrode from each subject using MATLAB's interior point method (fmincon).

$$\text{SWA}(x) = r + \frac{s - r}{1 + \exp\left(-\frac{x - t}{u}\right)} \quad [1]$$

Power at slow-wave activity saturation ( $P_{\text{SWAS}}$ ) was defined as 95% of the sigmoid maximum. Concentration at SWAS ( $C_{\text{SWAS}}$ ) was defined as the propofol effect-site concentration at SWAS. The baseline slow-wave power was quantified by the  $r$  parameter (hereafter referred to as 'baseline'). An electrode fit was excluded if  $C_{\text{SWAS}}$  was well above the propofol concentration used in the experiment ( $C_{\text{SWAS}} > 4.5 \mu\text{g/ml}$ ), or if  $C_{\text{SWAS}}$  was in the lowest 1<sup>st</sup> percentile and not a real number ( $C_{\text{SWAS}} < 0.8 \mu\text{g/ml}$ ). Subjects with more than 4 excluded electrodes were excluded from subsequent analysis entirely ( $N=1$ ). Topographies of group-mean values of relevant fit parameters were plotted using EEGLAB (baseline,  $P_{\text{SWAS}}$ ,  $P_{\text{SWAS}}$ -baseline,  $C_{\text{SWAS}}$ ).

### 2.2.3 Lempel-Ziv Complexity analysis

There are various ways of computing Lempel-Ziv complexity (e.g. LZ77, LZ78, LZW) that have minor differences in how they build up a dictionary of patterns. In this study, Lempel-Ziv Welch complexity (LZW) was used. This is a version designed for larger

datasets<sup>145,159</sup> that has previously been used to identify a potential prodrome of Parkinson's disease<sup>160</sup>.

The Lempel-Ziv-Welch (LZW) complexity metric<sup>145,161</sup> was extracted by Dr Di Zang to describe complexity of the EEG signal, and was used for this analysis with permission. The code to compute LZW is available at <https://github.com/giulioruffini/StarLZW>. Using the pre-processed EEG signal, LZW complexity matrices were calculated in sliding windows (9s window length, 4s overlap) to explore the temporal dynamics of complexity. Signal was binarized around the mean and normalised by word length (also known as  $\rho_0$ <sup>161</sup>). In local LZW analyses, complexity of each channel was calculated separately.

#### 2.2.4 Topographical relationship of complexity and slow-wave saturation

To explicate connections between slow waves and brain complexity, I compared each electrode's mean LZW complexity and SWAS fit parameters for (i) a baseline period of first 10 minutes of the experiment (propofol effect-site concentration less than 1 $\mu$ g/ml, baseline parameter  $r$  vs mean LZW) and (ii) a 10-minute SWAS period around the peak of effect-site concentration ( $P_{\text{SWAS}}$ ,  $P_{\text{SWAS-baseline}}$ ,  $C_{\text{SWAS}}$  vs mean LZW). Spearman correlation and associated P-values (after appropriate False Discovery Rate multiple comparisons correction; FDR) were used to compare both effects on each electrode (correlation across subjects, N=15) and similarities of spatial patterns (correlation across channels, N=31).

### 2.2.5 Linking SWAS and LZW to local gamma-aminobutyric acid receptor density

To test my hypothesis that SWAS parameters would be linked to propofol's GABA<sub>A</sub> receptor targets, I used a recently developed open-access brain atlas of human GABA<sub>A</sub> benzodiazepine receptor density<sup>155</sup>. To estimate GABA<sub>A</sub> receptor density under each 10-20 EEG electrode, I used previous work localising EEG positions on the cortical surface of the standard MNI-52 brain<sup>158</sup>. Using FMRIB Software Library v6.0 (FSL)<sup>162</sup>, I found the mean GABA<sub>A</sub> receptor density in a 10mm radius sphere centred on the cortical projection point of each surface electrode. Midline and TP electrodes were excluded as the receptor density atlas did not cover those areas. The relationship between the mean GABA<sub>A</sub> density and other parameters of interest (baseline slow-wave power, C<sub>SWAS</sub>, P<sub>SWAS</sub>, P<sub>SWAS</sub>-baseline, LZW at SWAS, LZW at baseline) was tested across N=26 electrodes by computing the Spearman rank correlation coefficient and associated Bonferroni-corrected permutation P-value in MATLAB (function corr).

### 2.2.6 Comparison of SWAS with the Bispectral Index (BIS)

BIS index values were computed using a custom MATLAB implementation of a recently developed and validated emulator<sup>163</sup>. Fz EEG signal was first resampled to 128Hz and re-referenced to TP9 to emulate the BIS montage. Five BIS values were extracted for each subject using the emulator: mean BIS during 10min awake baseline, BIS at loss of behavioural responsiveness (LOBR), BIS when SWAS was achieved, mean BIS during 10min at peak propofol, and BIS at return of behavioural responsiveness (ROBR). These were compared using repeated-measures ANOVA

with post-hoc Tukey's tests. Within-subject variability of BIS during 10min at SWAS was also examined, as was the Spearman correlation of BIS values and power at SWAS across participants.

The dataset analysed in this chapter is available on reasonable request via <https://zenodo.org/record/1168447>.

## 2.3 Results

### 2.3.1 Slow-wave activity saturation (SWAS) across brain regions

Slow-wave activity saturation is a potential individualised marker of loss of perception<sup>31,94</sup>. To explore how this phenomenon varies across the brain, I computed slow-wave power (0.5-1.5Hz) and fitted a sigmoid slow-wave saturation curve for each electrode in each participant (Figure 2.1, also see Methods). This way the baseline slow-wave power, power at SWAS ( $P_{\text{SWAS}}$ ), and concentration required to reach the slow-wave plateau ( $C_{\text{SWAS}}$ ) were extracted at each electrode (Figure 2.2A). In the baseline period, slow wave power was low across the brain but highest pre-frontally (Figure 2.2A(i)). During deep anaesthesia, slow-wave power drastically increased but was still frontally dominant (Figure 2.2A(ii)). Compared to baseline, central and lateral parietal regions showed the largest increases in slow-wave power (Figure 2.2A(iii)).

The concentration required to reach the slow-wave plateau varied across brain regions (within-subject  $C_{SWAS}$  range  $0.85 \pm 0.21$ , median  $\pm$  median absolute deviation; Figure 2.2A(iv)). This effect was consistent between subjects with a repeated-measures ANOVA effect of Channel on  $C_{SWAS}$   $F=12.55$ ,  $P<0.001$ . Fronto-central regions required the highest dose to reach slow-wave activity saturation. The spatial distribution of  $C_{SWAS}$  across the brain was significantly correlated with power change from baseline ( $P_{SWAS}$ -Baseline, Spearman  $\rho=0.8988$ ,  $P<0.001$ ) and its baseline topography ( $\rho=-0.7298$ ,  $P<0.001$ ), but had a weaker correlation with power at SWAS ( $\rho=-0.4194$ ,  $P=0.0263$ ). After correcting for multiple comparisons, correlations at individual electrodes did not show significant associations between  $C_{SWAS}$  and the other slow-wave curve fitting parameters (i.e. Baseline,  $P_{SWAS}$  or  $P_{SWAS}$ -Baseline).

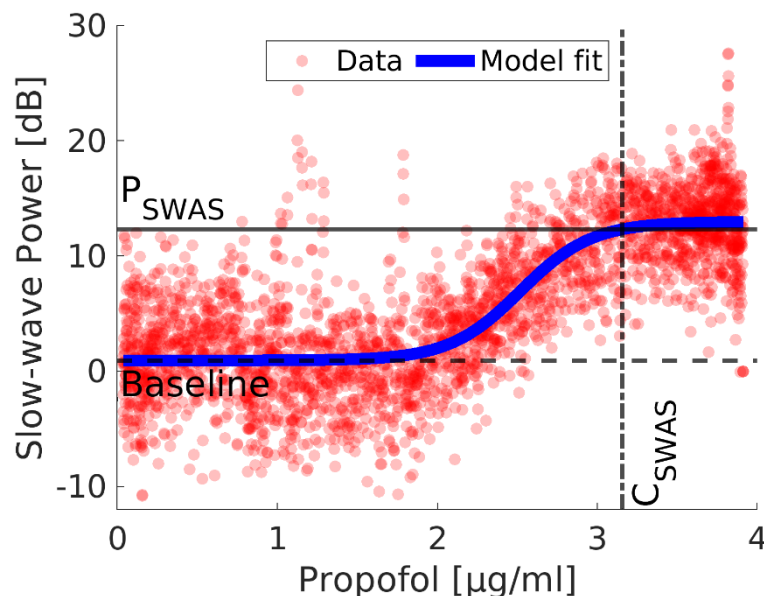
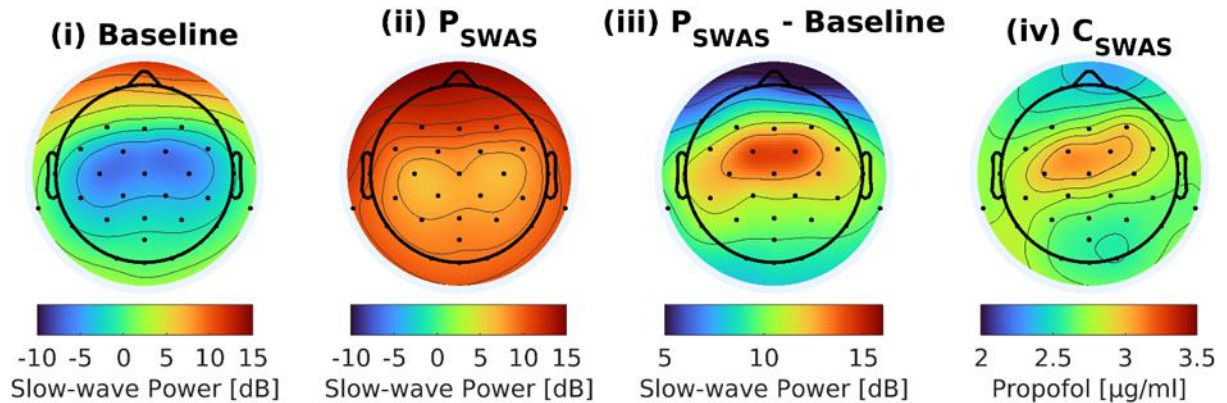


**Figure 2.1:** Slow-wave activity saturation sigmoid modelling. Time-varying slow-wave power (0.5-1.5Hz, 1 red dot = 4s window) is plotted against propofol effect-site concentration. A sigmoid is fitted to find power at slow-wave activity saturation ( $P_{SWAS}$ , 95% saturated), baseline power, and concentration at SWAS ( $C_{SWAS}$ ).

## (A) Slow-wave Parameter Topography



## (B) Slow Waves vs LZW

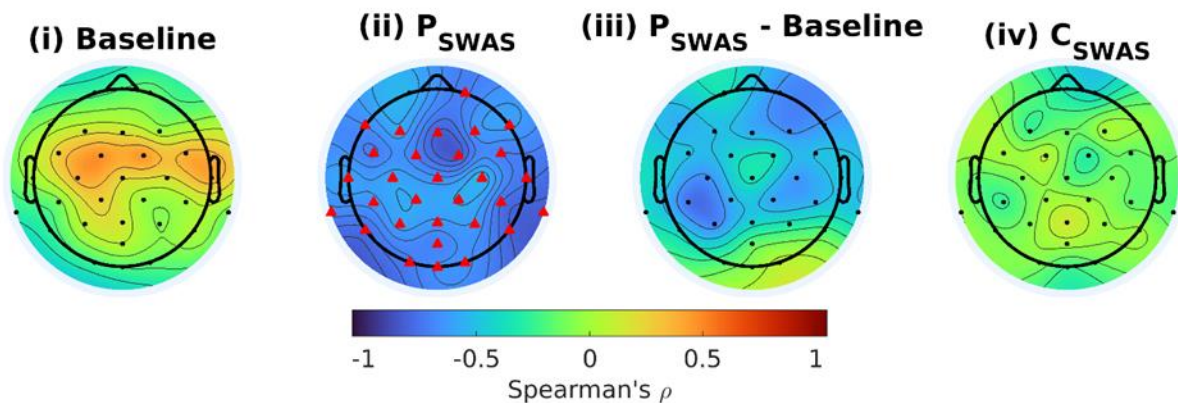


**Figure 2.2:** Local slow-wave parameter topography **(A)** and its relationship with local complexity **(B)**. **(A)** shows the spatial distribution of the (i) baseline slow-wave power, (ii) power at slow-wave activity saturation ( $P_{SWAS}$ ), (iii) increase in power at SWAS compared to baseline, and (iv) concentration required to reach SWAS,  $C_{SWAS}$ . **(B)** shows the Spearman correlation between the slow-wave parameters and local broadband LZW complexity at each electrode location. Red triangles indicate significant single-electrode correlations (FDR-corrected  $P < 0.05$ ).

### 2.3.2 Topographical relationship of complexity and slow-wave saturation

Low brain complexity has been previously linked with low-frequency brain oscillations<sup>118</sup>. I therefore hypothesised high slow-wave power should be associated with low Lempel-Ziv-Welch complexity at each electrode location. I compared mean LZW in the baseline and deep anaesthesia conditions with the slow wave activity saturation sigmoid parameters (Figure 2.2B). In the baseline condition, individual electrodes did not demonstrate a significant correlation between the local LZW complexity and baseline slow-wave power (Figure 2.2B(i)).

In deep anaesthesia, high slow-wave activity saturation power was significantly associated with low local complexity across subjects (FDR-corrected  $P < 0.05$  across almost all electrodes, Figure 2.2B(ii)). Additionally, the average spatial patterns of power at SWAS and local LZW complexity showed a moderate, significant negative correlation (Spearman  $\rho = -0.5375$ ,  $P = 0.0021$ ). When comparing the change from baseline to SWAS, local complexity displayed a negative correlation with the accompanying slow-wave power increases, though this was not significant after FDR-correction (Figure 2.2B(iii)) and the spatial patterns were not significantly correlated ( $\rho = 0.2133$ ,  $P = 0.2482$ ). Concentration needed to reach SWAS ( $C_{SWAS}$ ) was not significantly related to peak anaesthesia LZW at any electrode (Figure 2.2B(iv)), though their spatial patterns were significantly correlated (spatial correlation Spearman  $\rho = 0.7645$ ,  $P < 0.001$ ).

### 2.3.3 Links with local gamma-aminobutyric acid receptor density

To test the hypothesis of topographical differences in SWAS being linked to differing local GABA<sub>A</sub> density, I used a recent *in vivo* atlas of GABA<sub>A</sub> receptor density. Associations between the regional binding site density and the baseline,  $P_{\text{SWAS}}$ ,  $P_{\text{SWAS}}$ -baseline, and  $C_{\text{SWAS}}$  topographies were tested. I found the concentration needed to achieve local slow wave activity saturation ( $C_{\text{SWAS}}$ , Figure 2.3B) was significantly negatively associated with local GABA<sub>A</sub> receptor density (N=26 electrodes, Spearman  $\rho=-0.6861$ , Bonferroni-corrected  $P=0.0018$ , Figure 2.3B). There was no significant correlation with GABA<sub>A</sub> receptor density and the power at SWAS topography ( $P=0.4361$ ), though there was a significant correlation between the slow-wave power at baseline ( $\rho=0.58611$ ,  $P=0.0187$ ) and for the increase in slow-wave activity from baseline ( $\rho=-0.6287$ ,  $P=0.0077$ ). Correlation between GABA<sub>A</sub> receptor density and Lempel-Ziv complexity was also present during slow-wave saturation and peak anaesthesia stages (Supplementary Figure 2.1 with permission of Dr Di Zang; at peak anaesthesia Spearman  $\rho=-0.70$ , Bonferroni-corrected  $P=0.0013$ ).



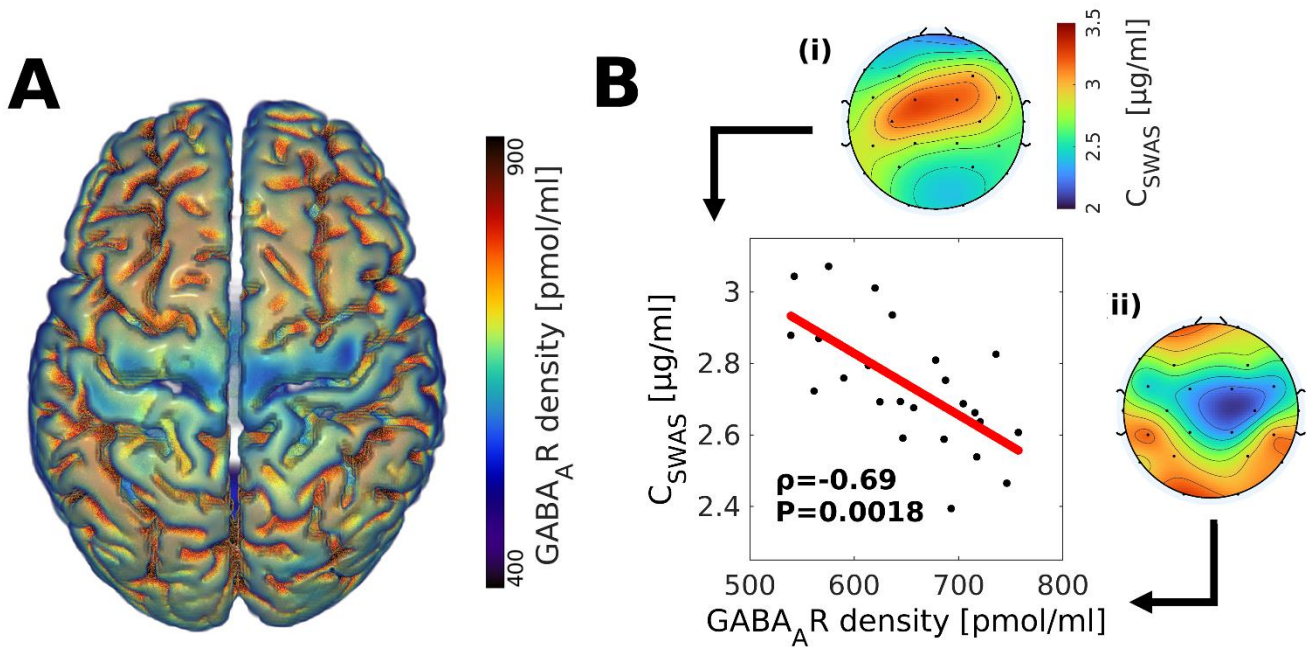


**Figure 2.3:** Spatial differences in slow wave activity saturation and complexity correlate with local GABA<sub>A</sub> receptor (GABA<sub>A</sub>R) density. **(A)** Local brain distribution of GABA<sub>A</sub> receptor density, obtained from <sup>155</sup>. **(B)** Correlation of C<sub>SWAS</sub> with GABA<sub>A</sub> receptor density (N=26 electrodes, Spearman  $\rho = -0.69$ , Bonferroni-corrected  $P = 0.0018$ ). The black dots indicate the individual electrode averages and the linear best fit line is shown in red. The insets indicate where data comes from, i.e., (i) group-average C<sub>SWAS</sub> topography and (ii) local GABA<sub>A</sub>R density from (A) projected onto the standard 10-20 EEG system.

### 2.3.4 Comparison with the Bispectral Index (BIS)

Finally, I was interested in how slow-wave activity relates to the commonly used Bispectral Index depth of anaesthesia measure. In this ultra-slow propofol infusion experiment, BIS values changed significantly (Figure 2.4, repeated measures ANOVA  $P < 0.001$ ). BIS dropped from  $86 \pm 7$  when awake to  $76 \pm 9$  at LOBR ( $P = 0.012$ ),  $49 \pm 4$  at SWAS ( $P < 0.001$ ),  $49 \pm 9$  at peak concentration (n.s.), rising to  $86 \pm 12$  at ROBR ( $P < 0.001$ ; subsequent stages compared). This pattern of BIS decreasing before reaching a floor was observed in every subject (Supplementary Figure 2.2).

For subjects that achieved SWAS, during 10 minutes at SWAS, within-subject BIS values fluctuated, with standard deviation of  $\sigma = 4.7$  (Figure 2.5). The mean BIS value at SWAS correlated with slow-wave power at SWAS across individuals (Spearman  $\rho = -0.675$ ,  $P = 0.010$ , Figure 2.6). A linear best fit indicated  $\text{BIS at SWAS} = 72 - 1.6 * P_{\text{SWAS}} [\text{dB}]$ .

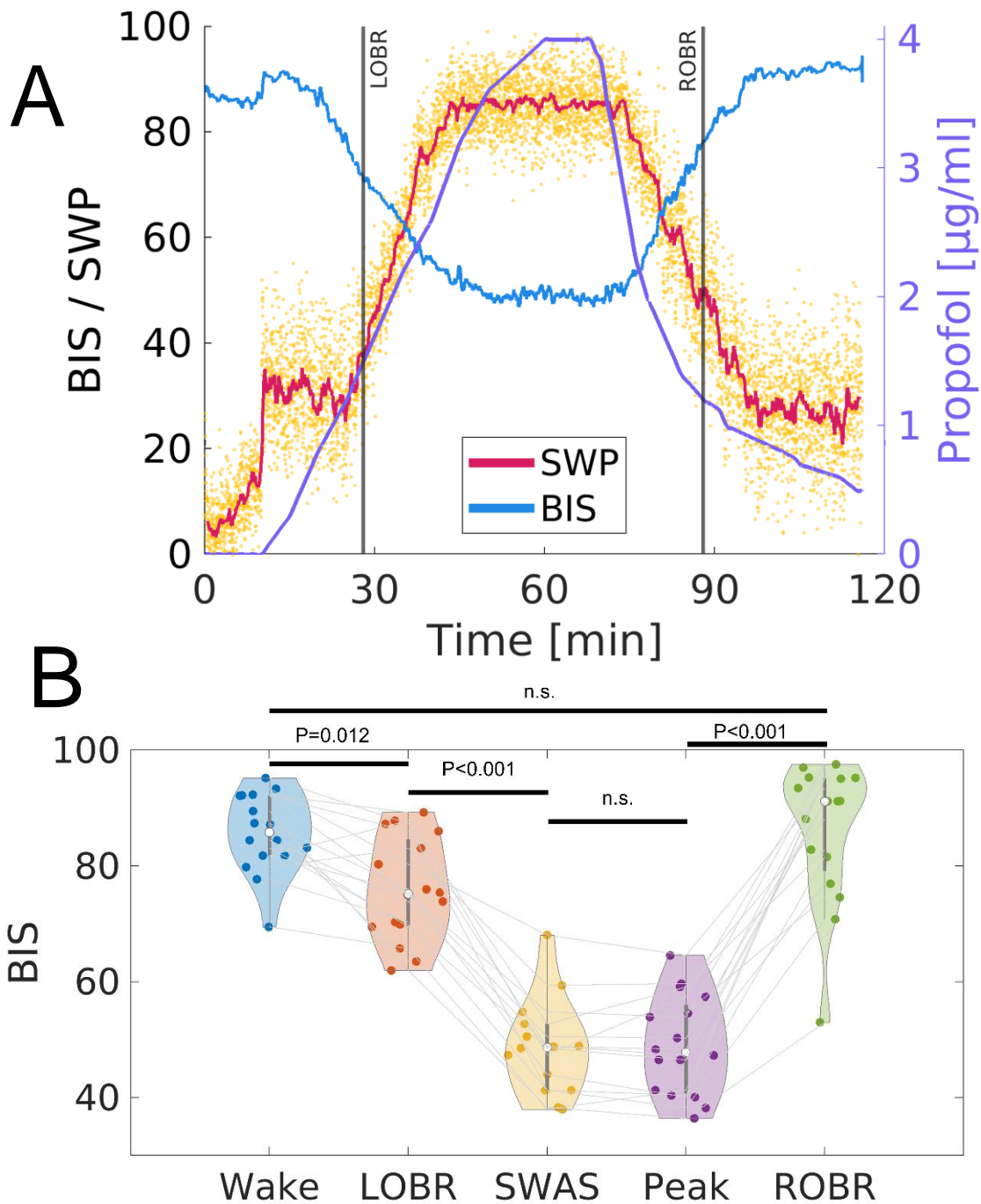


**Figure 2.4:** Bispectral Index (BIS) and Slow-wave power (SWP). **(A)** Group-mean BIS, SWP, and estimated propofol effect-site concentration through the entire experiment, with mean loss (return) of behavioural responsiveness (LOBR / ROBR) indicated. **(B)** Average BIS values for each subject at different experimental stages: awake baseline, LOBR, slow-wave activity saturation (SWAS), peak propofol concentration, and ROBR.

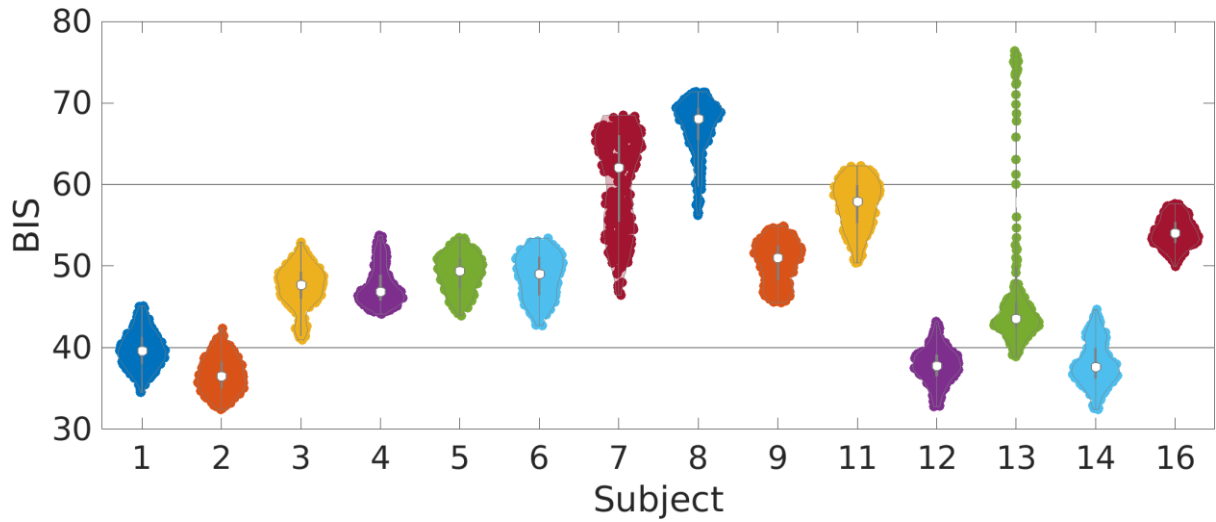


**Figure 2.5:** Variability of the Bispectral (BIS) Index value during 10 minutes at slow-wave activity saturation (SWAS) for each participant that achieved SWAS in the experiment.

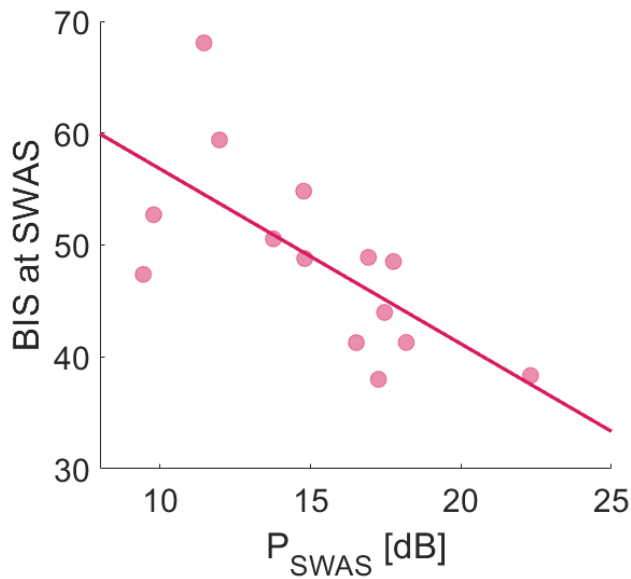


**Figure 2.6:** Bispectral Index at slow-wave activity saturation (BIS at SWAS) against power at slow-wave activity saturation ( $P_{\text{SWAS}}$ ).

## 2.4 Discussion

In this chapter, slow-wave activity saturation (SWAS) was analysed across the cortex and in relation to two existing EEG-based markers of anaesthesia: the Lempel-Ziv-Welch complexity and the Bispectral Index (BIS).

### 2.4.1 SWAS across the cortex

There is an ongoing debate about the distinct roles of frontal and parietal regions in supporting consciousness<sup>115,117,146,149</sup>. Slow waves have traditionally been considered as a frontally dominant phenomenon<sup>86,164</sup>. Identifying regional differences in the SWAS parameters adds nuance to this view. It was indeed observed that slow-wave power (0.5-1.5Hz) at SWAS was highest (pre)frontally both in the awake and deep anaesthesia states. However, the increase in slow-wave power with propofol anaesthesia was greatest across central and lateral parietal regions. These central and lateral brain regions also achieved slow-wave activity saturation at higher doses, with propofol concentrations needed to achieve SWAS varying across the brain on average by 0.85µg/ml. Given the average effect-site concentration at SWAS was around 2.8µg/ml, this is a variation of about 30%, a change in concentration comparable to dose reductions when co-administering ketamine or magnesium as an adjunct<sup>165</sup>, and can thus be considered clinically significant.

Slow-wave activity saturation has been proposed as an individualised loss of perception marker<sup>31</sup> with the slow wave power at saturation ( $P_{SWAS}$ ) linked to the number of neurons undergoing the bistable slow oscillation. Here, this was extended by showing that the regional variation in the concentration needed to reach full bistability ( $C_{SWAS}$ ) is related to target receptor density within those regions. By

projecting a recent *in vivo* atlas of receptor density onto relevant cortical locations, it was shown this reduced regional susceptibility to propofol anaesthesia was attributable to lower local GABA<sub>A</sub> receptor density, as would be expected with GABA<sub>A</sub> as the primary hypnotic target. Effectively, the spatial differences in anaesthetic effect could be explained by differences in local receptor target densities, suggesting a link between this non-invasive brain activity-derived measure and the underlying neurobiology.

Evidence for such receptor-function relationships such as this is growing. For example, changes in GABA<sub>A</sub> have been shown to allow for better modelling of functional magnetic resonance imaging (fMRI) results during anaesthesia<sup>156</sup> and, similarly, serotonin 2A receptor (5HT<sub>2A</sub>R) effects on brain complexity have been shown in psychedelic states<sup>166</sup>. A relationship between regional receptor density and metabolic changes under anaesthesia has also been noted previously<sup>154</sup>, but here the underlying molecular target is linked to an EEG-based anaesthesia marker for the first time.

This finding is supported by other work that has demonstrated broadband slow-wave modulation envelopes posterior regions first after loss of responsiveness<sup>117</sup>. It may therefore be the case that although slow-wave effects start appearing in posterior regions at low doses, higher doses are needed to achieve full bistability of the cortex and the subsequent disruption of fronto-parietal communication<sup>34,117,167</sup>. Furthermore, if whole-brain slow-wave activity saturation is required for complete loss of perception, frontal EEG monitoring, as is commonly used clinically, may underestimate the dose required to achieve complete disconnection from the environment. This may explain some of the 'black swan' cases of positive isolated forearm test (IFT) responses under seemingly adequate alpha-delta frontal EEG patterns<sup>111,112</sup>. The spatial variation is also pertinent in light of recently proposed 'islands of awareness' in patients with

disorders of consciousness<sup>168,169</sup> and work showing local sleep dynamics co-occurring with conscious states<sup>170</sup>.

## 2.4.2 Brain complexity and slow waves

Slow oscillations in the brain may offer a causal explanation of the disrupted information flow and lower complexity observed in anaesthesia<sup>117–119,171</sup>. This can be interpreted within leading theories of consciousness, where information and complexity in the system are hypothesised to underlie features of phenomenal consciousness<sup>98,102,159,172,173</sup>. To support this, it was observed that as the anaesthetic dose increased, the drop in brain complexity tracked the increase in slow-wave power. A significant negative correlation between the spatial organisation of maximal slow-wave power and brain complexity was also found. This is consistent with the idea that slow-wave activity can act as a controlling mechanism for the cortical circuits responsible for the integration of high complexity information from top-down priors and bottom-up data streams<sup>159,174–177</sup>.

Local concentration to reach SWAS demonstrated a statistically significant association with local drug target binding site density. However, there may be multiple types of slow waves with distinct generators and functional roles<sup>123,124,178</sup>, sometimes leading to the appearance of wakeful slow-wave power in certain syndromes<sup>179</sup>. The possibility of distinguishing different oscillation types is explored in Chapter 4. Despite this, slow-wave activity saturation is directly interpretable in terms of cortical slow oscillations and may be easier to compute in real time<sup>31</sup>. Taken together with the fact that there are many ways to compute complexity with slightly differing results<sup>100</sup>, SWAS may

potentially prove more robust to use as an individualised, brain-based depth of anaesthesia index than measures of complexity<sup>94</sup>.

### 2.4.3 Slow waves and the Bispectral Index

Comparing novel metrics to currently used clinical measures of depth of anaesthesia is important, as it allows for better interpretability and easier understanding for anaesthetists without an interest in research. In this work, I showed for the first time that in a cohort of young healthy volunteers undergoing a slow propofol infusion, slow-wave activity saturation (SWAS) corresponds to around BIS 50 at the group average, with significant within-subject and between-subjects variability within a range of around BIS 30 to BIS 70.

It is reassuring to see that most of the time, people at SWAS fall into the manufacturer recommended zone of BIS 40 to BIS 60. However, there are several reasons why the BIS should not be seen as the gold-standard and SWAS may be a superior measure. In this experiment, all participants at SWAS can be taken to be in the same brain state, as supported e.g. by concurrent fMRI<sup>31</sup>. Despite this, BIS at SWAS was linearly related to the slow-wave power plateau. This makes sense in the context of existing literature, as BIS is also higher in older adults, who tend to have lower EEG power<sup>139</sup>. Furthermore, unlike BIS, SWAS is specific for each individual, relating to their number of cortical neurons and GABA<sub>A</sub> receptor densities. In this dataset, SWAS was a well-defined stable end point, with BIS being variable despite the brain likely being in the same physiological state. If anaesthesia was titrated using the BIS 40-60 range, 6/14 of these subjects would have likely experienced either over- or under-anaesthesia. Finally, unlike BIS, SWAS is not as susceptible to high-frequency muscle artifacts or



changes brought on by neuromuscular blockade. However, as the BIS emulator does not incorporate artifact detection and subjects were not paralysed, this could not be directly shown in the present dataset.

#### 2.4.4 Limitations of the study

In this work, I assessed Lempel-Ziv-Welch complexity as it is a well-understood and robust measure<sup>102,146,149,161</sup>. However, it comes with certain limitations. Firstly, it is affected by linear signal properties such as frequency changes<sup>180</sup>. By a phase shuffling surrogate analysis, it was shown this is not the case in our data (data from Dr Di Zang, currently being prepared for a publication). However, LZW is still a so-called type 1 complexity, where maximum randomness is equated with maximum complexity<sup>100</sup>. Other alternative metrics where maximal complexity falls near the critical point between order and chaos exist<sup>181</sup>. They behave similarly in propofol, but for other non-GABAergic agents (e.g. ketamine), this difference may be important and the results here may not generalise. Also, average GABA<sub>A</sub> receptor density and anaesthetic dose response were linked here, but further work would be needed to establish to what extent differences between GABA<sub>A</sub> receptor expression between subjects lead to different individual anaesthetic susceptibility<sup>182</sup>, or whether the former can be used to optimise clinical monitoring. Lastly, different analysis methods may be better suited at finding discrete short-lived states in the data (for instance the Hidden Markov Model<sup>183</sup> explored in Chapter 5). This may be relevant for identifying properties of states associated with worse postoperative prognosis such as burst-suppression<sup>78</sup>, which was only present in one subject in our dataset.



# **3 Effect of propofol on heart rate and its coupling to cortical slow waves in humans**

## **3.1 Introduction**

In the previous chapter, I explored the variation of slow-wave saturation across the scalp, its links to GABA<sub>A</sub> receptor density, and a comparison to existing depth of anaesthesia metrics. Monitoring of the heart and lungs is still the most common method used by anaesthetists to assess anaesthetic depth. Cardiac monitoring therefore forms a key part of anaesthetic practice, and heart physiology has known effects on the brain<sup>108,184</sup>. Thus, in this chapter, I aimed to link the two together and explore propofol's effect on heart rate and its links to slow waves.

Propofol is the most widely used intravenous anaesthetic hypnotic drug<sup>185</sup>. In contrast to halogenated ether anaesthetics, it causes significant cardiovascular depression manifesting mainly as arterial hypotension<sup>186</sup>. However, despite decades of clinical and laboratory use, the effect of propofol on heart rate (HR) remains controversial. In clinical settings, propofol administration has been reported to carry a risk of bradycardia<sup>185,187</sup> and several texts state propofol decreases the heart rate as an accepted fact<sup>188,189</sup>. Others however find propofol to have no effect on the heart rate<sup>186,190</sup>, and much of the literature, especially in laboratory settings, appears to show significant *increases* in heart rate<sup>31,191–195</sup>. Clinical research is complicated by common

co-administration of opioids with bradycardic effects. On theoretical grounds, propofol's effect on the heart rate may be due to modulation of GABAergic neurotransmission to cardiac parasympathetic neurons in the brainstem<sup>194</sup>.

Propofol also affects peripheral nervous activity. This can be indexed by heart rate variability (HRV), i.e. the beat-to-beat variation in heart rate (distinct from the mean heart rate, HR). Specifically, propofol appears to decrease heart rate variability, in part through lowered parasympathetic tone<sup>190</sup>.

In the brain, propofol causes neuronal hyperpolarisation by prolonging GABA-activated opening of chloride channels. At the network level, this causes the cortex to switch between up states of relatively high activity and silent down states. This switching can be observed as slow (~1Hz) waves on the electroencephalogram<sup>73</sup>. As propofol dose is increased, power in the slow-wave band (typically 0.5-1.5Hz) saturates, at which point the thalamocortical system becomes largely isolated from environmental stimuli<sup>31</sup>. By disrupting information processing, these slow waves may have a causal role in sustaining unconsciousness<sup>118</sup>. Similar slow waves are observed in non-rapid eye movement sleep<sup>86</sup>. In sleep, individual slow waves have been linked to changes in autonomic activity including individual heartbeats<sup>120,196,197</sup>.

For this chapter, I first performed an advanced secondary analysis of electroencephalographic (EEG) and electrocardiographic (ECG) data collected in the study presented in Chapter 2. As effects of propofol may depend on induction speed, the ultra-slow infusion provides a unique perspective on propofol effects in this context<sup>198</sup>. My first aim was to study the propofol ECG data. I hypothesised that in this study, free of concomitant medication, propofol would increase the mean heart rate and decrease parasympathetic effects as indexed by high-frequency heart-rate

variability (HRV). My second aim was to explore a possible link between ECG activity and frontal cortical slow waves seen in the EEG. I hypothesised that similar to non-rapid eye movement sleep, slow waves would preferentially occur time-locked to individual heart beats. Finally, to aid clinical translation and see if the heart rate findings held validity in patients, I also analysed clinical EEG and heart rate data from N=96 ASA-2/3 patients collected as part of the AlphaMax study<sup>199</sup>.

## **3.2 Materials and methods**

### **3.2.1 Data collection**

This dataset is the same as that studied in Chapter 2. In brief, 32-electrode EEG and single-channel ECG was collected in N=16 healthy subjects (8 female, age  $28.6 \pm 7$  years) during slowly increasing intravenous infusion of propofol up to an estimated effect-site concentration of 4  $\mu\text{g/ml}$ . The experiment was separated into 4 main periods: 10 minutes awake, 48 minutes induction, 10 minutes peak anaesthesia and 48 minutes emergence. Informed written consent was obtained from all participants; details of this experiment have been published previously<sup>31</sup>.

### **3.2.2. Data pre-processing**

EEG data pre-processing was carried out with BrainVision Analyzer version 2.1 (BrainProducts GmbH), custom written MATLAB code (MATLAB 2020a, Math Works Inc.), and the EEGLAB (v2019.1) analysis toolbox. The EEG and ECG data were re-referenced to the common average of signals from all EEG channels. This was done as theoretical reasons suggest scalp average to be a robust null reference which

decreases volume conduction effects<sup>200</sup>. Independent component analysis and bad channel rejection was performed to remove EEG data with blinks and ocular movements. EEG data were band-pass filtered with a phase-preserving third order 0.5Hz-45Hz Butterworth filter. EEG data was down-sampled to 100Hz and ECG to 500Hz.

### 3.2.3 Time-series ECG analysis

Heart rate, ECG waveform templates, and R-wave amplitudes were extracted using the biospy toolbox (<https://github.com/PIA-Group/BioSPPy/>) which uses Hamilton segmentation<sup>201</sup> to identify individual R-wave peaks, the heart rate, and ECG waveform templates. This was used on each subject to extract an instantaneous heart rate trace and ECG properties, which were subsequently Spearman-correlated to the propofol effect-site concentration.

### 3.3.4 Heart rate variability ECG analysis

To explore correlates of autonomic activity, standard heart rate variability metrics were extracted for 5-minute segments in each subject using the pyHRV toolbox<sup>202</sup> and Spearman-correlated with propofol effect-site concentration at the group level. These included root-mean-square successive difference between R peaks as well as frequency domain metrics. These were ratio of low-frequency (0.04Hz-0.15Hz) and high-frequency (0.15Hz-0.4Hz) heart rate variability and peak frequency in the high frequency band.

### 3.3.5 Slow-wave analysis

Slow-wave activity (SWA) was found as the spectral power in the 0.5Hz-1.5Hz band on the frontal Fz channel. Correlation between SWA and heart rate / effect-site concentration was found using Spearman correlation and its P-value in 5-minute segments. Individual slow waves were identified using standard methodology based on amplitude and duration thresholding implemented in the yasa toolbox<sup>86,120,203</sup>. In brief, each slow wave had to have amplitude in the 99<sup>th</sup> percentile of the 0.5-4Hz amplitude and negative duration between 0.25s and 1.25s. Slow-wave frequency was extracted as inverse of slow-wave period.

### 3.3.6 Cortico-cardiac coupling analysis

Once heartbeats and slow waves were identified, I aimed to test whether heartbeats occur at preferential times in the slow wave cycle. For each slow wave detected, the time delay relative to the slow wave start (initial downward zero crossing) was noted for 8 heartbeats closest to it. Eight beats were chosen at this fully covers a potential 0.5Hz slow wave without overlapping with neighbouring slow waves. This resulted in 8 R-wave to slow wave (RS) intervals, using methodology similar to previous cardio-respiratory analyses<sup>204,205</sup>.

I wanted to know if ECG R-wave to EEG slow wave timings were distributed randomly or in phase with the slow wave onset. For robustness, this was tested against a surrogate null distribution in several ways. First, I utilised the same method that has previously been used to study cardiorespiratory coupling<sup>206</sup>. This method compares the RS<sub>-1</sub> interval (time interval between slow-wave start and preceding R-wave peak) to a uniformly random null distribution. Starting from the beginning of each subject's

RS-1 time-series, I used a moving window of 40 slow waves, and placed the corresponding RS-1 intervals in a 10-bin histogram with outer limits of 0 and the mean heart period for that window. From the histogram, the proportional Shannon entropy is calculated as follows:

$$\text{Shannon entropy} = \text{SH} = \sum_{b=1}^N P_b \times \log P_b$$

$$\text{Maximum Shannon entropy} = \text{SH}_{\max} = -\log \frac{1}{N}$$

$$\text{Proportional Shannon entropy} = \text{SH}_P = \text{SH} / \text{SH}_{\max},$$

Where  $P_b$  is the histogram probability of bin  $b$  and  $N$  is the number of histogram bins.

During perfect coupling, all RS-1 intervals fall into one bin and  $\text{SH}_P=0$ . In the absence of coupling, RS-1 intervals are distributed randomly, producing maximum entropy with  $\text{SH}_P=1$ . For each subject, the mean  $\text{SH}_P$  across the whole experiment was computed. To determine a significance threshold,  $\text{SH}_P$  was computed for  $N=10,000$  surrogate series of 200 random numbers each, drawn from a uniform distribution between 0 and 1 (mean heart rate of 60bpm). The 0.1<sup>st</sup> percentile was used to indicate significance at the  $P=0.001$  level ( $\text{SH}_P=0.970$ ). Finally, for a preliminary multivariate extension, the analysis was repeated on all channels and  $\text{SH}_P$  and mean RS-1 extracted.

Additionally, for each slow wave identified,  $\pm 2s$  of EEG and ECG activity were saved around the slow wave start. This was then averaged across slow waves and subjects to reveal any coherent ECG patterns during a slow wave.

### **Further tests of robustness**

As the Galletly et al. method only tests RS-1 intervals, I wanted to perform further robustness tests to verify the presence of an ongoing oscillation, not just RS-1. To test



this in each subject and at the group-mean level, a histogram of RS timings (range -3s to 3s) was computed and adjusted for between-subject heart rate differences by multiplying it by the mean heart rate across the entire experiment for each subject. Next, the histogram's autocorrelation was calculated. Significant, sine-like autocorrelation would signify an ongoing ECG oscillation around the slow-wave onset. To assess significance, autocorrelation for the same histogram but with uniformly random RS timings in the (-3s, 3s) interval was computed for N=1000 surrogate distributions. To further assess whether autocorrelation showed sinusoidal behaviour, and to find the delay between this possible ECG oscillation and slow wave, an exponentially decaying sinusoid was fitted to it (`scipy.optimize.curve_fit`) and significance established using the Bartlett test on residuals compared to the mean. Additional methods using simulations were used to further verify that this result does not follow trivially from having two oscillations both around 1Hz (slow waves and heart rate, Appendix 2).

### 3.3.7 Clinical dataset analysis

In order to explore whether the heart rate results could be replicated in clinical data, I performed a post-hoc analysis of heart rate and drug concentrations in N=96 patients collected as part of the AlphaMax study (median age 74yrs (range 61 to 86yrs), 66 male, ASA 2/3, variety of procedures)<sup>199</sup>. These patients received a standardised desflurane and fentanyl-based maintenance general anaesthesia that was titrated to maximise the EEG alpha power in the intervention group. For each patient, heart rate, and drug concentrations (propofol, fentanyl, desflurane) were sampled every 5 seconds. Individual ECG waveforms from this dataset were not available, so heart rate variability or R-wave to slow wave time intervals could not be determined. The heart rate was smoothed with a 2min moving median window to suppress artifacts and any

heart rate above 250bpm or below 10bpm was not used. A large mixed-effects general linear model was constructed with heart rate, drug concentrations, and demographic variables. Specifically, the fixed effects of propofol, fentanyl, and desflurane (+ their linear interaction terms), as well as age, BMI, ASA status, and sex were studied. A random effect of each individual's mean heart rate was included. In summary, the model equation was

$$\text{HR[bpm]} = \beta_0 + \beta_1 \cdot \text{age} + \beta_2 \cdot \text{BMI} + \beta_3 \cdot \text{ASA} + \beta_4 \cdot (\text{sex}=\text{F}) + \beta_5 \cdot \text{prop} + \beta_6 \cdot \text{fent} + \beta_7 \cdot \text{des} \\ + \beta_8 \cdot \text{prop} \cdot \text{fent} + \beta_9 \cdot \text{prop} \cdot \text{des} + \beta_{10} \cdot \text{fent} \cdot \text{des} + (1 \mid \text{patient number}),$$

Where  $\beta_i$  are model coefficients, prop=propofol, des=desflurane, fent=fentanyl. To compare some of the slow wave results, individual slow waves were extracted from intraoperative EEG (from first incision to the end of closing up) and mean slow-wave frequency per subject extracted and compared with the mean heart rate.

### 3.3.8 Statistical analyses

As these analyses were all post hoc analyses of previously collected and published data, no power calculation was done. Spearman correlation and its P-value were used to test associations between ECG/EEG parameters (heart rate, R-wave amplitude, root-mean-square successive difference, low frequency to high frequency ratio, peak high frequency, slow-wave power) and propofol concentration. Repeated-measures analysis of variance (RM-ANOVA) was performed on ECG/EEG-derived parameter traces in 5-minute segments to further test for significant changes. For display purposes, mean  $\pm$  standard error across participants is shown, except where the data was not normally distributed (tested with D'Agostino and Pearson's test). In these non-normally distributed cases, median  $\pm$  bootstrapped 95% confidence interval (10,000

iterations) are shown. Mean  $\pm$  SD (or median [25<sup>th</sup>, 75<sup>th</sup> percentile]) are given in the text. Significance was set at the  $P=0.05$  level unless otherwise specified. Custom code used in this study is available at [gitlab.com/marcoFabus/fabus2022\\_brain\\_heart](https://gitlab.com/marcoFabus/fabus2022_brain_heart).

## 3.3 Results

### 3.3.1 Time-series ECG analysis

First, I tracked the heart rate and time-series ECG properties across a slow propofol cycle in  $N=16$  healthy volunteers (Figure 3.1). At higher propofol doses, a shortening of the QT segment and decrease in R-wave amplitude was observed (Figure 3.2.1A). In every subject, the heart rate increased and very robustly tracked the propofol dose with Spearman correlation of  $\rho=0.923$ ,  $P<0.001$  (Figure 3.1B). Heart rate increased from  $58.2\pm 10$  bpm at baseline to  $73.4\pm 8.8$  bpm at peak anaesthesia, an increase of  $4.2\pm 1.5$  bpm/ $(\mu\text{g}\cdot\text{ml}^{-1})$ . The maximum effect size comparing HR at baseline and peak propofol was Cohen's  $d=1.546$ . A linear regression showed the heart rate / propofol relationship to be  $\text{HR} [\text{bpm}] = 56.1 (54.9, 57.2) + 4.23 (3.75, 4.80) * \text{propofol} [\mu\text{g}/\text{ml}]$ , where brackets show 95% confidence intervals. Similarly, the R-wave amplitude was also strongly inversely correlated with the propofol effect-site concentration (Spearman  $\rho=-0.902$ ,  $P<0.001$ , Figure 3.1C). R-wave amplitude decreased from 966 [707, 1133]  $\mu\text{V}$  at baseline to 742 [627, 1068]  $\mu\text{V}$  at peak anaesthesia, a decrease of  $-83 [-245, -28]$   $\mu\text{V}$ .

### 3.3.2 Heart rate variability analysis

Next, I studied autonomic activity through heart-rate variability (HRV; Figure 3.2). The root-mean-square successive difference between heartbeats, which indexes parasympathetic tone, decreased in proportion to propofol concentration, and rebounded on emergence (Figure 3.2A; Spearman  $\rho=-0.785$ ,  $P<0.001$ , Cohen's  $d=1.296$  for baseline vs peak concentration). This was confirmed by a repeated measures ANOVA (RM-ANOVA) with  $P<0.001$ .

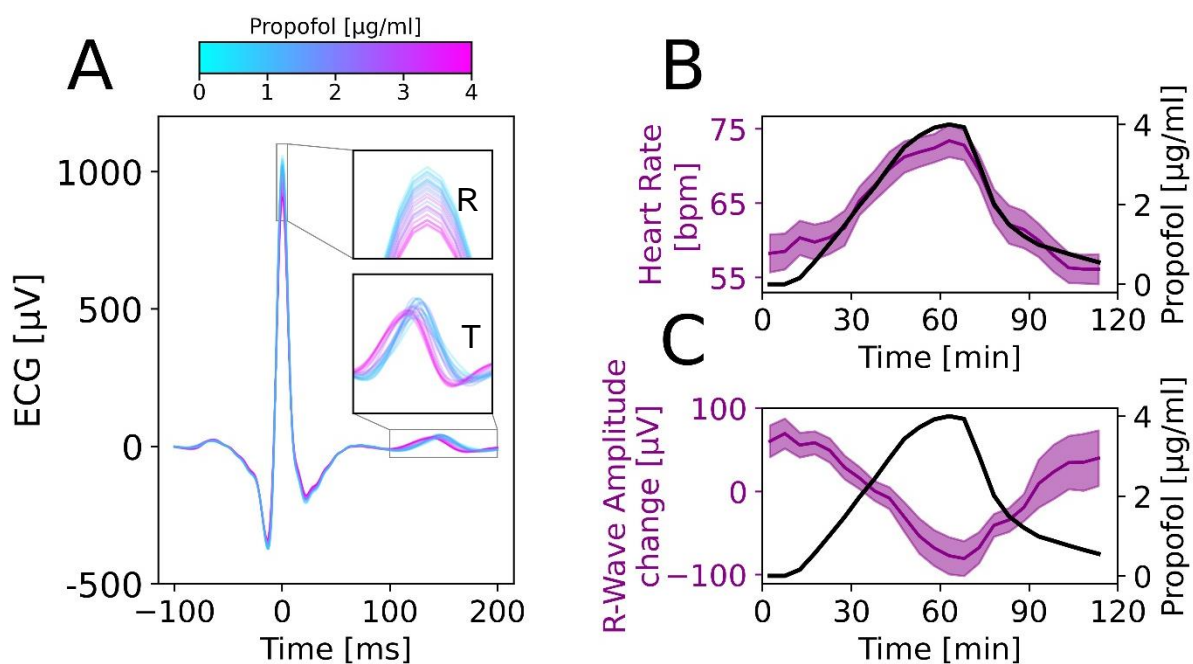


**Figure 3.1:** Propofol increased heart rate and changed ECG shape in healthy volunteers. **(A)** Mean ECG waveform for all heartbeats across N=16 subjects across propofol doses. High propofol concentration (pink) was characterized by a decrease in R-wave amplitude (top inset) and an earlier T-wave (lower inset). **(B)** Propofol increased the heart rate. Group-level heart rate results (purple; mean  $\pm$  SEM) and propofol effect-site concentration (black; Spearman  $\rho=0.923$ ,  $P<0.001$ ). **(C)** At the group level, R-wave amplitude (RWA; purple; mean  $\pm$  SEM) inversely tracked propofol concentration (black; Spearman  $\rho=-0.902$ ,  $P<0.001$ )

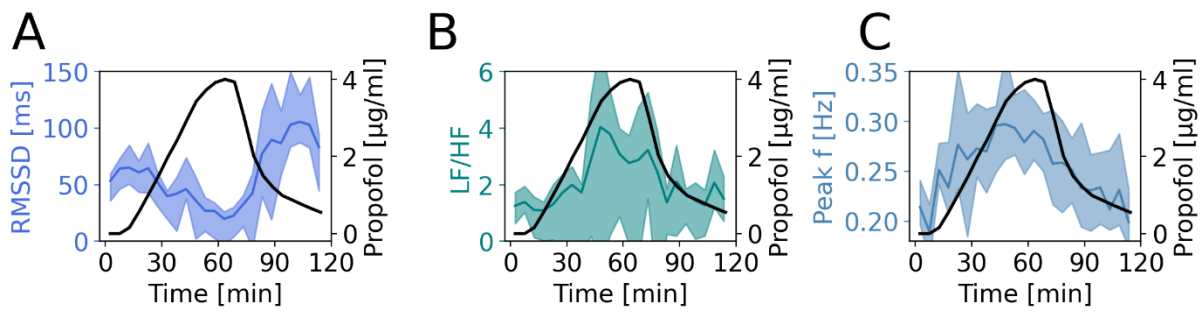


**Figure 3.2:** Propofol decreased parasympathetic activity, as indexed by heart rate variability in healthy volunteers. **(A)** Root-mean-square successive difference (RMSSD) between heart beats (blue; median  $\pm$  95% CI) that is a measure of parasympathetic activity inversely tracks propofol concentration (black) and rebounds on emergence. **(B)** The low to high frequency ratio (green; median  $\pm$  95% CI), which is a metric thought to index balance of sympathetic and parasympathetic activity, is noisy but suggests an increase with propofol (black). **(C)** Peak frequency in the high-frequency heart rate variability band that indexes the respiratory vagal peak (blue; median  $\pm$  95% CI) tracks propofol concentration (black).

With regard to the frequency domain metrics, the low frequency to high frequency ratio showed higher between-subject variability, but the group average confirmed the shift towards a relative predominance of sympathetic activity with increasing propofol concentration (Figure 3.2B; Spearman  $\rho = -0.763$ ,  $P < 0.001$ ), and the RM-ANOVA result also showed a significant change with  $P = 0.003$  with Cohen's  $d = 0.539$  between baseline and highest propofol concentration. The peak frequency in the high-frequency parasympathetic HRV range also tracked with propofol concentrations (Spearman  $\rho = 0.885$ ,  $P < 0.001$ ; RM-ANOVA  $P < 0.001$ ).

### 3.3.3 Slow-wave analysis

Cortical activity during propofol anaesthesia is known to be associated with sleep-like slow-wave activity (Figure 3.3). I first confirmed the previous finding of saturation of frontal slow-wave activity with propofol dose (Figure 3.3A). However, more strikingly, this slow-wave activity increase correlated very strongly with the increasing heart rate (Figure 3.3B; Spearman  $\rho=0.910$ ,  $P<0.001$ ).

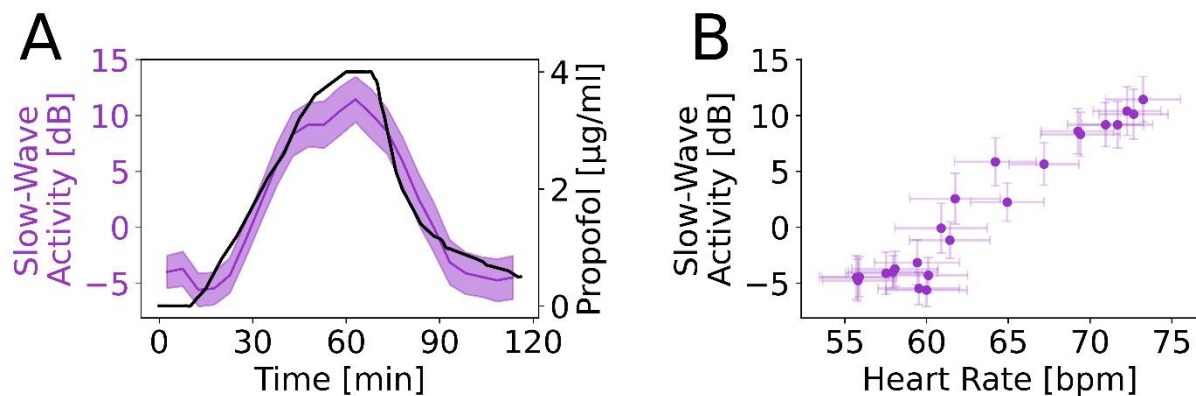


**Figure 3.3:** Propofol increased frontal cortical slow-wave activity and this increase tracked heart rate increases in healthy volunteers. **(A)** Group-level Fz slow-wave activity results (purple; mean  $\pm$  SEM) against propofol concentration (black). Slow-wave activity increases and plateaus with drug dose. **(B)** On the group level, increases in heart rate correlate with increases in slow-wave power (Spearman  $\rho=0.910$ ,  $P<0.001$ ). Each purple dot represents a 5-minute segment of the experiment with standard errors across subjects shown.

### 3.3.4 Cortico-cardiac coupling

The observed association between slow-wave activity and heart rate in conjunction with previous literature describing their coupling in sleep, led to a focus on quantifying the presence of any time-related coupling between individual slow waves and heartbeats (Figure 3.4). After identifying individual slow waves, I studied the distribution of heartbeats around each slow-wave onset (defined as the initial zero crossing of the wave). As observed in previous work on cardio-respiratory coupling<sup>204</sup>, the distribution of time intervals between R-waves and slow wave (RS intervals; Figure 3.4B) was non-uniform and concentrated around specific phases in the slow-wave cycle. This appeared as a residual low-frequency oscillation in the ECG, after averaging around the slow-wave onset (Figure 3.4C); and as peaks in the distribution of heartbeat timings (Figure 3.4D). This effect was also present and significant at the group level (Figure 3.5). The group-average lag between the ECG peak and slow-wave onset was 447 [392, 510] ms (Figure 3.5B). The slow-wave/R-wave coupling, as measured by entropy in relation to a uniform null distribution was  $SH_P=0.866\pm 0.05$  ( $P<0.001$  compared to a uniform null hypothesis, see Methods). Additional tests to verify this is not a random effect were carried out and are described below together with Supplementary Figures 3.1-3.3. Furthermore, at the group level, the subjects' mean heart rates and slow-wave frequencies were significantly linearly correlated (Pearson  $r=0.519$ ,  $P=0.0395$ ).

The above analysis results were qualitatively unchanged when EEG data was re-referenced to linked mastoids and when ECG was time-locked to slow-wave trough instead of downward zero crossing – full results of these control analyses will be included in the forthcoming publication based on the work in this chapter.

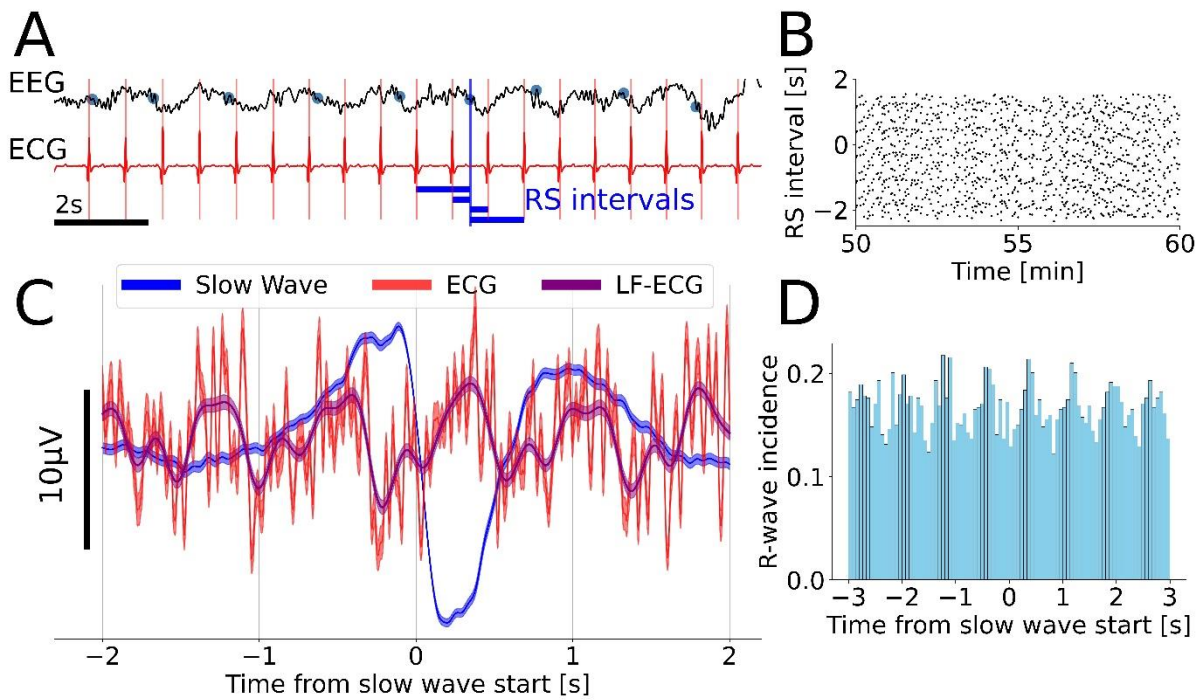


**Figure 3.4:** Single-subject low-frequency cortico-cardiac coupling. **(A)** Example 15s of EEG and ECG data at high propofol concentrations. Slow-wave starts are shown with blue dots. For each slow-wave start, duration of intervals to nearest heartbeats is determined (RS intervals, R-wave/Slow wave). Individual R-waves are marked with red vertical lines. **(B)** Example raster plot of RS intervals during 10 minutes of peak anaesthesia. Heartbeats cluster in horizontal lines, demonstrating non-random coupling to slow-wave onset (proportional entropy  $SH_P=0.890$ ). **(C)** Single-subject average slow wave (blue; mean  $\pm$  SEM across all slow waves) and ECG (red = broadband, purple = 0.5Hz-1.5Hz only) time-locked to slow-wave onset. The ECG pattern is not uniform random noise but shows a clear ongoing low-frequency ECG oscillation. **(D)** Histogram of R-wave timings relative to slow-wave onset. Individual heartbeats preferentially occur in phase with the slow wave, explaining the oscillatory appearance of (C) and stripes seen in (B).



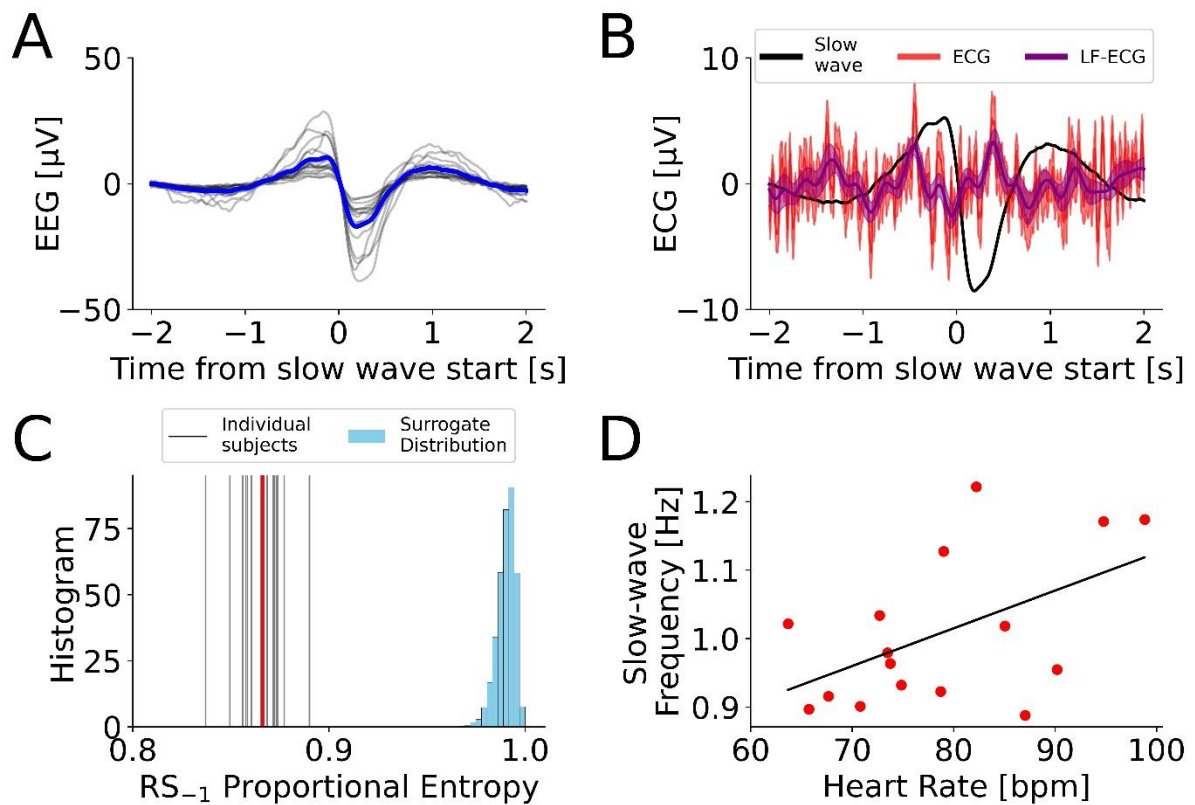


**Figure 3.5:** Group-level cortico-cardiac coupling in healthy volunteers. **(A)** Mean slow wave detected (blue) with each subject mean in grey. **(B)** Group-average ECG (red = broadband, purple = 0.5Hz-4Hz only) time-locked to slow-wave (black) onset. The ongoing low-frequency ECG oscillation is also present at the group-level. **(C)** Slow-wave onset is significantly linked to the preceding heartbeat. Proportional entropy of intervals between slow-wave start and previous R-wave. Mean is in red, each of N=16 subjects is shown with a grey vertical line, surrogate distribution assuming random timings is in blue. **(D)** Individual heart rate and slow-wave frequency are related (Pearson  $r=0.519$ ,  $P=0.0395$ ).

For a preliminary analysis to explore potential spatial differences in cortico-cardiac coupling, the group-average lag between the ECG peak and slow-wave onset was extracted for each electrode, as was the coupling strength measured by entropy SHP (Figure 3.6).

The coupling strength and R-wave / slow-wave delay were similar across the scalp. The only trending exception was a difference in the temporo-parietal R-wave/slow-wave difference between the left and right hemispheres, where some electrodes had a significantly different delay compared to the mean ( $P < 0.1$  on permutation test with  $N = 1000$  random shuffled permutations of delays between electrodes in each subject). For the significant electrodes, the mean delay was  $446 \pm 15$ ms on the average of TP9/T7/CP5 and  $462 \pm 17$ ms on P8/CP6 (uncorrected Wilcoxon  $P = 0.025$ , average left-right difference of 16.5ms).

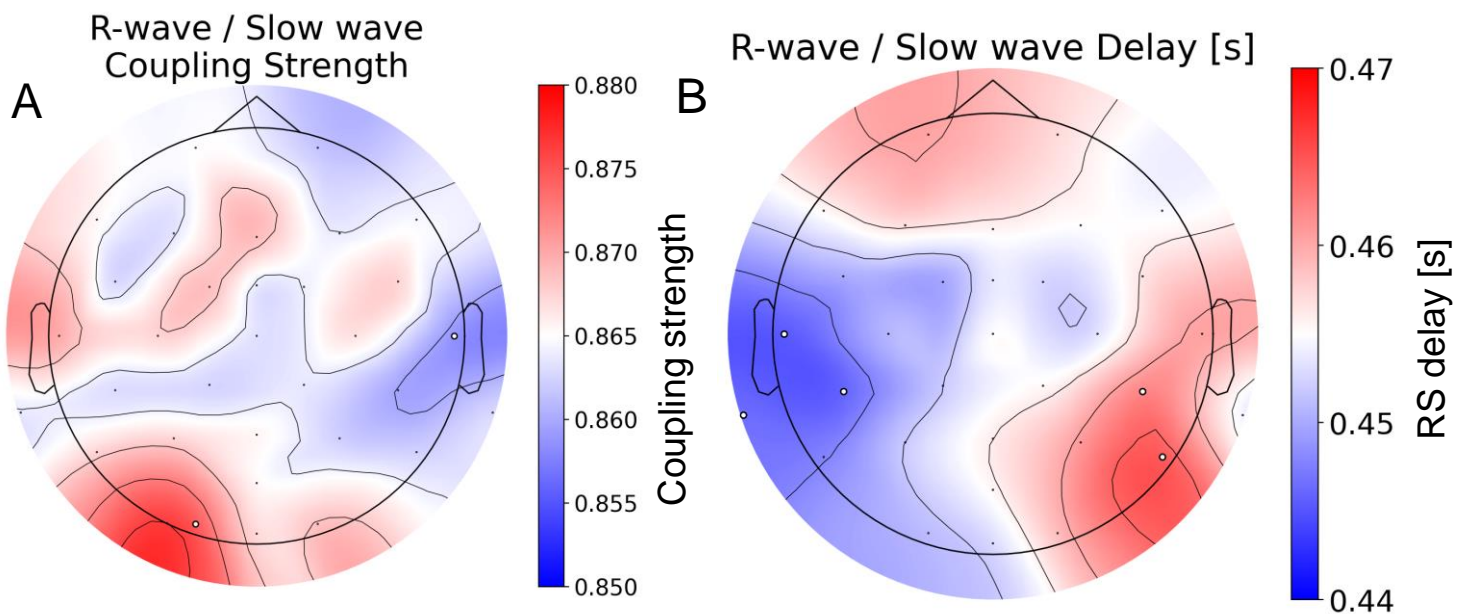


**Figure 3.6:** Multivariate extension of the analysis. **(A)** Coupling strength across channels shows virtually no significant differences (permutation  $P > 0.1$ ). **(B)** R-wave / Slow wave delay shows potential small differences between right and left temporoparietal regions (permutation  $P < 0.1$ ).

### Further robustness analyses

The method introduced by Galletly et al<sup>207</sup> was used above to test the presence of coupling against a uniformly random distribution. An alternative autocorrelation-based test was also used to verify the robustness of this result (see Methods). It revealed the presence of an ongoing oscillation at the group level (Supplementary Figure 3.1), present strongly in 10 out of 16 subjects (Supplementary Figure 3.2). In these subjects, the mean P-value for a sinusoidal fit was  $P=0.0012$  with  $R^2=0.723\pm 0.056$ . On the group level across all participants, the distribution of heartbeat timings in relation to the slow-wave onset showed significant autocorrelation with  $P<0.001$  and  $R^2=0.857$  to a decaying sinusoid fit with exponential half-life of 2.51s (Supplementary Figures 3.1C, D).

I also wanted to know if the strength of coupling varies with dose or is a general slow-wave phenomenon (Supplementary Figure 3.3). When plotting the proportional entropy  $SH_P$  across time, no significant effect was observed, i.e. no dose-dependent effects could be detected ( $P>0.5$ ).

Finally, simulations were used to check this coupling does not arise trivially in presence of two oscillators around 1Hz (the heart rate and slow oscillation). These confirmed that the effect seen here only arises when the two waves are coupled (Appendix 9.2.1).

### 3.3.5 Clinical dataset analysis

In order to explore whether the above heart rate results hold in a clinical setting, I analysed the association between effect-site drug concentration and heart rate using a large general linear model with  $N=96$  older patients collected as part of the AlphaMax

trial (Table 3.1, Supplementary Figure 3.4). After adjusting for age, BMI, sex, and ASA status, all agents (propofol, fentanyl, and desflurane) had a significant effect on the heart rate ( $P < 0.001$ ). Propofol led to a mild increase in heart rate, on average with a coefficient of  $+1.3 \text{ bpm} / (\mu\text{g ml}^{-1})$  (95%CI 1.1, 1.5). Fentanyl however led to a decrease in the heart rate, on average  $-2.6$  (95%CI  $-2.7, -2.5$ )  $\text{bpm} / (\text{ng ml}^{-1})$ , as did desflurane with average of  $-1.84$  (95%CI  $-1.90, -1.78$ )  $\text{bpm} / (1\% \text{ET})$ . The interaction terms were also significant though with smaller coefficients. With mean individual heart rate included as a regressor, no demographic parameters were significant, suggesting that the drug effects on the heart rate may be independent of these. The effect size comparing HR with propofol  $< 0.5 \mu\text{g/ml}$  and  $> 3 \mu\text{g/ml}$  was Cohen's  $d = 0.796$ . Interestingly, at the group level, mean intraoperative slow-wave frequency was not related to the mean heart rate in this dataset ( $P = 0.65$ ).

Name	Estimate	Lower	Upper	Standard Error	t-statistic	P-Value
<b>Intercept</b>	45.444	17.620	73.267	14.196	3.201	<b>0.001</b>
<b>Age</b>	0.213	-0.142	0.568	0.181	1.177	0.239
<b>BMI</b>	0.122	-0.288	0.532	0.209	0.584	0.559
<b>ASA</b>	1.976	-2.853	6.806	2.464	0.802	0.423
<b>Sex = F</b>	0.367	-4.181	4.915	2.320	0.158	0.874
<b>Propofol [<math>\mu\text{g/ml}</math>]</b>	1.319	1.120	1.517	0.101	13.016	<b>&lt;0.001</b>
<b>Fentanyl [<math>\text{ng/ml}</math>]</b>	-2.604	-2.706	-2.501	0.052	-49.682	<b>&lt;0.001</b>
<b>Desflurane [%]</b>	-1.838	-1.895	-1.780	0.029	-62.566	<b>&lt;0.001</b>
<b>Propofol*Fentanyl</b>	0.988	0.946	1.030	0.021	46.510	<b>&lt;0.001</b>
<b>Propofol*Desflurane</b>	-0.711	-0.766	-0.656	0.028	-25.266	<b>&lt;0.001</b>
<b>Fentanyl*Desflurane</b>	0.463	0.437	0.489	0.013	35.018	<b>&lt;0.001</b>

**Table 3.1:** General linear model coefficients for heart rate in the AlphaMax clinical study. Lower / Upper columns indicate 95% confidence intervals. The model confirms propofol's tendency to increase the heart rate independent of other regressors, unlike fentanyl and desflurane.

## 3.4 Discussion

### 3.4.1 Propofol and the heart rate

In this chapter, it has been shown that administration of propofol leads to increases in the mean heart rate. The ultraslow propofol administration in healthy volunteers led to an increase in the mean heart rate of roughly +4 bpm / ( $\mu\text{g/ml}$  propofol concentration). The effect of propofol on heart rate in the older patient population was about three-fold smaller, with an average +1.3 bpm / ( $\mu\text{g/ml}$ ). These clear and significant mean heart rate increases confirmed my hypothesis but are surprising in view of the mixed reporting in the existing clinical literature.

Several experimental studies have seen a heart rate increase across a variety of research paradigms<sup>191–195,208</sup>. I contend the lack of heart rate increase (or heart rate decrease) with propofol frequently reported in some clinical studies may be due to other drugs given, the patient population, the surgical context, as well as dose and rate-dependent effects. Clinically, it is common to administer opioids and other premedication, many of which decrease the heart rate and affect cardiovascular dynamics<sup>208,209</sup>. This even includes pre-oxygenation which tends to decrease the heart rate<sup>210</sup>. The smaller heart rate increase observed in the older clinical population could be in part due to a previously proposed U-shape relationship between propofol and heart rate<sup>194</sup>. Older patients have higher anaesthetic sensitivity and therefore may be more susceptible to a heart rate decrease at relatively high propofol concentrations. This is supported by a previous healthy volunteer study where propofol plasma concentrations of about  $7.4\mu\text{g/ml}$  increased the heart rate by about 30bpm, consistent with the results of this study; but excessively high concentrations up to mean plasma levels of  $18.3\mu\text{g/ml}$  reversed the effect and decreased the heart rate compared to

lower concentrations<sup>195</sup>. Additionally, autonomic system balance and baseline activity are age-dependent<sup>211</sup>. Finally, clinical procedures may provide autonomic stimulation which could affect intrinsic heart rate increases with propofol.

The ultraslow induction rate used in the healthy volunteer study may also affect the cardiac changes. This is supported by previous work finding rate-dependent cardiac effects of propofol with greater decrease in heart rate in fast induction rates, perhaps due to a rate-limiting central nervous system distribution process<sup>198,212</sup>.

Some could argue the heart rate increase is due to the presence of anxiety. However, this is unlikely to be the case as in the experimental setting, whilst heart rate increased from baseline to loss of responsiveness, it continued to increase at the same rate when the drug concentration increased beyond the point of loss of consciousness (Supplementary Figure 3.5).

### 3.4.2 Propofol and heart rate variability

The biological basis for the increase in mean heart rate may be due to propofol inhibiting cardioinhibitory vagal neurons in the brainstem<sup>194</sup>. Studies of propofol's effect on autonomic cardiac influences have also produced mixed results.

The literature agrees that propofol reduces heart rate variability<sup>190,195,213–215</sup>, a result also confirmed in this experiment. The distinct sympathetic and parasympathetic contributions to this are less clear. An early study proposed that propofol mostly depresses sympathetic activity and suggested this as a mechanism for propofol bradycardia and hypotension. However, opioids were also used in that study<sup>214</sup>. Several studies since have concluded that propofol predominantly decreases high-frequency heart rate variability, which is thought to reflect parasympathetic vagal

influences<sup>190,195,213,215</sup>. This vagolysis could be an explanation for the increased heart rate, especially as it distinguishes propofol from sevoflurane<sup>190,195</sup>. It is less likely to be a reflex tachycardic response to vasodilation, as propofol has been shown to depress the baroreflex<sup>23</sup>.

### 3.4.3 Propofol and ECG morphology

Dose-dependent changes in ECG morphology that may reflect both direct cardiac effects and central nervous system-mediated changes of propofol were also observed. After adjusting for heart rate changes, propofol was found not to affect the QT interval<sup>216</sup> so the earlier T-wave seen in this study could just reflect a faster heart rate. However, the R-wave amplitude decrease seen in the present study might be related to previously observed propofol effects on ventricular depolarisation<sup>217</sup>. Propofol may decrease myocardial contractility, possibly due to a direct propofol effect on myocyte ability to expel intracellular calcium<sup>218</sup>. However, another study suggested this only happens at doses beyond common clinical ranges<sup>219</sup>. A change in the mean electrical axis or direct vagal effect could also explain the R-wave amplitude decrease; findings have been mixed so far<sup>217,220</sup>.

### 3.4.4 Cortico-cardiac coupling in propofol

Low-frequency cortico-cardiac coupling has been observed in sleep<sup>120,221</sup>. As propofol slow waves show some sleep-like properties<sup>86</sup>, it was hypothesized this effect would also be present in anaesthesia. In healthy volunteers, it was found that the increase in mean heart rate was strongly correlated with increases in cortical slow-wave power. Obviously, this correlation might be explained as being driven by a common cause –

that of increasing propofol concentration. However, individual cortical slow waves and cardiac R-waves were found to be coupled as hypothesized. A heartbeat was most likely to precede the slow-wave onset by about 450ms with another heartbeat near the slow-wave nadir, a time interval similar to that seen in sleep<sup>120,221</sup>. Further robustness analyses showed that in 10 out of 16 subjects, this effect was not restricted to just the preceding heartbeat, but there was a significant autocorrelation between a slow wave and heart beats with a half-life of 2.5s. Interestingly, Mensen et al. also found significant results at the single-subject level only in 9-13/16 subjects depending on the sub-analysis (ECG vs near-infrared spectroscopy, NIRS). Further studies should explore what drives these between-subject differences. Finally, simulations demonstrated that the results here are not trivially due to similar heart rate and slow wave frequencies, and only hold up when the two waveforms are genuinely coupled (Appendix 9.2.1).

Mensen et al. proposed several hypotheses for why this coupling may occur<sup>120</sup>. The first was a possible metabolic constraint. Overall, neurochemical tone favours hyperpolarized down states with heartbeats acting as a potential stimulus to evoke a down state. Neurons may enter a hyperpolarized state when their resources are depleted. Slightly lower regional blood flow between heart beats could have this effect on a few critical neurons leading to an entire network change. However, this seems unlikely because the necessary time resolution of changes in metabolic energy demand seems shorter than that of a damped feeder capillary blood flow, coupled with the diffusion time of energy substrates and the presence of intrinsic neuronal energy stores. The other possibility is a third generator controlling both the heart rate and slow-wave genesis. Knowing this effect is present both in sleep and propofol anaesthesia gives us a clue as to the possible nature of such a generator. Sleep and



anaesthesia differ in their noradrenaline levels, but both show low levels of acetylcholine<sup>222</sup>. Combined with the fact that the brainstem projects both in a cephalad direction to higher brain areas and, caudally to the heart, here it is proposed as a possible place for a common generator. For instance, the nucleus of the solitary tract or cholinergic pontine nuclei may project both to fast-spiking GABAergic interneurons in the thalamus and to medullar regions controlling the heart rate<sup>223,224</sup>. Given that the thalamus is likely involved in slow-wave generation *in vivo*, this brainstem connection could explain the observed cortico-cardiac coupling, perhaps by weak-coupling synchronization<sup>81,225</sup>. This is supported by the finding that subjects with a faster heart rate also had faster slow-wave frequency. Finally, a preliminary analysis of the cortico-cardiac coupling effect across all electrodes did not reveal any notable differences in coupling or delays across the scalp, except for trending left/right heartbeat/slow wave delay differences in temporoparietal regions.

Interestingly, this frequency relationship was not observed during desflurane-fentanyl slow waves in the clinical dataset, suggesting volatile anaesthetics may differ in their cortico-cardiac coupling effects. Different types of slow waves have also been proposed (see <sup>123,124</sup> and Chapter 4). Here a traditional slow wave definition was used that allows for comparison with previous literature<sup>120,124</sup>, but wave sub-types may show differences in coupling to the heart rate.

Further work is needed to explain the relationship between slow waves and cardiac activity, especially as pertains to wider coupling of autonomic and central activity<sup>196,197</sup>. The proposed common brainstem generator could be ruled out if patients with pacemakers also show this coupling.

In summary, slow propofol administration in healthy subjects robustly led to an increase in mean heart rate that was strongly proportional to drug concentration, and not influenced by changes in behavioural responsiveness. This result was replicated in a larger clinical dataset but with a decreased effect size. The heart rate increase could be explained with decreased cardiac parasympathetic inputs, as indexed by decreased high-frequency heart rate variability. Frontal cortical slow waves preferentially occurred coupled to the heart rhythm similarly to cortico-cardiac coupling that is seen in sleep, perhaps due to a common brainstem generator. More work is needed to elucidate the mechanism and role of these cardiac changes and the clinical significance of their coupling to the cortex.

Thus, in the clinical management of patient haemodynamics, propofol should not be assumed to decrease the heart rate. In fact, particularly for slow infusions and younger patients, propofol is likely to increase the heart rate. Ultimately, heart rate will be a complex result of opioid, hypnotic, and surgical factors.



# **4 Automatic decomposition of electrophysiological data into distinct non-sinusoidal oscillatory modes**

## **4.1 Introduction**

The synchronized activity of neuronal populations can be observed in dynamic oscillations recorded in electrophysiology<sup>65,226</sup>. These oscillations are often visible in raw data traces but are challenging to isolate in an objective, data-driven manner. Methods for signal isolation must contend with signals being obscured by noise or by simultaneous oscillations at different frequencies. Neuronal oscillations are often non-sinusoidal and change over time, which leads to ambiguities in standard analyses based on the Fourier transform<sup>227,228</sup>. These dynamic and non-sinusoidal features are of growing importance in electrophysiological research but remain difficult to analyse using existing methods<sup>121,126,226,229–231</sup>. As such, there is a pressing need for data-driven methods that can isolate oscillations from noisy time-series whilst preserving their non-sinusoidal features.

In previous chapters, slow waves were analysed using well-established and traditional, Fourier-based filtering methods, allowing direct comparison with the wider literature. However, brain waves during anaesthesia are non-sinusoidal<sup>121,232</sup>, and their shape may have potential physiological relevance<sup>122</sup>. To address this, I tackled the problem

of non-sinusoidal neural oscillations more broadly, before applying my new data-driven analysis technique to propofol anaesthesia.

Empirical Mode Decomposition (EMD)<sup>233</sup> is able to provide a different perspective on analysing transient oscillations. It offers a radically different approach to signal separation based on a flexible, local, and data-driven decomposition with weaker assumptions about stationarity and linearity of the signal. Single channel data is decomposed by a sifting process into Intrinsic Mode Functions (IMFs) based on finding successively slower extrema. Unlike Fourier or Wavelet methods, EMD does not a-priori assume the shape of its functions. It is therefore believed IMFs can capture non-sinusoidal oscillations and may better reflect the underlying processes in physical and physiological signals<sup>227,233,234</sup>. This can especially aid analyses sensitive to waveform shape, such as calculations of phase and cross-frequency coupling<sup>228,235</sup>.

The original EMD algorithm can in theory produce arbitrarily shaped IMFs, but in noisy neural signals it struggles with signal intermittency and high non-sinusoidality. In the presence of transient oscillatory bursts, the sifting process may detect extrema on different time scales at different times. This is referred to as *mode mixing*. It presents a major challenge in analysis and interpretation of IMFs<sup>236,237</sup>. This is especially the case in analysis of brain signals, where transient states are common and have functional significance<sup>126,238–240</sup>. Furthermore, in the presence of pure Gaussian fractional noise, EMD has been shown to act as a dyadic filter bank<sup>241,242</sup>. This means that for highly noisy signals, EMD tends to produce IMFs with fixed bandwidths rather than adapting to capture signals present in the data, further complicating analysis.

Various improvements to the sifting process have been proposed to make EMD more applicable to real-world data<sup>243–250</sup>. A unifying characteristic of the existing approaches

is to inject a secondary signal into the data to alter the extrema distribution and overcome mode mixing. *Noise-assisted methods*, as exemplified by Ensemble EMD (EEMD)<sup>243,245</sup>, use white noise as the injected signal. This reduces mode mixing due to signal intermittency. However, the use of noise can limit IMF bandwidth, possibly making mode mixing worse. *Masking methods* inject sinusoids into the data before sifting<sup>244,247</sup>. With a suitable mask, this technique can recover non-sinusoidal waveforms and/or intermittent bursts in presence of noise. However, the frequency of masking signals that should be used is often not known a-priori.

Mask optimization can become an arduous manual process, prohibiting generalizability and introducing uncertainty on analysis outcomes. This is exacerbated by the presence of high noise and non-sinusoidal signals near dyadic boundaries, where a small change in the masking signal frequency may dramatically alter the quality of resulting IMFs. Mask frequency selection can be done semi-automatically by choosing an initial frequency based on the number of zero-crossings in the first IMF and dividing this successively by two for later IMFs<sup>244</sup>. If the approximate frequency content of the signal is known, then mask frequencies may be directly selected to isolate the specific components of interest<sup>234</sup>. Though effective, the semi-automatic method is relatively inflexible, and the direct specification method can be manually intensive to validate.

Finally, *multivariate* EMD is also a subject of active research<sup>251,252</sup>. The extension of EMD to multi-channel data is not trivial as interpolating extremal envelopes becomes computationally expensive in higher dimensions and additional methods are needed, such as only sifting along most important directions. Alternatively, pseudo-multivariate EMD can be computed by simply performing EMD on each channel separately and

checking cross-channel mode correspondence afterwards, for example, by comparing their frequency content.

Existing versions of Empirical Mode Decomposition have been applied to anaesthesia. The first application was by Li and colleagues (2008)<sup>253</sup>, where after standard Empirical Mode Decomposition, the Hilbert-Huang transform was computed to obtain a spectrum and its entropy was found, the Hilbert-Huang spectral entropy. This entropy decreased with increasing sevoflurane concentration and was more resistant to noise than commercial M-Entropy. This paper illustrates a common trend in the literature on applying EMD to anaesthesia. Because in existing EMD-based methods individual cycles are difficult to interpret due to mode mixing, either EMD is used as just a pre-processing tool to remove noise, or further analysis is done by using the modes as input into entropy, spectral, or neural network measures. This has been done with Ensemble EMD<sup>254,255</sup> and Multivariate EMD<sup>256,257</sup>. The validity of extracting slow-wave activity during general anaesthesia using EMD has also been demonstrated<sup>258,259</sup>. More recently, masked EMD was used to suggest different spectral components of EEG show different rates of return to baseline after burst-suppression<sup>260</sup>. The existing work suggests EMD is a promising technique to study EEG changes under anaesthesia, but methodological improvements to reduce mode mixing are needed.

In this chapter, I introduce Iterated Masking EMD (itEMD), which is a novel sifting technique that I have developed that builds on the masking method. This method retains all the advantages of using a masking signal whilst being more generalizable and automated. I validated itEMD by comparing it with existing methods using simulations and multi-species, multi-modal experimental data, and discuss its range of applicability and limitations. After developing and validating the novel methodology,

I applied itEMD to the propofol dataset presented in Chapters 2 and 3. Using itEMD in this way, I found three distinct low-frequency modes in the data. These were termed high delta, low delta, and slow modes. I hypothesised that these modes should show changes in spatiotemporal structure with increased anaesthetic doses of propofol.

Additionally, to explore changes in the brain following anaesthesia, I adapted a trough-based traveling wave analysis that has been previously used in anaesthesia and sleep<sup>85,86</sup>. For the first time, I resolved properties of travelling waves across changing anaesthetic concentration thanks to the ultra-slow infusion paradigm. I found dose-dependent changes in globality, frequency, and amplitude for each of the three wave types.

## 4.2 Methods

The methodological and validation part of this chapter is based on my existing first-author publication<sup>261</sup>.

### 4.2.1 Empirical Mode Decomposition (EMD) Algorithms

Empirical Mode Decomposition decomposes a signal  $x(t)$  into a finite number of Intrinsic Mode Functions (IMFs)  $c_i$  with a *sifting* algorithm<sup>233</sup>. The IMFs are constructed to have locally symmetric upper and lower envelopes with no peaks below zero or troughs above zero. A smooth signal with these features is well-behaved during instantaneous frequency analysis, allowing for a full description of non-sinusoidal waveform shape<sup>234</sup>.



Ensemble EMD<sup>243</sup> is typical of a class of noise-assisted sifting methods. An ensemble of  $N$  sift processes is created, each with different white noise injected. The final IMFs are computed as the average across this ensemble. The goal is to exhaust all possible sifting solutions, leaving only persistent real signals. However, due to a finite size of the ensemble, IMFs may contain unwanted residual noise unless further improvements are introduced<sup>248,249</sup>. Furthermore, due to the stochastic nature of white noise, signals of interest might shift between modes across the ensemble, leading to some mode mixing in the final result. Finally, the use of noise reinforces the dyadic filtering behaviour of EMD. This means any signal near dyadic boundaries is likely to be split between modes. This effect is especially pronounced for non-sinusoidal signals which change in instantaneous frequency, making waveform shape analysis difficult as they become smeared over multiple IMFs.

Masked EMD<sup>244</sup> works by injecting a masking signal  $s_i(t)$  into signal  $x(t)$  before sifting. This reduces mode mixing by making the sift ignore signal content slower than the frequency of the masking signal. The masking signal is introduced uniformly across  $n_p$  phases at each step to further minimize mode mixing<sup>245</sup>. The IMFs  $c_i$  are thus calculated with the following algorithm:

1. Construct a masking signal  $s_i(t)$ .
2. Perform EMD on  $x_k = x(t) + s_{i,k}(t + \phi_k)$ , where  $\phi_k = 2\pi(k-1) / n_p$ , obtaining IMFs  $c_{i,k}(t)$ .
3. Compute the final IMF as  $c_i(t) = 1/n_p \sum c_{i,k}$ .
4. Compute the residue  $r_i(t) = x(t) - c_i(t)$ .
5. Set  $x(t) = r_i(t)$  and repeat 1-4 with the next masking signal to extract the next IMF.

This technique permits analysis with intermittent bursts and non-sinusoidal oscillations (Figure 4.1). EMD is locally adaptive, and as such fast bursts get mixed with slower activity when bursts are not present. With a mask, any signal content with frequencies much lower than the masking frequency will be ignored by the sift in that iteration and is replaced by the mask. The mask is finally removed, allowing for correct recovery of intermittent activity. In presence of noise, EMD also acts as a dyadic filter<sup>241,242</sup>. This means non-sinusoidal oscillations are often split across multiple IMFs. With a suitable mask, the bandwidth of modes can be adapted and more of the waveform shape recovered.

The choice of masking signals remains an area of active research. The original paper by Deering and Kaiser suggested the first mask frequency to be the energy-weighted mean of instantaneous frequency obtained from the first IMF found by ordinary EMD, with subsequent mask frequencies chosen as  $f_0$  divided by powers of 2 to account for the dyadic nature of EMD<sup>244</sup>. Other approaches have included computing the mask from zero crossings of the first IMF of a standard sift and purely dyadic masks<sup>247</sup>. However, the choice of optimal masks remains a manual process in many cases. This requires experience and may introduce subjective bias<sup>234,244,250,262</sup>.

### **Iterated Masking EMD (itEMD) technique**

As seen above, noise-assisted and masking approaches to EMD sifting improve mode mixing in some cases, but mode mixing may still be present to complicate further analysis. Mask choice in noisy datasets is complicated, especially with signal frequencies near dyadic boundaries. Iterated masking solves this problem by finding and using an adaptive, data-driven mask.

In science, it is common to rely on intuition to guide study of complex dynamical systems<sup>263</sup>. Consider then a simple example where there is a signal burst  $x(t)$  with some base frequency  $f_{\text{sig}}$  and possible deviation around it due to non-sinusoidality. Take as a start the masked EMD process with a single mask of frequency  $f_{\text{mask}}^{(0)}$ . A good choice of frequency would be near  $f_{\text{mask}} = f_{\text{sig}}$ , as this would extract most of  $x(t)$  into one IMF, resulting in noise reduction and allowing for a simple IMF interpretation. This is because adding a mask at  $f_{\text{mask}} = f_{\text{sig}}$  forces the IMF to ignore any spectral content below  $\sim 0.67 * f_{\text{mask}}$ <sup>250</sup>.

In real data however,  $f_{\text{sig}}$  is often unknown. Assume then  $f_{\text{mask}}^{(0)}$  is chosen with little to no knowledge of the system frequency  $f_{\text{sig}}$ . After applying masked EMD, the resulting IMF will contain a part of the burst with some noise or other signal mixed in. However, its instantaneous frequency will be  $f_{\text{sig}}$  for sections of the IMF attributable to the signal. Assuming signal amplitude is distinguishable from noise in this IMF, the amplitude-weighted instantaneous frequency mean (AW-IFM) will be closer to the desired  $f_{\text{sig}}$  than  $f_{\text{mask}}^{(0)}$ . Thus, if one uses this AW-IFM as the masking frequency for the next iteration  $f_{\text{mask}}^{(1)}$ , the resulting mask sift IMF will be even closer to the optimal IMF. This is the case both if  $f_{\text{mask}}^{(0)}$  is greater and smaller than  $f_{\text{sig}}$ , as both lead to mode mixing. Following this reasoning, the natural equilibrium of this iteration process is when  $f_{\text{mask}} = f_{\text{sig}}$ , and one can apply this approach to a signal consisting of multiple signal frequencies and noise. This leads to the following algorithm:

1. Choose an initial set of mask frequencies  $m = \{f_0\}$ .
2. Perform masked EMD to obtain IMFs.
3. Find the instantaneous frequency (IF) for each IMF using the Hilbert transform.
4. Compute the amplitude-weighted average of each IMF's IF and set  $m_i = \text{AW-IFM}$ .

5. Repeat 2-4 until a stopping criterion  $\Sigma$  is reached.

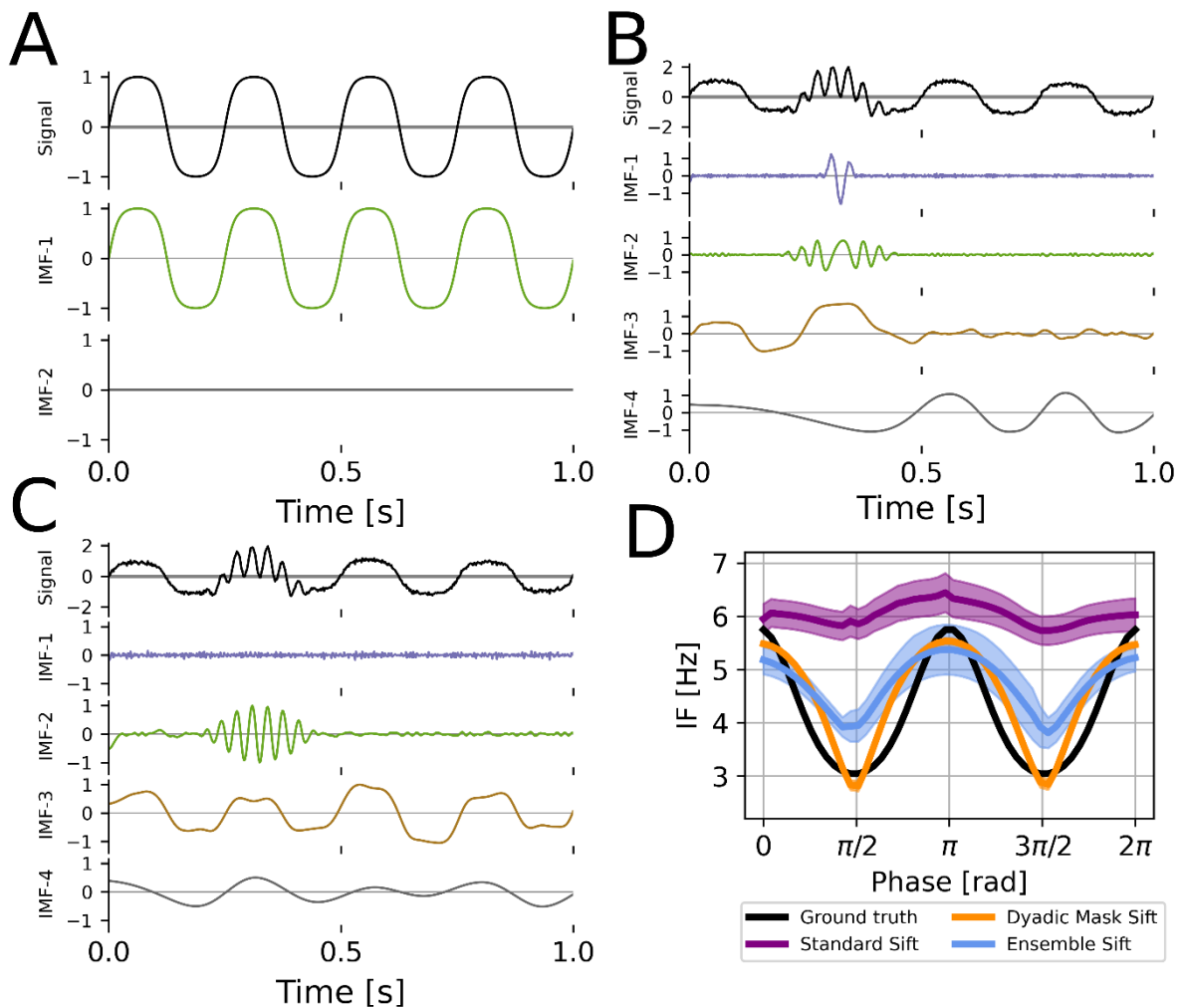


**Figure 4.1:** Limitations of EMD. **(A)** Standard EMD sifting applied on a pure 4Hz iterated sine function. With no noise, EMD can accurately identify an Intrinsic Mode Function (IMF) that represents the non-sinusoidal signal. **(B)** In presence of white noise and a 30Hz burst (arrow), standard EMD shows heavy mode mixing. **(C)** EMD with an appropriate dyadic mask sift will recover most of the iterated sine (IMF-3) and the intermittent burst (IMF-2) signals. **(D)** Masked EMD and Ensemble EMD can better reconstruct non-sinusoidal wave shape in signal with low noise unlike standard EMD. The figure shows the phase-aligned instantaneous frequency calculated from 100 runs of (B) and (C). Mean  $\pm$  standard error (shaded) shown.

Here the stopping criterion was chosen such that the relative difference between current and previous mask frequencies is small, i.e.  $(m_i - m_{i-1}) / m_{i-1} < \epsilon$ . Instantaneous frequency averaging was weighted by the square of instantaneous amplitude for a given IMF, i.e. by instantaneous power. Mask frequencies were initialized by the dyadic masking technique, though it was found that itEMD is not sensitive to mask changes and can rapidly identify correct IMFs even with a random initial mask (Figure 4.2). Due to rapid convergence (<10 iterations in most cases), itEMD is computationally comparable to existing techniques including ensemble EMD and uniform phase EMD, each of which requires repeated sifting<sup>245</sup>. More formally, the computational complexity of itEMD is  $T = 41n_{\text{iter}} * n_s * n_p * n \log_2(n)$  for  $n_{\text{iter}}$  iterations,  $n_s$  sifting steps,  $n_p$  mask phases, and data length  $n$ .

#### 4.2.2 Simulations

I ran simulations to compare the performance of itEMD to existing sifting methods, namely Ensemble EMD (EEMD<sup>243</sup>) and Masked EMD<sup>244</sup>. Simulations were performed along three dimensions that are important to analysis of neural signals: noise, sparsity, and waveform shape distortion (non-sinusoidality). These were chosen as they are all common features of neurophysiological data which cause issues for extracting neural oscillations. In standard EMD, they result in mode mixing and prohibit accurate representation of waveform shape and robust interpretation of identified modes.

All noise and frequency distortion simulations were 10s long and sampled at 512Hz with signal amplitude normalized to 1. In each simulation, IMFs were computed using three different methods that are used to address mode mixing: Dyadic Mask Sift, Ensemble Sift, and the novel iterated masking EMD (itEMD). Dyadic Mask Sift utilized

a single set of masking frequencies. The first was computed from zero-crossings of first IMF obtained by a standard sift and subsequent masking frequencies were divided by powers of 2. Masks were applied with 4 phases uniformly spread across 0 to  $2\pi$  following Wang et al. (2016)<sup>245</sup>. Ensemble sift was run with 4 noise realizations and ensemble noise standard deviation of 0.2. The novel itEMD was run on top of the masked EMD implementation with a stopping criterion  $\sum = 0.1$  and maximum number of iterations  $N_{\max} = 15$ . In all simulations, number of IMFs was limited to 6 and the sifting threshold was  $1e-08$ . After finding IMFs, individual cycles were found from jumps in the instantaneous phase found by the amplitude-normalized Hilbert transform. Each set of simulations (noise, distortion, sparsity) was repeated  $N=100$  times with the mean +/- standard error results presented.

Waveform shape was quantified by computing the average phase-aligned instantaneous frequency (IF) across cycles<sup>234</sup>. IF measures how an oscillation speeds up or slows down within a cycle. It is computed as the time derivative of the instantaneous phase. IF was phase-aligned to correct for differences in timing and duration between cycles and allow for comparisons at each phase point. It can intuitively be understood as fitting a sinusoid with frequency that of the instantaneous frequency at each time point, capturing shape deviations away from a sinusoid with a constant frequency<sup>264,265</sup>. Within-cycle IF variability is thus a measure of how non-sinusoidal each cycle is.

Performance of each method was assessed by two methods. The first was finding Pearson correlation between reconstructed phase-aligned instantaneous frequency (proxy for waveform shape) and its ground truth. The second was computing the Pseudo-Mode Splitting Index (PMSI) introduced by Wang et al. (2018)<sup>245</sup>. PMSI

estimates the degree of mode mixing between two adjacent IMFs by computing the normalized dot product between them:

$$PMSI_{i,i+1} = \max\left(\frac{\vec{c}_i \cdot \overrightarrow{c_{i+1}}}{|c_i|^2 + |c_{i+1}|^2}, 0\right) \quad [1]$$

Orthogonal, well-separated modes with no mode mixing thus have PMSI=0. Fully split modes have PMSI=0.5. This index was chosen as it can be applied to both simulated and real data and is easy to interpret. For simulations with a known ground truth, the IMF of interest was taken to be the one with mean instantaneous frequency closest to that of the ground truth and calculated PMSI as the sum of PMSIs with the above and below IMF.

## **Noise Simulations**

For analysing noise-dependent properties, white noise was created using the `numpy.random.normal` Python module with zero mean and standard deviation  $\sigma$  (also equal to its root-mean-square, RMS). White noise was chosen because performance results tested on it are independent of signal frequency. This is because white noise has equal power throughout the frequency spectrum. For simulations of neurophysiological data, in a supplementary analysis, signals with brown noise were also considered. For this set of simulations, white noise RMS  $\sigma$  was varied between  $\sigma=0.05$  and  $\sigma=3$  in 100 uniformly spaced steps. Waveform shape distortion was held constant at FD=68% (see below).

## Waveform Shape Distortion Simulations

For analysing waveform shape, signal was simulated as an iterated sine function, i.e.  $\sin(\sin(\dots\sin(2\pi f_0 x)))$  iterated  $N_{\text{sin}}$  times with  $f_0=4\text{Hz}$ . This function was chosen because i) it is easy to manipulate its non-sinusoidal distortion by increasing  $N_{\text{sin}}$ , ii) it is well-understood analytically<sup>266</sup>, iii) it has been used before in context of EEG time-frequency analysis<sup>267</sup>, and iv) it has a well-behaved instantaneous frequency by satisfying conditions outlined in Huang et.al. (1998)<sup>233</sup>. It also qualitatively captures parts of waveform shape of the sensorimotor mu oscillation and slow oscillations in depth EEG recordings by its 'flat top' structure<sup>121,268</sup>. The base frequency of 4Hz was chosen as it is physiologically plausible in the delta range and was near a Nyquist boundary, where current EMD sifting methods may have issues. Its non-sinusoidality was captured by a frequency distortion metric FD defined by

$$FD = \frac{\max(IF) - \min(IF)}{f_0} \cdot 100\% \quad [2]$$

A signal with FD=0% is a pure sinusoid and FD=100% indicates a waveform with IF range equal to that of the original frequency, i.e.  $4\pm 2\text{Hz}$ . An example waveform can be seen in Figure 4.1 (FD=68%). In this set of simulations, frequency distortion was varied between FD= 18% and 101% by repeating simulations with iterated sine order varying from  $N_{\text{sin}}=1$  to  $N_{\text{sin}}=18$ . White noise RMS was held constant at  $\sigma = 1$ .

## Signal Intermittency Simulations

For analysing effects of signal intermittency on itEMD performance, bursts of different length in a 25s segment of data were simulated. Sparsity was measured as the number of individual oscillations in the burst. The number of cycles in the burst was varied from



5 to 95 in 100 steps. Noise RMS was kept constant at  $\sigma_{\text{noise}} = 1$  and distortion at FD=68% (8<sup>th</sup> order iterated sine).

Statistical testing was done using one-sided Welch's t-test corrected for multiple comparisons using Bonferroni's method unless otherwise specified<sup>269</sup>.

### 4.2.3 Validation using Experimental Data

#### **Rat Local Field Potential (LFP) Data**

To validate the method with well-described hippocampal theta oscillations, a publicly available data set of Long-Evans rats was used<sup>270,271</sup>. The full 1000s local field potentials (LFP) recording from rat EC-013 sampled at 1250Hz was used for analysis. The electrode analysed was implanted in the hippocampal region CA1. EMD cycle analysis was the same as during simulations. In short, three types of sifting methods were compared: dyadic masking sift with zero-crossing initialization, ensemble sift, and the novel itEMD. The recording was split into 20 segments of 50s duration before sifting. For itEMD (as in simulations), the stopping criterion was set at  $\sum=0.1$ , the maximum number of iterations was  $N_{\text{max}}=15$ , the mask was weighted by squared instantaneous amplitude, and the iteration process was initialized by the zero-crossing dyadic mask result. Instantaneous phase, frequency, and amplitude were computed from the IMFs using the amplitude-normalized Hilbert transform with an instantaneous phase smoothing window of  $N=5$  timepoints. The theta IMF was chosen as that whose average instantaneous frequency was closest to the Fourier spectral theta peak estimated using Welch's method (peak in 4-8Hz, function `scipy.signal.welch`, 8s segment length / 0.125Hz resolution). Cycles were computed from jumps in the wrapped instantaneous phase. To discard noisy cycles, only cycles with monotonic

instantaneous phase, instantaneous amplitude above the 50<sup>th</sup> percentile, and instantaneous frequency below 16Hz were used for further analysis. Cycles were phase-aligned with N=48 phase points and the shape was represented by the mean of the phase-aligned instantaneous frequency. To compare mode mixing, the PMSI (see above) was also computed as the sum of PMSIs of the theta IMF with the IMF above and below it in frequency.

Finally, the Wavelet transform of the LFP data was also computed for comparison with the Hilbert-Huang transform (HHT). This was done using the `scipy.signal.cwt` function with the Complex Morlet wavelet with  $\omega_0=4$  and N=100 frequency points between 1Hz and 64Hz as the widths. HHT was computed using the `emd.spectra.hilberthuang` function in the same frequency range with a gaussian image filter from `scipy.ndimage` with  $\sigma=0.5$  applied for visualization purposes.

### **Human Magnetoencephalography (MEG) Data**

Ten resting state MEG recordings were randomly chosen from the CamCAN project ([www.cam-can.org/](http://www.cam-can.org/))<sup>272,273</sup>. The participants were randomly chosen from the project (mean age 43.5 years, range 18-79, 6 female). The maxfilter processed data were downloaded from the server and converted into SPM12 format for further analysis using the OHBA Software Library (OSL; [ohba-analysis.github.io/osl-docs/](https://ohba-analysis.github.io/osl-docs/)). Preprocessing was done by Prof Andrew Quinn. Each dataset was down-sampled to 400Hz and bandpass filtered between 0.1 and 125Hz. Two notch filters were applied at 48-52Hz and 98-102Hz to attenuate line noise. Physiological artefacts were removed from the data using Independent Components Analysis. 62 components were computed from the sensor space data and artefactual components identified by

correlation with EOG and ECG recordings. Any independent component with a correlation greater 0.35 with either the EOG or ECG was considered artefactual and removed from the analysis. This resulted in two to four components removed from each dataset. EMD analyses proceeded with the cleaned MEG data from a single gradiometer MEG2112 over midline occipital cortex. Each recording was about 10 minutes (median 565s, range 562s-656s). The power spectrum of the whole recording was estimated using Welch's method (function `scipy.signal.welch`, 8s segment length / 0.125Hz resolution). The frequency of the spectral alpha peak was then extracted in the 8-12Hz range as a local maximum (function `scipy.signal.find_peaks`). For itEMD analysis, each recording was segmented into 10 parts of the same length (median segment length 56.2s). EMD was performed with the mask sift, ensemble sift, and itEMD. Sift parameters were identical to those used for the rat LFP analysis above. The IMF representing alpha oscillations was chosen as the one whose mean instantaneous frequency was closest to the alpha peak frequency. Subjects were excluded if no alpha peak was present (one subject). After extraction of cycles from the Hilbert-computed instantaneous phase jumps, only those with instantaneous frequency between 7Hz and 14Hz and instantaneous amplitude above the 50<sup>th</sup> percentile were kept. For further analysis, cycles were phase-aligned to N=48 uniformly spaced phase points between 0 and  $2\pi$  and the mean across cycles was computed for each subject. To evaluate mode mixing, the PMSI for each sifting method was also calculated.

#### 4.2.4 Application of itEMD to human propofol electroencephalography (EEG) data

itEMD was applied to the propofol EEG dataset presented in Chapters 2 and 3. More details about participant recruitment and the experiment can be found in Chapter 2 and in the original study<sup>31</sup>. For this analysis, after Independent Component Analysis removal of ocular and cardiac artifacts, data was re-referenced to linked earlobes, down-sampled to 200Hz, and filtered with an 8th-order zero phase Butterworth filter in the 0.1-30Hz band.

In order to understand the spectral content of the data, itEMD was used on data from the anaesthetic induction segmented into one-minute segments. This was done because anaesthetic induction is a non-stationary process where dominant oscillations change over time<sup>274</sup>. Iteration was performed until mask frequencies stabilised to within 10% with a maximum number of iterations of  $N_{\max}=15$ . After applying itEMD to data from each channel, cross-channel and cross-patient mode correspondence was checked by comparing the modes' frequencies. The number of IMFs was limited to 6 and the sifting threshold was  $10^{-8}$ .

#### **Trough-based analysis**

The low-frequency spectral modes were analysed using previously utilised methods<sup>85,86,275</sup>. Each intrinsic mode function (IMF) was analysed separately. First, on each channel, single cycles were identified from jumps in instantaneous phase computed using the amplitude-normalised Hilbert transform. Cycles were filtered and only those negative duration of at least 125ms, monotonous instantaneous phase, and amplitude in the upper 50<sup>th</sup> percentile were kept. Those with a trough (minimum)

appearing on at least 3 channels within +/- 200ms of an arbitrary reference channel were analysed further. The arbitrary reference channel was varied 10 times and only unique slow waves with earliest troughs separated by at least 0.75s were kept. For each wave, its time / anaesthetic concentration of first detection, peak-to-peak amplitude, average instantaneous frequency, and globality were calculated. Globality was calculated as the % of channels on which each individual wave was detected. For each subject, wave density was found as number of waves detected per minute and evaluated on a two-minute bins throughout the induction. Lastly, topographical properties were calculated for waves in each mode and anaesthesia level. On each channel, the mean wave amplitude, frequency, and frequency difference from scalp mean were calculated. Detection probability was the probability that a given channel was involved in a detected wave. For statistical analysis, three regions of interest were chosen similar to those used by other researchers<sup>276</sup>. They were frontal (Fz, F3, F4, FC1, FC2), posterior (Pz, P3, P4, CP1, CP2), and temporal (T7, T8) regions.

### **Statistical Testing**

The effects of anaesthetic level (light, medium, deep – each one third of the induction) and wave type (high delta, low delta, slow) on properties of waves were tested using a two-way repeated measures analysis of variance (ANOVA) followed by post-hoc Bonferroni-corrected Wilcoxon signed rank tests. All data was checked for normality before performing ANOVAs. In cases where this test indicated non-normality, the data was inspected visually to check. This sometimes happened for light anaesthesia levels where there are fewer waves and more potential outliers. ANOVA tends to be robust to violations of normality<sup>277</sup>, so in cases where only one sub-group failed the normality

test (e.g. light propofol high delta), ANOVA was still performed. If multiple sub-groups showed non-normality, outlier subjects outside  $3 \times$  (interquartile range) for any of the ANOVA levels were excluded before proceeding with ANOVA. If any specific ANOVA factor in a subject had no data, that subject was excluded from the ANOVA. This happened mostly due to light anaesthesia not having many waves, especially in the high delta range. This and outlier exclusion reduced the number of subjects for ANOVAs down to a minimum of  $N=14$ , largely due to the temporal regions lacking light anaesthesia waves. Specific  $N$  values are given with each test result. ANOVA  $P$ -values were corrected for lack of sphericity. All subjects were included in the non-parametric post-hoc tests as these do not require normality.

For testing effects of brain region (frontal, parietal, temporal in trough-based analysis), same tests as above were carried out except with brain region as another factor in a three-way repeated measures ANOVA.

Throughout this work, significance was set at  $P=0.05$  (after appropriate multiple comparisons corrections) unless otherwise specified. All tests were two-sided unless otherwise specified.

#### 4.2.5 Data and Code Availability

Figures and analysis for the validation of iterated masking EMD can be replicated with Python code available at [gitlab.com/marcoFabus/fabus2021\\_itemd](https://gitlab.com/marcoFabus/fabus2021_itemd). Hippocampal LFP data is available from the CRCNS platform (<https://crcns.org/data-sets/hc/hc-3>) and human MEG data is available from the Cam-CAN archive (<https://camcan-archive.mrc-cbu.cam.ac.uk/dataaccess/>)<sup>272,273</sup>. Analyses were carried out in Python 3.9.4, building on the open-source EMD package (v0.4.0), available with tutorials at

<https://emd.readthedocs.io><sup>278</sup>, which now contains an implementation of itEMD, too. Underlying dependency packages were numpy<sup>279</sup>, scipy<sup>280</sup>, pandas<sup>281</sup>, pingouin<sup>282</sup>, and statsmodels<sup>283</sup> for computation and matplotlib<sup>284</sup> for visualization.

## 4.3 Results

### 4.3.1 Simulations

Iterated masking sift (itEMD) rapidly converged on signal in presence of noise and intermittency. An initial ten second data segment with a 30Hz transient burst, a 4Hz non-sinusoidal oscillation, and low white noise was first simulated (Figure 4.2). The iteration process was started with a set of six random masks drawn uniformly from 1-128Hz. Despite this initial complete lack of knowledge about the signal, itEMD correctly recovered the non-sinusoidal waveform and the beta-frequency burst. The iteration process converged with noise in IMF-1, the 30Hz beta burst in IMF-2, and non-sinusoidal 4Hz signal in IMF-3. Subsequently, convergence was determined automatically. The convergence criterion was set to the mask stabilizing within 10% between iterations with a maximum number of iterations of 15 (see Methods). Further simulations were initialized with the zero-crossing masked sift results for faster convergence. All simulations were repeated with N=100 different noise realizations.

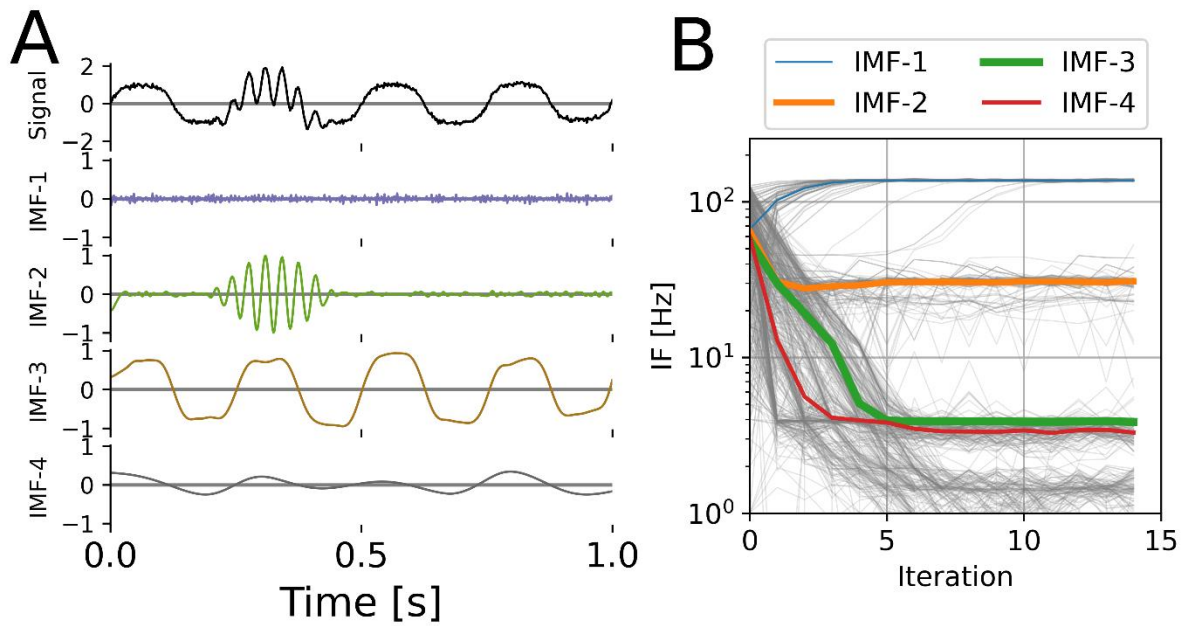


**Figure 4.2:** Iterated Masking EMD (itEMD) on simulated data. **(A)** Example endpoint of itEMD, i.e. IMFs from last of 15 iterations on the same signal as in Figure 4.1B. **(B)** itEMD convergence to equilibrium starting with a mask drawn randomly from a uniform distribution of 1-128Hz. Thin gray lines are all 100 individual runs, coloured lines are median trajectories with line thickness scaled to maximum value of that IMF. itEMD converges rapidly, adapts mask frequencies to the signal content, and correctly finds both the non-sinusoidal 4Hz oscillation and intermittent 30Hz burst with no prior knowledge about the frequencies contained in the signal.



## Influence of noise

It was desirable to establish how different sifting methods reconstruct waveform shape in presence of noise (Figure 4.3). Ten seconds of a 4Hz non-sinusoidal iterated sine signal with white noise was simulated. The standard deviation of zero-mean white noise (root-mean-square of noise, RMS noise) was varied as the shape of the wave remained constant with 8<sup>th</sup> order iterated sine (frequency distortion FD=68%, see Methods). Iterated masking was compared to existing dyadic masking and ensemble sifting techniques.

First, performance was measured by computing Pearson correlation of reconstructed and ground truth waveform shape measured by the instantaneous frequency (Figure 4.3A).

For low to medium noise amplitudes ( $\sigma_{\text{noise}} \lesssim 1$  with normalized signal amplitude of one), existing techniques were sufficient to represent the waveform shape well. Ensemble-sift reconstructed waveform shape had a high correlation with the ground truth shape with  $r > 0.75$ , but its performance quickly deteriorated past  $\sigma_{\text{noise}} = 0.1$ . Dyadic mask sift had poor shape reconstruction for no noise but performed well from  $\sigma_{\text{noise}} = 0.1$  onward. The novel iterated masking performed well except for a dip in performance around ultra-low noise below  $\sigma_{\text{noise}} = 0.1$ . This was found to be the level where noise RMS is equal to the amplitude of one of the higher signal harmonics. As such, this harmonic was sometimes included in the IMF of interest and sometimes not, depending on exact noise details, introducing stochastic mode mixing. Noise levels in neurophysiological data are seldom this low. However, these pathological cases could be automatically identified because the mask did not reach a stable equilibrium and the maximum number of iterations was reached (red shading).

For high noise amplitudes ( $1 \lesssim \sigma_{\text{noise}} \lesssim 2$ ), the new itEMD significantly

outperformed existing techniques. Ensemble sift produced sine waves and failed to capture non-sinusoidal waveform behaviour (correlation near zero). Dyadic mask sift suffered from mode mixing, with the waveform split across IMF-4 and IMF-5 (Figure 4.1D). Because of this, dyadic masking failed to accurately reconstruct waveform shape, especially above  $\sigma_{\text{noise}} = 1$ . In contrast, itEMD accurately isolated the signal even at high noise levels (Figure 4.3B). Its reconstructed shape correlated with the ground truth significantly better than the existing techniques with  $P < 0.01$  (Bonferroni corrected across 100 noise levels) across the high noise range  $1 \lesssim \sigma_{\text{noise}} \lesssim 2$ .

In the region of very high noise with  $\sigma_{\text{noise}} > 2$ , all methods behaved as dyadic filters and failed to capture waveform shape. This is because higher Fourier harmonics encoding shape details became submerged in noise, making it impossible to recover the non-sinusoidal shape.

Mode mixing performance was also evaluated by computing the PMSI (Pseudo-Mode Splitting Index, Figure 4.3C), a mode mixing metric previously used in the literature <sup>245</sup>. A high PMSI value indicates severe mode mixing and poor sift.

For low noise amplitudes ( $\sigma_{\text{noise}} \lesssim 0.3$ ), the dyadic mask sift produced the least amount of mode mixing (lowest PMSI). In this region, itEMD was again susceptible to stochastic mode mixing due to noise levels matching higher harmonics, increasing the PMSI. Ensemble sift had the most mode mixing in this region.

For medium to high noise ( $0.3 \lesssim \sigma_{\text{noise}} \lesssim 2$ ), itEMD had significantly less mode mixing than existing techniques (lowest PMSI  $P < 0.01$ , Bonferroni-corrected). Ensemble sift had a largely unchanging amount of mode mixing, suggesting it was driven by the added noise. Dyadic masking had the most mode mixing in this region.

All three methods had similar PMSI in the very high noise region with  $\sigma_{\text{noise}} > 2$  due to inherent dyadic filtering behaviour of EMD.

Neurophysiological signals typically show auto-correlated 1/f noise (also termed aperiodic activity or fractal noise) <sup>285</sup>. To verify the technique works with 1/f noise simulations, all the main analyses were re-run with brown noise. As with white noise, itEMD outperformed existing techniques over a wide range of parameters.

Finally, mask frequency stability was compared across itEMD iterations for a mode known to have signal (IMF-4) and a pure noise mode (IMF-5). The mask frequency was significantly less variable when signal was present.

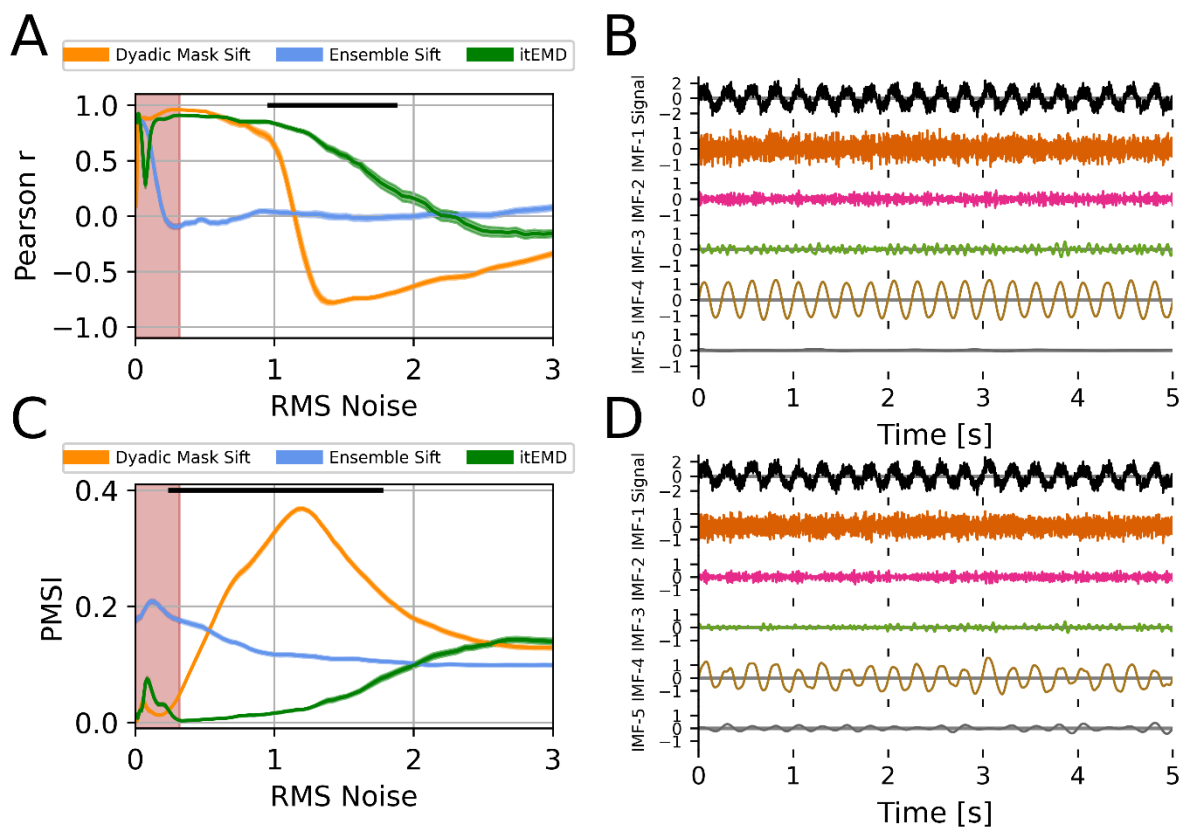


**Figure 4.3:** Influence of noise on EMD performance in simulated data. **(A)** Pearson correlation coefficient between reconstructed and ground truth instantaneous frequency against increasing white noise amplitude. **(B)** Example 5s of itEMD sift results for  $\sigma_{\text{noise}} = 0.5$ , FD=68%. Iterated sine function is captured by IMF-4. **(C)** Pseudo-Mode Splitting Index (PMSI) against white noise amplitude, with higher PMSI values indicating higher mode mixing. Mean  $\pm$  standard error across N=100

noise realisations shown. Black line indicates regions where itEMD performs significantly better than the best of the other techniques with  $P < 0.01$  (Bonferroni corrected). Red shaded region shows noise levels where itEMD reached maximum number of iterations in  $>20\%$  of noise realisations. itEMD performs significantly better for highly noisy data in the region between  $\sigma_{\text{noise}} \approx 1$  and  $\sigma_{\text{noise}} \approx 2$  with reduced mode mixing and accurate waveshape reconstruction. **(D)** Example dyadic mask sift results for  $\sigma_{\text{noise}} = 0.5$ ,  $\text{FD} = 68\%$ . IMF-4 shows more mode splitting than itEMD results.

### **Influence of frequency distortion (non-sinusoidality)**

Highly non-sinusoidal waveforms have been observed across a variety of neural data (see Introduction). As such, existing techniques and itEMD performance were compared in data with progressively more waveform distortion. Ten seconds of a 4Hz non-sinusoidal iterated sine signal with white noise of standard deviation  $\sigma_{\text{noise}} = 1$  was simulated. Frequency distortion was varied by iterating the sine function between 1 and 18 times. Each frequency distortion level was simulated with  $N = 100$  different noise realizations. Performance was again compared using Pearson correlation to ground truth shape and the PMSI.

Iterated masking performed significantly better than existing methods for highly non-sinusoidal signals (Figure 4.4, Bonferroni-corrected  $P < 0.01$  for lowest PMSI and higher Pearson  $r$ ). Dyadic mask shape correlation with ground truth was not significantly different from itEMD for  $\text{FD} < 50\%$ , but severe mode mixing was present. This meant the average frequency and amplitude were poorly reconstructed. At this noise level, ensemble sift behaved as a dyadic filter and completely failed to capture waveform shape. It produced a sinusoid at the dyadic boundary of  $f = 4\text{Hz}$  with no non-

sinusoidality. itEMD performance also improved with increasing frequency distortion. This is due to higher frequency harmonics increasing in magnitude with more shape distortion, allowing better convergence of itEMD.

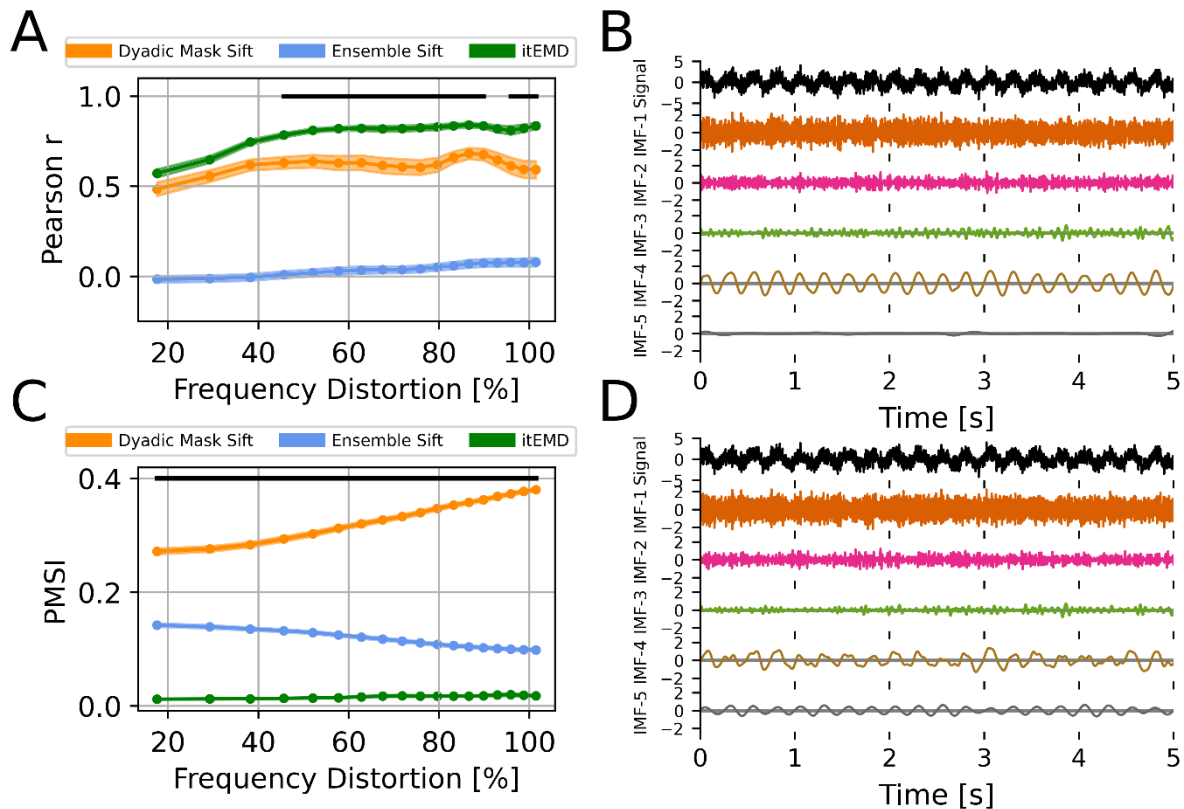


**Figure 4.4:** Influence of frequency distortion on EMD performance in simulated data. **(A)** Pearson correlation coefficient between reconstructed and ground truth instantaneous frequency against increasing frequency distortion. **(B)** Example 5s of itEMD sift results for  $\sigma_{\text{noise}} = 1$ ,  $\text{FD}=80\%$ . **(C)** Pseudo-Mode Splitting Index (PMSI) against frequency distortion, with higher PMSI values indicating higher mode mixing. Mean  $\pm$  standard error across  $N=100$  noise realisations (shaded) shown. Black line indicates regions where itEMD performs significantly better than the best of the other techniques with  $P<0.01$  (multiple comparisons Bonferroni corrected). The novel itEMD performs significantly better for highly non-sinusoidal data in the region  $\text{FD} > 50\%$  with reduced mode mixing and accurate waveshape reconstruction. **(D)** Example 5s of

dyadic mask sift results for  $\sigma_{\text{noise}} = 1$ , FD=80%. IMF-4 shows significantly more mode mixing with existing methods than with the novel itEMD.

### **Reconstructed Waveform**

Next, individual IMFs, reconstructed waveforms, and their instantaneous frequency were examined (Figure 4.5). As expected from the Pearson  $r$  and PMSI results in Figure 4.4, itEMD best reconstructed a highly non-sinusoidal waveform in the presence of noise. A noise level of  $\sigma_{\text{noise}} = 0.1$  and 4<sup>th</sup> order iterated sine were chosen as they are qualitatively similar to experimental LFP and MEG recordings analysed (cross-reference Figure 4.7). The ensemble sift was able to capture most of the non-sinusoidality but suffered from heavy mode mixing (PMSI = 0.0943). The dyadic mask sift had slightly less mode mixing (PMSI = 0.0923) but failed to capture any non-sinusoidal waveform shape details. The novel iterated masking captured the waveform shape best with the least mode mixing (PMSI = 0.0003). However, the waveform was still not perfectly reconstructed. This was due to i) some of the harmonics encoding the finer details being lower in spectral density than the noise and ii) due to intrinsic finite bandwidth of EMD modes. However, itEMD performed significantly better than the other techniques with the root-mean-square error to the ground truth instantaneous frequency being significantly lower ( $P < 0.0001$  vs dyadic mask,  $P = 0.045$  vs ensemble sift, Bonferroni-corrected).

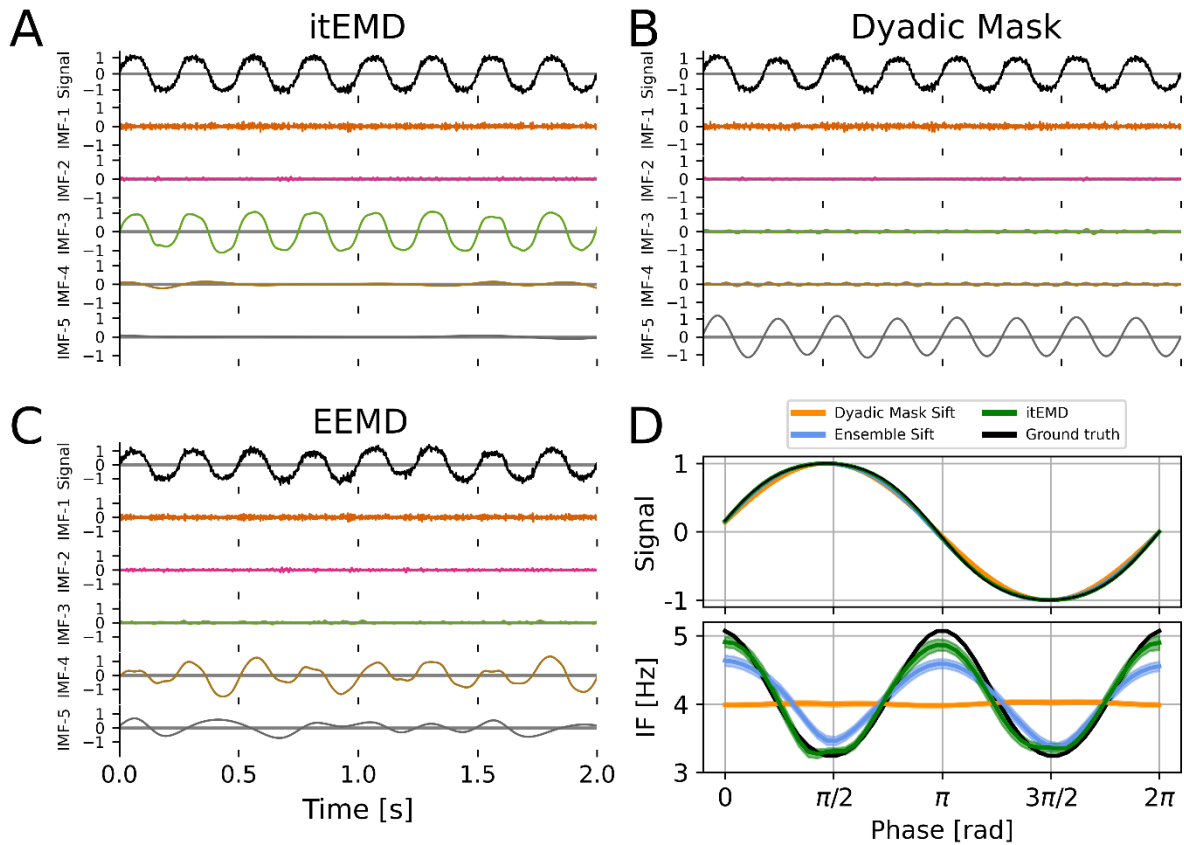


**Figure 4.5:** Example 2s of sifting results for 4<sup>th</sup> order iterated sine with white noise  $\sigma_{\text{noise}} = 0.1$  in simulated data. **(A)** IMFs for the novel itEMD. Iterated sine is in IMF-3 with very little mode mixing. **(B)** IMFs for dyadic mask sifting. Signal is split between IMF-2 and IMF-5. **(C)** IMFs for ensemble sifting. Iterated sine is mostly in IMF-4, but mode mixing is present. **(D)** Top: average reconstructed waveform, bottom: reconstructed phase-aligned instantaneous frequency (IF); mean (line)  $\pm$  standard error across cycles (shaded) shown. Dyadic mask sift waveform (orange) fails to reconstruct non-sinusoidality. Ensemble sift recovers more shape detail but suffers from high mode mixing. itEMD is able to reconstruct more of the waveform shape than either existing method whilst lowering mode mixing.

## **Influence of signal sparsity**

Neural activity often consists of intermittent bursts<sup>240</sup>. To test itEMD performance when signal is sparse, 25 seconds of zero-mean white noise with  $\sigma_{\text{noise}} = 1$  were simulated, to which a 4Hz non-sinusoidal 8<sup>th</sup> order iterated sine signal with frequency distortion  $FD = 68\%$  and variable length of 5-100 cycles was added. When reconstructing waveform shape of this burst, itEMD performed significantly better than either the dyadic mask sift, or the ensemble sift (Figure 4.6). Even in the presence of high noise and non-sinusoidality, itEMD was able to extract the burst and identify its waveform shape. Its correlation with ground truth waveform shape was significantly higher than the other methods for all burst lengths considered (Figure 4.6A,  $P < 0.01$ , Bonferroni corrected across number of cycles in the burst). Mode mixing measured by the PMSI was also significantly lower than with existing methods (Figure 4.6C,  $P < 0.01$ , Bonferroni corrected). Performance of itEMD improved as burst length increased. Overall, this demonstrates the potential benefits of itEMD when characterizing transient bursts, which is increasingly used to describe oscillations in electrophysiological data<sup>126</sup>.



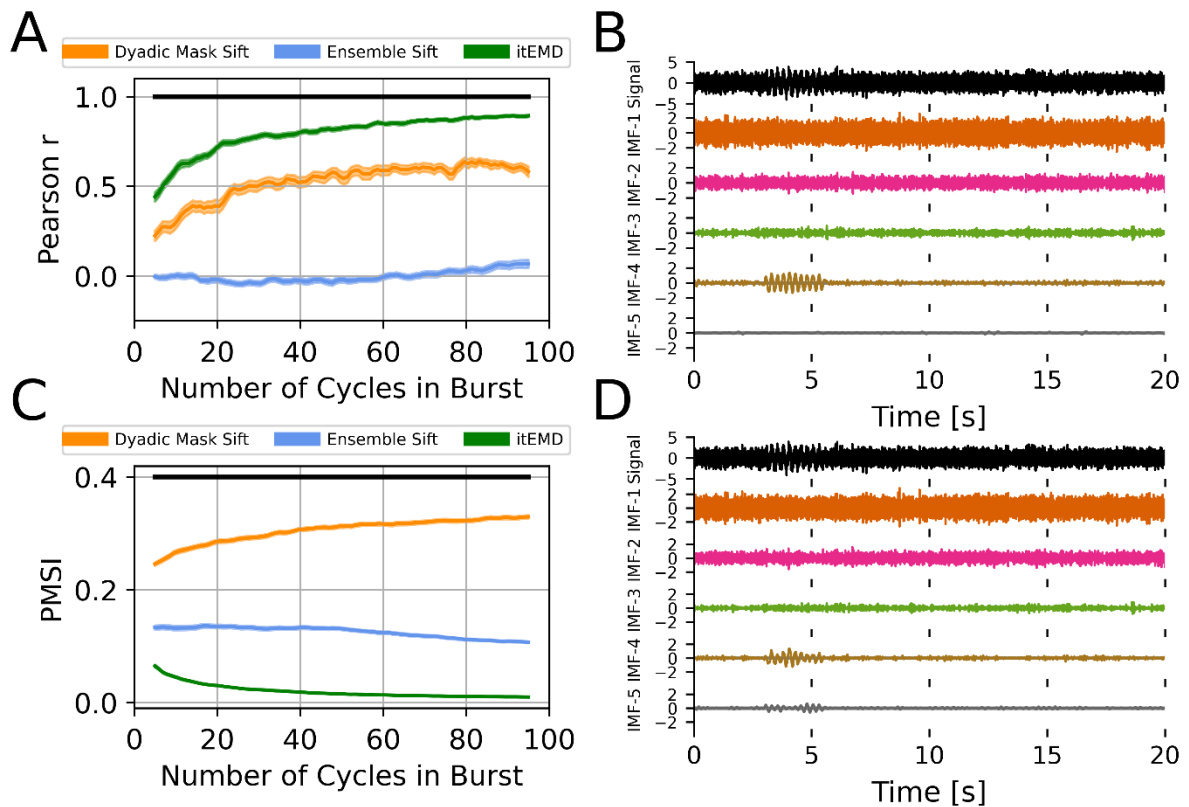


**Figure 4.6:** Influence of signal sparsity on EMD performance in simulated data. **(A)** Pearson correlation coefficient between reconstructed and ground truth instantaneous frequency against increasing burst length. **(B)** Example itEMD sift results for  $\sigma_{\text{noise}} = 1$ ,  $\text{FD}=68\%$ , 10 cycles. **(C)** Pseudo-Mode Splitting Index (PMSI) against burst length. Mean  $\pm$  standard error across  $N=100$  noise realisations (shaded) shown. Black line indicates regions where itEMD performs significantly better than the best existing technique with  $P<0.01$  (multiple comparisons Bonferroni corrected). The novel itEMD performs significantly better for a wide range of burst durations. **(D)** Example dyadic mask sift results for  $\sigma_{\text{noise}} = 1$ ,  $\text{FD}=60\%$ , 10 cycles in burst. Iterated sine function is captured by IMF-4 and IMF-5 due to mode mixing.

### 4.3.2 Validation in experimental datasets

#### **Rat Local Field Potential (LFP)**

The technique was first validated by applying it to the well-understood hippocampal theta signal in a 1000s recording of publicly available rat hippocampal LFP data. The recording was split into  $N=20$  segments of 50s each. This theta oscillation has been previously observed to be non-sinusoidal with, on average, a faster ascending than descending edge<sup>230,286,287</sup>. The novel iterated masking EMD (itEMD) converged after  $N_{\text{iter}} = 6 \pm 1$  iterations and extracted cycles with a wide instantaneous frequency sweep (Figure 4.7). It reproduced the known shape with a faster leading edge (leading edge frequency  $7.87 \pm 0.02\text{Hz}$ , falling edge frequency  $7.62 \pm 0.02\text{Hz}$ , mean  $\pm$  SEM,  $P < 0.0001$  on a paired t-test across all cycles). In comparison to itEMD, existing ensemble and dyadic mask sifting failed to capture the high non-sinusoidality of this oscillation. Existing methods also suffered from higher mode mixing as measured by the PMSI (lowest PMSI for itEMD with Bonferroni-corrected  $P < 0.0001$ ). This was confirmed by visualizing the Hilbert-Huang transforms, where theta IMF has the cleanest sweep for itEMD. This could allow for improved cross-frequency coupling analysis.

To compare this analysis with more traditional methods, the Wavelet transform was also computed (Figure 4.7G). The spectrum was qualitatively very similar to the itEMD HHT except with a smoothed lower time-frequency resolution. The wavelet transform also confirmed the artifactual components present in HHTs from existing methods. This was as there was no continuous low-frequency component nor high/low frequency switching seen in dyadic masking and EEMD respectively due to mode mixing.

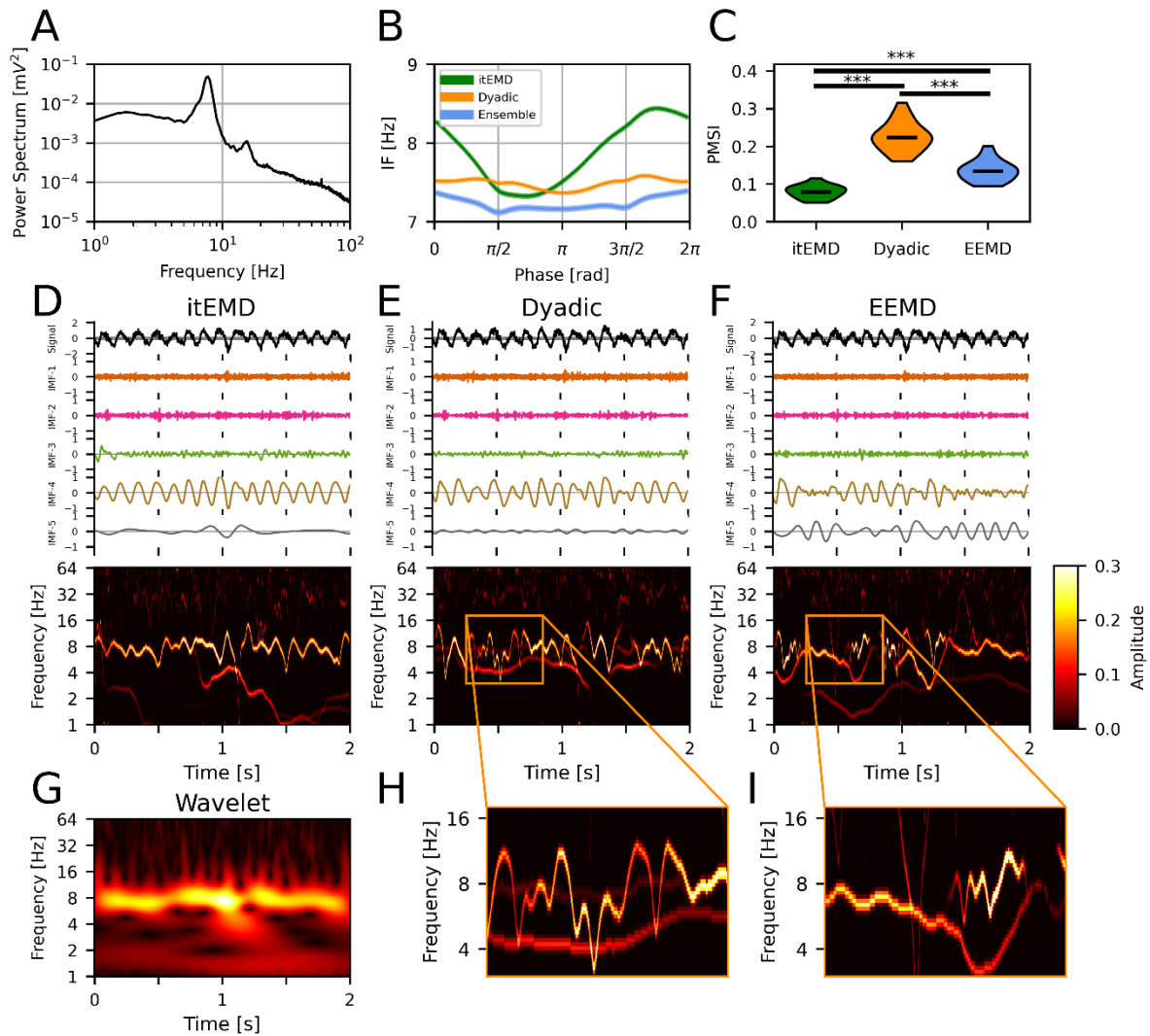


**Figure 4.7:** Rat hippocampal LFP results. **(A)** Power spectrum of the full recording showing a theta peak and harmonic. **(B)** Phase-aligned instantaneous frequency of theta cycles (mean  $\pm$  standard error across all cycles shown). Existing methods including dyadic mask sift and ensemble sift fail to capture high non-sinusoidality of theta oscillations unlike itEMD. **(C)** Violin plots of the pseudo-mode splitting index (PMSI, a measure of mode mixing) across N=20 segments of the 1000s recording. Iterated masking had significantly lower PMSI than both dyadic mask sift and ensemble sift ( $P < 0.0001$ , Bonferroni-corrected across methods). **(D)** Top - example itEMD sift results from two seconds of the LFP recording, bottom - Hilbert-Huang Transform (HHT) for the same data. Theta oscillations are well-captured by IMF-4 with minimal mode

mixing. **(E)**, **(F)** Same as (D) but for the dyadic mask sift and ensemble EMD. Significant mode mixing is present. **(G)** Wavelet transform of the same data as in (D)-(F). Similar dynamics to the HHT in (D) are present but with lower resolution. Comparing to (E) and (F), the artifacts in poor sifts are seen (red arrows). **(H)**, **(I)** expanded sections showing mode mixing.

### **Human Resting-state Magnetoencephalography (MEG)**

For further validation, 10 minutes of occipital resting-state data were analysed in each of N=10 subjects (Figure 4.8). One subject was excluded as their spectrum did not show an alpha peak. It was found itEMD successfully and rapidly converged on the intermittent alpha oscillation around 10Hz ( $N_{\text{iter}} = 5 \pm 1$  iterations across all subjects, mean  $\pm$  standard deviation). Compared to Dyadic mask sift and ensemble sift, mode mixing measured by the PMSI was significantly lower ( $P < 0.0001$  vs dyadic mask,  $P = 0.0033$  vs ensemble sift, Bonferroni-corrected paired t-test).

Alpha peak frequency is known to vary between people, conditions, and changes with age<sup>288,289</sup>. EMD has the advantage of representing spectral components with fewer assumptions about frequency bands unlike traditional Fourier analyses. As such, it may be well-suited to represent these inter- and intra-individual spectral differences. Variability in alpha peak frequency was also seen in data analysed here. Moreover, itEMD was able to replicate this result, with the mean subject phase-aligned instantaneous frequency found to be linearly related to spectral peak frequency (Figure 4.8D,  $F = 13.89$ ,  $P = 0.00739$ ). Recordings also showed the presence of beta-band elements around 20Hz in IMF-2, which were also present in the Fourier spectrograms (Figure 4.8E).

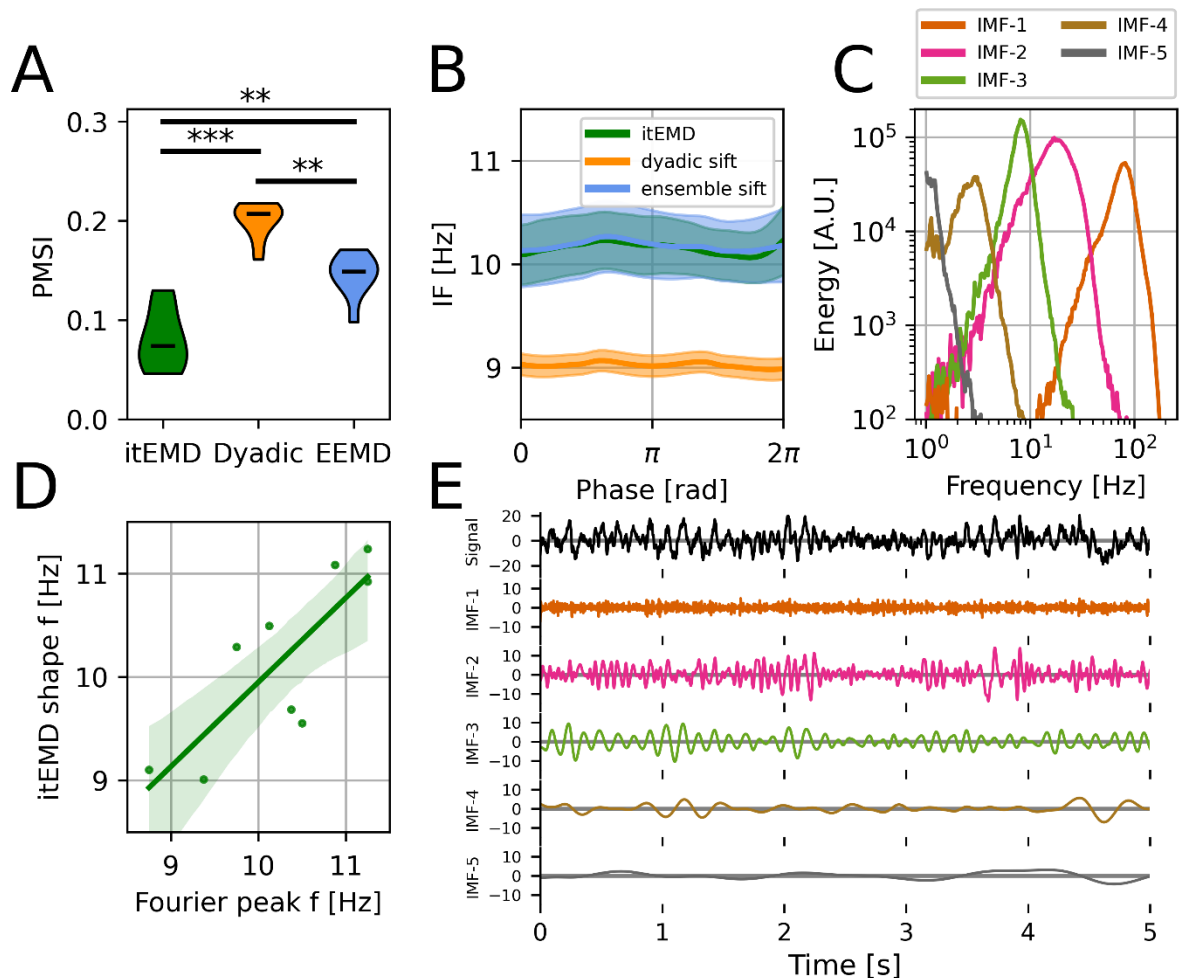


**Figure 4.8:** Human MEG occipital alpha results. **(A)** Group-level violin plots of the pseudo-mode splitting index (PMSI, a measure of mode mixing). Iterated masking had significantly lower PMSI than both dyadic mask sift ( $P < 0.0001$ ), and ensemble sift ( $P = 0.0062$ , both Bonferroni-corrected). **(B)** Group-level phase-aligned instantaneous frequency (mean  $\pm$  SEM shaded). Both itEMD and EEMD detect the 10Hz occipital alpha oscillation with no significant non-sinusoidality. Masked sift fails to capture the oscillation well due to mode mixing. **(C)** 1D HHT for IMFs from an example subject. **(D)** Mean subject phase-aligned instantaneous frequency against peak alpha frequency from the Fourier power spectral density. Iterated masking linearly reproduces between-subject variability in alpha frequency ( $P = 0.00739$ , F-test against constant null hypothesis). **(E)** Example 5s of raw itEMD sift results. Alpha oscillations are in IMF-3 with sharp features in IMF-2 and minimal mode mixing.

### 4.3.3 Application to human propofol anaesthesia EEG data

#### **Three different low-frequency modes**

Using traditional hard cut-off frequency bands can lead researchers to miss important features of the data<sup>290</sup>. Instead of using traditional frequency bands, iterated masking EMD was applied (itEMD, Figure 4.1). Unlike Fourier or Wavelet decompositions, the EEG is decomposed into a handful of non-sinusoidal modes. In this data from an ultra-slow anaesthetic infusion, data was split into four intrinsic modes. The first was dominated by spindle features in the alpha/beta band (10-20Hz), as well as high-frequency noise in the data. The other three modes were termed high delta (~5Hz), low delta (~1.5-2Hz), and slow (<1Hz). These modes were consistently found in each subject and each channel. The modes had significantly different frequencies ( $P < 0.0001$ , Bonferroni-corrected), which meant modes had a good between-electrode and between-subject correspondence, allowing for analysis of changing spatiotemporal patterns for each mode separately. Mode mixing as measured by the PMSI was also low, and instantaneous frequency suggested that the slow mode was most non-sinusoidal, with square-wave-like features (Appendix 3).

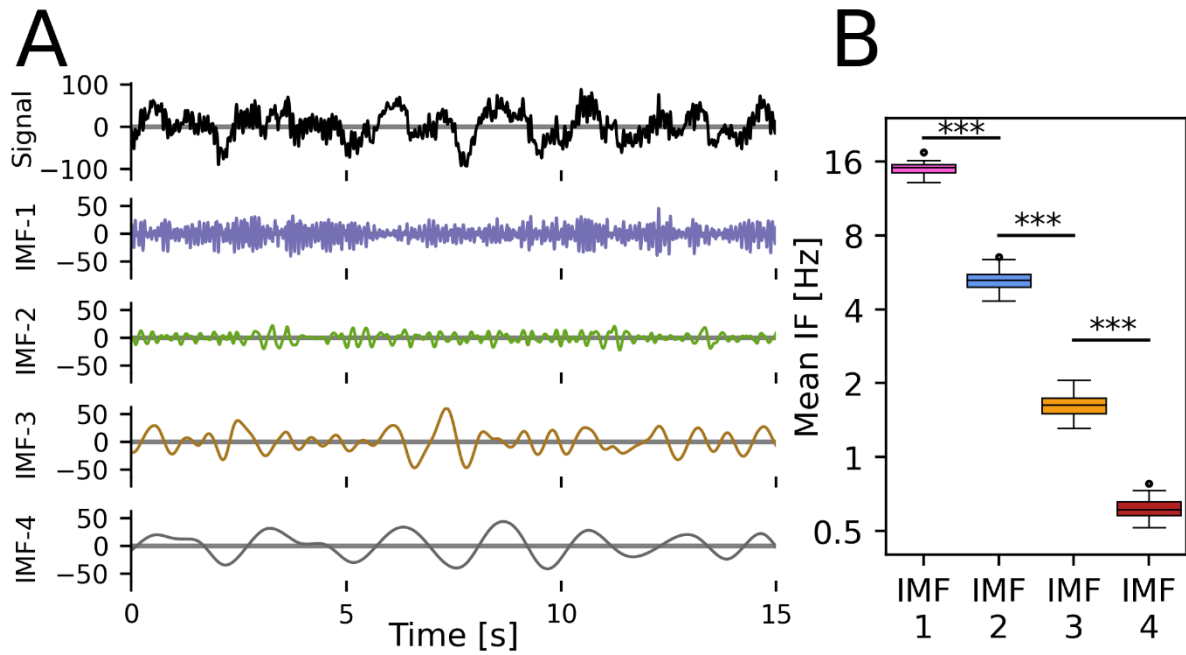


**Figure 4.9:** Iterated EMD sift results in propofol anaesthesia. **(A)** Decomposition of 15s of EEG during deep sedation with propofol anaesthesia from an example patient. The signal is decomposed in a data-driven way into four IMFs with physiological relevance: IMF-1 (spindles), IMF-2 (high delta), IMF-3 (low delta), IMF-4 (slow oscillation). **(B)** Boxplots of mean IMF instantaneous frequencies across N=16 subjects. Modes are well-separated in frequency and are consistent between subjects and between channels (c.f. Fig. 2 (G),  $P < 0.0001$ , Bonferroni-corrected t-test between mode frequencies).

## Trough-based analysis

To get an understanding of traveling waves in the data, a standard wave detection method based on finding and aligning oscillation troughs in the data was applied (Figure 4.10) <sup>85,86,275</sup>. Traveling waves were found in each of the three low-frequency modes. Properties of the waves changed in a dose-dependent and mode-dependent manner.

Wave globality represented the average number of channels implicated in a wave (Figure 4.10A). Wave type (N=14, F=124.94, P<0.0001), propofol level (N=14, F=31.68, P<0.0001), and their interaction (N=14, F=26.80, P<0.0001) all had significant effects on globality. Between the first third of induction (light anaesthesia, up to 1.3µg/ml propofol concentration) and the last third of induction (deep anaesthesia, up to 4µg/ml propofol concentration), low-delta and slow wave globality decreased (N=16, P=0.000275, Bonferroni-corrected post-hoc Wilcoxon signed rank test). In contrast, high-delta globality increased from medium (up to 2.67µg/ml propofol) to deep anaesthesia (N=16, P=0.00522). Comparing modes, low-delta globality was highest, followed by slow waves and high-delta waves.

Because of using itEMD, each wave had a well-defined mean instantaneous frequency (Figure 4.10B). Wave type (N=14, F=2274.47, P<0.0001), propofol level (N=14, F=38.28, P<0.0001), and their interaction (N=14, F=4.70, P=0.0246) all had significant effects on the wave frequency. All wave types showed significant decrease in frequency (light to deep: N=16, P=0.005493, P=0.000275, P=0.000275 for high delta, low delta, and slow waves respectively), though wave frequencies remained well-separated between modes.



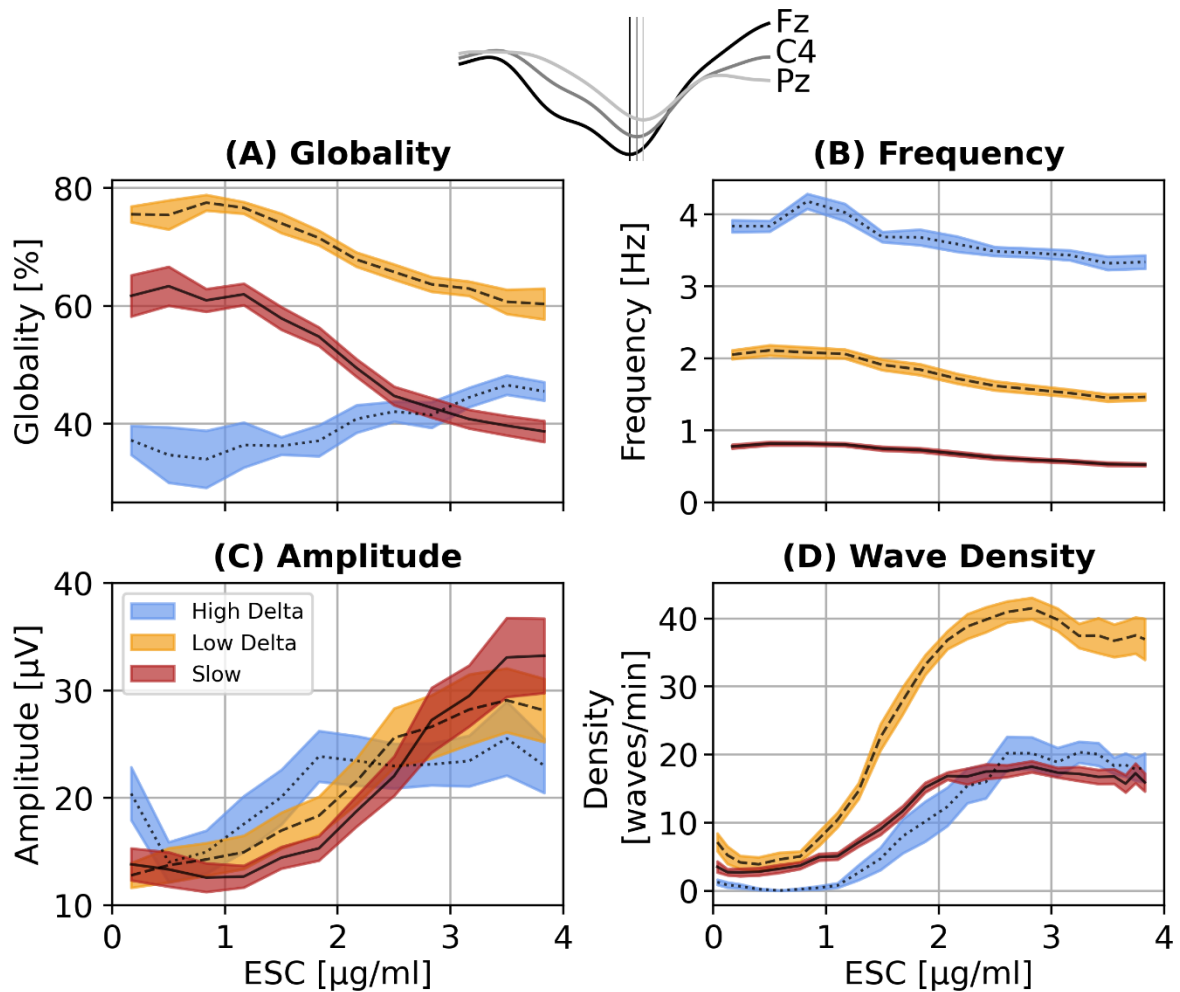


**Figure 4.10:** Trough-based wave analysis results. (A)-(D) show mean  $\pm$  standard error across subjects for properties across changing propofol effective site concentration (ESC). Top: Wave detection method – wave trough is detected across channels. **(A)** Mean wave globality (% of channels involved in a wave). Global low delta and slow waves become more localised, high delta waves increase in globality. **(B)** Mean wave frequency decreases with increasing concentration, but modes remain well-separated. **(C)** Mean wave amplitude increases with increasing propofol, with low delta and slow waves being more dominant at high doses. **(D)** Wave density (number of waves detected per minute) against ESC. All three wave types increase in number but show saturation at high doses.

It is well-known EEG power increases and plateaus in the low-frequencies as anaesthesia is induced<sup>31</sup>. This power is in part due to the amplitude of traveling waves and their density (number per time). The results here confirmed this. Propofol level had a significant effect on wave amplitude (N=14, F=35.49, P<0.0001), though wave amplitude was not significantly affected by wave type (N=14, F=0.698, P=0.465). Waves from all modes showed a significant increase in amplitude (Figure 4.10C, N=16, P=0.000092 between light and deep anaesthesia). Interestingly, wave plateau appeared at different concentrations for each mode. High-delta amplitude saturated first, low-delta next, and slow wave amplitude only saturated in some subjects.

Wave density was the number of waves detected per minute (Figure 4.10D). Both wave type (N=16, F=120.11, P<0.0001) and propofol level (N=16, 134.66, P<0.0001), as well as their interaction (N=16, F=37.23, P<0.0001), had a significant effect on the wave density. Similar to the amplitude, wave density significantly increased until saturation for all wave types. Low-delta waves had the highest wave density (N=16, P=0.000092 vs slow and high delta, Bonferroni-corrected Wilcoxon signed rank test).

I also analysed topographical properties of the traveling waves from each mode (Figure 4.11), focusing analysis on the frontal, posterior, and temporal regions.

Detection probability showed on which channels waves were most likely to be detected (Figure 4.11, top). At light propofol doses, high-delta waves were mostly found centrally and low-delta / slow waves were predominantly found frontally. This shifted at high propofol doses, where high-delta waves were mostly found frontally (N=16, P=0.003296 frontal vs posterior detection probability) and low-delta / slow waves shifted more centrally.

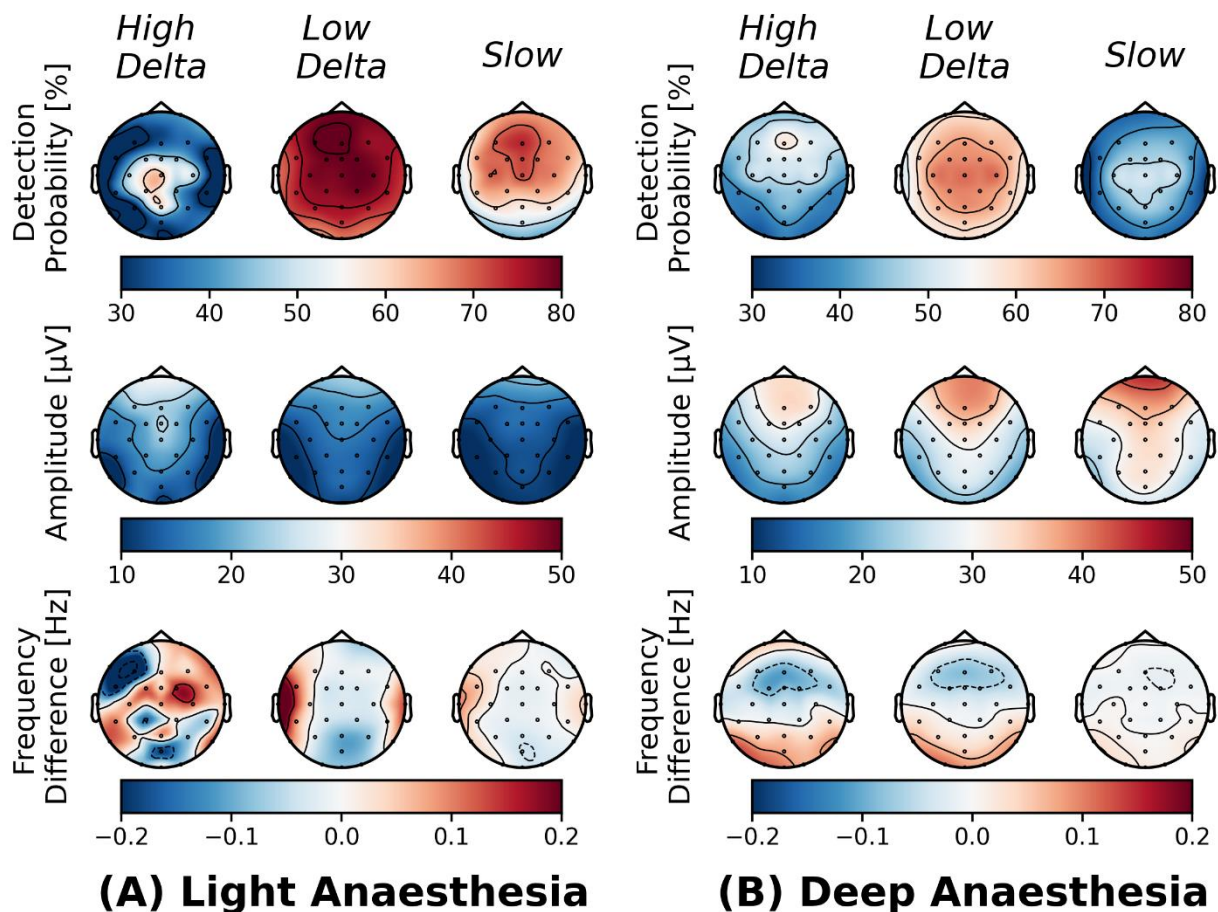


**Figure 4.11:** Wave topography in trough-based analysis. All panels show mean topographical wave properties across three wave types in **(A)** light anaesthesia (first third of induction) and **(B)** deep anaesthesia (last third of induction). (Top) Detection probability (probability of any given wave being detected at a channel). Waves become more fronto-central in deep anaesthesia. (Middle) Wave amplitude. Waves are frontally dominant and increase in amplitude, which slow waves being more fronto-central than frontal high and low delta. (Bottom) Frequency difference from the scalp mean. Early induction has lowest frequency in posterior regions. This shifts to frontal regions being lowest frequency in deep anaesthesia.

Topographical distribution of wave amplitude also showed differences between wave types and anaesthesia levels (Figure 4.11, middle). As seen in Figure 4.10C, here a large increase in amplitude was also observed between light and deep propofol doses. More interesting were the changes between wave types. High delta waves had largest amplitude pre-frontally. Low-delta waves amplitude was also high in central locations. Slow wave amplitude was the only one that notably penetrated into posterior regions, but only at deep anaesthetic levels. At light doses, frontal amplitude was significantly higher than posterior (N=16, P=0.0461). In contrast, at deep doses, frontal and posterior amplitude was not different (N=16, Bonferroni-corrected P>0.1).

Traveling waves had different frequencies across the scalp (Figure 4.11, bottom). During light anaesthesia, low-delta wave frequency was highest in temporal regions (N=16, P=0.00659 vs frontal and posterior region, Bonferroni-corrected post-hoc Wilcoxon test). This changed during deep anaesthesia where frontal regions were lowest in frequency and posterior/occipital regions highest (N=16, P=0.023 for frontal vs posterior frequency).

## 4.4 Discussion

In this chapter, I introduced a novel way of performing Empirical Mode Decomposition (EMD) called iterated masking EMD (itEMD). This technique is capable of robustly decomposing signals into spectral components in presence of noisy, sparse, and highly non-sinusoidal oscillations. In itEMD, masking signals are introduced at frequencies identified by an iterative, data-driven process. I demonstrated the utility of this sifting technique in comparison with existing EMD solutions to the mode mixing problem. Through extensive simulations, it was shown that itEMD performs significantly better than the existing methods in cases with highly noisy and strongly non-sinusoidal signals, where the technique significantly reduces mode mixing and accurately extracts oscillations and their shape.

The method was further validated using rat LFP and human MEG recordings. itEMD reproduces the well-known hippocampal theta waveform shape better than existing techniques and successfully reconstructs occipital alpha peak frequency with no a-priori information about mask frequencies. Rat hippocampal theta was found to be highly non-sinusoidal with a faster ascending edge as previously reported<sup>230,286,287</sup>. Intermittent human occipital alpha was found to be nearly sinusoidal with a between-subject variable peak frequency around 10Hz. Furthermore, itEMD significantly reduced mode mixing in both validation datasets studied. Iterated masking EMD has the potential to enable more wide-spread use of EMD in neurophysiology and shed light on single-cycle dynamics across a wide range of modalities and conditions. It automates the selection of mask frequencies and can thus enable a wide range of

analyses about bursts of neural activity, genuine cross-frequency coupling, and analysis of neural phase.

Non-EMD based analysis methods may complement itEMD. Traditionally, analysis has been done by calculating the Hilbert transform on narrowband filtered data<sup>230</sup>. This works well if frequencies of interest are defined a priori. However, it poses limitations on how non-sinusoidal oscillations can be and does not allow for large between-subject variabilities. Furthermore, the use of Fourier filters may introduce bias into the analysis<sup>233,291</sup>. More recently, methods based on detecting phase control points (peaks, troughs, etc) have been developed<sup>262</sup>. These provide important summary statistics for cycles, such as peak-trough asymmetry and rise-decay asymmetry. EMD-based analysis describes the shape with phase-aligned instantaneous frequency without restricting analysis to certain phase points. The cycle-by-cycle approach could thus be cross-validated by itEMD detecting asymmetry around the phase points used for its statistics. Finally, additional novel algorithms for extracting summary waveforms for a whole recording have been developed<sup>292,293</sup>. Unlike itEMD and the techniques described above, these are however not sensitive to changes in waveform within a recording.

#### 4.4.1 Limitations of itEMD

Although itEMD represents a significant step towards extracting non-sinusoidal neural oscillations in a data-driven way, there may be situations where other techniques are more appropriate. A full description of the limitations is included in the paper<sup>261</sup>, but a brief overview is given here.

First, itEMD adapts IMF bandwidth to capture more waveform shape detail. This can however also include more noise, and if non-sinusoidal features are not being studied, other methods may have better signal-to-noise ratio.

itEMD was designed to handle sparse oscillations, but it may be necessary to adjust the amplitude weighting method if signals of interest are very sparse (<10% of a data segment being processed). This can be done by changing the weighting of instantaneous frequency when iterating. Here weighting by the square of instantaneous amplitude ( $IA^2$ , instantaneous power) was used at each iteration. Higher powers of instantaneous amplitude may help if sparsity is preventing itEMD from converging on oscillations of interest.

In this work, iteration convergence was defined as the point when the relative mask change between iterations was under 10%. It was qualitatively observed that only minimal changes occurred after the 10% convergence point. However, in datasets not studied here, it may be necessary to tune the convergence criterion depending on exact noise structure present.

itEMD implicitly assumes that the mean frequency of oscillations of interest is not changing greatly and an equilibrium can be found. Hence, if peak frequencies may shift over time, it is recommended to segment the data. Furthermore, I analysed a single MEG sensor. This means that the recorded signal may be a superposition of multiple underlying sources. To separate sources both spectrally and spatially, other methods should be used in conjunction with itEMD, e.g. Independent Component Analysis (ICA) or Source Reconstruction.

#### 4.4.2 Three distinct low-frequency modes in propofol anaesthesia

Interpreting the electroencephalogram (EEG) in terms of pre-defined frequency bands remains the most common form of analysis, but it comes with serious limitations<sup>290,294</sup>. Splitting the signal into strict bands does not consider the heterogeneity between subjects or non-sinusoidality (frequency changes) in the data<sup>288,295</sup>. This is a particular problem for studying low-frequency rhythms in unconscious states including anaesthesia. It is known these waves are highly non-sinusoidal<sup>121</sup>, and the specific frequency boundaries used vary between studies, ranging from 0.1Hz all the way to 6Hz<sup>85,86,124,275,296</sup>. There are hints in the literature that different parts of the delta / slow band may have different function. For instance, during surgical skin incision, it was observed that <2Hz activity decreased while 2-4Hz activity increased<sup>297</sup>. In sleep, two types of slow-waves with different frequencies have been proposed<sup>123,124</sup>. In this chapter, an automatic, data-driven spectral decomposition method was used to identify physiologically relevant modes in noisy electrophysiological data<sup>298</sup>. Three distinct low-frequency modes were found: high delta (~4Hz), low delta (~2Hz), and slow (<1Hz). These modes had different topographical and traveling wave properties and showed different behaviour as anaesthesia deepened. High delta waves were locally circumscribed, frontal, and appeared last as propofol concentration increased. Low-delta waves had the highest density and globality. Slow waves saturated in amplitude last, but consisted of large, persistent, and slowest patterns which reached into posterior parts of the brain. It is possible these three modes have distinct roles in anaesthesia, for instance in mediating noxious response<sup>299</sup>. Power in the 0.5-1.5Hz band has been shown to saturate, producing a potentially individualised marker for perception loss<sup>31,94</sup>. The analysis shows that slow-wave saturation is likely a mix of slow and low-delta effects.



It is interesting to consider the results in the light of an ongoing debate about the role of frontal and posterior regions in consciousness and anaesthesia<sup>115–117</sup>. Aligning with results from Chapter 2, it was shown that the decrease in wave frequency that accompanies anaesthesia was initially more present in the posterior regions, but later the lowest frequencies were over frontal regions (Figure 4.11). This supports the idea that losing consciousness includes several shifts in brain states, which may start in the posterior but later envelop most of the cortex<sup>117</sup>. The DOWN state of neuronal silence in the slow oscillation has been implicated in decreasing cortical complexity<sup>143</sup>. It was seen that most slow waves originated frontally, so the fact the slow mode amplitude (but not high or low delta) extended to posterior regions may reflect their role in disrupting the hot zone or higher frequency frontoparietal communication, both thought to be important in maintaining consciousness<sup>115</sup>.

#### 4.4.3 Limitations of the propofol analysis

Using EMD to spectrally decompose the data was validated in this chapter and has proven fruitful in other studies<sup>258,300,301</sup>, but other alternatives exist. For instance, EEG data can be split into its oscillatory and aperiodic parts<sup>285</sup> (which change in anaesthesia<sup>97</sup>), and they could be analysed separately. Moreover, itEMD produces modes with large bandwidth<sup>298</sup>, so the alpha/spindle mode also contained high-frequency noise, making it unsuitable for analysis. If researchers wanted to focus on alpha, other approaches are recommended, such as masked EMD with hypothesis-driven masks<sup>244</sup>.

In this chapter, linked mastoid EEG referencing was chosen. This was because it is the standard in anaesthesia and sleep literature when analysing traveling waves, as it

reflects the underlying global oscillations well<sup>85,86,123,124</sup>. However, previously it has been shown using other references (e.g. average reference) results in similar key topographical properties, even if individual waves may look different<sup>302</sup>. Finally, the potential role of low-frequency subtypes in clinical settings could not be explored in this dataset. In the future, applying itEMD to a larger patient dataset with behavioural and clinical outcomes would be desirable.

In summary, I have introduced a novel way to robustly extract oscillatory modes from neural recordings using iterated masking EMD. The method has all the advantages of using EMD whilst resolving limitations of existing sifting techniques by significantly reducing the mode mixing and robustly capturing oscillations even in presence of noise, sparsity, and high non-sinusoidality. By validating it on extensive simulations and real multi-modal, multi-species data, as well as applying it to propofol anaesthesia, I have demonstrated its potential to bring the full power of EMD into neurophysiology and help elucidate the role of dynamic neural oscillations.



# 5 Spatiotemporal brain states in propofol anaesthesia

## 5.1 Introduction

The phenomenal richness of consciousness is one of the defining features of human existence. Whilst a complete theory of consciousness has so far eluded scientists and philosophers alike, existing scientific theories of consciousness have tried to link phenomenal consciousness with brain function<sup>172,303,304</sup>. Despite major differences, one area of overlap in leading theories is the postulate that in order to support consciousness, the brain must possess sufficient complexity to have processes that are at once integrated and diverse<sup>172,303</sup>. For example, in the Global Workspace theory, this means broadcasting segregated information in order to produce unified experience<sup>305</sup>, and in the Integrated Information Theory, diversity and integration are combined into a quantity of integrated information. Importantly, a wide variety of metrics estimating brain complexity and integration have been able to discriminate between different levels of consciousness, including anaesthesia and disorders of consciousness<sup>32,99,102,146,306,307</sup>. At present, a dynamic repertoire of brain activity appears to be a robust correlate of consciousness independently of the chosen brain imaging modality, species, or state of consciousness<sup>100,146,307–315</sup>.

Rather than describing brain dynamics as continuously evolving, emerging evidence suggests that brain activity can be well-represented as switching between discrete metastable spatiotemporal states<sup>126,127,240,316,317</sup>. These states can be found in a data-

driven way using Hidden Markov Modelling, as has been done for sleep<sup>128</sup>, disorders of consciousness<sup>318</sup>, and ketamine anaesthesia<sup>183</sup>. In this framework, states are characterised by mean activity in each brain region, functional connectivity between regions, and a transition probability matrix between states. This can complement traditional analyses as it allows for modelling of time-varying network behaviour, rather than looking at static networks averaged over time<sup>319</sup>. This time variance appears relevant for brain processing, as time spent in states and transitions between states have been associated with a wide variety of conditions and cognitive processes including sleep stages<sup>128</sup>, memory replay<sup>320</sup>, motor impairment in Parkinson's disease<sup>321</sup>, and cognitive therapy in PTSD<sup>322</sup>.

As was demonstrated in Chapter 3, linked heart-brain activity is observed under anaesthesia. Cortico-cardiac information is exchanged bi-directionally through the sympathetic and parasympathetic nervous system, with the latter chiefly through the vagus nerve. This brain-heart connection and associated monitoring of afferent visceral signals has been extensively studied in the context of emotional processing, where for example anterior cingulate activity associated with emotional regulation covaries with cardiac vagal tone<sup>184</sup>. More recently, it has been suggested heart-brain interactions may play a role in the neuroscience of consciousness itself, with the heart-beat evoked response distinguishing patients with and without covert consciousness in disorders of consciousness<sup>108</sup>, disappearing in a case of ventricular fibrillation before death<sup>323</sup>. Neural monitoring of visceral inputs may shape upstream neural dynamics and be involved in forming self-awareness through integration of interoceptive information<sup>107,324</sup>. Thus, to fully understand states of (un)consciousness under anaesthesia, inclusion of cardiac information may be necessary.

In order to utilise EEG in routine surgical settings, it is impractical to rely on high-density montages with dozens of electrodes as they take a long time to set up and may overlap with the surgical field. On the other hand, high-density montages are commonly deployed in neuroscience to capture underlying neural activity with higher accuracy<sup>325</sup>. In recent years, the possibility of capturing relevant EEG features with an intelligently chosen low-density montage has been explored with promising results<sup>326–328</sup>. The aim for translational neuroscience in this approach is to find montages capable of monitoring relevant brain features in routine clinical settings.

In this Chapter, using Hidden Markov modelling and EEG, the spatiotemporal brain states underlying loss and recovery of consciousness under an ultra-slow infusion of propofol are investigated. State dynamics are studied in relation to changing propofol concentration as well as behavioural responsiveness. Baseline predictors of anaesthetic sensitivity are also analysed. Then, the definition of a ‘state’ is expanded to include heart-brain information, presenting combined EEG/ECG HMM (“EXG-HMM”) results. Finally, to aid future clinical translation, how the HMM properties translate to subsets of EEG electrodes is explored in order to simulate a low-density, potentially clinically utilisable system.

## **5.2 Materials and Methods**

### **5.2.1 Data Acquisition and Pre-processing**

This dataset was described in detail in the Methods section of Chapter 2. Briefly, N=16 healthy volunteers (8 female, age  $28\pm 6$  years) underwent ultra-slow propofol induction up to  $4\mu\text{g/ml}$  and subsequent emergence whilst 32-electrode EEG was recorded. For analysis in this chapter, after ICA clean-up and re-referencing to the common average

as per Chapters 2 and 3, data was re-sampled to 100Hz and bandpass-filtered 0.5-45Hz. One subject was excluded as they were the only one showing burst-suppression, which has a very different frequency signature that would have likely biased the HMM. Burst suppression is however not uncommon in clinical settings, particularly during induction, so further studies with more burst suppression in their datasets may benefit from including it. Hidden Markov Modelling was run on data concatenated across all of the experiment. For further analysis, after Hidden Markov Modelling (see below), the experimental data was divided into 8 stages matching the original staging of the experiment<sup>31</sup>: 10-minute baseline recording, three 16-minute induction segments, 10-minute hold at peak propofol concentration, and three 16-minute emergence segments.

### 5.2.2 Hidden Markov Modelling

Spatiotemporal brain states were estimated in a data-driven way using the time-delay-embedded Hidden Markov Model (TDE-HMM) implemented in the MATLAB HMM-MAR toolbox<sup>127,317</sup>. This approach describes the data as a sequence of a finite number of states, where at each time-point only one state is active and each state has its own oscillatory power and connectivity characteristics, linked to the data through a probabilistic observation model. It was chosen as it is a flexible, data-driven approach that can provide insights beyond static power or connectivity measures commonly used.

In this analysis, K=6 states were chosen. This number of states showed the best replication in a split-half matching test (Supplementary Figure 5.1), but K=4-20 states were also explored (Supplementary Figures 5.4, 5.5) with broadly similar results. Time-embedding was done using 11 lags (100ms window, chosen to capture the alpha

rhythm present throughout the data). HMM states were then estimated on the space reduced by Principal Component Analysis (24 components, 90% variance captured) using stochastic inference<sup>127</sup> with batch size of N=8 experimental stages. Robustness of results across stochastic effects was verified by repeating the analysis N=5 times (Supplementary Table 5.1).

### **State fractional occupancies and Power spectra estimation**

After state estimation, the state fractional occupancies were computed, defined as the temporal proportion of the recording for which an HMM state is active, as well as the switching rate, for each stage in each subject. Significance of differences in switching rate and fractional occupancies between states and experimental stages were tested using 2-way omnibus repeated-measures analysis of variance (ANOVA) with Huynh-Feldt P-value adjustment for sphericity violations, followed by Tukey's Honest Significant Difference post-hoc tests.

Power spectra (0.5-45Hz) for each state were estimated using a state-wise multitaper approach<sup>126</sup>. Connectivity patterns were similarly estimated as the demeaned broadband coherence. State power maps were then computed using EEGLAB topoplot on standard 10-20 electrode locations, relative to the mean weighted by across-experiment fractional occupancy<sup>329</sup>. States are randomly numbered when estimated by the HMM-MAR toolbox. For visualisation and interpretation purposes, states were re-ordered by decreasing total (broadband) power.



## **Transition probability matrices**

We were interested in the states' network graph, i.e. which states transition to which other states. Thus, the mean transition probability matrix was computed, as well as individual matrices for each stage in each subject. State communities (sub-networks) were found using Louvain community detection (MATLAB's Brain Connectivity Toolbox<sup>330</sup>). Significant changes in transition probabilities between the baseline and peak anaesthesia stage were tested using permutation testing. Briefly, the condition (baseline / peak stage) was randomly swapped for each subject and state and differences re-computed for N=1000 permutations. This produces a null distribution across all state transition matrix elements and state transition changes with Bonferroni-corrected  $P < 0.05$  were kept. For visualisation, the mean transition probability graph was plotted (MATLAB's graphplot) for probabilities  $> 20\%$ .

## **Associations with behavioural responsiveness and SWAS**

Next, we wanted to know if time spent in a state until a clinically observable outcome (loss of behavioural responsiveness, LOBR) was linked with propofol concentrations during behavioural and SWAS outcomes. After finding HMM states and their fractional occupancies, Spearman correlations and associated FDR-corrected P-values were computed between time spent in a given state until LOBR and propofol concentrations at LOBR, ROBR, as well as  $C_{\text{SWAS}}$  and  $P_{\text{SWAS}}$  at induction and emergence. SWAS parameters were calculated as per Chapter 2.

## 5.2.6 EXG-HMM

In order to explore states in the combined cortico-cardiac system, another HMM was estimated. The dataset and HMM hyper-parameters (e.g. the number of states) were identical to the original EEG-HMM, except the single-lead ECG channel was included in the model, with each channel standardised to mean zero and standard deviation of one (HMM-MAR toolbox default). After HMM estimation, model properties across the scalp (switching rate, power maps, transition probability matrix) were studied in the same way as in the original model. In addition, heart rate in each state was estimated as the number of R-peaks occurring whilst that state is active relative to overall time spent in each state, with R-peaks identified using *biosspy* as in Chapter 3. Furthermore, an ECG spectrum was computed for each channel following the same multi-taper method as above.

## 5.2.7 Low-density HMM translation

Finally, an exploratory study of how the 32-electrode HMM states would translate to potentially clinically more useful two-electrode montages was undertaken. A *single-channel* EEG dataset was created using every possible combination of electrode pairs, giving  $32 \times 31 / 2 = 496$  total possible unique combinations. An HMM was estimated on each of these possible single-channel EEG with hyper-parameters identical to the original 32-electrode EEG HMM run.

Then, correspondence between the HMM fitted to each single-channel EEG dataset (i.e. the low-density model) and the HMM fitted to the original 32-channel EEG (i.e. the high-density model) was assessed as follows. First, the Spearman correlation between switching rates obtained from the low-density and full models was computed.

Then, the repeated measures ANOVA F-value for the switching rate across segments was computed for each model. Finally, the Spearman correlation between fractional occupancy in the low-density and full model was computed for each state, with states matched between models to maximise this correlation. The results were visualised by plotting top 5% of electrode combinations using *topoplot\_connect* in MATLAB. To further probe what was driving the strength of switching rate correlation between the full and low-density models, scatterplots and associated Spearman correlations were computed for distances between electrodes in a given montage (fronto-parietal, left-right distance, and distance from midline) and associated correlations with the full model.

## 5.3 Results

### 5.3.1 32-channel EEG-HMM

#### **Spatiotemporal brain states during a propofol infusion**

Using EEG data from an ultra-slow propofol infusion estimated effect-site concentration of 4 $\mu$ g/ml in 15 healthy volunteers, we estimated six whole-brain states using a data-driven Time-Delay-Embedded Hidden Markov Model (TDE-HMM) approach (Figure 5.1).

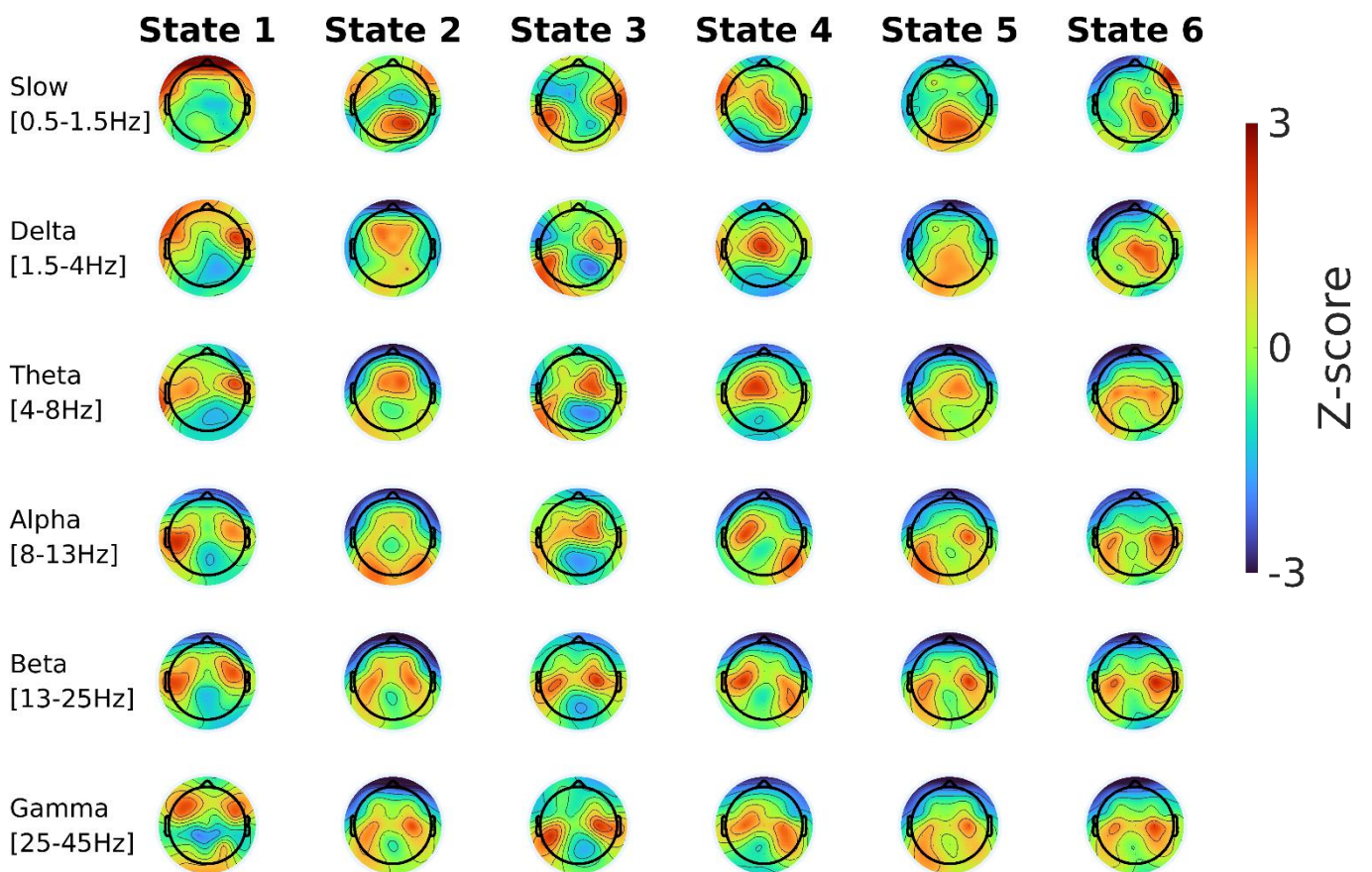


**Figure 5.1:** Z-scored scalp topographical maps of power of Hidden Markov Model states across frequency bands, relative to the power across the whole experiment.

This technique describes brain activity as switching between discrete brain states. Each state has its own spectral and spatial activity distribution, and each subject has its own state time course. For better interpretability, we re-numbered the states in order of decreasing broadband (0.5-45Hz) power. The experiment was split into eight stages and the switching rate between states as well as fractional occupancy of each state in each stage was computed. In repeated measures ANOVAs, there was a significant effect of State ( $P=0.0166$ ) and State \* Stage interaction ( $P=0.0083$ ) on the fractional occupancy (Figure 5.2) and of Stage on the switching rate ( $P<0.001$ , Figure 5.3).

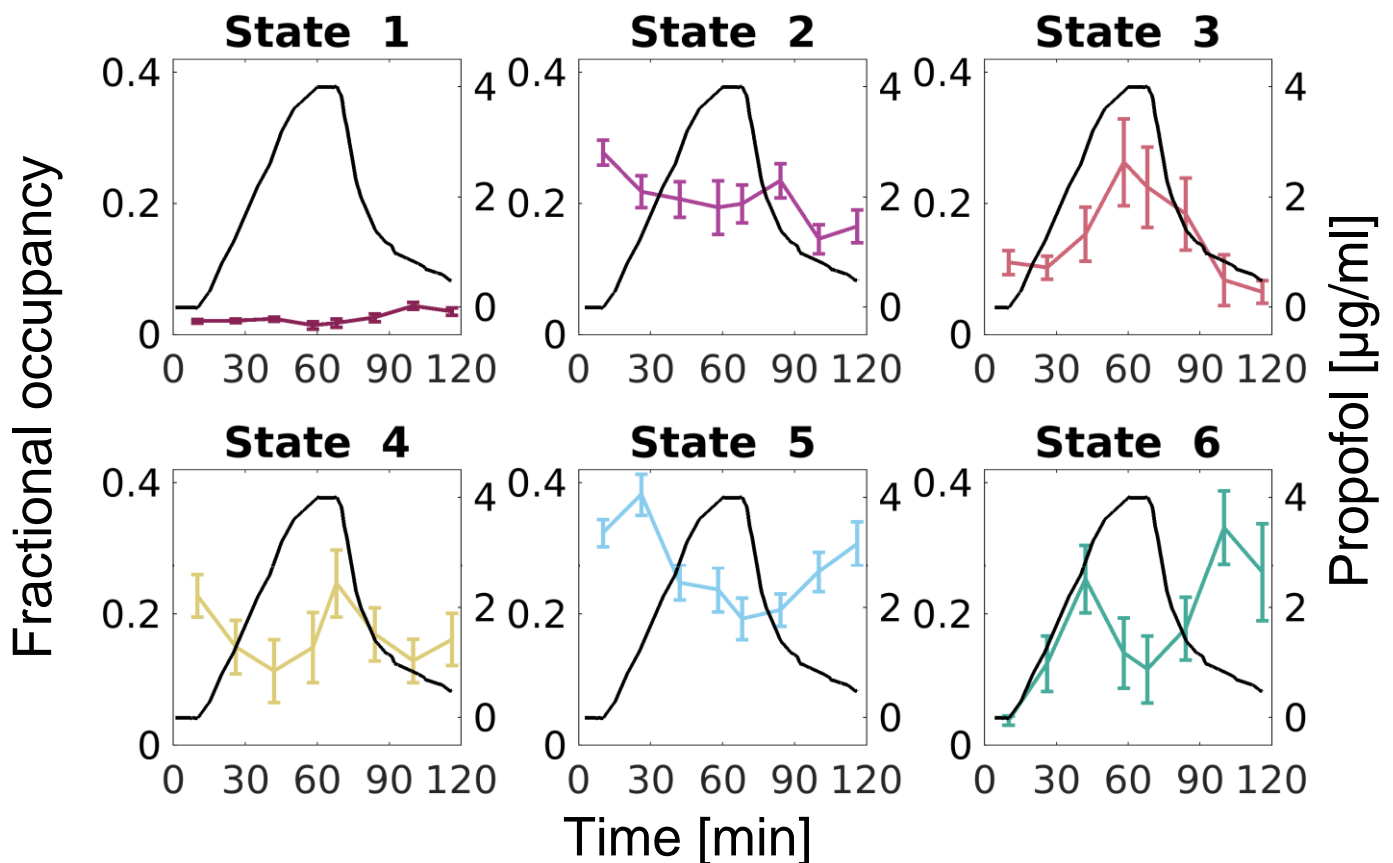


**Figure 5.2:** State fractional occupancies across time in the experiment (coloured, mean across participants  $\pm$  standard error) and estimated propofol effect-site concentrations (black) for each of  $K=6$  Hidden Markov Model states.

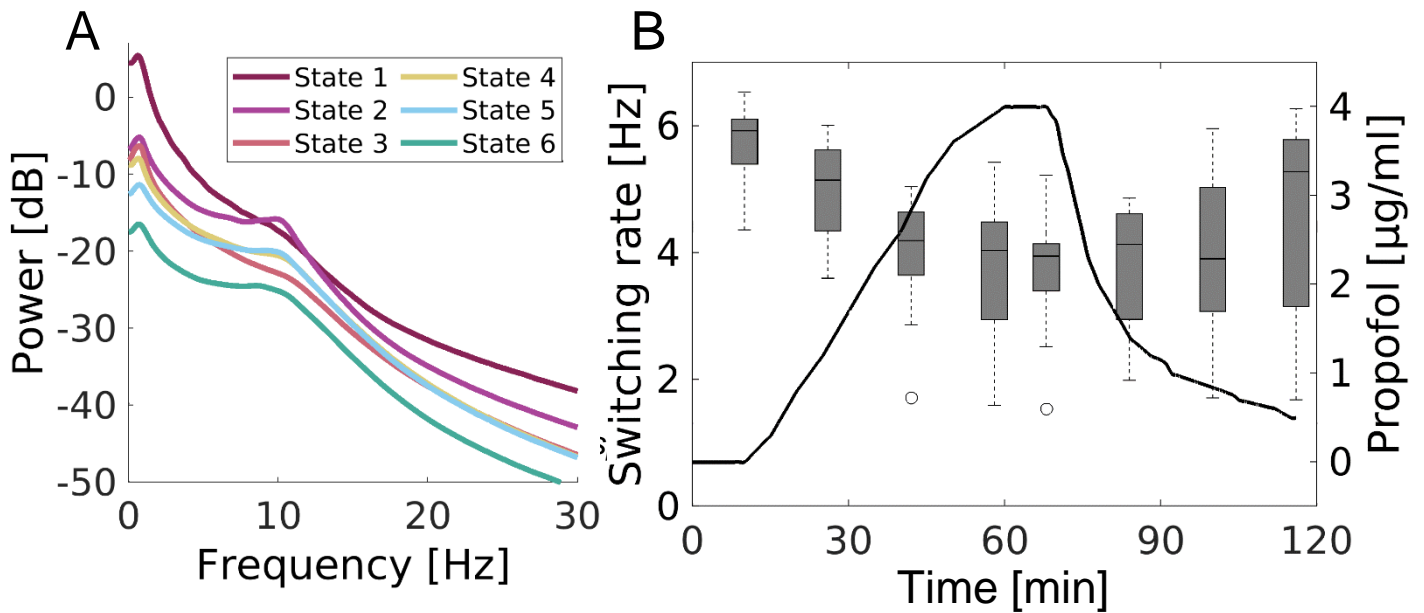


**Figure 5.3:** (A) Average power spectrum across all channels for each Hidden Markov Model state. (B) Switching rate between states across the experiment (boxplot across participants) and estimated propofol concentration (black line). Switching rate was significantly across the experiment (repeated measures ANOVA  $F=10.1$ ,  $P<0.001$ ).

State 1 was a high-power state (Figure 5.3A) that only appeared sporadically, most often during emergence (Figure 5.2). As it showed high frontal low-frequency and gamma activity (Figure 5.1), it is likely this state was driven by residual muscle, movement, and ocular noise. State 2 showed high occipital alpha activity as well as high frontal theta/delta and was most present during the baseline. State 3 had fractional occupancy that increased in line with propofol concentration (across-subjects Spearman  $\rho=0.22$ ,  $P=0.0346$ , FDR-corrected) and had predominantly frontal alpha activity. State 4 was present throughout the infusion and had lateralized alpha/beta activity, as well as fronto-central theta/delta activity. State 5 fractional occupancy was negatively correlated with propofol concentration (across-subjects Spearman  $\rho=-0.46$ ,  $P<0.001$ , FDR-corrected) and had posterior slow/delta activity.

State 6 had the lowest overall power, occurred most around loss and recovery of responsiveness, and showed alpha/beta activity around motor areas. Broadband coherence for states is in Supplementary Figure 5.2.

In summary, we found a likely artifactual state (State 1), a state associated with wakefulness (State 5), a state associated with propofol concentration (State 3), a state most present around loss and recovery of responsiveness (State 6), and two states broadly present throughout the infusion (States 2 and 4).

### **Associations with behavioural responsiveness and SWAS**

Next, we examined whether cumulative time spent in a particular state before loss of responsiveness correlated with propofol concentration at loss / recovery of responsiveness (LOBR/ROBR) or the SWAS metrics (power at SWAS,  $P_{\text{SWAS}}$  and propofol concentration at SWAS,  $C_{\text{SWAS}}$ , for both induction and emergence, Figure 5.4).

After a False Discovery Rate correction across these 36 tests (6 states x 6 metrics), there was a significant correlation between cumulative time spent in State 2 until LOBR and propofol concentration at LOBR and ROBR (Spearman  $\rho=0.725$  and  $0.739$  respectively,  $P=0.0226$ ), as well as  $C_{\text{SWAS}}$  on emergence ( $\rho=0.706$ ,  $P=0.0389$ ). There was also a significant correlation between cumulative time spent in State 5 until LOBR and propofol concentration at LOBR and ROBR (Spearman  $\rho=0.800$  and  $0.732$  respectively,  $P=0.0197$  and  $P=0.0226$ ). Finally, there was a significant correlation between cumulative time in State 6 and  $P_{\text{SWAS}}$  at emergence (Spearman  $\rho=0.757$ ,  $P=0.0226$ ). It was also noted there was a significant correlation between propofol

concentration at LOBR and ROBR ( $\rho=0.639$ ,  $P=0.0123$ ), though not between propofol concentration at LOBR and  $C_{SWAS}$  at emergence ( $\rho=0.437$ ,  $P=0.120$ ).

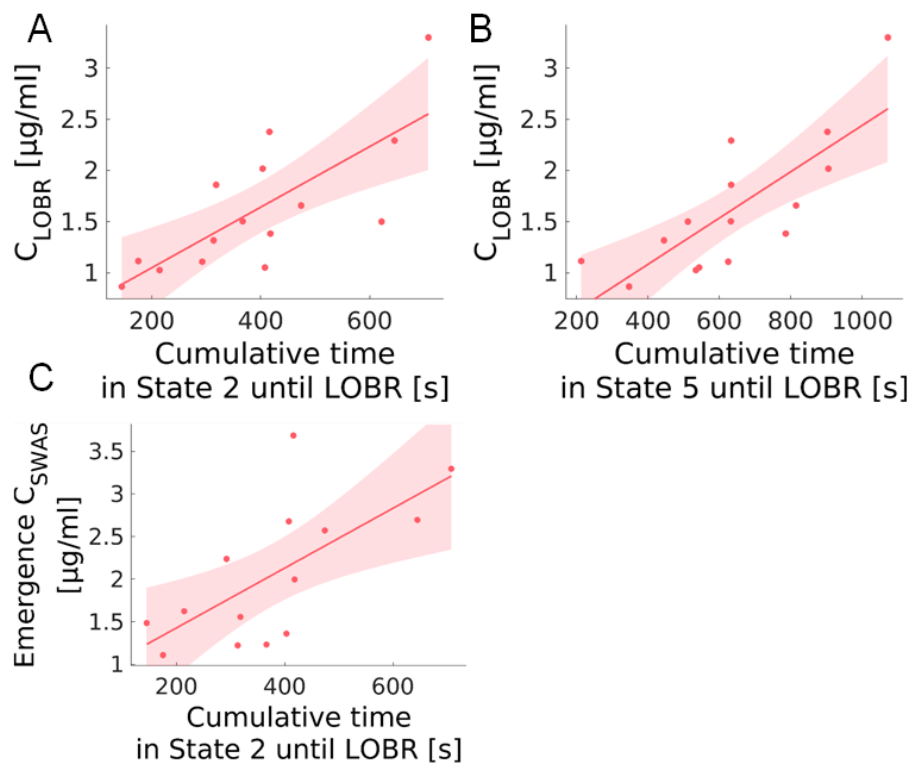


**Figure 5.4:** (A), (B) Scatter plots of propofol concentration at LOBR against cumulative time spent in State 2 and State 5 until LOBR across subjects. (C)  $C_{SWAS}$  during emergence against cumulative time spent in State 2 until LOBR.

### Network state transitions

Next, we focused on transitions between HMM States (Figure 5.5). Using Louvain community detection<sup>330</sup>, we found the states split into two sub-modules with high-power States 1-3 and lower-power states 4-6. During peak propofol concentrations, State 1 transitioned significantly less into State 6 and significantly more into State 2 compared to baseline (Figure 5.5B). Looking at the network as a graph, a cycle was present with States 2, 3, 4, and 5, with States 1 and 6 on the periphery (Figure 5.5C).



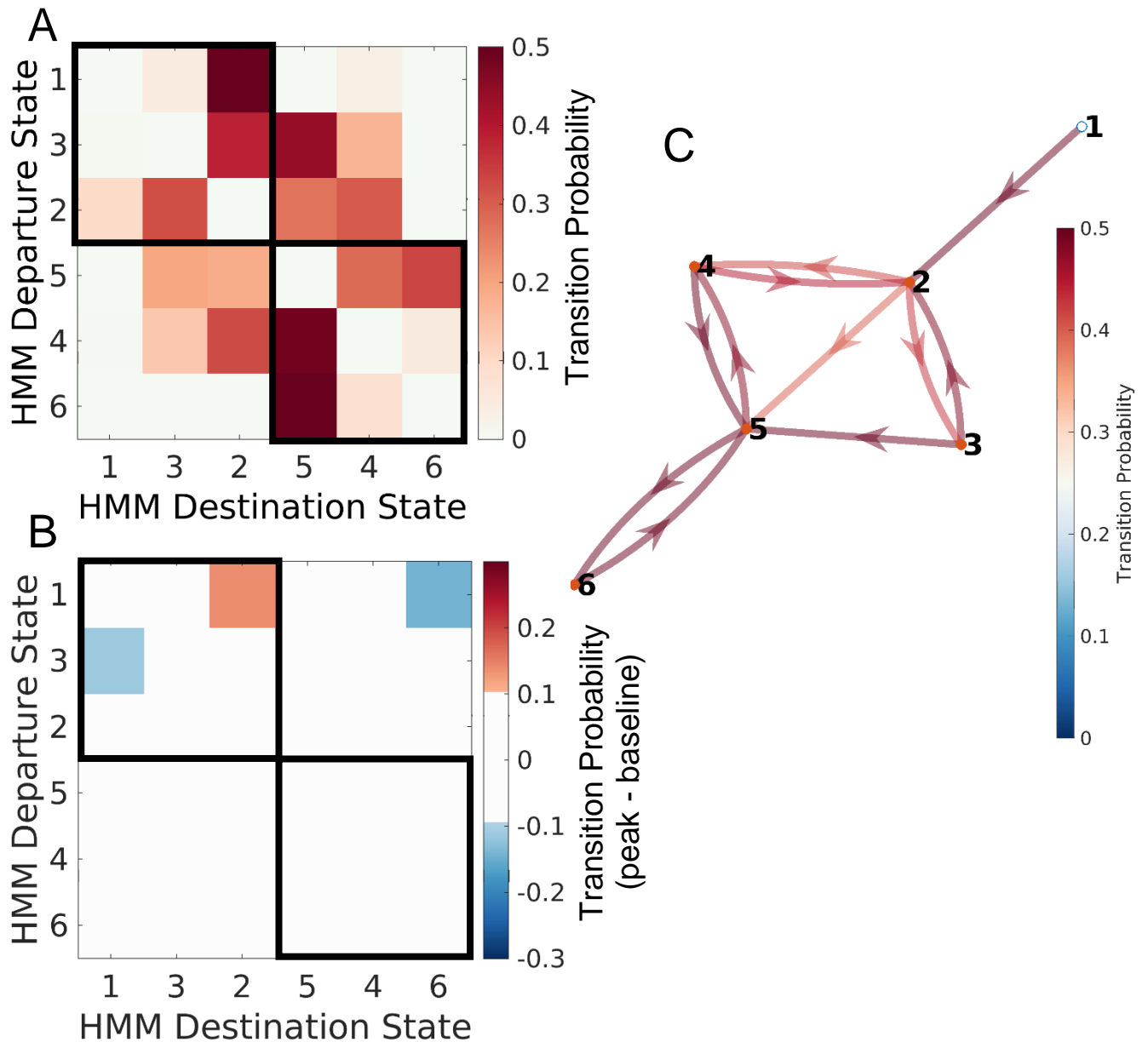


**Figure 5.5:** **(A)** Transition probability matrix for the experiment (mean across experimental stages). Data-driven community detection identified two modules. **(B)** Significant transition probability changes, peak propofol concentration - baseline (Bonferroni-corrected permutation test  $P < 0.05$ ). **(C)** A graph representation of the thresholded state transition matrix in (A). Darker colours represent more probable transitions. A cycle between States 2-5 is visible, with States 1 and 6 on the periphery.

### 5.3.2 EXG-HMM

As was shown in Chapter 3, the electrocardiogram (ECG) also contains information that tracks the propofol infusion. As such, I was interested in how a combined EEG-ECG HMM (EXG-HMM) would compare to an HMM run on the EEG alone.

Broadly, the model was similar, with notable exceptions (Figures 5.6-5.8). The switching rate was still significantly different between experimental stages (RM-ANOVA  $F=5.69$ ,  $P=0.0042$ ). The heart rate differed significantly between states (RM-ANOVA  $F=3.61$ ,  $P=0.0046$ ).

State 1 was still scarce and likely artifactual based on the topographical map. State 6 was still most present around LOBR/ROBR and showed motor alpha/beta activity.

State 3 and State 5 were associated with wakefulness and diminished with increasing propofol, though with correlation strengths weaker compared to the EEG-HMM run (Spearman  $\rho=-0.357$ ,  $P<0.001$ ,  $\rho=-0.267$ ,  $P=0.0049$  respectively, FDR-corrected). They both showed occipital alpha activity, with State 3 having more frontocentral and State 5 more posterior delta activity. Heart rate was also lowest in these states. What distinguished them was a strikingly different ECG spectrum (Figure 5.8C). State 5 had a broader, higher-activity ECG power spectrum, typically more associated with QRS complexes. State 3 had a low-power ECG power spectrum, more associated with inter-beat intervals.

State 2 and State 4 were more present at higher propofol concentrations (State 2 Spearman  $\rho=0.356$ ,  $P<0.001$ ; State 4  $\rho=0.149$ , n.s.). State 2 had higher power, particularly in slow, delta, and alpha frequencies, with delta/theta power more frontal. Heart rate was higher in these states than State 3 or 5. State 2 had higher, QRS-like ECG power (though lower than State 5), with State 4 having lower ECG power.

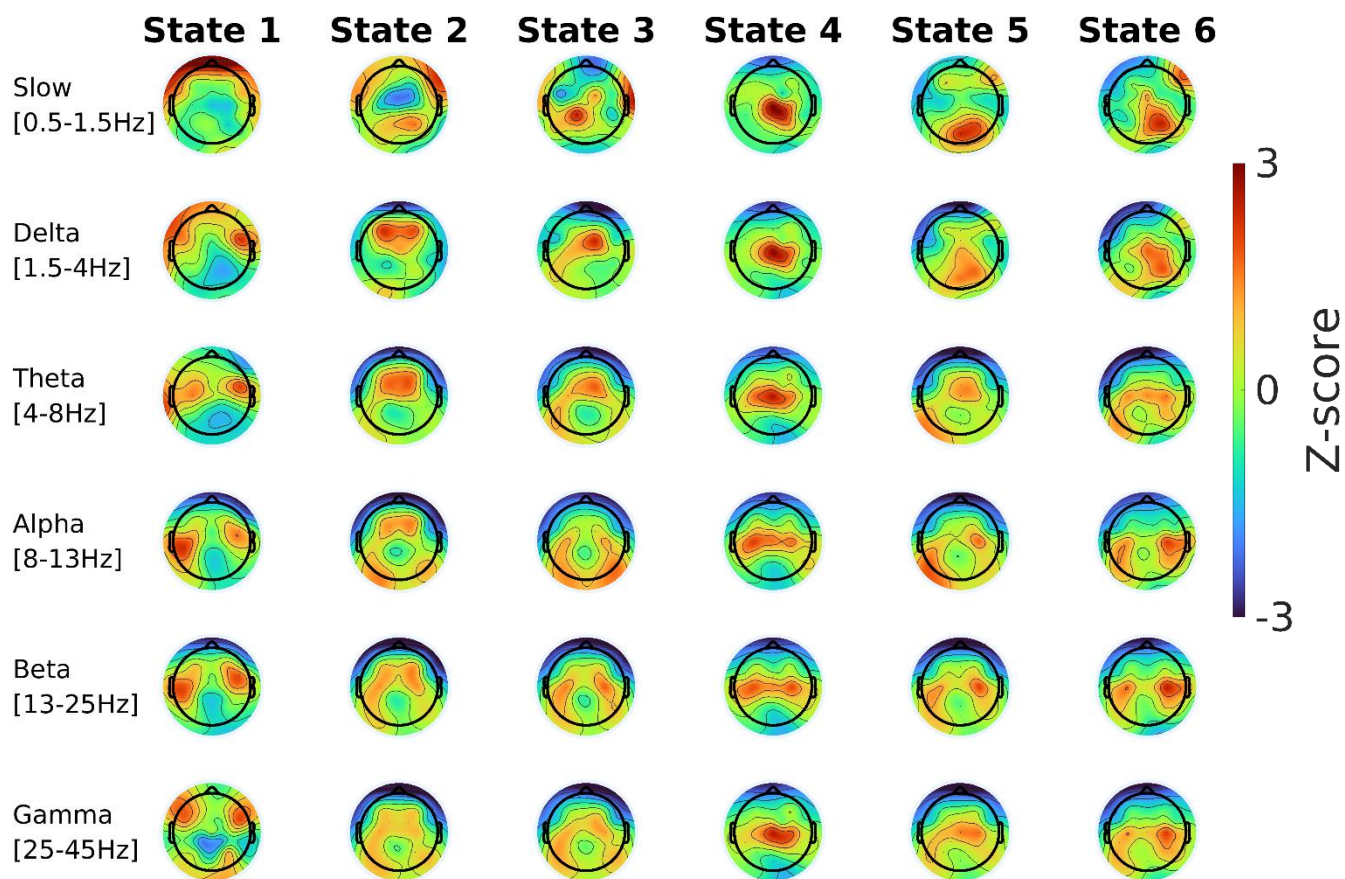


**Figure 5.6:** Z-scored scalp topographical maps of power of Hidden Markov Model states across frequency bands for an HMM that included the ECG signal. Most topographies look similar to those of Figure 5.1, with State 3 and 4 topographies changing the most.

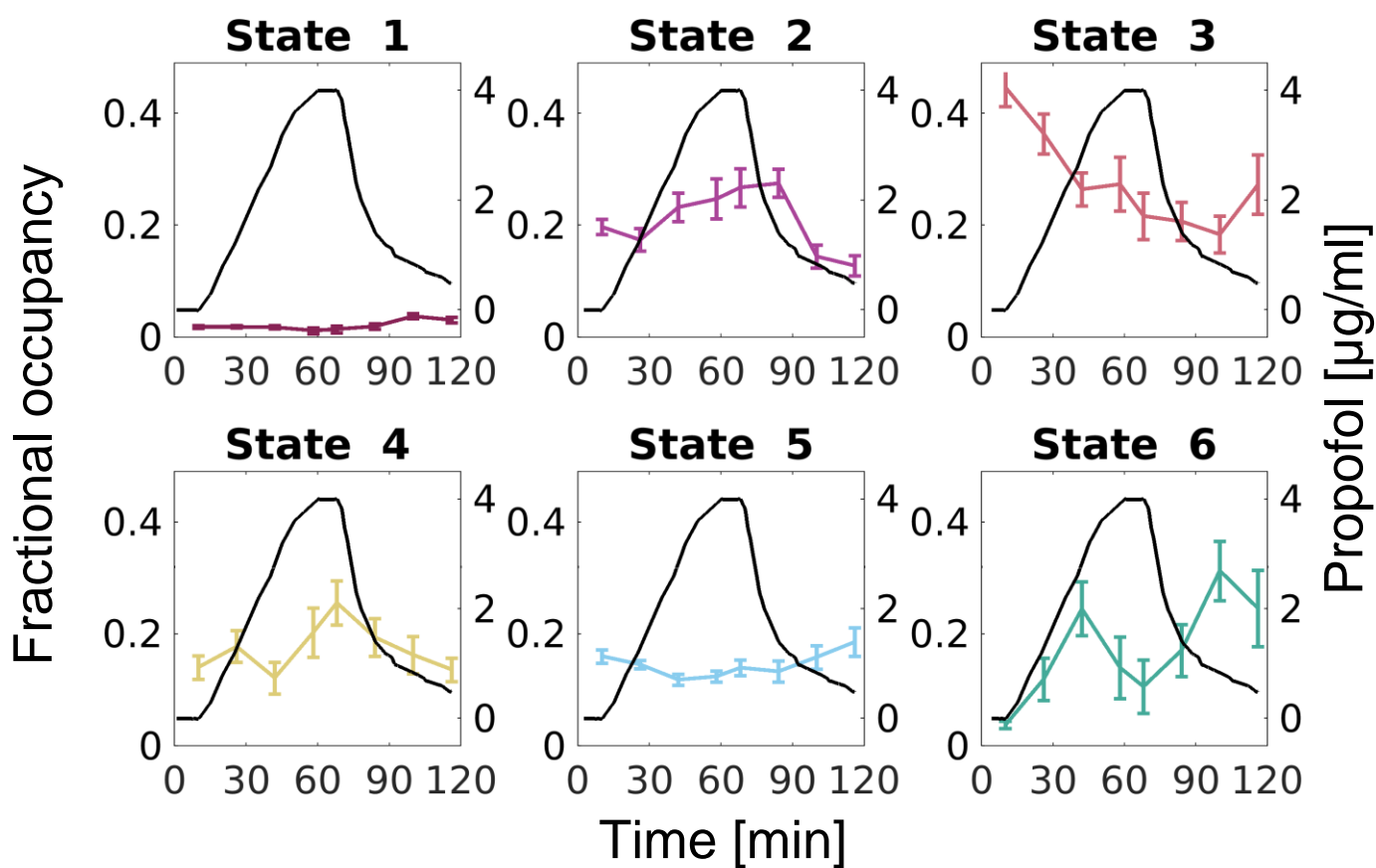


**Figure 5.7:** State fractional occupancies across time in the experiment (coloured, mean  $\pm$  standard error) and estimated propofol effect-site concentrations (black) for each of K=6 Hidden Markov Model states in the EXG-HMM run.

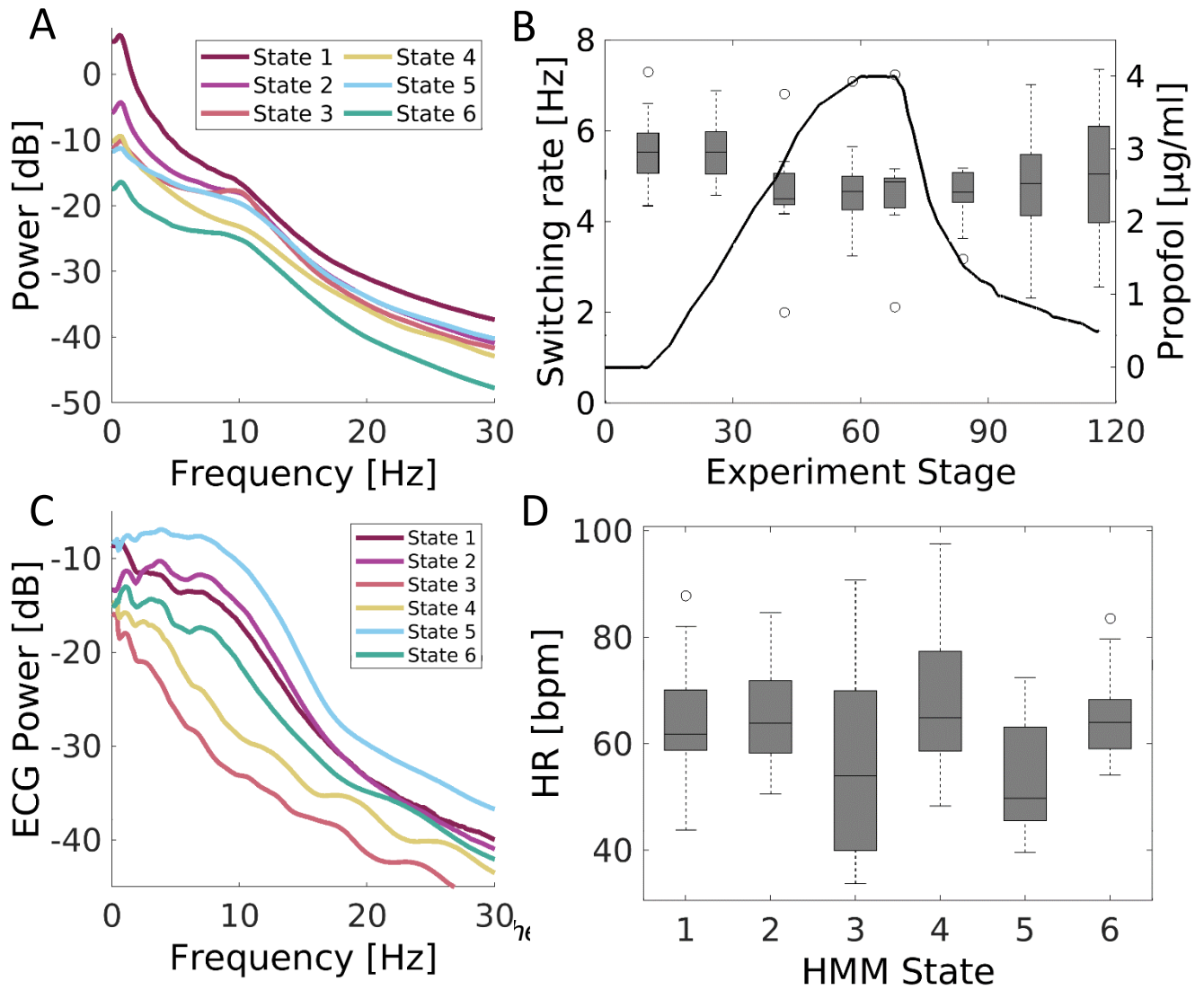


**Figure 5.8:** (A) Average EEG power spectrum for each state. (B) Switching rate between states across the experiment (boxplot) and estimated propofol concentration (black). Switching rate was significantly different between experimental stages (repeated measures ANOVA  $F=5.69$ ,  $P=0.0042$ ). (C) ECG power spectrum for each State. (D) Estimated heart rate for each state. Heart rate was significantly different between states (repeated measures ANOVA  $F=3.61$ ,  $P=0.0046$ ).

### 5.3.3 Low-density HMM translation

Finally, I wanted to know how the full 32-electrode EEG HMM model would scale to a more clinically translatable bipolar montage. Thus, N=496 HMM models were trained for each possible bipolar montage (i.e. every possible combination of electrode pairs). HMMs estimated on these low-density montages were compared to an HMM estimated on the full, 32-electrode montage, using the switching rate and fractional occupancy results.

Overall, there was a high correlation between switching rates in the full 32-electrode EEG HMM and the reduced low-density EEG HMMs (Figure 5.9). However, there were differences between montages and structure emerged (Figure 5.10). When we optimised for switching rate ANOVA F-test significance, the best low-density montages were posterior (Figure 5.10A). Optimising instead for maximal correlation with the full model, the best low-density montages appeared to have large left-right separation and were closer to the midline (Figure 5.10B). This was confirmed by studying the switching rate correlation as a function of left-right, front-back, and midline distances (Figure 5.10C-E, all Spearman  $P < 0.001$ ). The highest correlation montages were at the same front-back level, had larger left-right separation, and were close to the midline.

Finally, optimising for highest correlation between fractional occupancy of a given state in the full and reduced models, more structure emerged (Figure 5.10F). Notably, the optimal State 5 montage was fronto-parietal near the midline.

A brief exploratory analysis of including the ECG channel (i.e. 1 EEG + 1 ECG channel) was also undertaken (Supplementary Figure 5.7). Broadly, the models appeared more driven by the heart rate increase rather than neural dynamics.

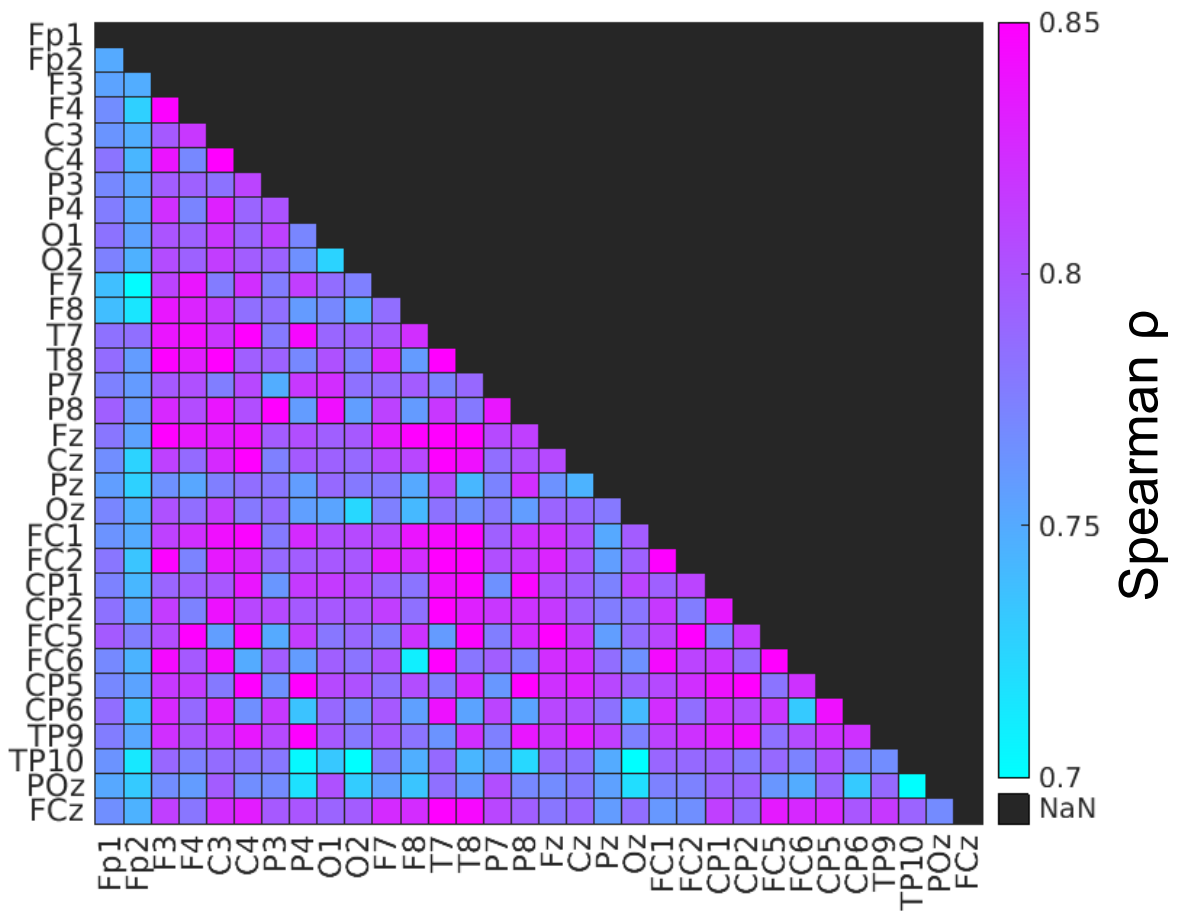


**Figure 5.9:** Spearman correlation between state switching rate from an HMM fit to the full 32-electrode model and switching rate from an HMM fit to low-density EEG montages (corresponding to every possible combination of electrode pairs from the full 32-electrode data). Whilst a good correlation ( $>0.7$ ) between high- and low-density EEG HMM models is observed overall, certain montages perform significantly better.

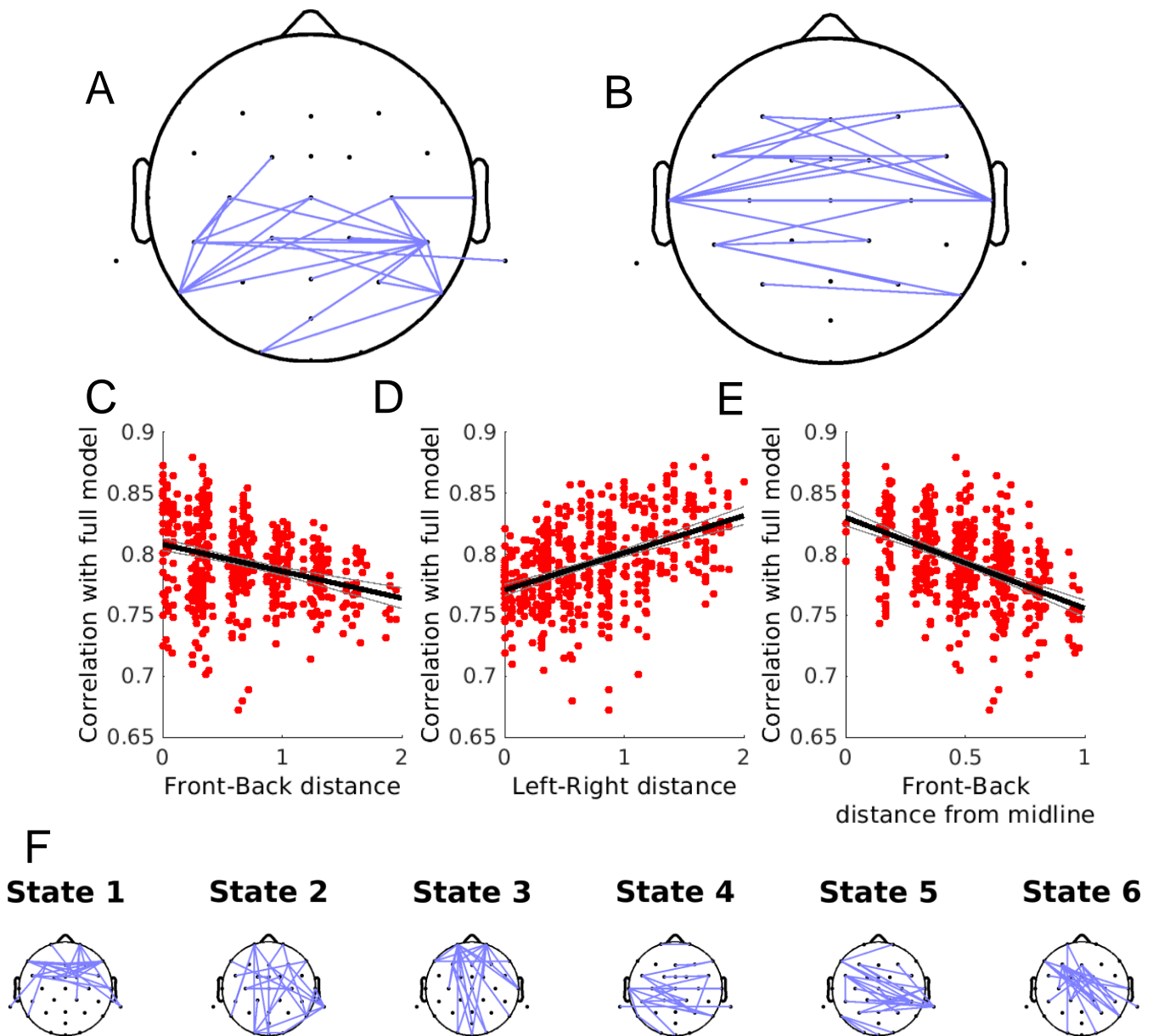


**Figure 5.10:** Best low-density montages for optimising various criteria. **(A), (B)** Top 5% of low-density montages to maximise switching rate (A) F-statistic significance and (B) correlation with full model. **(C), (D), (E)** Switching rate correlation between the full and reduced models against normalised distance between electrodes for all possible electrode pairs (C) front to back ( $\rho=-0.31$ ), (D) left to right ( $\rho=0.45$ ), and (E) from midline ( $\rho=-0.47$ , all Spearman  $P<0.001$ ). **(F)** Top 5% of bipolar montages to maximise correlation between state fractional occupancy in the full and reduced 2-electrode models.



## 5.4 Discussion

In this chapter, spatiotemporal brain dynamics during propofol anaesthesia was studied using Hidden Markov Modelling. First, using 32-electrode EEG data, K=6 HMM states were estimated and studied in relation to behaviour and slow-wave activity saturation. Then, a single-lead electrocardiogram was added to the dataset and HMM states re-fitted and analysed. Finally, the possibility of capturing the EEG HMM model with only two electrodes was explored and optimal electrode montages for different parameters were found.

### 5.4.1 Spatiotemporal brain states in propofol-mediated unconsciousness

Hidden Markov Modelling identified states associated with wakefulness, loss / recovery of behavioural responsiveness (LOBR/ROBR), and propofol anaesthesia in a data-driven way.

Decreased switching between states was a very robust finding in this chapter, present in the original model, the model with ECG signal added (although with a lower significance), and in all low-density montages. This can be interpreted as further evidence for a reduced functional repertoire under anaesthetic-induced unconsciousness, which has been demonstrated across a range of species, modalities, and unconscious states<sup>32,331–334</sup>. In a post-hoc analysis, the state switching time-series also showed reduced complexity (Supplementary Figure 5.6), supporting results from Chapter 1.

Time spent in States 2 and 5 until LOBR correlated with propofol concentration at these stages. This suggests States 2 and 5 were essentially tracking wakefulness,

with the ROBR correlation likely due to an overall correlation between concentrations at which responsiveness was lost and recovered. Interestingly, more time spent in State 2 (but not State 5) before loss of responsiveness correlated with higher  $C_{SWAS}$  on emergence, and thus potentially regaining perception at higher propofol concentrations (i.e. earlier). State 2 had higher overall power, so this could be a marker of more resilient brains that are less likely to become 'stuck' in the anaesthetic state and experience neural inertia<sup>94</sup>. However, unlike the rest of the results presented, this correlation was not robust across stochastic HMM initialisations (Supplementary Table 5.1) and should thus be taken as preliminary. Both States 2 and 5 were characterised by higher fronto-parietal connectivity and occipital alpha activity.

In contrast, State 3 had lower fronto-parietal connectivity and its fractional occupancy correlated with propofol concentration and showed anterior alpha activity. Alpha anteriorisation is a known correlate of propofol anaesthesia<sup>31,335</sup>, likely generated by thalamocortical loops<sup>336</sup>. Impaired fronto-parietal connectivity is a further established correlate of anaesthetic unconsciousness across a variety of drugs<sup>34</sup>.

In this chapter, Hidden Markov Modelling was used to capture spatiotemporal dynamics. This was done as it's a flexible, data-driven method that has previously been successfully used across a range of conscious states including sleep<sup>128</sup> and ketamine anaesthesia<sup>183</sup>. However, alternative methods exist. These include traditional EEG microstate analyses, which have been applied to propofol anaesthesia previously<sup>337-339</sup>, with one study suggesting a U-shaped dose-response in state occurrence<sup>340</sup>. Such a U-shaped state occurrence was not observed in this study. This could be due to deeper propofol concentrations in the previous study (achieved in part by using opioids at the deepest stage), or due to Hidden Markov Models capturing different dynamics to microstates, in part by leveraging full spectral information<sup>341</sup>.

### 5.4.2 Combined heart-brain states

In Chapter 3, an exploration of the cardiac effects of propofol and its effects on cortico-cardiac coupling (as measured by the ECG / EEG) was presented. This indicated there was useful dose-dependent information in the ECG, so here including it in the HMM was investigated. Despite radically different time-series and origins, the flexible nature of the HMM meant a combined EXG-HMM run produced sensible results. Most states were not affected by the single ECG channel, and overall the switching rate was still reduced, though with a smaller effect size. Including the ECG allowed for heart rates to be calculated, which further supported state interpretation with heart rate increasing as per Chapter 3. What's more, calculating the ECG spectra in each state revealed states associated with the cardiac QRS complex and those more likely to be present in-between R-peaks<sup>342</sup>. Thus, the fronto-central delta/theta in States 2 and 4 (low ECG power) could be interpreted to partially include heartbeat-evoked activity<sup>343,344</sup>. A formal comparison was not undertaken here, but the potential for Hidden Markov Models to extract both brain and heart states in a unified, data-driven framework warrants further exploration. However, State 3 and 5 associations with propofol dose were weaker in the EXG-HMM model, so there may be a trade-off between increased state interpretability and association with external variables depending on the cardiac response. Anaesthetists routinely monitor cardiac and other peripheral activity in detail, and this chapter advocates for advancing in research what is already clear to the clinician – that the physiological state does not end at the brainstem.

### 5.4.3 Low-density EEG

In the last few years, there has been a growing interest in finding optimal low-density EEG montages for specific purposes including source localisation<sup>326</sup>, epilepsy monitoring<sup>327</sup>, sleep stage classification<sup>328</sup>, and others. In this chapter, studying HMM in mocked-up low-density two-electrode EEG montages (obtained by spatially subsampling the full EEG montage) revealed structure in the electrode montage data during anaesthesia.

The switching rate decrease was most prominent in models trained on posterior electrodes. Reduced functional diversity in the unconscious brain has been previously localised to posterior cortical areas including the posterior cingulate and precuneus<sup>32,345</sup>. The results here suggest that the reduced state switching, at least as captured by the Hidden Markov Model, may be captured even with just two electrodes in this area. Interestingly, the switching rate change F-test significance on the best two-electrode montages was even higher than that of the full 32-electrode model. This is in line with recent work showing that low-density EEG montages can perform better than high-density montages if chosen optimally<sup>326–328</sup>.

Capturing individual states with a low-density montage also proved possible. For example, State 3, whose presence correlated with propofol concentration, was best captured in a fronto-parietal montage. Recent work has challenged the frontal montages commonly used during surgical anaesthesia monitoring<sup>112,117</sup>. State 3 also showed reduced frontoparietal connectivity previously suggested as a robust correlate of anaesthetic unconsciousness across a variety of drugs<sup>34,346</sup>. It remains to be seen in future research which anaesthetic effect on brain dynamics (e.g. reduced state switching, complexity, or fronto-parietal connectivity) causes consciousness to fade and presents clinically optimal conditions. Nonetheless, it is likely that once it is known,

a procedure similar to that in this chapter could reveal the optimal EEG montage to capture the effect.

#### 5.4.4 Limitations

Whilst this chapter contributes to our understanding of anaesthetic unconsciousness, combined heart-brain states, and low-density EEG montages, it comes with some limitations. Firstly, the original EEG montage was only of medium density (32 electrodes). This means it was not suitable for source localisation and it is possible higher-density montages would reveal finer details of relevant HMM states.

Secondly, only two-electrode low-density montages were explored here. This was done as commonly used surgical monitoring systems often only have a single bipolar channel and it allowed for a search of the full montage space. However, even though these montages yielded models with good correspondence compared to the full model, it is possible that low-density montages with more electrodes (say 8-12) could be a better trade-off. Combining this with other parameters (e.g. also varying number of HMM states) in a multi-optimisation problem, perhaps using a genetic algorithm<sup>326</sup>, is an ongoing research area in the group.

In summary, unconsciousness caused by propofol is associated with a shift to less complex brain dynamics with diminished state switching and fronto-parietal connectivity. Hidden Markov Modelling can reveal brain states as well as combined heart-brain states under anaesthesia, even with just two electrodes. Translating a better understanding of anaesthetic states into clinical settings remains to be achieved – but perhaps it starts with moving beyond forehead electrodes.



# 6 Neural correlates of ketamine dissociation in healthy volunteers

## 6.1 Introduction

### 6.1.1 Psychedelics as novel antidepressants

Depression is a leading cause of disability in the world and affects around 1 in 6 adults in the UK. Up to 30% of patients have a treatment-resistant form of depression, defined as failure to respond to two or more antidepressants<sup>347</sup>. Treatment-resistant depression (TRD) presents a major challenge for patients' lives as well as for the healthcare system. In recent years, novel, rapid-acting antidepressants have begun to be investigated<sup>348</sup>. These include classical serotonergic psychedelics (e.g. psilocybin<sup>349</sup>), as well as atypical psychedelics such as subanaesthetic ketamine and nitrous oxide<sup>350</sup>. Their use comes as part of a broader renaissance in psychedelic research in the last decade, with various substances being investigated as treatments for mental illnesses including 3,4-Methylenedioxymethamphetamine (MDMA) for post-traumatic stress disorder (PTSD)<sup>351</sup> and psychedelics for treatment of substance use disorders<sup>352</sup>. Theories of a common mechanism of action include increased neural plasticity (e.g. through activation of mechanistic target of rapamycin, mTOR) and anti-inflammatory immunomodulation, though placebo effects are large and blinding is difficult<sup>352,353</sup>. Intriguingly, classical anaesthetic agents including propofol<sup>354</sup> and isoflurane<sup>355</sup> have also demonstrated antidepressant properties at anaesthetic levels, perhaps due to GABAergic disinhibition or action on NMDA receptor modulation<sup>356</sup>,

and perioperative ketamine administration may prevent postoperative depressive symptoms<sup>357,358</sup>.

Low-dose ketamine is a particularly promising option for treatment-resistant depression. Since the publication of the first randomised, double-blind study of ketamine in depressed patients in 2000<sup>359</sup>, a large number of randomised control trials have established the rapid antidepressant effects of ketamine lasting up to two weeks<sup>360</sup>. S-ketamine nasal spray has been licenced by the Food and Drug Administration (FDA) for treatment of depression and racemic ketamine is used in a number of specialised clinics as an off-label depression treatment<sup>361</sup>.

However, concerns about the use of ketamine remain due to its abuse potential and urotoxic effects<sup>362</sup>. This is particularly important in the context of developing tolerance over time that can lead to high doses in patients, with some studies reporting anaesthetic-level doses to achieve sub-anaesthetic states in long-term patients (i.e. doses >2mg/kg)<sup>363</sup>. There is a lack of high-quality long-term safety data. Furthermore, development of drug liking behaviours in patients treated for depression has been reported and more research is needed, particularly given the potential for ketamine to affect  $\mu$ -opioid receptors<sup>364,365</sup>. All of the above warrants a cautious clinical approach with optimising the dose to minimise adverse effects whilst retaining the antidepressant response. A defining aspect of ketamine phenomenology is that of *dissociation*. A complete description of the brain dynamics underlying this state and its importance for clinical outcomes remains elusive and could benefit from methods commonly deployed in anaesthetic research (and in this thesis).



### 6.1.2 Ketamine dissociation

The psychomimetic effects of sub-anaesthetic ketamine were already recognised by Domino and colleagues when the first human was given intravenous ketamine on August 3, 1964<sup>366</sup>. It was soon noted that subjects described feelings of floating and being in outer space<sup>367</sup>. Upon hearing how people become ‘disconnected’ from their environment, Antoinette (Toni) Domino coined the term ‘dissociative anaesthetic’<sup>368</sup>.

It is important to note that the term ‘dissociation’ had a rich and complex history in psychiatry long before the introduction of ketamine, at least since Moreau de Tours’ 1845 description of personality division and isolation of ideas under hashish<sup>369</sup>. The idea of a ‘split mind’ underlies some theories of clinical dissociative disorders such as dissociative identity disorder (DID), conditions often linked to early trauma<sup>370</sup>.

In volunteers without a dissociative disorder, sub-anaesthetic ketamine induces key dissociative symptoms including amnesia, depersonalization, derealization, disembodiment, and temporal distortions<sup>371</sup>. However, ketamine phenomenology also replicates positive (e.g. concept disorganisation, hallucinations) and negative (e.g. blunted affect, motor retardation) symptoms of schizophrenia, with ketamine often utilized as a model of schizophrenia<sup>372</sup> and psychosis<sup>373</sup>. Furthermore, considered as an atypical psychedelic, ketamine can produce a therapeutically useful non-ordinary state of consciousness that may feature near-death experiences, ego dissolution, and feelings of unity depending on the dose, setting, and person’s mindset<sup>374</sup>. Capturing the full ketamine state of consciousness may be limited by psychometric scales being used<sup>375,376</sup>, as many of them were developed for other purposes, e.g. the Clinician-Rated Dissociative States Scale (CADSS) for dissociative symptoms in post-traumatic stress disorder (PTSD)<sup>377</sup>. In view of these complexities, this thesis adopts the term

'dissociation' to broadly describe the dissociative symptomatology produced by ketamine, i.e. the perceived separation of mind and body.

### 6.1.3 Chapter overview

This chapter focuses on correlates of sub-anaesthetic ketamine infusions, which have increasingly been administered by anaesthetists and psychiatrists in the context of treating depression<sup>359</sup>. Unlike traditional antidepressants that take weeks to produce effects, ketamine produces rapid antidepressant and anti-suicidal effects within hours of administration that last for 1-2 weeks<sup>365</sup>.

Recent work has done much to elucidate the brain correlates of sub-anaesthetic ketamine infusions. Neural oscillations robustly shift towards less alpha activity<sup>89,378–380</sup> and cortical complexity increases, mirroring effects of more classical psychedelics<sup>183,381,382</sup>. Changes in canonical resting-state networks have been observed, especially in the salience and default mode networks (DMN)<sup>41,383</sup>, and functional diversity of metastable states has been shown to increase<sup>183,382</sup>. However, it is less clear how these effects link to dissociative phenomenology. Several studies failed to find a significant link between changes in the electroencephalogram (EEG) data and dissociation scales<sup>380,384</sup>. However, others have found associations between dissociation psychometric scales and key nodes of the DMN and salience networks, including the anterior insula, a region involved in integrating interoception and self-awareness<sup>378,383,385,386</sup>. This may be in part due to different instruments used to capture dissociation (e.g. 5D-ASC vs CADSS).

Action of ketamine can be understood in relation to its molecular targets. On the molecular level, ketamine is known as an NMDA antagonist, but it also acts on the

cholinergic, aminergic, and opioid systems<sup>39</sup>. NMDA hypofunction has been proposed as the source of ketamine's schizophrenia-like phenomenology<sup>383</sup>, but action at distinct receptors may be responsible for different effects of ketamine, with e.g. the antidepressant effects reduced by blocking the opioid system<sup>387</sup>.

Novel analyses methods have been used to extract new insights from neural data. For instance, a decrease in alpha power may be due to fewer transient alpha bursts or a lower-amplitude continuous alpha oscillation, with these different features linked to different mechanisms<sup>240</sup>. In particular, Hidden Markov Modelling (HMM) has emerged as a way to describe brain dynamics in a dynamic, data-driven fashion with the brain seen as switching between discrete states<sup>126,127,317</sup>. Such states have been linked to altered states of consciousness including sleep<sup>128</sup> and scalp EEG ketamine data<sup>183</sup>.

In this chapter, I apply techniques from previous chapters to the case of the dissociated brain under the influence of sub-anaesthetic ketamine. I utilise a secondary analysis of high-density EEG data collected during sub-anaesthetic ketamine infusions in healthy volunteers together with subjective dissociation reports from the 5D-ASC questionnaire<sup>380</sup>. My goal was to use Hidden Markov Modelling on reconstructed cortical activity (source-projected) data to identify dynamic brain states during ketamine administration. It was hypothesised that state visits and transitions which included the default mode and salience network would be predictive of individuals' dissociation scores. Using a recent bank of 19 PET-derived receptor density maps<sup>388</sup>, a preliminary exploration of these states in relation to ketamine's molecular targets was undertaken, hypothesising a role for other receptors beyond NMDA. To explore how translatable the states may be, the states were studied in a simulated low-density montage. Finally, a case study of altered heartbeat-evoked potentials in a dissociated

participant is presented, suggesting a potential role for impaired interoception in dissociation.

## 6.2 Materials and Methods

A summary of the methods used for the main Hidden Markov Model analysis is presented in Figure 6.1.

### 6.2.1 Data collection

Details of the data collection have been published previously<sup>379,380</sup>. Briefly, the study was approved by the Institutional Review Board (HUM00061087) of the University of Michigan Medical School and written informed consent was obtained from all participants. Fifteen healthy volunteers (7 male/8 female, age 20–40 years, BMI <30 kg m<sup>-2</sup>, no history of drug use or psychiatric disorders) underwent a sub-anaesthetic intravenous infusion of racemic ketamine 0.5 mg kg<sup>-1</sup> administered over 40 min, followed by a subsequent 30 min pause for rest and psychometric testing using the Altered States of Consciousness (5D-ASC) questionnaire<sup>389</sup>, and then a hypnotic induction of bolus i.v. ketamine 1.5 mg kg<sup>-1</sup>. A 128-channel electroencephalogram (EEG; HydroCel nets, NetAmps 400 amplifiers, Net Station 4.5 software; Electrical Geodesics Inc, Eugene, OR, USA) was recorded continuously during the experiment, sampled at 500Hz and referenced to the vertex.

## 6.2.2 Signal pre-processing

For this study, only the 5 min closed-eyes awake baseline and 40 min subanaesthetic i.v. ketamine infusion were analysed. After trimming the datasets, each subject dataset was pre-processed in MATLAB 2020a (MathWorks Inc, Natick, MA, USA) using the EEGLAB<sup>390</sup> and OSL (<https://ohba-analysis.github.io/>) toolboxes together with custom MATLAB scripts. Briefly, i) the neck and face electrodes were removed leaving 102 channels, ii) default bad channel rejection was run using excess kurtosis>5, iii) bad time segments with excessive EMG noise were automatically rejected (35-128Hz power above 10dB, 35s (16s, 55s) rejected; median (quartiles)), iv) the data was bandpass-filtered (1-30Hz, eegfiltnew, default zero-phase, Hamming-windowed FIR filter), v) data were re-referenced to the scalp average and resampled to 100Hz. I then used temporal independent component analysis (pop\_runica, 35 components) to remove non-neural components (eye, muscle, cardiac, single-trial, or single-channel focus). This left a median of 10 independent components (range=7-20) per participant, consistent with previously established numbers of retained neural components<sup>380,391</sup>. Data was finally visually inspected to ensure quality control and interpolated back to 102 channels. This ensured high-quality data necessary for subsequent source reconstruction and dynamic brain state modelling. For further analysis, after Hidden Markov Modelling (see below) the experimental data was divided into 8 stages (each approximately 5 minutes, 320s±28s). Stage 1 was taken as the baseline and stage 8 as the pharmacological steady-state end-point of the experiment.

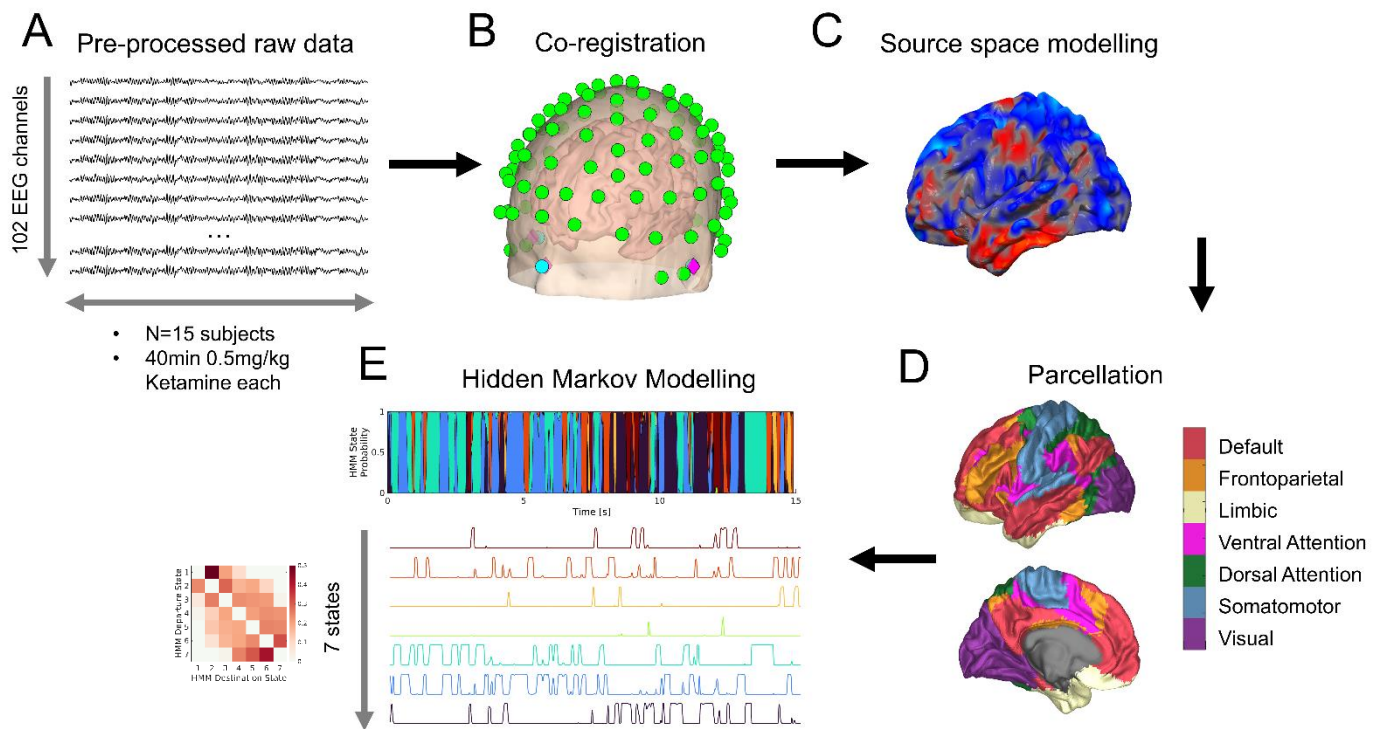


**Figure 6.1:** Overview of the study methodology. **(A)** EEG data from a sub-anaesthetic ketamine infusion in N=15 participants is pre-processed. **(B)** Electrodes (green) are co-registered to the MNI-152 template using fiducials (cyan) and a forward model is computed. **(C)** Data is projected into 8mm isotropic voxel source space using an LCMV beamformer. **(D)** Source space data is parcellated into the Yeo 7 networks, orthogonalized, and sign-flipped. **(E)** A 7-state Hidden Markov Model (HMM) is fit to the data to capture brain dynamics as switching between discrete, data-driven states. State occupancies (coloured time-series) and transitions (red matrix) are then related to dissociation scores.

### 6.2.3 Source reconstruction

As individual structural MRI images were not collected, data was aligned to the MNI-152 template using fiducial markers (nasion, left/right preauricular points - LPA, RPA; Figure 1B). A forward model was created using the boundary element method (OSL/SPM12 defaults). Source reconstruction was done using LCMV beamforming to 8mm isotropic brain voxels (Figure 1C; Westner et al., 2022). Source-space data was then parcellated to the 7 Yeo resting-state networks, thresholded at 25% probability<sup>393</sup> and orthogonalized (Figure 1D; Colclough et al., 2015) to minimise source leakage caused by volume conduction. A coarse, low-dimensional parcellation was chosen due to rank deficiency of the data and to account for potential anatomical differences between subjects in absence of MRI images. In this reduced parcellation, the ventral attention and salience networks largely overlap, including key nodes such as the anterior insula and cingulate, so these are referred to interchangeably. Finally, to address the source dipole ambiguity, sign flipping was performed ensuring maximal correspondence across participants<sup>127</sup>.

### 6.2.4 Hidden Markov Modelling

Similarly to Chapter 5, data-driven brain state dynamics were found using the time-delay-embedded Hidden Markov Model (TDE-HMM) implemented in the MATLAB HMM-MAR toolbox (Figure 6.1E)<sup>127,317</sup>. HMM has been successfully applied to detect transient brain states across a variety of paradigms including resting-state MEG<sup>395</sup> and fMRI<sup>316</sup>, as well as sensor-level EEG in this ketamine dataset<sup>183</sup>. The stochastic TDE-HMM approach is especially suited for large amounts of data<sup>127</sup>.

In this analysis,  $K=7$  states were chosen. This number of states showed the highest proportion of states well-replicated in a split-half matching test (Supplementary Figure 6.1) and was a natural choice given the 7-network parcellation, but  $K=3-12$  states were also explored (Supplementary Figures 6.2-6.4) with broadly similar results. Robustness of results across stochastic effects was verified by repeating the analysis  $N=4$  times (Appendix 5). Time-embedding was done using 11 lags (100ms window, chosen to capture the alpha rhythm present throughout the data). HMM states were then estimated on the top 21 principal components (80% variance captured, chosen using the elbow method) using stochastic inference<sup>127</sup> with batch size of  $N=2$  subjects.

### **State fractional occupancies and Power spectra estimation**

State fractional occupancy calculations were identical to those described in Chapter 5. Power spectra (1-30Hz) for each state were estimated using a state-wise multitaper approach<sup>126</sup>. State power maps were then computed by projecting total power in a state on the cortical surface derived from MNI-152 using the Human Connectome Project Workbench, relative to the mean weighted by across-experiment fractional occupancy<sup>329</sup>. States are randomly numbered when estimated by the HMM-MAR toolbox. As in Chapter 5, for visualisation and interpretation purposes, states were re-ordered by decreasing total power.

### **Transition probability matrices**

To compute the states' network graph and visualise which states transition to which other states, I used identical methods as those for transition probability matrices in Chapter 5.



## Dissociation associations

To link HMM brain state dynamics with subjective psychometric reports, the total score for the disembodiment 5D-ASC subscale was used as a measure of dissociation<sup>389</sup>. In the N=14 subjects where this score was known, a general linear model was built using individual participants' state fractional occupancies, starting with all states and using backward selection<sup>396</sup>. This was done separately for stage 8 (end of experiment) and stage 1 (baseline) to explore both acute dissociation markers and baseline predictors of dissociation susceptibility. Post-hoc Spearman correlations and P-values for relevant variables were also computed.

To find exploratory associations between state transitions and dissociation, a permutation test was used. Specifically, for both the end of experiment and baseline stages separately, Spearman correlation between individuals' transition probabilities between states and disembodiment scores was computed. Then, for each of N=500 permutations, the subject labels were randomly permuted and the correlations recalculated. From this null distribution, transitions with  $P < 0.01$  were taken as significant and post-hoc Spearman correlations computed for significantly associated transitions.

### 6.2.5 Receptor fingerprinting

Finally, to explore how the states related to molecular targets of ketamine, I used a recently published neuromaps databank of brain-wide receptor densities derived from PET<sup>388</sup>. Specifically, the spatial Pearson correlations of 19 receptor maps (serotonin (5HT): 5HT1a, 5HT1b, 5HT2a, 5HT4, 5HT6; dopamine (D): D1, D2, dopamine transporter (DAT); acetylcholine: alpha-4 beta-2 nicotinic receptor ( $\alpha 4\beta 2$ ), muscarinic M1, vesicular acetylcholine transporter (VACHT); norepinephrine transporter (NET);

histamine H3; GABA<sub>A</sub>; cannabinoid CB1; mu-opioid receptor (MOR); glutamate metabotropic receptor 5 (mGluR5), NMDA) with each of the 7 states was calculated. A significance P-value against a spatial null was then computed, taking autocorrelation into account<sup>397</sup>, and correcting for multiple comparisons across all receptors using the Bonferroni method, only keeping state-receptor associations with corrected  $P < 0.05$  and at least a moderate correlation of  $r > 0.3$ .

## 6.3 Results

### 6.3.1 Whole-brain ketamine-associated network states

Using eyes-closed EEG data from a 40-minute 0.5 mg kg<sup>-1</sup> ketamine infusion in 15 healthy volunteers mapped onto the Yeo-7 parcellation, seven whole-brain states were estimated using a data-driven Time-Delay-Embedded Hidden Markov Model (TDE-HMM) approach (Figure 6.1). Essentially, this technique describes brain activity as switching between discrete brain states. Each state has its own spectral and spatial activity distribution, and each subject has its own state time course. For better interpretability, the states were re-numbered in order of decreasing broadband (1-30Hz) power. The experiment was split into eight stages of equal length and the fractional occupancy of each state in each stage was computed. In a two-way repeated measures ANOVA, there was a significant effect of State ( $F=5.62$ ,  $P < 0.001$ ) and State \* Stage interaction ( $F=22.98$ ,  $P < 0.001$ ) on the fractional occupancy.

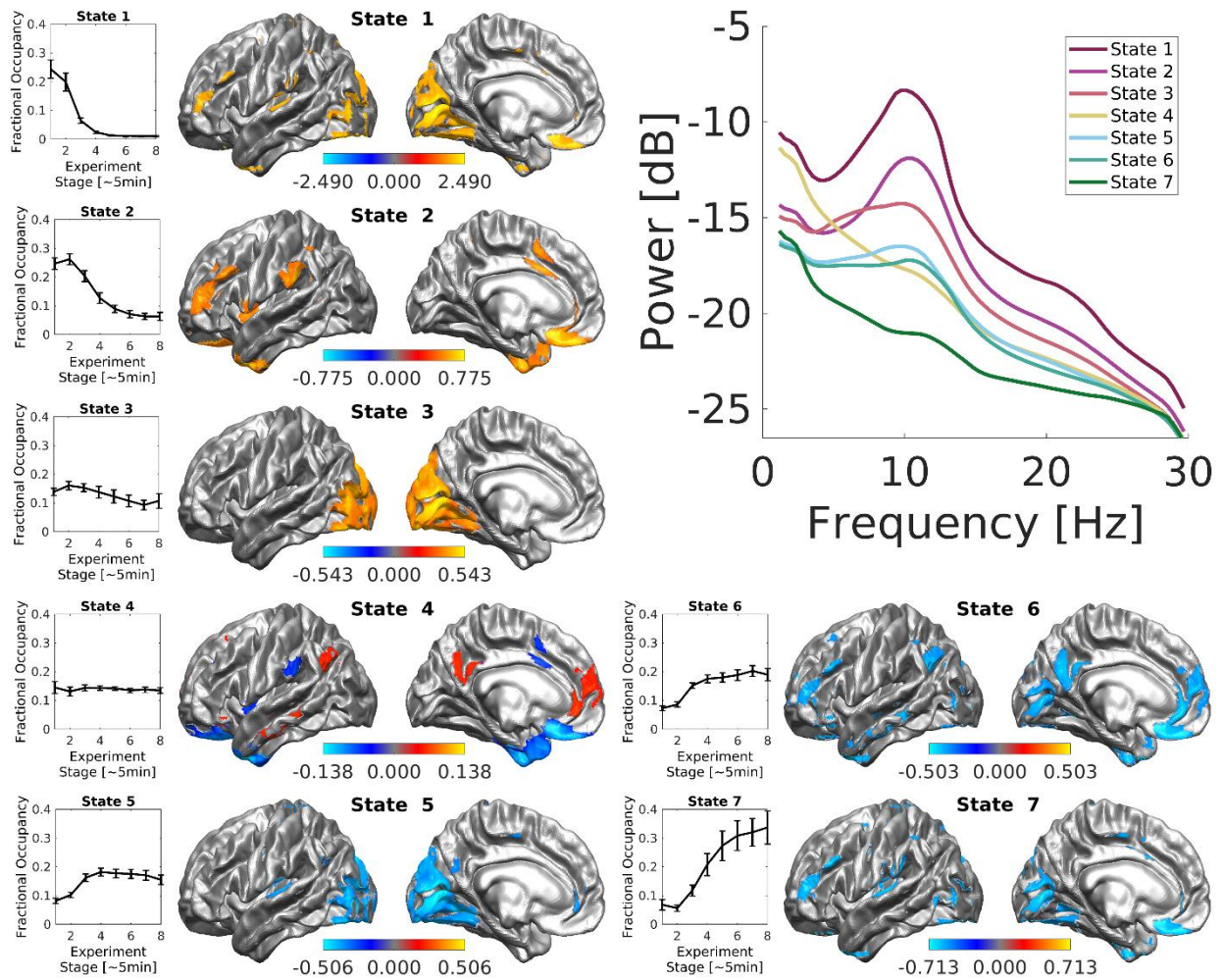


**Figure 6.2:** Data-driven brain states during a sub-anaesthetic ketamine infusion. **Left, Bottom Right:** Broadband (1-30Hz) thresholded power maps for each state (relative to temporal average), together with fractional occupancy (fractional time spent, mean  $\pm$  SEM across participants) for each state across the experiment. Ketamine causes less time spent in high alpha power states (States 1, 2) and promotes low-power states (State 7).

**Top Right:** Power spectrum for each state. States were re-ordered by total power for interpretability.

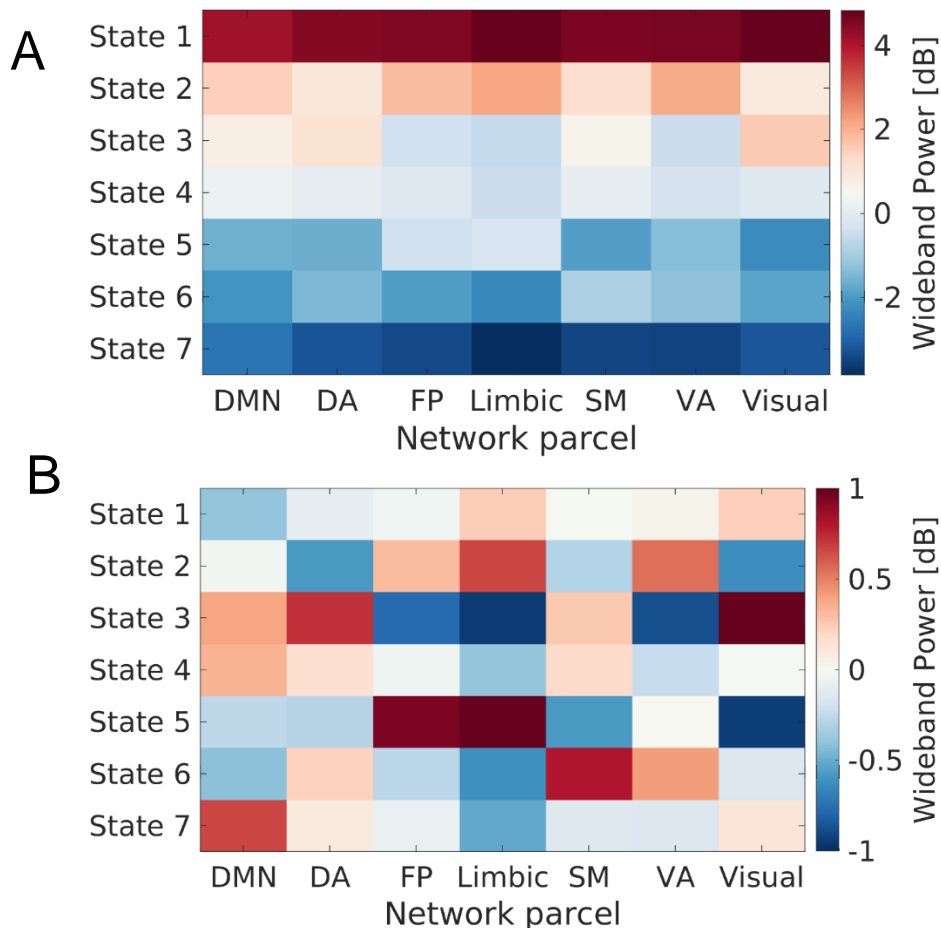


**Figure 6.3:** Alternative views of broadband activity in each state (c.f. Figure 6.2). **(A)** activity relative to mean across the experiment. **(B)** activity relative to mean across the brain in each state.

Regarding the states (Figure 6.2, 6.3), three high-power states were found characterised mainly by broadband activity in the visual network (State 1), salience (ventral attention) & limbic networks (State 2), and visual & dorsal attention networks (State 3). States 1 and 2 were dominant during the baseline with subjects spending  $24.4\% \pm 12\%$  and  $24.7\% \pm 8\%$  in them respectively (mean  $\pm$  standard deviation).

As ketamine was induced, time spent in States 1 and 2 reduced significantly (first vs last stage post-hoc t-test  $P < 0.001$ , FDR-corrected). State 4 had activity close to the experimental average, with activity highest in the default mode (DMN) combined with

suppression of limbic and ventral attention activity and was present throughout the experiment. State 5 showed suppressed visual activity and its fractional occupancy increased significantly ( $P=0.0014$ , FDR-corrected).

States 6 and 7 had overall lowest broadband activity, showing suppressed DMN / limbic and limbic activity respectively. They also significantly increased in their fractional occupancy ( $P<0.001$ , FDR-corrected), with State 7 being the state with lowest power overall. Subjects spent  $19\%\pm 8\%$  and  $33.7\%\pm 22\%$  of the time in State 6 and 7 respectively at the last stage of the experiment. No significant effect of stage on state switching frequency was observed ( $P>0.1$ ).

Functional connectivity of these states as measured by broadband coherence (demeaned across states) is presented in Figure 6.4. Strongest connections in states suppressed by ketamine were limbic-visual networks, salience–somatomotor networks, and default mode–frontoparietal networks (State 1), frontoparietal–somatomotor and frontoparietal–visual (State 2). State 7 most present at the end of infusion had lower than average connectivity between the default mode network and salience / somatomotor networks, as well as frontoparietal–somatomotor networks. State 6 had decreased limbic and visual / salience networks connectivity, with increased dorsal attention–somatomotor coherence.

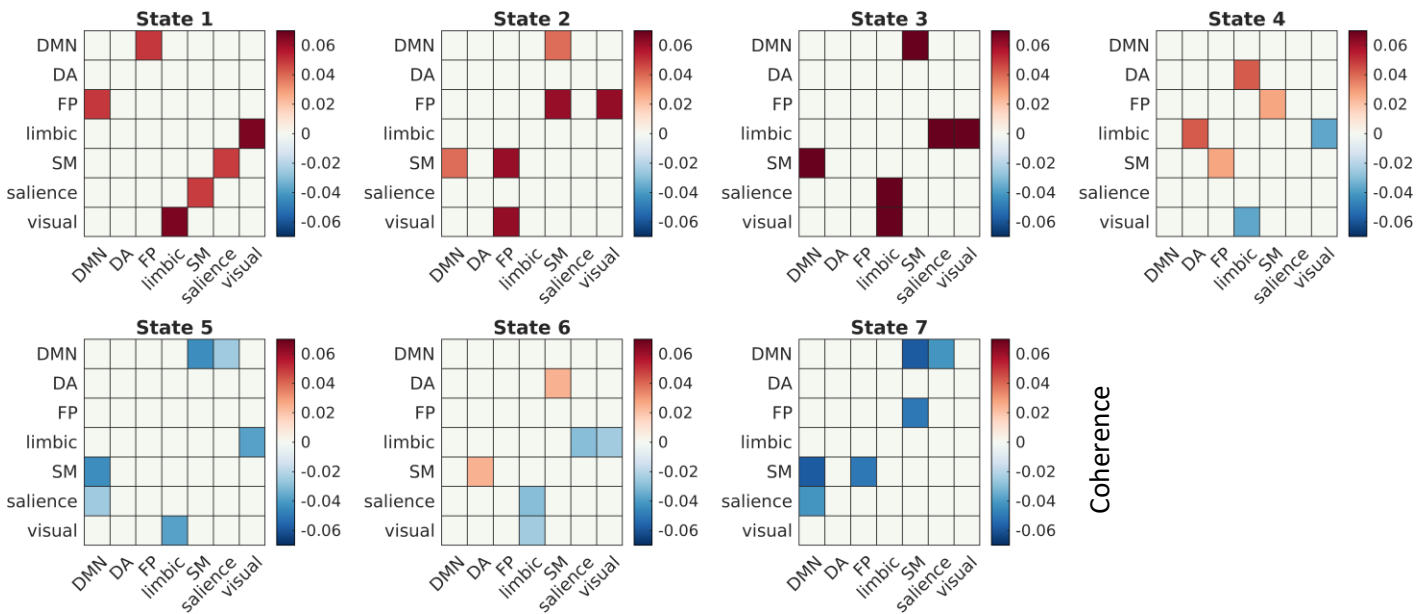


**Figure 6.4:** Connectivity (demeaned broadband coherence, top 10% of connections shown) in each of K=7 states presented in the main text.

### 6.3.2 Distinct baseline and ketamine state transitions

Next, I focused on the probability of transitions between the different HMM states (Figure 6.5). A transition probability matrix is calculated directly from the HMM state trajectory (Figure 6.5A). Using Louvain community detection, the states were found to be split into two sub-modules matching the differences between high-power States 1-3 and lower-power states 4-7. Module 1 was thus associated with baseline wakefulness and Module 2 with the psychedelic ketamine state.

Comparing transition matrices between the first (baseline) and last experimental stage, it was also found there were significantly fewer transitions into Module 1 at the end of the experiment and broadly more transitions into Module 2 (Bonferroni-corrected permutation test  $P < 0.05$ , Figure 6.5B). Visualising the state space as a graph (Figure

6.5C), ketamine shifted brain activity from mainly being an interplay between States 1, 2, and 3 to being dominated by cycling between states 4, 5, 6, and 7.

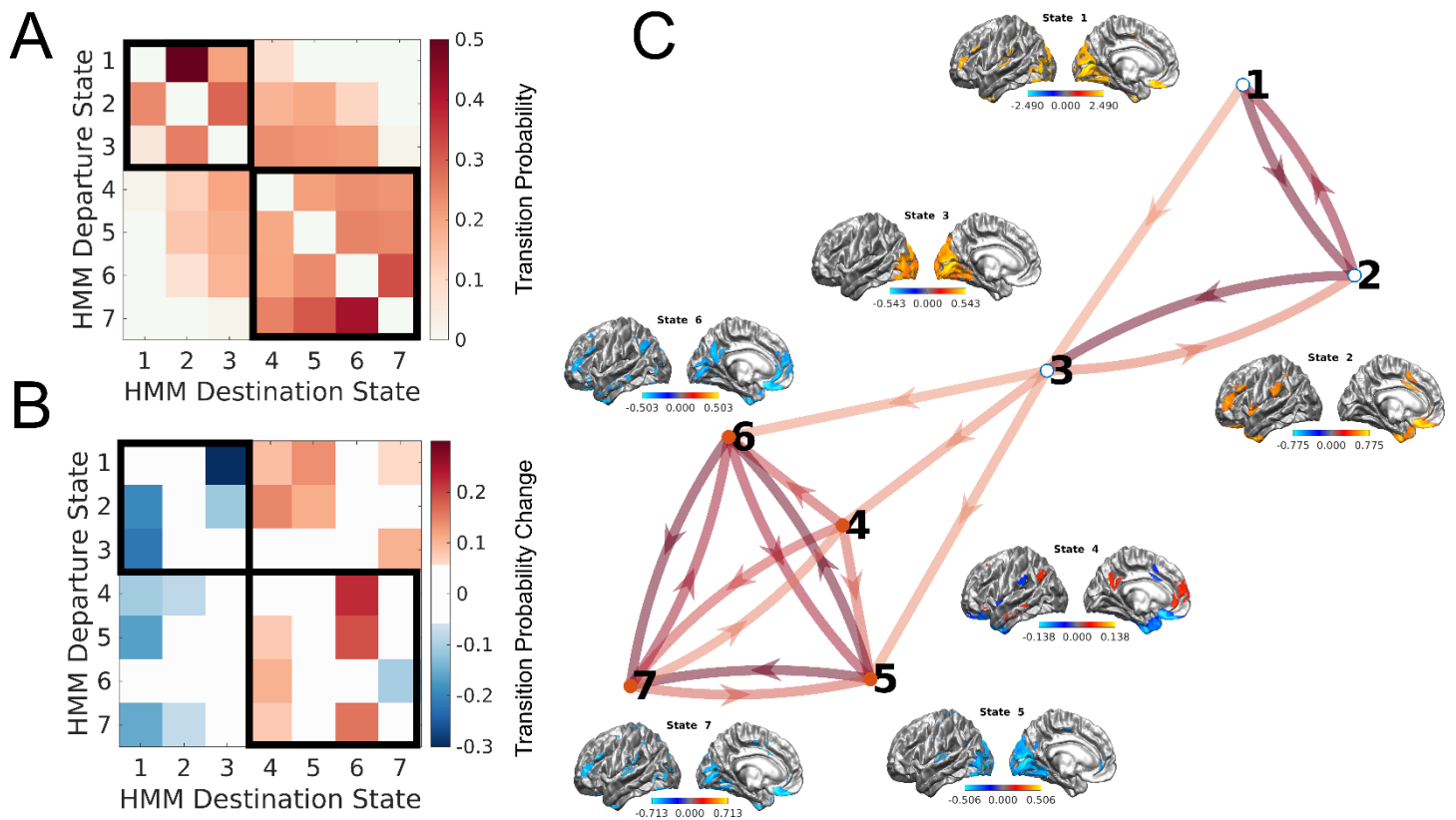


**Figure 6.5:** State transitions and modules. **(A)** Mean transition probability matrix across the entire experiment. Data-driven community detection identified two modules: high-power, baseline-associated Module 1 (States 1, 2, 3) and low-power, ketamine-associated Module 2 (States 4, 5, 6, 7). **(B)** Significant transition probability changes, end of infusion minus baseline (Bonferroni-corrected permutation test  $P < 0.05$ ). States transition significantly less into Module 1, and more into Module 2. **(C)** A graph representation of the thresholded state transition matrix in (A). Darker colours represent more probable transitions. Two modules are clearly visible, with State 3 acting as the dominant bridge between them.

### 6.3.3 Brain states associated with dissociative phenomenology

After estimating dynamic brain states present in the data, I assessed preliminary evidence of associations between state occupancies and transitions and the disembodiment sub-scale of the Altered States of Consciousness (5D-ASC) questionnaire, taken as the measure of dissociation. This psychometric data was available in N=14 subjects. Complete analysis of this questionnaire has been published before<sup>380</sup>.

#### **Baseline predictors of dissociation susceptibility**

All participants were given the same weight-adjusted dose (0.5 mg kg<sup>-1</sup>). Despite the dose equivalence, there was a wide range of dissociation scores in the cohort (mean 20.6, range 9-28 out of 30). Starting with all state occupancies in a general linear model and using backward selection, there was a suggestion that subjects that spent more time in State 5 experienced less dissociation at the end of the experiment (Figure 6.6A; Linear model  $F=7.11$ ,  $P=0.0205$ ; Spearman  $\rho=-0.48$ ,  $P=0.08$ ). Furthermore, a higher probability of transitions from State 3 to State 1 also appeared to be correlated with lower end-of-infusion dissociation scores (Figure 6.6B; permutation  $P<0.01$  and Spearman  $\rho=-0.79$ ,  $P<0.001$ ).

#### **Acute markers of dissociation**

Next, the same analyses were run on the last stage of the experiment. The general linear model identified was Dissociation [0-30] = 19 – 8.7\*FO[1] + 1.6\*FO[2], where FO[k] indicates fractional occupancy of State k (model  $F=7.31$ ,  $P=0.0096$ , each



parameter  $P < 0.005$ ; Figure 6.6C). As this suggested a joint role with State 1 being preventative of and State 2 promoting dissociation, I also post-hoc tested the correlation between dissociation scores and the ratio of times spent in State 1 and State 2 in the last experimental stage (Spearman  $\rho = -0.57$ ,  $P = 0.035$ ; Figure 6.6D). No significant correlations between end-of-infusion transition probabilities and dissociation were found ( $P > 0.1$ ).

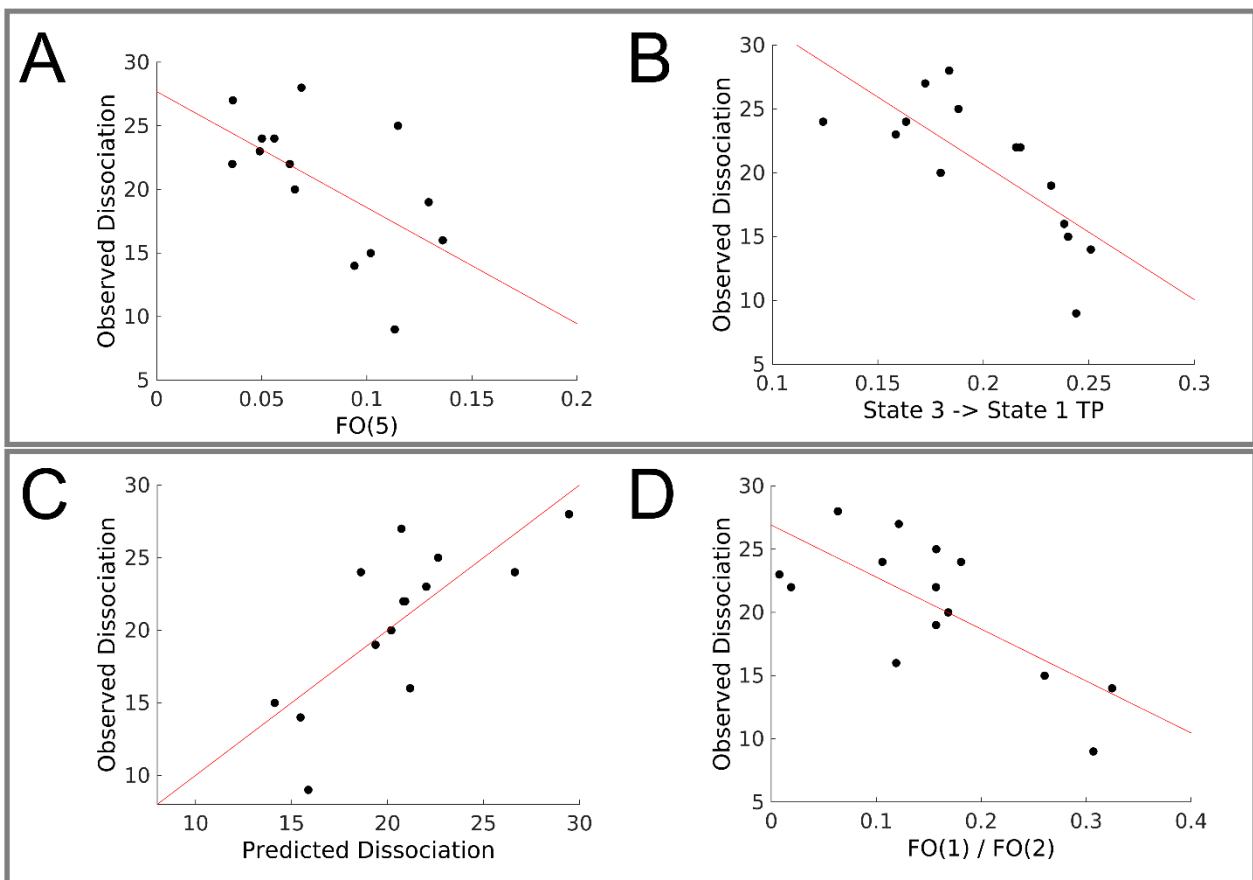


**Figure 6.6:** Brain states associated with disembodiment scores (max=30). Top plots show associations during the baseline period (predictors), bottom plots at the end of experiment (acute markers). **(A)** Observed dissociation scores for each participant against fractional occupancy (FO) of State 5 during the baseline period (Spearman  $\rho = -0.48$ ,  $P = 0.08$ ). **(B)** Same dissociation scores against baseline transition probability (TP) from State 3 to State 1 (Spearman  $\rho = -0.79$ ,  $P < 0.001$ ). **(C)** Predicted against

observed dissociation scores based on a general linear model using last-state fractional occupancy of State 1 and State 2 ( $F=7.31$ ,  $P=0.0096$ ). **(D)** Dissociation scores against the relative fractional occupancies of State 1 and State 2 at the last stage of the experiment (Spearman  $\rho=-0.57$ ,  $P=0.0348$ ).

#### 6.3.4 Receptor fingerprinting of dynamic brain states

Finally, I was interested in a preliminary analysis of how the states relate to underlying molecular targets of ketamine. To test this, spatial correlations were computed between broadband state activity maps and known local receptor densities for  $N=19$  receptors using the *neuromaps* Python package. After testing correlations against a spatial null model and Bonferroni-correcting across all receptors, most states were still found to have a multi-receptor profile (Figure 6.7). Specifically, State 1 activity was high in regions with higher nicotinic  $\alpha 4\beta 2$ ,  $GABA_A$ , CB1, and NMDA receptor densities, as well as in regions with high norepinephrine transporter (NET) density and low serotonin transporter (5HTT) density. State 2 activity map was correlated with  $\alpha 4\beta 2$ , CB1, and especially  $\mu$ -opioid receptor (MOR) density maps. State 3 activity was modestly inversely correlated with MOR density. State 4 activity was also modestly inversely correlated with  $GABA_A$ , CB1, and NMDA receptor presence. Areas of depressed State 5 activity were strongly correlated with local  $GABA_A$  density, as well as less strongly with  $\alpha 4\beta 2$ , CB1, NMDA, and NET. State 6 showed a similar receptor fingerprint to State 5 except for no NET association. State 7 receptor fingerprint appeared as the opposite of State 1.

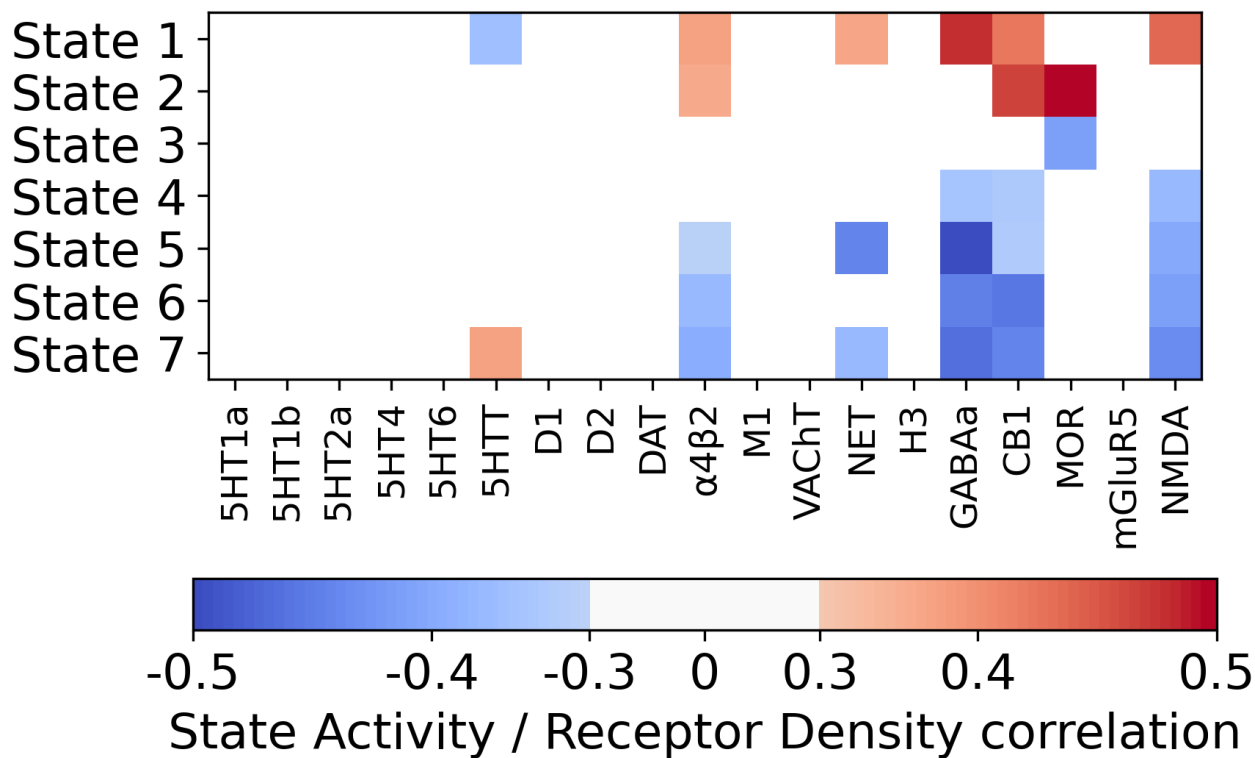


**Figure 6.7:** Receptor fingerprinting of ketamine-associated brain states. Spatial correlations between broadband state power maps and local receptor density maps computed using *neuromaps*<sup>388</sup> are shown. Only significant and moderate ( $r > 0.3$ , Bonferroni-corrected  $P < 0.05$ ) correlations are shown. States affected by ketamine are linked to multiple receptors beyond main NMDA antagonism, including GABA<sub>A</sub>, cannabinoid, nicotinic, and  $\mu$ -opioid receptors.

### 6.3.5 State appearance in low-density EEG

In order to translate insights about brain states into routine clinical practice, they should be recorded with more convenient EEG montages with fewer channels. For Chapter 7, I intended to study EEG in ketamine patients using the 'off-the-shelf' Muse-S headband with four EEG channels (TP9, AF7, AF8, TP10 referenced to FCz)<sup>398</sup>. Thus, using the state time courses estimated using the full high-density montage above, I extracted HMM state power spectra on a virtual montage that corresponds to the montage used in the Muse-S device (Figure 6.8, Chapter 7). State power spectra appeared qualitatively similar to that of the full model (Figure 6.2). This was especially true for States 1 and 2 on electrodes TP9 and TP10, where they had the highest signal-to-noise ratio. These results suggested recording with a low-density EEG device may still identify salient features that correlate with dissociation scores. This was confirmed in the patient study I undertook (Chapter 7).

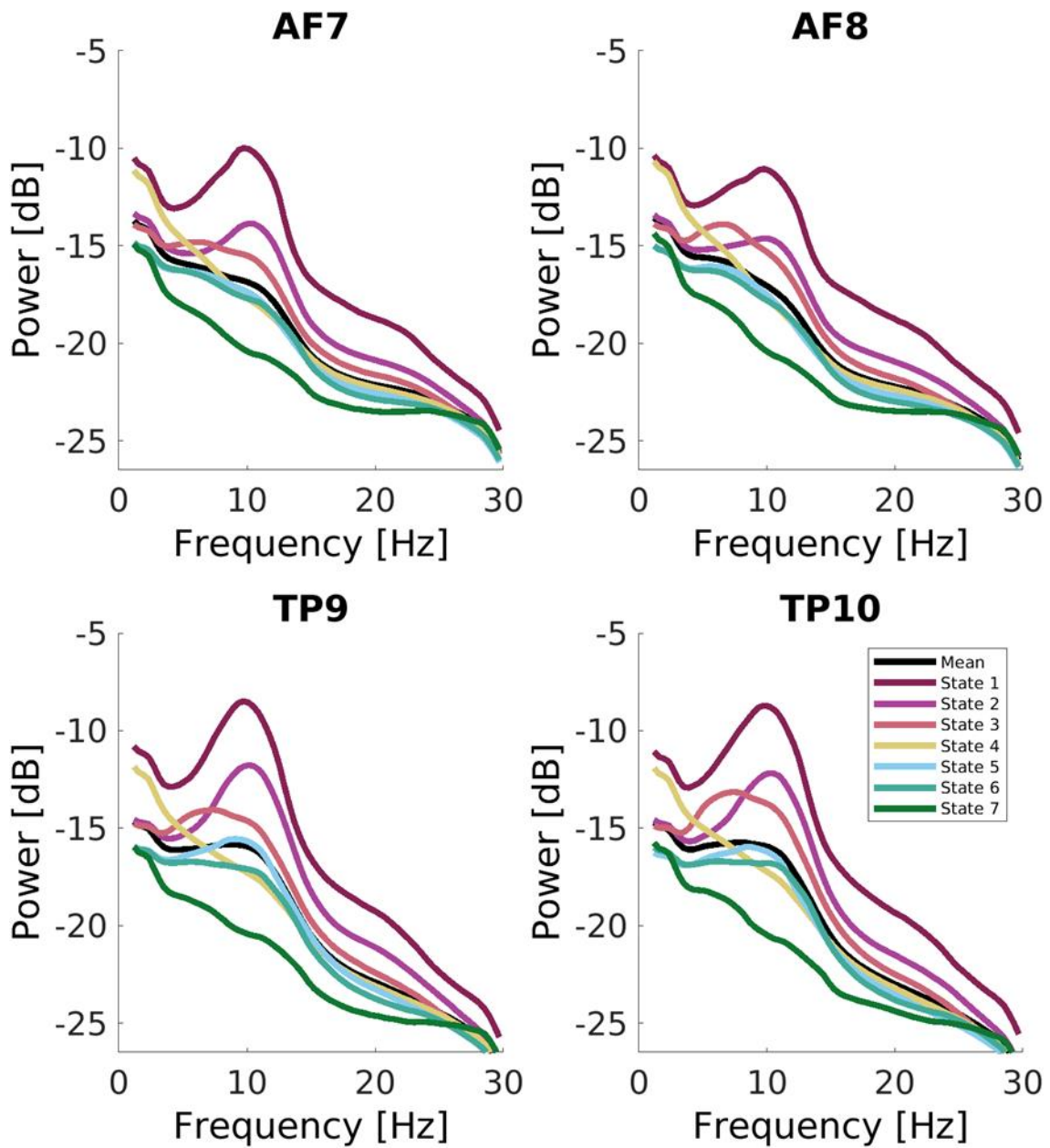


**Figure 6.8:** HMM state power spectra as appearing on a virtual Muse-S montage (electrodes AF7, AF8, TP9, TP10 in the international 10-20 system). States still show clear ordering based on power, with State 1 and State 2 having highest signal-to-noise ratio on channels TP9 and TP10.

### 6.3.6 Case study of heartbeat-evoked potentials under ketamine

Dissociated subjects often report altered perceptions of their body, including that they 'have no body'. Ascending visceral signals have an important role in maintaining bodily homeostasis and have been suggested to be involved in grounding the bodily self and emotions<sup>107,324</sup>. What's more, visceral afference can modify neural activity, chiefly through ascending vagal pathways converging in the nucleus of the solitary tract, thalamus, and the insula<sup>197,399</sup>. Ketamine has been shown to modify high-level interoceptive inference in the rubber hand illusion<sup>400</sup>, and it affects activity in key interoceptive network nodes including the insula<sup>401</sup>. This all suggests a potential role for explaining aspects of dissociative phenomenology (especially disembodiment) through impaired interoceptive signalling. Interoceptive signalling is typically quantified through cardiac interoceptive signals. This includes the robust heartbeat-evoked potential (HEP), the predominantly frontal brain evoked response observed around 400ms after the cardiac R-wave, source-localised to regions including the insular and anterior cingulate cortex<sup>344,402</sup>. Changes in HEPs have been observed in disorders including anxiety, depression, dissociative disorders, and in a variety of interoceptive tasks<sup>107,343,403,404</sup>. The effects of ketamine on cognitive predictive coding have been extensively researched<sup>405</sup>. However, surprisingly, to my knowledge direct ketamine effects on cardioception as quantified by HEPs have not been described in the literature. In one brief conference note, a single ketamine infusion did not affect the heartbeat-counting task, though HEPs were not reported and attention can modulate interoception<sup>406</sup>. Thus, I was interested if the Michigan dataset contained any preliminary evidence for this 'dissociation through altered interoception' hypothesis.

Unfortunately, the dataset provided did not contain ECG electrodes, which is a limitation of this analysis. However, in one participant (Subject 7), visual inspection of

ICA components identified a clean cardiac component with clearly visible QRS complexes throughout all of the infusion. This was used in lieu of an ECG recording as a case study. Similar to Chapter 3, R-peaks and instantaneous heart rate were identified with the *biosspy* toolbox and sensor-space EEG activity (filtered 1-7Hz to avoid effects from changing alpha activity) from 100ms before the R-peak to 700ms after the R-peak was saved for each heartbeat. These were grouped into eight segments and averaged as in the main analyses. A clear heartbeat-evoked potential around 400ms was observed (Supplementary Figure 6.5). What's more, the amplitude of the HEP decreased as the experiment progressed (Figure 6.9). This subject's 5D-ASC disembodiment score was also the second-highest in the group. N=8 other subjects showed ICA components with signs of cardiac activity, and the group-level result was similar (Supplementary Figure 6.6), though not significant. However, as these components were in part contaminated by brain activity and/or changed over time, only the N=1 case study is presented here.

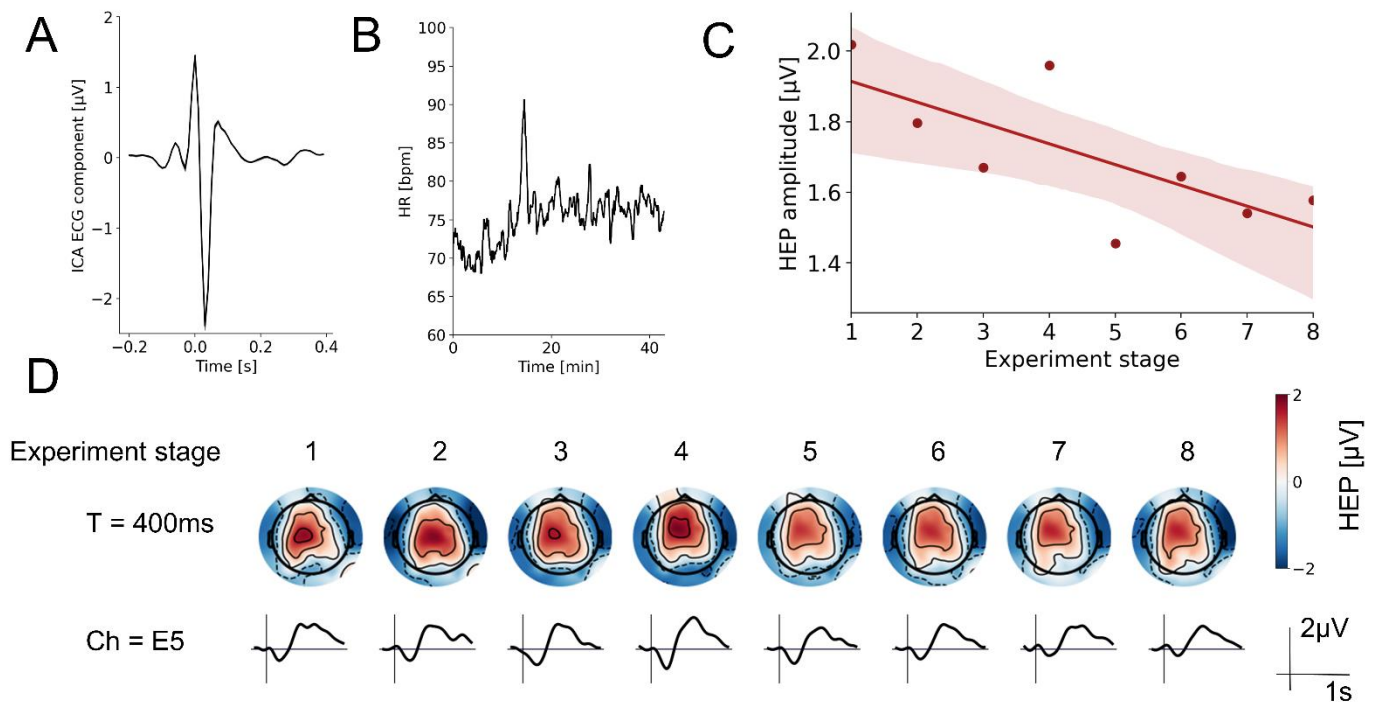


**Figure 6.9:** Case study of changing heartbeat-evoked potentials under ketamine. **(A)** ICA component activity around detected R-peaks (mean  $\pm$  SEM across all heartbeats) shows a clearly visible, ECG-like cardiac component. **(B)** Instantaneous heart rate showed a modest increase in heart rate throughout the ketamine infusion, as expected from its sympathomimetic properties. **(C)** Amplitude of the sensor-space heartbeat-evoked potential (HEP, each dot represents the mean across heartbeats for that experimental stage) decreased as throughout the ketamine infusion. A linear fit (95% confidence intervals shaded) shown in red. **(D)** Identified HEP had the expected fronto-central positive topographical peak around 400ms after the cardiac R-wave.



## 6.4 Discussion

In this chapter, I considered brain states under the influence of sub-anaesthetic ketamine in healthy volunteers. The rapid-acting antidepressant properties of low-dose ketamine call for a translation of insights from anaesthetic methodology (e.g. brain-based depth of anaesthesia monitoring like the Bispectral index) to a novel psychiatric setting in order to improve treatment for patients.

### 6.4.1 Hidden Markov Modelling of ketamine in healthy volunteers

First, I applied Hidden Markov Modelling to source-projected high-density electroencephalographic data in volunteers in order to identify dynamic network states in the brain during a sub-anaesthetic ketamine diffusion. A shift towards lower-power states (especially in the alpha band) was found, with reduced connectivity between the default mode network and salience and sensory networks. Distinct state modules were associated with baseline consciousness and the ketamine-induced state. Preliminary associations between state occupancies and transition probabilities with subjective dissociative phenomenology were studied, identifying states related to the sensory and salience networks as potential markers of both the acute dissociated state and baseline dissociation susceptibility. Finally, using a recent PET-derived databank for receptor fingerprinting, exploratory correlations were found between state power maps and receptor densities beyond NMDA blockade, including significant relationships with GABA<sub>A</sub>, CB1,  $\alpha$ 4 $\beta$ 2, and  $\mu$ -opioid receptors, as well as serotonin and norepinephrine transporters.

These data driven, dynamic brain states revealed a shift from an awake, high alpha power community of states to a different low-power community in a dose-dependent

way, both in state occupancies and transitions between states. This is in line with existing literature, which shows a robust decrease in low-frequency (<30Hz) activity with sub-anaesthetic doses of ketamine, especially in the alpha band<sup>378,380,407</sup>. *In vitro* studies suggest this may be related to direct NMDA and mGluR1a effects causing impaired glutamatergic transmission<sup>89</sup>. However, the present analysis highlights the possible distinct roles of alpha in different brain states. At baseline, more time spent in State 5 (suppressed visual alpha) and more transitions from a purely visual alpha state to a mixed visual / sensorimotor alpha state correlated with less dissociation at the end of the ketamine infusion. Alpha decrease occurs with anticipatory attention<sup>408</sup>, and conversely patients with dissociative disorders show a lack of alpha responsiveness<sup>409</sup>, suggesting more flexible alpha oscillations at baseline may indicate less dissociation susceptibility.

However, the full explanation is likely more complex, with more than one 'alpha' potentially present. At the end of the infusion, the balance of State 1 (high visual alpha) and State 2 (high salience & limbic alpha) presence was a neural correlate of acute dissociation intensity. Specifically, subjects that spent relatively more time in State 2 with elevated salience and limbic alpha reported higher disembodiment scores. The salience network (especially the anterior insula and anterior cingulate cortex) has a key role in linking interoception with the core self<sup>324,386,410</sup>. Diminished interoceptive processing under ketamine as a contributing factor to dissociation should be investigated further, and its presence is tentatively supported by the reduced heartbeat-evoked potential amplitude case study result. The only literature on this subject is one conference abstract where authors did not find a difference in interoceptive accuracy as measured by the heartbeat counting task after a ketamine

infusion<sup>411</sup>. However, in patients with depersonalisation / derealisation disorder, heartbeat-evoked potentials differed compared to healthy controls<sup>403</sup>.

Aberrant functioning in anterior insula and cingulate has been observed during classical psychedelics and has been suggested to underlie the experience of ego dissolution<sup>412,413</sup>. A previous study linked the decrease in alpha activity in the right anterior insula to depersonalisation scores<sup>378</sup>. However, in contrast, a recent fMRI study found the ketamine decrease in connectivity with the anterior insula was also found in sub-anaesthetic doses of propofol, suggesting regions in the temporoparietal junction may play a role instead<sup>380,414</sup>. Here, an overall alpha power decrease in the salience regions was observed, and it was found that the increase in salience alpha relative to sensory alpha was most predictive of dissociation. The differences with existing literature may be due to a different aspect of dissociation being considered (e.g. depersonalisation vs disembodiment), or due to the anterior insula not being representative of the entire salience network.

The role of the limbic cortex is less clear, though the limbic system has been implied in the pathophysiology of schizophrenia<sup>415</sup>, it is a known region affected by ketamine<sup>416,417</sup>, and may play a role in ketamine's antidepressant effects<sup>418</sup>. One may propose that abnormal alpha activity in key nodes of the salience network including the anterior insula and cingulate may be an acute marker of disrupted self-other processing and thus of acute core dissociative phenomenology. On the other hand, high baseline alpha flexibility and desynchronisation in the sensory systems may potentially be protective against pharmacologically-induced dissociation.

Ketamine effects on functional connectivity are more complex and may be modality-dependent<sup>419</sup>. In acute functional MRI studies of healthy volunteers, ketamine tends to increase between-network and decrease within-network connectivity<sup>41,420</sup>. In a recent publication, ketamine had this in common with nitrous oxide and the classical psychedelic LSD<sup>414</sup>. In electrophysiological studies, ketamine has been shown to reduce fronto-parietal connectivity, especially in the alpha band, a finding proposed to be linked to NMDA receptor hypofunction<sup>89,379,383,421</sup>. Similarly to the latter, in this analysis, ketamine broadly shifted the brain to states with reduced coherence between source-space EEG resting-state networks, notably lower DMN-salience and DMN-somatomotor coherence in State 7. The exception was increased somatomotor-ventral attention connectivity in State 6, a finding previously seen in fMRI studies<sup>422</sup>. DMN and salience network isolation have recently been proposed to account for ketamine's psychedelic and dissociative properties<sup>401</sup>, which is consistent with the results presented here.

A recent study using the same dataset as this one identified ten dynamic states using K-means clustering<sup>382</sup>. Similarly to the analysis presented here, the authors found a decrease in occupancy of states with posterior activity. The authors also found an increased switching rate and generally a richer functional repertoire in the sub-anaesthetic ketamine condition. This is in contrast to the present study, where dynamic changes in state occupancies were found but without an overall change in the switching rate. This may be due to differences in pre-processing. Here, data was low-pass filtered at 30Hz and ICA was performed to remove muscle noise components. In the study by Li et al, the low-pass filter was at 45Hz and ICA was not mentioned. This suggests the increase in functional diversity may be primarily driven by the gamma frequency range, though other differences (e.g. a different source reconstruction

method) may also influence this. Whilst gamma activity has been suggested as important during different altered states of consciousness including ketamine<sup>183,423</sup> (and is also observed in MEG and invasive studies<sup>424</sup>), here the conservative approach to avoid muscle noise influence was chosen. Despite extensive clean-up (even with ICA), residual muscle noise may remain in EEG data, as shown by *in vivo* studies of awake paralysis<sup>66–68</sup>. This is especially relevant as ketamine increases the muscle tone<sup>425</sup>, so it remains to be seen how much of the scalp gamma increase is attributable to muscle artefacts. In addition, the aforementioned study only analysed the last 5 minutes of the sub-anaesthetic ketamine condition, whereas here the full infusion was analysed. Finally, Li and colleagues focused on amplitude envelopes within canonical frequency bands, whereas here a time-delay embedding approach was used, a further potential reason for differences in states found.

#### 6.4.2 Receptor fingerprinting

Receptor fingerprinting of brain networks underlying a sub-anaesthetic ketamine infusion in our work suggested a complex picture beyond NMDA blockade. Whilst power decreases in States 4-7 spatially matched local NMDA density (and the converse was true for high-power State 1), this was non-specific and also true for GABA<sub>A</sub>, CB1, and  $\alpha 4\beta 2$  receptors. Whilst these are not the main targets of direct ketamine action, significant downstream effects may be present<sup>39</sup>. For instance, CB1 blockade attenuates ketamine-induced behaviour in rats<sup>426</sup> and GABA<sub>A</sub> blockade reduced ketamine-induced amnesia<sup>427</sup>, with GABAergic mechanisms potentially underlying ketamine disinhibition of the prefrontal cortex<sup>428</sup>. Interestingly, State 2 with high salience alpha was most strongly associated with  $\mu$ -opioid receptor density. Ketamine affects  $\mu$ -opioid signalling, potentially accounting for some of its

antinociceptive properties<sup>429</sup>. However, in depressed patients, antidepressant effects of ketamine have been observed to decrease with opioid antagonists without significantly affecting dissociation reported using the Clinician-Administered Dissociative States Scale (CADSS)<sup>387</sup>. The difference with this study, where State 2 was implicated in acute dissociation, may be due to studying healthy volunteers<sup>430</sup>, or perhaps due to the CADSS capturing different aspects of dissociation than 5D-ASC, which is supported by my findings in patients detailed in the next chapter<sup>431</sup>. In short, whilst this study cannot precisely explain the role of distinct neurotransmitter systems in ketamine dissociation due in part to the low resolution of EEG and lack of individual PET data, it calls for further consideration of non-NMDA mechanisms implicated in ketamine phenomenology.

### 6.4.3 Limitations

This study has several important limitations. Firstly, due to the lack of individual structural brain images, intrinsic EEG spatial resolution limits, and the need for strict pre-processing to gain clean data, a low-dimensional brain parcellation was used. As such, the results cannot distinguish between roles of individual brain regions and network nodes. This low spatial resolution renders the receptor-map associations as tentative. It would be interesting to apply a similar framework in data with better spatial resolution, e.g. magnetoencephalography<sup>421</sup>. This could allow for exploration of the roles of individual network nodes, such as the right vs left anterior insula<sup>385</sup>. Secondly, the use of the 5D-ASC disembodiment scale as a measure of dissociation might be a limitation. Whilst this is a validated and extensively used tool in psychedelic research<sup>389,432,433</sup>, dissociation is a complex experience that can also include derealisation, depersonalisation, and other phenomena, so developing more specific dissociation

measures is warranted<sup>431</sup>. Thirdly, whilst correlations between HMM states, dissociation scores, and receptor maps were found, causation cannot be inferred from the results. For robustness, the association between State 1/2 occupancy and disembodiment scores was tested across HMM runs with different numbers of states (Supplementary Figures 6.2-6.4), and whilst it was always in the same direction, it did not always reach significance, and should thus be interpreted with caution. Further work with targeted causal interventions (pharmacological, e.g. by considering dissociation induced by different substances, or through neurostimulation, e.g. transcranial current stimulation<sup>434</sup>) could better elucidate the mechanisms underlying brain dynamics under the influence of ketamine.





# 7 Ketamine dissociation in patients with treatment-resistant depression

## 7.1 Introduction

As was outlined in more detail in Chapter 6, ketamine is a novel, rapid-acting antidepressant<sup>365</sup>. However, tolerance development and urotoxicity call for dose optimisation. At present, anti-depressant ketamine infusion doses are not informed by any objective neural markers. This is unlike traditional anaesthetic settings, where complex monitoring (including brain-based monitoring, e.g. the Bispectral Index) is used to optimise dosing<sup>435</sup>. The feasibility of routine EEG-based monitoring of antidepressant ketamine treatment should be assessed, with a view to identify potential objective markers ketamine effect that could one day be used to determine dosing.

In clinical settings, the role of dissociation has been controversial<sup>130–132,436</sup>. Some authors have argued dissociative symptomatology is an adverse undesirable event with no relationship to treatment outcome<sup>437,438</sup>, whereas other research has suggested features of dissociation may be predictive of treatment response<sup>130,436</sup>. Some of the discordant results may be due to limitations in psychometric scales used to assess ketamine phenomenology<sup>131,365</sup>, and more research is needed to understand the role of acute subjective experience under ketamine in mediating therapeutic effects. Interestingly, a recent trial showed a comparable decrease in depression scores for ketamine and placebo when masked by general anaesthesia<sup>439</sup>,

though this may in part reflect intrinsic antidepressant effects of common general anaesthetics<sup>354,355</sup>.

After studying the neural effects of ketamine in a high-density EEG montage (Chapter 6), I wanted to see how this could translate to a system more suitable for routine clinical use. As Section 6.3.5 demonstrated, the alpha desaturation effect was expected to be robust enough to be measurable even with a low-density system, so an observational pilot study was designed in collaboration with the Oxford Health Ketamine Clinic. This chapter presents initial results from this ongoing study, where we have collected EEG, photoplethysmography (PPG), and psychometric data focused on dissociative experiences in patients with treatment-resistant depression. We hypothesised reduced alpha power would be measurable even in a low-density EEG montage, using commercially available 'off the shelf' technology.

## **7.2 Material and Methods**

### **7.2.1 Study protocol**

In collaboration with the Oxford Health Foundation Trust (OHFT) Interventional Psychiatry Service and under the guidance of Prof Rupert McShane, we designed an observational pilot study to explore the feasibility of routine EEG monitoring of antidepressant ketamine treatment in their clinic. The study ethics were approved by a regional research ethics committee (REC reference 22/EM/0226, IRAS ID 306474). N=30 patients gave informed consent to participate in the study after having procedures explained and a chance to review a Participant Information Sheet and ask questions. In brief, the study was purely observational and ketamine infusion frequencies and doses were determined clinically. During each in-clinic infusion,

patients wore a Muse-S headband (InteraXon) that streamed EEG, gyroscope, accelerometer data (all sampled at 256Hz) and PPG data (effectively sampled at 10Hz) to a dedicated smartphone device with the MindMonitor app<sup>440</sup>. This headband was chosen as it is relatively cheap (~£300/device), can stream data in real time, has frontal and temporal locations implicated in depression, and has been used in previous research. Treatment was given at the OHFT ketamine clinic, with each patient in a separate bay (Figure 7.1).

Before each infusion, after a patient entered the bay and was cannulated, they completed two baseline questionnaires assessing aspects of patient mindset (“Set”) and the physical and social environment (“Setting”) thought to be important to psychedelic experiences, using the previously validated Set and Setting visual analogue scale (VAS)<sup>441</sup> and a dedicated 4-item Light and Noise levels questionnaire. After completing these and fitting the EEG headband, a 5-minute baseline was recorded. During this baseline, objective noise and light levels were measured using a smartphone with the apps Sound Meter (Smart Tools co<sup>442</sup>) and Light Meter (Coolexp). The 40-minute ketamine infusion then proceeded as usual, with the Muse headband recording continuously throughout. It was noted whether a participant wore headphones or an eye mask during the infusion. Patients were instructed to keep their eyes closed throughout the whole recording to minimise eyeblink artifacts.



**Figure 7.1:** Example treatment bay in the OHFT ketamine clinic (photograph taken with permission of the clinic staff).

After the infusion, the Muse kept recording for at least 15 minutes. Then, the patients completed post-infusion questionnaires, either in the bay or recovery room, within 45 minutes of the infusion ending. This included the 6-item CADSS validated for ketamine infusions<sup>443</sup>, the 5D-ASC<sup>389</sup>, a single subjective dissociation VAS rating (“I felt dissociated”) and open-ended qualitative questions. All questionnaires used can be found in Appendix 7.

For this thesis, as per the original protocol, a preliminary analysis is presented with data collection for the full study on-going. Specifically, results from N=18 recordings from N=12 patients collected between November 2022 and February 2023 are presented here.

### 7.2.2 Study population

The study population were private patients undergoing ketamine treatment for treatment-resistant depression (TRD) at the OHFT Ketamine clinic. Demographic and other patient variables are summarised in Table 7.1.

Variable	Median (IQR)	Range
Age [years]	44 (16.5)	33 - 62
Gender	5 women / 7 men	
Ethnicity	White-British (67%), White-Other (17%), Other/Prefer not to say (17%)	
Weight [kg]	81.1 (13.9)	61 - 152
Ketamine dose [mg/kg]	0.70 (0.2)	0.5 - 1.0
Psychiatric medications beyond ketamine	1.5 (0.75, 2.25)	0 - 4
Known psychiatric diagnoses beyond TRD	0 (1)	0 - 3

**Table 7.1:** Study demographics

## **Inclusion / Exclusion criteria**

Patients had to be scheduled to receive ketamine treatment at the Oxford ketamine clinic. This meant initial inclusion / exclusion criteria matched that of the clinic. These can be found in detail at [www.oxfordhealth.nhs.uk/ketamine-service/](http://www.oxfordhealth.nhs.uk/ketamine-service/). In brief, to be eligible for the clinic, patients must be aged 18 years or above and:

- currently be suffering from depression,
- have tried at least two different types of antidepressants for at least six weeks each at an adequate treatment dose,
- have tried at least one type of psychological treatment,
- be referred to the service by a GP or psychiatrist,
- pass exclusion criteria including severe high blood pressure, raised eye or intracranial pressure, any illegal drugs taken in the last two years, pregnancy, inability to abstain from alcohol for at least three days.

In addition to this, for our study inclusion, participants had to be willing and able to give informed written consent and to have sufficient knowledge of English language to understand and complete study tasks. Patients would not be eligible if they had lesions or rashes on forehead that would prevent EEG sensors from being applied, or if they were deemed unlikely to comply with the study protocol in the opinion of the clinicians.

Of note is the fact that none of the patients presented here were ketamine-naïve, as they had all had infusions prior to those recorded for the study, often for many months. Furthermore, no exclusions were made on the basis of diagnoses secondary to treatment-resistant depression, or on the basis of other stable medication (Table 7.1). Our criteria were purposefully broad to capture the clinical reality of the Oxford clinic.

The most common documented secondary diagnoses were forms of anxiety (mixed anxiety/depression, generalised anxiety disorder; 25%), and the most common current psychiatric medication beyond ketamine was another antidepressant (50%, most commonly a selective serotonin reuptake inhibitor, SSRI, 33%).

### 7.2.3 Data pre-processing

Paper-based questionnaires were digitised and visual analogue scales converted to a score out of 100%. To explore dissociative phenomenology, Spearman correlations of individual dissociation-related items from all the scales used were computed. For the 5D-ASC, this meant using only the disembodiment sub-scale.

For physiological recordings (EEG, PPG), simple pre-processing that could in theory be performed in real time was done. Specifically, 5s epochs (4s overlap) were rejected if the gyroscope data indicated average head movement of above 10 degrees/s. This was found to robustly capture gross movement artifacts. In addition, EEG epochs were also rejected if their amplitude was above 200 $\mu$ V, and PPG epochs if their amplitude was outside 3 standard deviations. Next, recordings were aligned by the infusion start time, and data from 5min before infusion start until 55min after (40min infusion + 15min post-infusion) was kept. An electrode in a given subject was fully rejected if the proportion of rejected epochs was >90%.

### 7.2.4 Data analysis

To explore spectral changes, the short-time Fourier transform spectrogram (MATLAB *spectrogram*) was computed on each channel (4s window, 3s overlap, 4-30Hz, 0.25Hz resolution) and converted to dB. We chose to further analyse theta (4-8Hz), alpha (8-

13Hz), and beta (13-25Hz) bands as they are least susceptible to noise, which was especially a concern in the context of a routine clinical setting and dry EEG electrodes.

To calculate the heart rate, R-peaks were found in the infrared PPG channel (high-pass filtered at 0.5Hz) using MATLAB's findpeaks (0.5s minimum peak distance), with instantaneous heart rate in bpm as  $60 / \text{R-R interval}$ . Heart rate was then interpolated to 1Hz as well as mean in each 5-minute segment computed. As the PPG data is only streamed at 10Hz sampling rate, heart rate variability calculations were not possible.

Suggestions have been made that alpha asymmetry may be a marker of depression<sup>444</sup>. Thus, as an exploratory, non-prespecified analysis, left-right alpha power asymmetry (left – right alpha power in dB) was also computed.

Finally, this study allows for longitudinal data collection. In this preliminary dataset, the median number of recordings per participant was only one, but we had one participant with N=4 recordings. Thus, as an exploratory case study, these N=4 recordings and associated scales were analysed longitudinally.

### 7.2.5 Statistical analyses

Repeated-measures analysis of variance (RM-ANOVA) with Huynh-Feldt P-value adjustment for sphericity violations was computed on 5-minute segment means across heart rate and all 4 channels and 3 frequency bands of the EEG, with post-hoc Tukey's honest significant P-values examined. Effect sizes for each band were computed as Cohen's d between the baseline and subsequent 5-minute segments.

For exploratory analyses of links between physiological measures and dissociation scores, general linear models (GLMs) were employed. Specifically, for the subjective



report (“I felt dissociated”), CADSS-6 total, and 5D-ASD disembodiment total, a GLM was fitted with baseline / infusion band powers that showed significant changes included as regressors. Age, gender, and dose in mg/kg were also included as covariate regressors as previous work has suggested these may independently affect dissociation<sup>445</sup>. Significance was set at  $P=0.05$  after appropriate multiple-comparisons corrections (specified in the text).

## 7.3 Results

### 7.3.1 Pre-infusion measurements and Set & Setting scales

Objective light and noise levels were available in  $N=14$  recordings. From these, the median noise level was 54.5dB (IQR 5.9dB, range 44-64dB). The median light level was 86 lux (IQR 71 lux, range 26-224 lux). This places the setting as equivalent to a relatively quiet and dark office, quieter than the common 60dB+ of a nursing unit<sup>446</sup>.

From patient noise and light level ratings, a similar picture emerged (Table 7.2 and Figure 7.2). No patient answered that noise or light levels bothered them above ‘somewhat’, with median response being ‘not at all’. Whilst correlations between objectively recorded and patient-reported noise and light levels were positive, these correlations were not significant. Importantly, there was no significant differences in objective noise and light levels between patients who felt these bothered them ‘not at all’, ‘a little bit’, and ‘somewhat’, suggesting it’s likely to be more of a personal preference. Furthermore, a large majority of recordings had patients wearing headphones (94%) and an eye mask (76.5%).

Question	Median (IQR)	Range
Room is noisy	1 (0.25)	0 - 3
Noise bothers me	0 (1)	0 - 2
Room is bright	2 (1.25)	0 - 3
Light bothers me	0 (0)	0 - 2

**Table 7.2:** Light and noise questionnaire responses

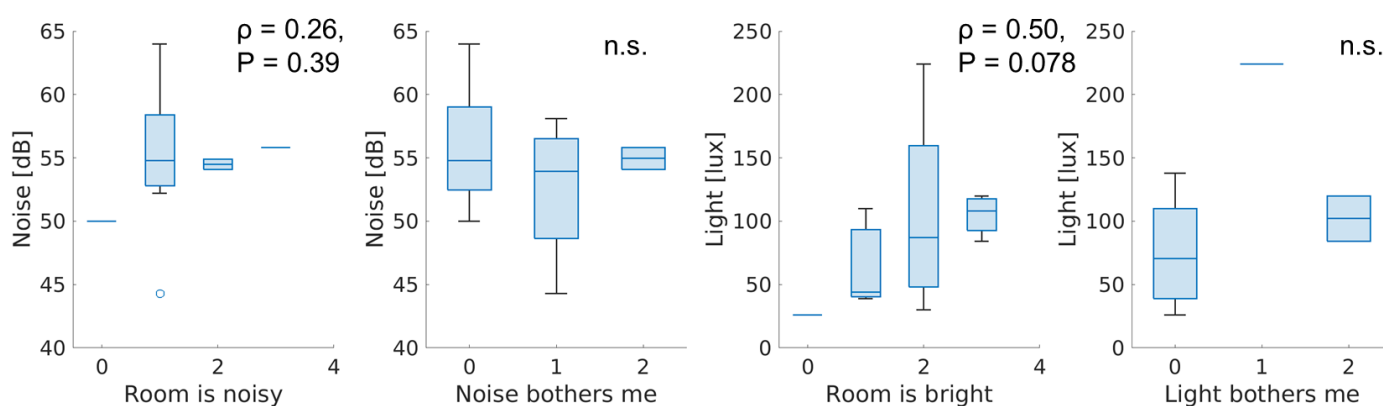


**Figure 7.2:** Light and noise questionnaire responses against objective measurements.

In the Set and Setting questionnaire results (Figure 7.3), patients broadly reported being comfortable about their upcoming experience (median 82%), feeling well-prepared (83%), and having a good relationship with the main clinician (85%) and clinical staff in general (80%). People varied most in their reporting of anxiety (IQR 46%), good mood (IQR 31%), and their expectations (IQR 32%) / intentions (IQR 34%). Exploratory correlations (not corrected across questions) suggested a negative correlation between patient-reported comfort with the upcoming experience and their anxiety (Spearman  $\rho = -0.54$ ,  $P = 0.026$ ), a positive correlation between being comfortable about the experience and having a good relationship with people in the clinic (Spearman  $\rho = 0.58$ ,  $P = 0.015$ ), and a correlation between reporting a good

relationship with the main clinician and people in the clinic in general (Spearman  $\rho=0.74$ ,  $P=0.0007$ ). There were no significant correlations between any Set & Setting items and objective light or noise levels.

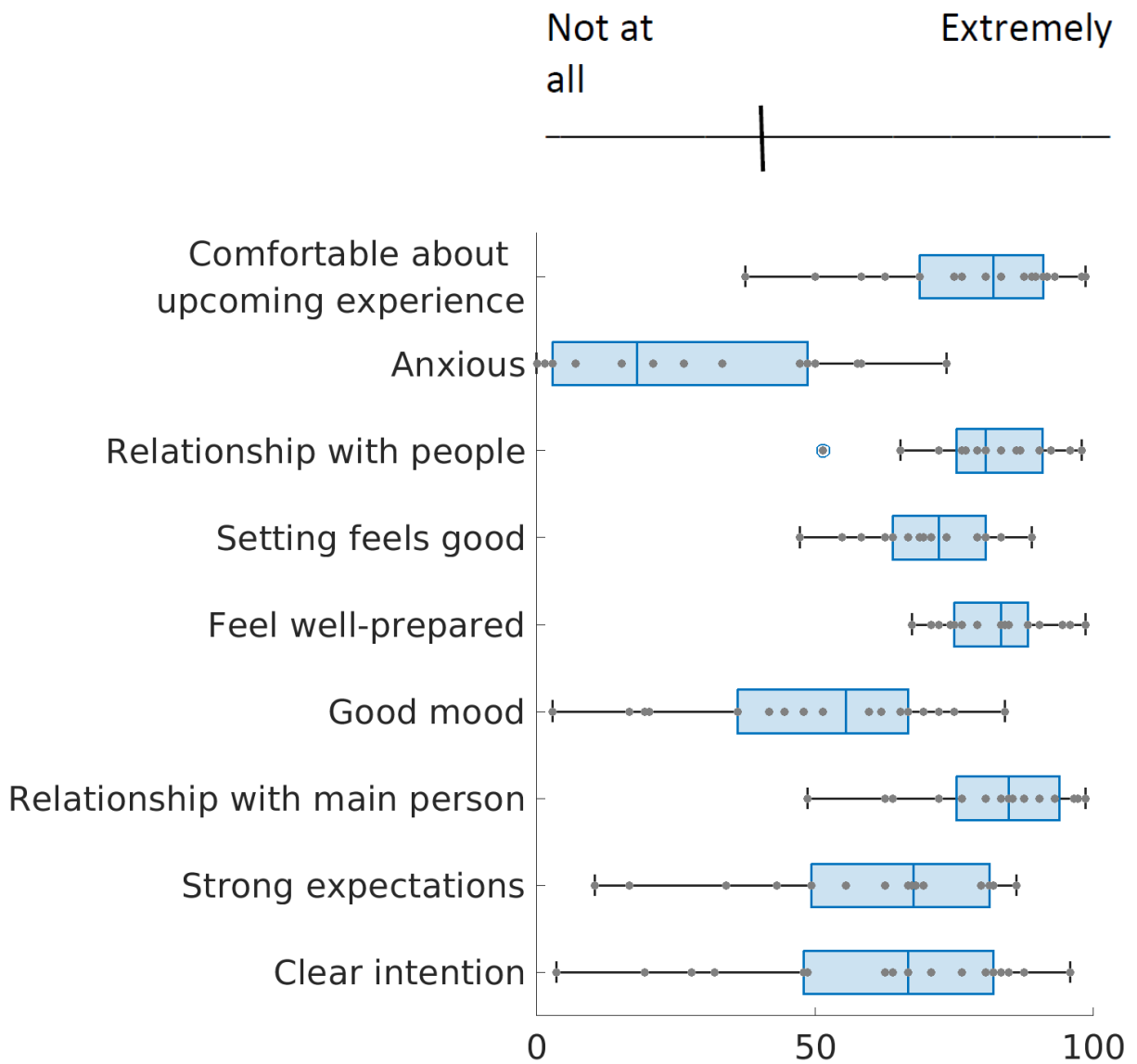


**Figure 7.3:** Set & Setting questionnaire responses (distribution across all sessions).

### 7.3.2 Post-infusion dissociation scales

Next, we analysed N=18 responses on the post-infusion dissociation scales: the disembodiment subscale of the Altered States of Consciousness (5D-ASC) questionnaire, the 6-item version of the Clinician Administered Dissociative States Scale (CADSS-6), and a novel single-item subjective visual analogue scale rating (“I felt dissociated”) (Figure 7.4). Ketamine induced relatively high dissociation scores, with subjective rating of 87% (25%), 5D-ASC disembodiment total of 64% (23%), and CADSS-6 total of 13.5 (10) out of 24, median (IQR).

Next, Spearman correlations and FDR-corrected P-values between individual item responses were computed (Figure 7.5). This revealed that subjective patient ratings (“I felt dissociated”) correlated strongly and significantly with items describing body disconnect. Specifically this was the 5D-ASC items: “It seemed to me as though I did not have a body anymore” ( $\rho=0.798$ ,  $P=0.0012$ ), “I had the feeling of being outside my body” ( $\rho=0.768$ ,  $P=0.0018$ ), and the 5D-ASC disembodiment total ( $\rho=0.611$ ,  $P=0.0367$ ), as well as the CADSS-6 item “Did you feel disconnected from your own body?” ( $\rho=0.644$ ,  $P=0.0237$ ). Importantly, the CADSS-6 total was not significantly correlated with patient-reported dissociation ( $\rho=0.404$ ,  $P=0.1$  uncorrected), nor with the 5D-ASC disembodiment total ( $\rho=0.237$ ,  $P=0.34$  uncorrected). Within CADSS-6, the strongest correlations were between reporting feeling spaced out (“Did you space out, or in some other way lost track of what was going on during this experience?”) and reporting memory gaps (“Did you have gaps in your memory?”) with  $\rho=0.745$ ,  $P=0.0031$ .

There were no significant correlations between items known at baseline and dissociation scores (Set & Setting scores, noise & light levels, age, dose in mg/kg, all uncorrected  $P>0.1$ ). There was a trending difference between subjective dissociation

reported by men and women (men: median 79.5%, IQR 50%; women: median 93%, IQR 9%; Mann-Whitney test  $P=0.032$  uncorrected).

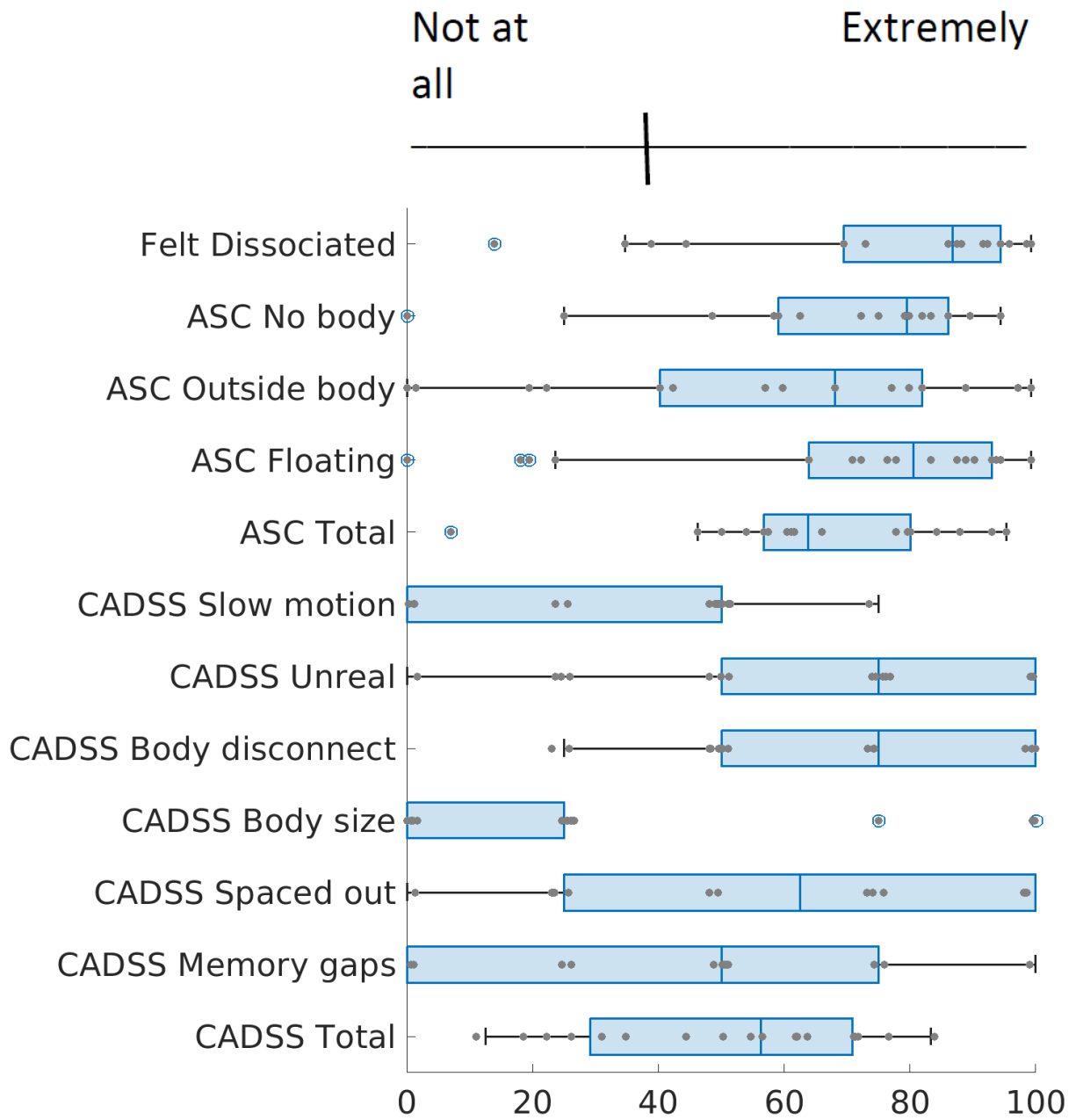


**Figure 7.4:** Dissociation scales questionnaire responses (distribution across all sessions in the dataset).

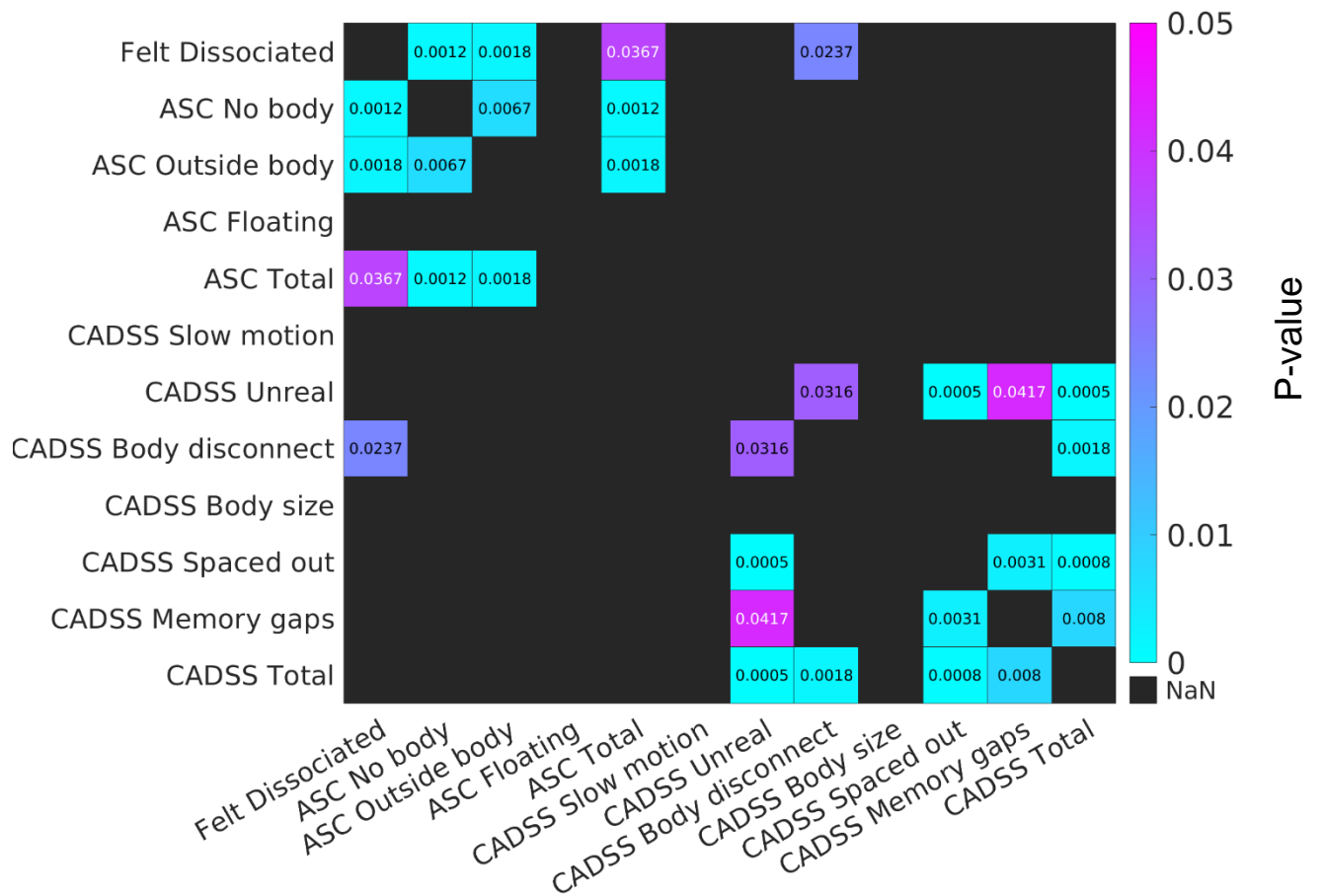


**Figure 7.5:** Spearman correlation P-values (FDR-corrected) for items tracking dissociative experiences.

### 7.3.3 Photoplethysmography (PPG) results

At the group level, there was a significant difference in PPG-derived pulse rate (PR) across the 5-minute segments from baseline to post-infusion (RM-ANOVA  $F=3.62$ ,  $P=0.012$ , Figure 7.6). The group-median increase in heart rate was +3.1 (+1.4, +8.9) bpm (median, quartiles). Upon post-hoc inspection, this effect was heterogeneous between patients, with 2/12 patients (17%) showing a pulse rate increase >10bpm. There was no significant correlation between self-reported baseline anxiety and the intra-infusion pulse rate ( $P=0.55$  uncorrected), but there was a trend for a higher baseline pulse rate correlating with higher self-reported baseline anxiety (Spearman  $\rho=0.505$ ,  $P=0.0325$  uncorrected). There was a trend for those subjects who reported being more bothered by noise to experience a larger PR increase (Mann-Whitney test between bothered=0 and bothered>0,  $P=0.0152$  uncorrected), and for those with a greater intra-infusion PR increase to report more subjective “floating” on the 5D-ASC (Spearman  $\rho=-0.584$ ,  $P=0.011$  uncorrected). There were no significant correlations between age or dose in mg/kg and intra-operative PR increase, nor any significant differences between men and women.

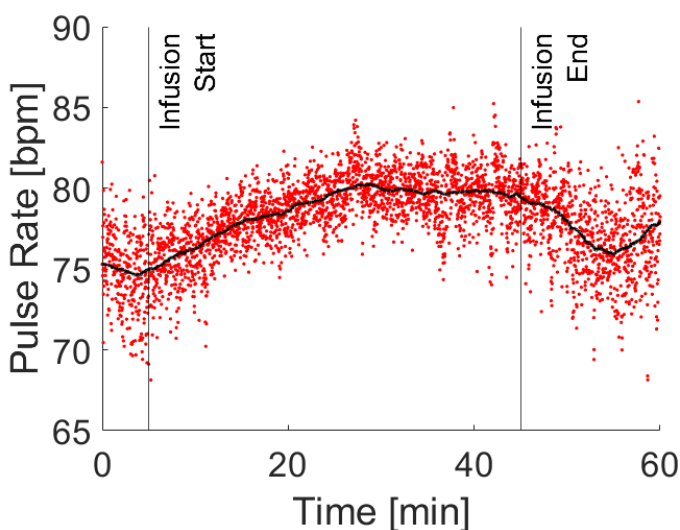


**Figure 7.6:** Group-mean pulse rate (resampled to 1Hz) during infusions (each red dot = 1s) and a 5-minute moving median (black). On average, pulse rate was slightly increased during ketamine infusions (RM-ANOVA  $F=3.62$ ,  $P=0.012$ ).

### 7.3.4 Electroencephalography (EEG) results

Dry EEG collected in a routine clinical setting was of highly varying quality (see Supplementary Figure 7.1 for example individual spectrograms). There was no significant difference in fraction of data rejected between recordings where patients wore an eye mask or headphones. However, significantly more data was rejected on the temporal electrodes in women, TP9 ( $P=0.038$ ) and TP10 ( $P=0.016$ ), which is very likely attributable to more hair. The median fraction of data rejected for each electrode was 0.273 (0.03-1) for TP9, 0.042 (0.003-0.92) for AF7, 0.037 (0.003-0.86) for AF8, and 0.043 (0.003-0.88) for TP10. In 3/18 recordings (17%), the headband Bluetooth disconnected towards the end of experiment without any apparent cause, causing some data loss (10, 20, 35min).

Group-median spectrogram showed a dropout and desaturation of theta, alpha, and beta power, with an electronic artifact at 22Hz (Figure 7.7). Repeated measures ANOVA on banded power across 5-minute segments of the experiment revealed an overall significant time effect ( $F=3.65$ ,  $P=0.0105$ ), as well as a significant Channel \* Time interaction ( $F=3.80$ ,  $P<0.001$ ). Post-hoc analyses showed the changes have largest effect sizes on the temporal electrodes, particularly TP9 in the alpha and theta bands (Table 7.3). In an exploratory, non-prespecified analysis, there was a trend for left-right temporal alpha asymmetry to reverse during the ketamine infusion, with RM-ANOVA  $P=0.10$ , post-hoc  $P=0.047$  baseline vs 15min, Cohen's  $d=0.20$  (Figure 7.8).

There were no significant univariate correlations between dissociation item scores and desaturation minimum of the banded power, absolute or relative to baseline. However, when controlling for age, gender, and dose in mg/kg, an exploratory general linear model with temporal alpha and theta powers was significantly predictive of the



subjective dissociation report ( $P=0.0109$ , Table 7.4), but not 5D-ASC disembodiment total ( $P=0.161$ ) or CADSS-6 total ( $P=0.475$ ).

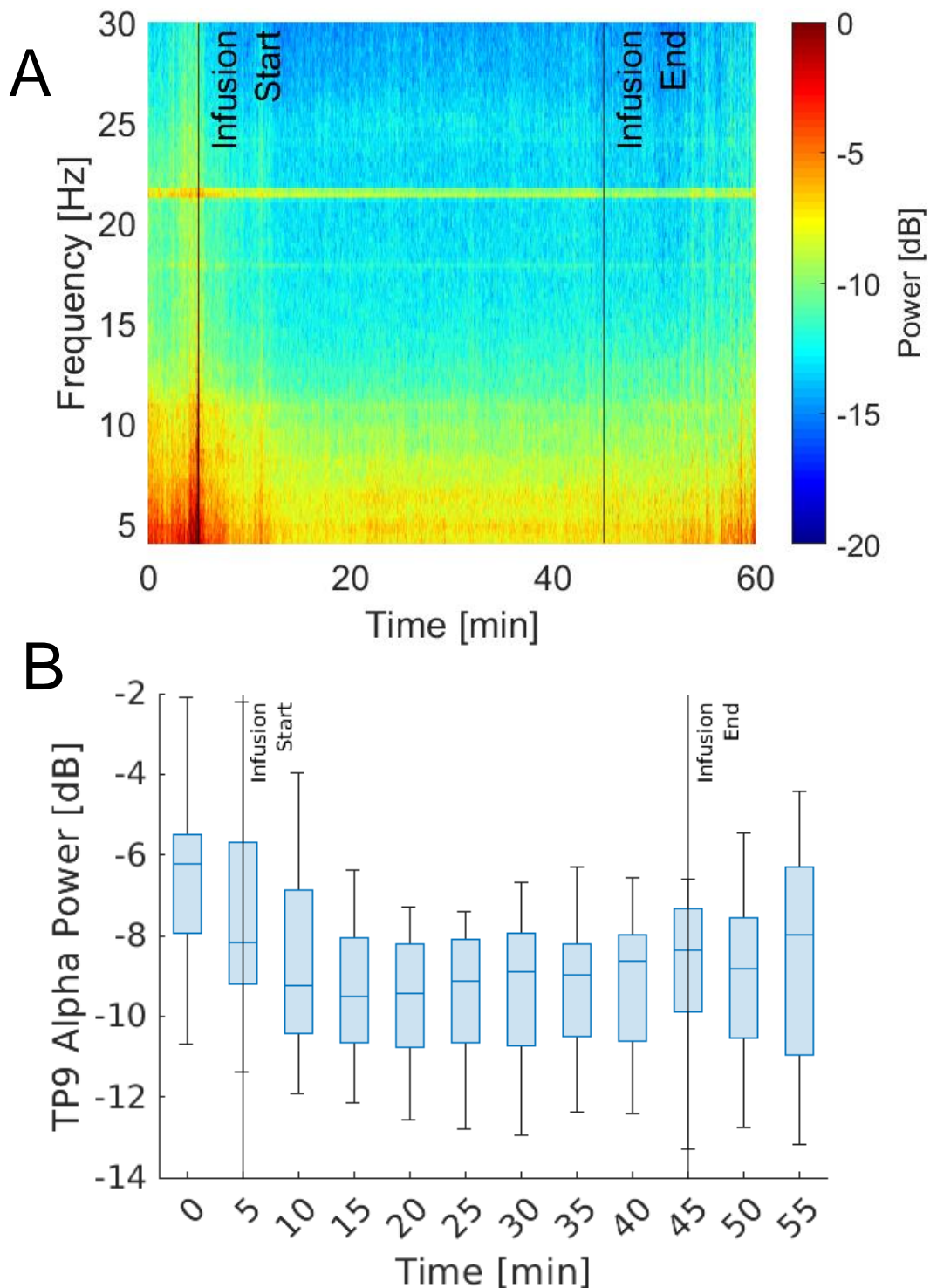


**Figure 7.7:** (A) Group-average spectrogram for the OHFT ketamine experiment (median across all subjects and channels). (B) Boxplot across all recordings of TP10 alpha powers showing rapid alpha desaturation within 15 minutes of infusion start.

Channel / Band	TP9	AF7	AF8	TP10
Theta	1.16 (P=0.019)	0.11 (n.s.)	0.11 (n.s.)	0.42 (P=0.113)
Alpha	1.41 (P<0.001)	0.12 (n.s.)	0.17 (n.s.)	0.605 (P=0.113)
Beta	1.19 (P=0.112)	0.03 (n.s.)	0.08 (n.s.)	0.21 (n.s.)

**Table 7.3:** Effect sizes (Cohen's d) and FDR-corrected P-values for the RM-ANOVA time effect for each channel and frequency band.

Parameter	Estimate	SE	t-statistic	P-value
(Intercept)	138	3.0	45.4	0.014
Age	-2.53	0.04	-59.6	0.011
Gender	26.5	0.98	27.1	0.023
Theta minimum TP9	23.8	0.43	55.4	0.011
Alpha minimum TP9	-17.0	0.35	-48.0	0.013
Theta minimum TP10	-11.5	0.47	-24.5	0.026
Alpha minimum TP10	-4.08	0.73	-5.60	0.112
Theta baseline TP9	-2.67	0.22	-12.3	0.051
Alpha baseline TP9	19.0	0.60	31.6	0.020

**Table 7.4:** General linear model predictive of subjective dissociation report ("I felt dissociated."); Overall F-test P=0.0109).

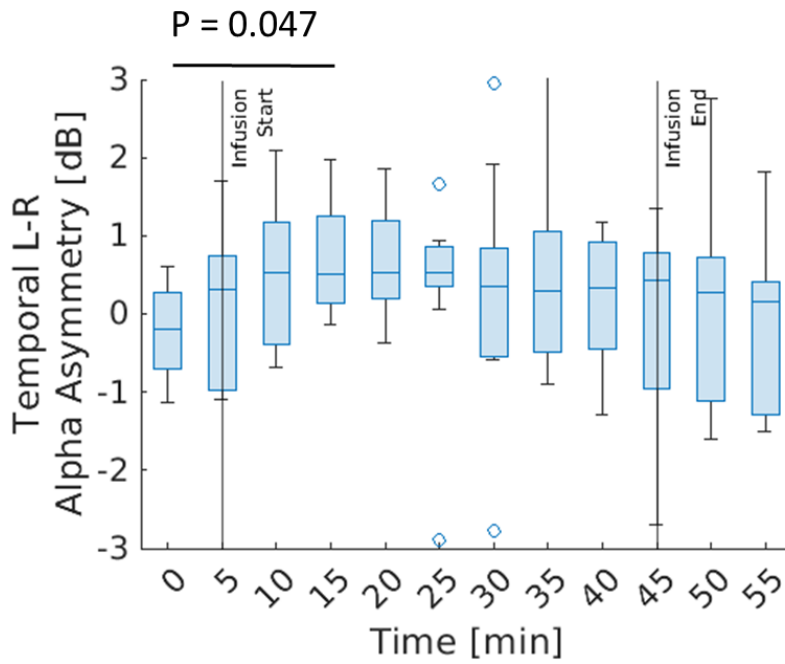


**Figure 7.8:** Boxplot across all recordings of TP9/TP10 left-right alpha asymmetry across the experiment (RM-ANOVA P=0.10).

### 7.3.5 Longitudinal case study

There was not enough longitudinal data in the preliminary dataset to warrant a full longitudinal analysis (only N=4 patients with 2+ recordings), but there was one patient with N=4 recordings, which is presented here as a case study. This patient was in their 'induction' phase, where they received 6 initial weekly IV ketamine infusions at the clinic, of which 4 were recorded (Infusion 2, 4, 5, 6), at doses 0.5mg/kg, and 3 x 0.7 mg/kg.

The patient's Set & Setting questionnaire indicated their anxiety about the upcoming infusion decreased over time, they got more comfortable with the experience, and their relationship with the clinical staff and mood at baseline improved (Table 7.5).

From their dissociation scores, the CADSS-6 total appeared to track the dose change and possible subsequent tolerance development, particularly with the amnesiac (spaced out / memory gaps) items (Table 7.6).

The patient's spectrograms showed a poorly connected AF7 electrode, but a consistent alpha dropout with a possible frontal high beta increase (Figure 7.9).

Question	Infusion 2	Infusion 4	Infusion 5	Infusion 6
Comfortable about upcoming experience	76%	81%	98%	99%
Anxious	58%	21%	0%	1%
Relationship with people	77%	96%	90%	98%
Setting feels good	58%	55%	69%	74%
Feel well-prepared	94%	90%	99%	85%
Good mood	42%	60%	65%	67%
Relationship with main person	83%	93%	99%	97%
Strong expectations	86%	82%	67%	69%
Clear intention	49%	3%	32%	83%

**Table 7.5:** Set & Setting responses from the longitudinal case study.

Question	Infusion 2	Infusion 4	Infusion 5	Infusion 6
Felt dissociated	86%	86%	73%	88%
ASC – No body	49%	80%	82%	83%
ASC – Outside body	40%	0%	89%	68%
ASC – Floating	83%	90%	93%	89%
ASC Total	57%	57%	88%	80%
CADSS – Slow motion	2	2	2	2
CADSS – Unreal	3	4	4	3
CADSS – Body disconnect	3	4	2	4
CADSS – Body size	1	3	1	4
CADSS – Spaced out	2	4	4	2
CADSS – Memory gaps	0	3	2	2
CADSS – Total	11	20	15	17

**Table 7.6:** Dissociation scores from the longitudinal case study.

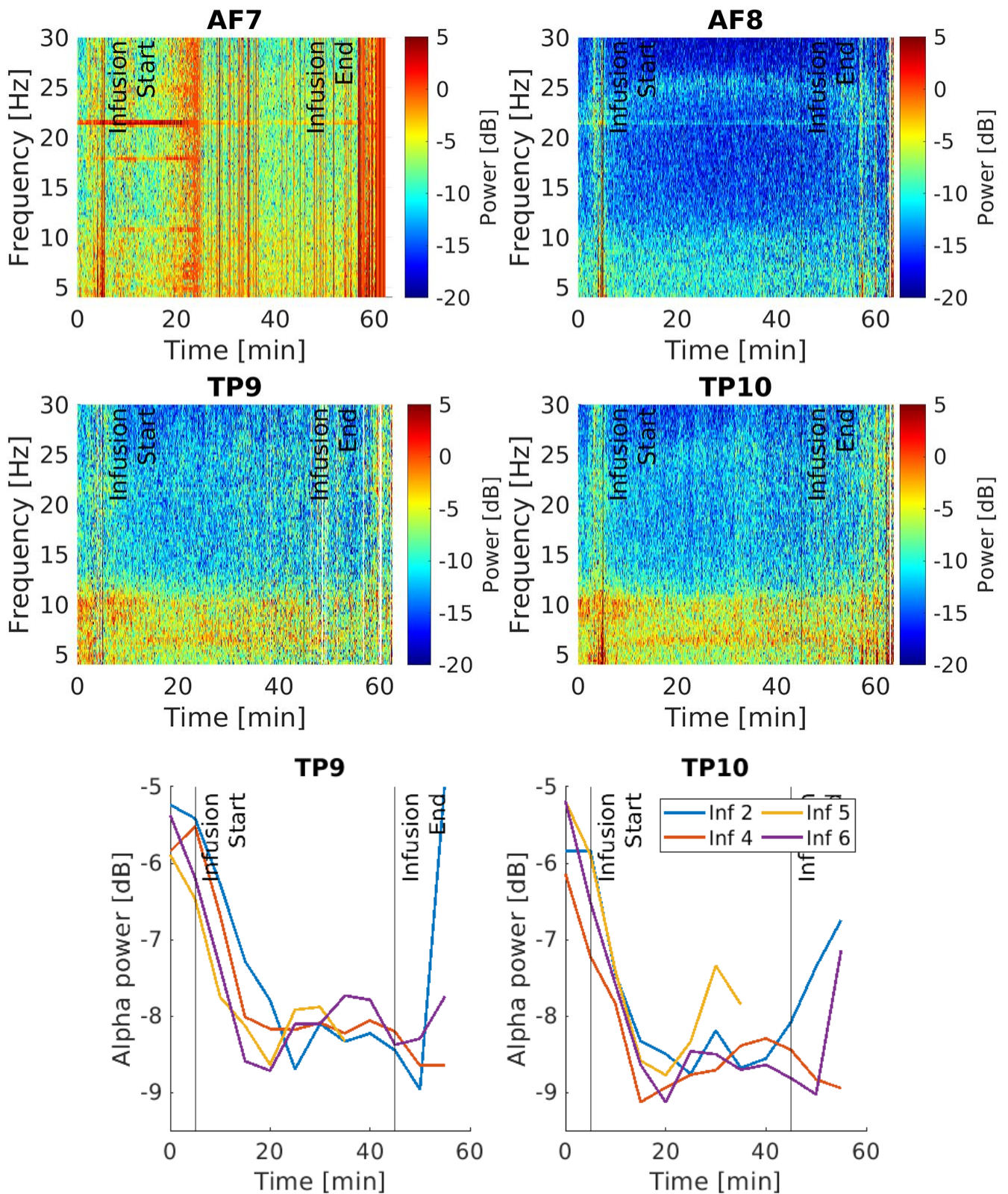


**Figure 7.9: (A)** Median spectrogram for each channel across N=4 longitudinal recordings for one patient. Alpha dropout and possible increased theta / high beta are seen. **(B)** Temporal alpha power in 5-minute segments is consistent across infusions.

## 7.4 Discussion

In this chapter, the study of dissociation in Chapter 6 was extended to patients with treatment-resistant depression using a commercially available low-density EEG device, with the goal of informing future EEG-based ketamine monitoring systems that could optimise dosing.

### 7.4.1 Translating EEG markers of dissociation into the clinic

We chose to work with the 4-channel Muse-S system due to its affordability, ease of use, and prior research validation<sup>447</sup>. Using this system, a decrease in alpha power was indeed observed, most strongly on the TP9 and TP10 electrodes (FCz reference). In a four-infusion case study, this alpha decrease was consistent within a subject. The decreased EEG power, particularly in the alpha band, is thus likely to present a robust, potentially clinically translatable EEG marker of acute ketamine effect. Existing literature and exploratory analyses here suggest aberrant alpha may be linked to the acute dissociative state<sup>378,448</sup>. However, it remains to be seen which aspects of dissociation are most predictive of treatment response, and for which patient groups. In addition to this, a suggestion of alpha asymmetry reversal was observed, though the effect size was small, the result was not significant, and the use of alpha asymmetry as a depression marker has been questioned<sup>449</sup>. Finally, the PPG channel showed a mild increase in heart rate during ketamine infusions consistent with its known sympathomimetic properties<sup>365</sup>.

In this study, a variety of dissociation scores was collected. We also collected a simple patient subjective rating, “I felt dissociated”. In the context of patients with regular ketamine infusions, we felt this was warranted as we hypothesised patients would

understand what dissociation meant to them. Interestingly, this simple subjective rating was most strongly correlated with items related to disembodiment / body disconnect. A limitation is that this may be a function of priming, as during preparatory sessions in the Oxford clinic ideas of mind/body separation are introduced when explaining dissociation. However, it is still notable there was no significant correlation between the subjective rating and the clinically validated CADSS-6. The CADSS is the most commonly used assessment of dissociation during ketamine infusions, but this and previous work suggests it may fail to capture some aspects of dissociation<sup>375</sup>. Items specific to body disconnect (but not e.g. floating<sup>438</sup>) have been previously linked to antidepressant response<sup>436</sup>, highlighting the importance of better dissociation scales. A full phenomenological characterisation of pharmacologically induced dissociation by ketamine and related compounds (e.g. nitrous oxide<sup>450</sup>) would likely help disentangle its relationships to the antidepressant (and sedative or potentially antinociceptive<sup>451</sup>) effects of these compounds.

#### 7.4.2 Notes on feasibility of routine brain-based ketamine monitoring

I spent significant time over several months at the ketamine clinic. This merits a few observations on the possibility of introducing routine brain-based monitoring into ketamine treatments of depression.

Firstly, the Muse-S devices were relatively cheap, quick to obtain, and the majority of patients were keen to be involved in the study. Patients broadly reported the headband did not affect their experience, with the exception of 1 out of 12 patients who chose to withdraw from the study as they felt it affected their treatment routine. It took less than 2 minutes to set up the device each time, and so fitted well into a busy clinical setting. At the analysis stage, the gyroscope data proved very useful in detecting movement-

related EEG artifacts. However, a disadvantage of the dry EEG system was poor performance in people with long or thick hair, especially on the temporal channels. Furthermore, in 3/18 recordings (17%), the headband Bluetooth disconnected towards the end of experiment, causing a few minutes of data loss. A wired, gel-based EEG system may be more robust for routine monitoring, as is used in e.g. the BIS system.

Secondly, whilst it was straightforward to teach clinical staff how to operate the Muse system, due to shortages of staff, data was most consistently collected if a dedicated person was present. In order for EEG monitoring to become more widespread, it would need to be better integrated into existing clinical pathways.

#### 7.4.2 Limitations

The patient study presented here had significant limitations. The first was that routinely collected depression scores were not available due to an ongoing error in the system used by the clinic, so no conclusions can be made about links between the EEG, dissociation, and treatment response. Second, the patients were not ketamine naïve, and had varying numbers of infusions prior to joining the study. This means study results may be affected by possible tolerance development. Third, the clinical nature of the data meant a high artifact burden, which meant analyses of the delta and gamma band were not pursued. Third, the number of patients reported here is low, though the cohort was broadly representative of the Oxford Ketamine Clinic population and data collection is ongoing. Fourth, this was a purely observational, uncontrolled study without randomisation. This meant patients had a variety of ongoing stable secondary psychiatric medications and no causal statements can be made. Finally, the PPG analysis was limited by the slow 10Hz effective streaming rate, which meant pulse rate variability analyses could not be undertaken.





# 8 Concluding remarks

The overarching goal of this thesis was to study brain states brought on by propofol and ketamine. In this final chapter, I bring relevant conclusions together and place them in context, together with considering general limitations and future directions of the work.

## 8.1 Spatiotemporal brain states identified by data-driven methods

The first common theme in the thesis has been exploring spatial, temporal, and spectral properties of brain activity in a given state.

In Chapter 2, the state was that of slow-wave activity saturation (SWAS), which has previously been demonstrated to be a well-defined anaesthetic end point in both experimental and clinical data<sup>31,94</sup>. We saw that the concentration needed to reach SWAS varied across the scalp in ways that correlated with local GABA<sub>A</sub> receptor density. Furthermore, the state of SWAS largely coincided with the Bispectral Index (BIS) range of 40-60, though it had the potential to be more individualised as it did not depend on population metrics unlike the BIS, presenting a more coherent definition of a 'state'. Similarly, SWAS coincided with a drop in brain complexity computed using the Lempel-Ziv-Welch algorithm. Taken together with previous literature on SWAS, this suggests that this end-point (or state) is well-primed for clinical translation and has a sound neurobiological basis. Ongoing research in the group is developing a real-

time expert advisory system based on SWAS and validating it in routine surgical settings<sup>iv</sup>. In Chapter 4, using a newly developed itEMD decomposition framework, we saw that the traditional SWAS range (0.5-1.5Hz) is in fact likely composed of two modes, termed 'low delta' and 'slow' in this thesis, with another 'high delta' mode also present in the low-frequency (<4Hz) range. Travelling waves in these modes had different properties, including low delta waves being more global and of higher amplitude, but also being more frontal than the slow mode waves. Future research should focus on potential differences in physiological and clinical meaning of these modes. Existing literature supports this direction as different types of low-frequency waves have been suggested previously. Firstly, in sleep, type I and type II slow waves have been proposed, with bottom-up type I waves being of large amplitude, steeper slope, and lower frequency, and corticocortical type II waves of opposite properties<sup>123,124</sup>. Secondly, in surgical settings, noxious stimulation can lead to paradoxical delta arousal, potentially due to visceral pain pathway stimulation<sup>299</sup>, with <2Hz and 2-4Hz activity differing in one study<sup>297</sup>. However, slow-wave frequencies can vary between agents (seen e.g. in Chapter 3 here), so it remains to be seen which mode could be optimal for monitoring in a given surgical case. In the theoretical realm, the role of itEMD in explaining harmonics in the data could be pursued<sup>452</sup>, as could a multivariate extension<sup>251</sup>. Given its ability to robustly extract waveform shape, it could also be used to shed light on mechanisms behind waveform shape pathologies, e.g. in Parkinson's disease<sup>226</sup>.

---

<sup>iv</sup> The present author contributed to several aspects of this system including modelling hypnotic-opioid interactions and implementing pharmacokinetic models. This has not been included in the thesis for brevity and coherence.

In Chapters 5 and 6, the state was defined in a data-driven way using Hidden Markov Modelling. Each state had its own distribution of power, connectivity, and transition probabilities. We saw that this approach was able to identify physiologically meaningful states whose presence correlated with drug concentrations. In the case of propofol anaesthesia, the most robust finding was that of reduced switching between states, which was not observed for sub-anaesthetic ketamine administration. The functional repertoire of brain states thus appears to be a reliable correlate of conscious vs unconscious states here, as has been demonstrated for other modalities<sup>32,331–334</sup>. It is possible that at anaesthetic doses of ketamine, the repertoire would again be decreased<sup>183</sup>, in part due to the appearance of slow waves<sup>103</sup>, which may signify a decrease in brain complexity and information processing capacity<sup>118</sup> (as for propofol in Chapter 2 here).

An anteriorised alpha state was characteristic of propofol anaesthesia, whereas ketamine dissociation brought on diminished alpha activity across most of the cortex. Recently, using a dataset of human electrocorticography (ECoG) recordings<sup>424</sup>, the alpha decrease in posterior regions was proposed to be due to inhibition of HCN-1 channels, with prior modelling studies suggesting the hyperpolarisation-activation cationic current ( $I_h$ ) abolishing occipital alpha activity by inhibiting thalamocortical cells<sup>336</sup>. Changes in  $I_h$  have further been proposed as the mechanism behind alpha anteriorisation in propofol GABAergic inhibition. Thus, future work could combine the HMM results from this thesis with maps of local HCN-1 density (or direct causal manipulations of HCN-1, e.g. in pre-clinical models<sup>16</sup>) to test this hypothesis. We did not observe significant increases in scalp theta or delta activity in ketamine dissociation. HCN-1 mediated activity in the 3Hz range in deeper posteromedial

regions has previously been causally linked with dissociation in mice and humans<sup>424,453</sup>. EEG source localisation performs poorly in deep regions, so it may be that this rhythm is not observable on the scalp (at least without a specialist montage).

One further direction for future research would be comparing the present HMM results with alternative ways of finding states in data-driven ways. In recent years, there has been a renewed interest in microstate analysis during anaesthesia<sup>338,454,455</sup>. Hidden Markov Models capture slightly different dynamics with lower correlations of temporal state time courses, but they may also fail to capture very long-term dynamics due to the Markovian assumption<sup>341</sup>. Alternatively, to capture long-range dependencies and relax the HMM assumption of only one state being active at one time, Dynamic Network Modelling (DyNeMo) has recently been proposed<sup>456</sup>.

## 8.2 Translational aspects of EEG analyses

The ultimate goals of neuroscience of anaesthesia are two-fold: one, to explain the anaesthetic state and consciousness in scientific terms for the sake of gaining insight into the human condition, and two, to use this knowledge to improve patient care in routine manipulations of consciousness and physiology during surgery. The second translational goal requires specific methods and analyses, some of which have been explored in this thesis.

First, we saw in Chapter 1 that to achieve SWAS across all of the cortex, frontal monitoring is insufficient. This extends previous work which showed that connected consciousness can occur in presence of classical frontal depth of anaesthesia markers (slow waves, alpha-delta pattern, reduced complexity)<sup>111,112</sup>. Furthermore, in specific cases, consciousness is present despite widespread delta activity, e.g. in Angelman

syndrome<sup>93</sup>. This demonstrates the complexity of the brain and the need to consider more specific markers, including specific locations and spatio-spectro-temporal properties. This was confirmed in Chapter 5 when considering scaling down HMM results to two-electrode montages. Depending on what we want to capture, the best montage may for instance be fronto-parietal (for alpha anteriorisation monitoring) or posterior (for monitoring reduced state switching).

A key aspect of translational work continues to be the development of more individualised markers<sup>457,458</sup>. At the level of a population average, the existing anaesthetic monitors work reasonably, but it is in large part the between-patient variability that means current depth of anaesthesia indices often contradict each other and produce poor advice<sup>459,460</sup>. This was seen in Chapter 2, where the emulated Bispectral Index varied widely between subjects who were all in the well-defined state of SWAS; if anaesthesia had been guided by the BIS, 6/14 of these subjects would have likely experienced either over- or under-anaesthesia. Targeting a specific, individualised state (e.g. SWAS in Chapter 2, an anteriorised alpha HMM state in Chapter 5, or a desaturated alpha state in Chapters 6 & 7) would have the potential to provide expert advice even for subjects at the tails of the population curve, and ongoing research in our group aims to validate this for SWAS during routine surgery.

Another aspect of translation is moving from healthy volunteers to patients. In Chapter 6, alpha desaturation under ketamine was a widespread and robust effect in healthy volunteers. This agrees with previous work on ketamine neurophysiology<sup>89,380</sup>. Importantly, the effect size was large enough and the effect so widespread that we

were able to capture this even in a commercial four-electrode montage in a routine clinical setting in depressed patients, suggesting this EEG marker would be suitable for translation. Recent work has also demonstrated an alpha decrease after the infusion in ketamine patients with a medium-density montage<sup>448</sup>. However, they also saw a similar alpha drop for midazolam. Future work should focus on whether alpha desaturation monitoring can improve clinical outcomes and whether it is distinct in ketamine and midazolam. Due to the lack of depression scores in our study and its observational nature, this was not possible. For now, alpha desaturation remains a marker in search of a use. Another limitation of the ketamine analyses in Chapters 6 and 7 is that there was no EEG data available for the day after the ketamine infusion, which is when the antidepressant response tends to peak. It would be interesting to know if some of the brain dynamics shifts persist beyond the acute effect.

Similarly, in Chapter 3, the increase in heart rate attributable to propofol was present in both younger healthy volunteers and older patients. However, the effect size was notably smaller, and it was overshadowed by bradycardic effects of opioids or sympathetic effects of surgical stimulation. This illustrates the importance of distinguishing statistical and clinical significance. When considered as a scientific question, it really appears propofol increases the heart rate by downregulating parasympathetic cardiac control, at least at moderate doses. However, the clinical significance is less clear. It is no wonder literature on this phenomenon has been mixed, chiefly with laboratory and clinical research at odds, as the clinical setting includes concomitant medication that often dwarfs the propofol effect. Future research should consider whether markers identified are robust and individualizable enough to be translatable.

Finally, several publications have recently advocated for optimising low-density EEG electrode location selection to aid clinical translation<sup>326,327</sup>. Rather than considering all possible montages as was done in Chapter 5, future work should focus on the full multi-objective optimisation problem, perhaps using a genetic algorithm<sup>326–328,461</sup>. Considering how different optimal montages were depending on the goal in Chapter 5, together with optimal montages differing across sleep<sup>328</sup>, epilepsy<sup>327</sup>, and motor imagery classification<sup>461</sup> both in terms of numbers of channels and their location, it is likely this will be a highly domain-specific problem.

### **8.3 Cardiac influences on brain states**

Possessing a bodily existence has been called the brain's 'first prior'<sup>462</sup>. Amongst the plethora of interoceptive signals, the heart is privileged in providing a continuous, regular ascending input and engaging in an active dialogue with the brain through vagally mediated feed-forward and feed-back signalling. Some have gone as far as placing the bodily basis of selfhood in the neural monitoring of visceral signals, emphasising the heart<sup>463</sup>. In this thesis, cortico-cardiac coupling was demonstrated in Chapter 3, with slow waves being preferentially preceded by a heartbeat, similarly to heartbeat coupling previously observed in sleep<sup>120</sup>. We hypothesise that this is due to a common brainstem generator influencing both slow waves and the heart. However, Mensen et al argued this could be a direct result of heartbeats, similarly to how auditory stimuli can modulate slow waves in NREM sleep<sup>464</sup>. Brain-heart interactions have recently been proposed to be involved in neurobiology of consciousness itself, modulating contents of consciousness, contributing to cognition, and even potentially providing a biomarker of phenomenal consciousness<sup>108,465</sup>. Future work should



consider heartbeat-slow wave coupling in patients with pacemakers to test the common generator hypothesis.

Using Hidden Markov Modelling in a novel way to include the ECG signal, in Chapter 5 we extended the definition of a 'state' to include the cardiac state. This worked surprisingly well given how different frequency dynamics of EEG and ECG are. EXG-HMM captured the increase in heart rate with anaesthesia as per Chapter 3, and even potentially distinguished between QRS complexes and inter-beat intervals when considering the ECG power spectra. In future, this could be investigated as a way to automatically extract both brain and heart dynamics from the same dataset and to capture heartbeat-evoked activity or bidirectional cortico-cardiac interactions. The present dataset was limited to a single-lead ECG and including full 12-lead ECG for spatial information may provide more insights.

As expected for a sympathomimetic agent, ketamine increased the heart rate, both in a volunteer case study and in a pilot patient study. The case study of heartbeat-evoked potentials showed a decreased HEP amplitude as the infusion progressed, suggesting that ketamine may impair cardioception. The analysis was limited by not having access to ECG data for all patients. In the future, a full ECG-EEG analysis could test the 'dissociation by diminished interoception' hypothesis. Surprisingly for a dissociative agent, literature on this is scarce. One study of heartbeat counting (a measure of interoceptive accuracy) did not find any changes after a ketamine infusion<sup>411</sup>. On the other hand, in patients with depersonalization/derealization disorder (DPD) which overlaps in dissociative phenomenology with ketamine, HEP amplitude during a heartbeat perception task was higher in healthy controls than DPD patients, suggesting impaired cortical representation of afferent cardiac signals<sup>403</sup>. As was argued in Chapter 6, this and other research on dissociation may be limited by the

psychometric instruments available, with the CADSS-6 and 5D-ASC disembodiment scores being unrelated to each other, and a role suggested for a simple subjective report, particularly in patients familiar with the dissociative state. The role of heart-brain interactions in altered states of consciousness should be a subject of future research, particularly given the salience of heart signals in as wide of subjects as interoception<sup>344</sup>, attention<sup>406</sup>, anxiety<sup>466</sup>, and emotions<sup>343</sup>. This could be extended to wider monitoring of interactions between the body and the brain, with respiration coupling having been investigated extensively<sup>467</sup>. After all, we are (hopefully) not just brains in a vat.

Anaesthetics present treasured assets in medicine and neuroscience of consciousness. In their tranquil embrace, we find a unique opportunity to study and repair the human condition. Depending on the combination of drugs given, we can manipulate the brain to one full of synchrony, one with a mind disconnected from the body, one that dreams, or one that is blissfully unaware.

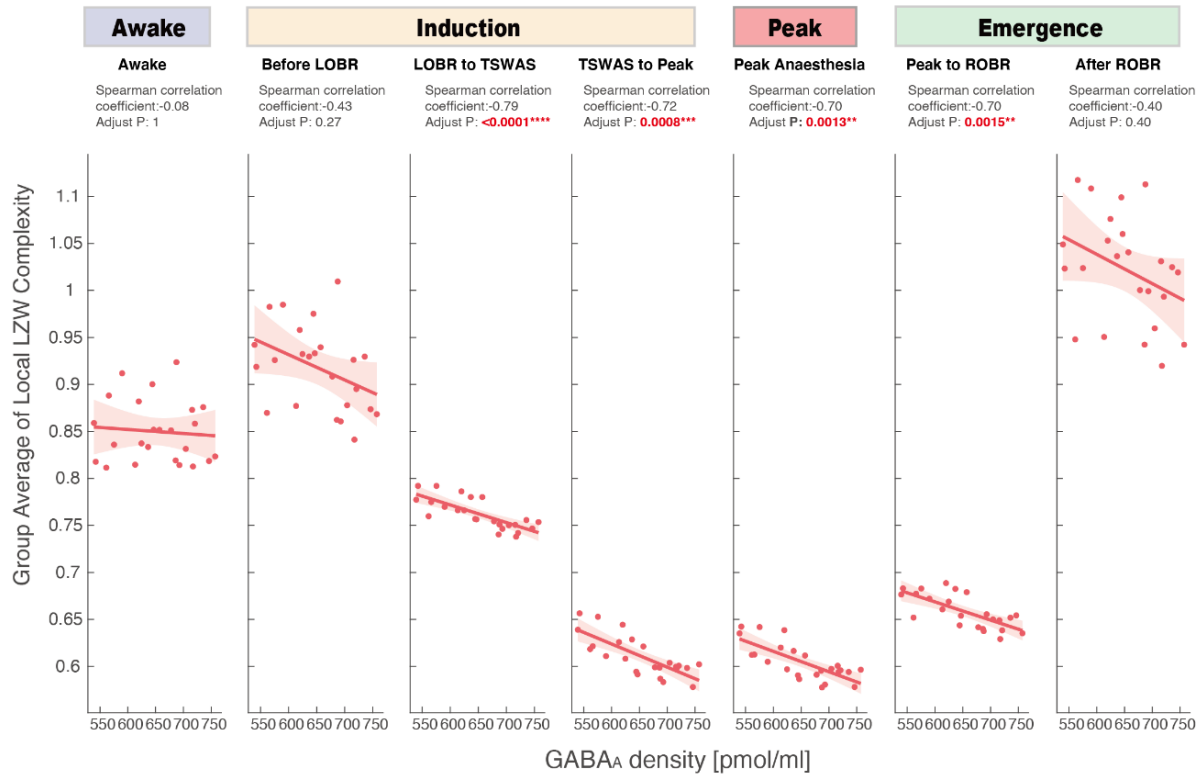
The work of this thesis was to continue uncovering waves in the unconscious brain's *mare incognitum* and to navigate the state space available in a way that may one day improve patients' lives. To quote Bertrand Russell<sup>468</sup>:

"A little of this, but not much, I have achieved."

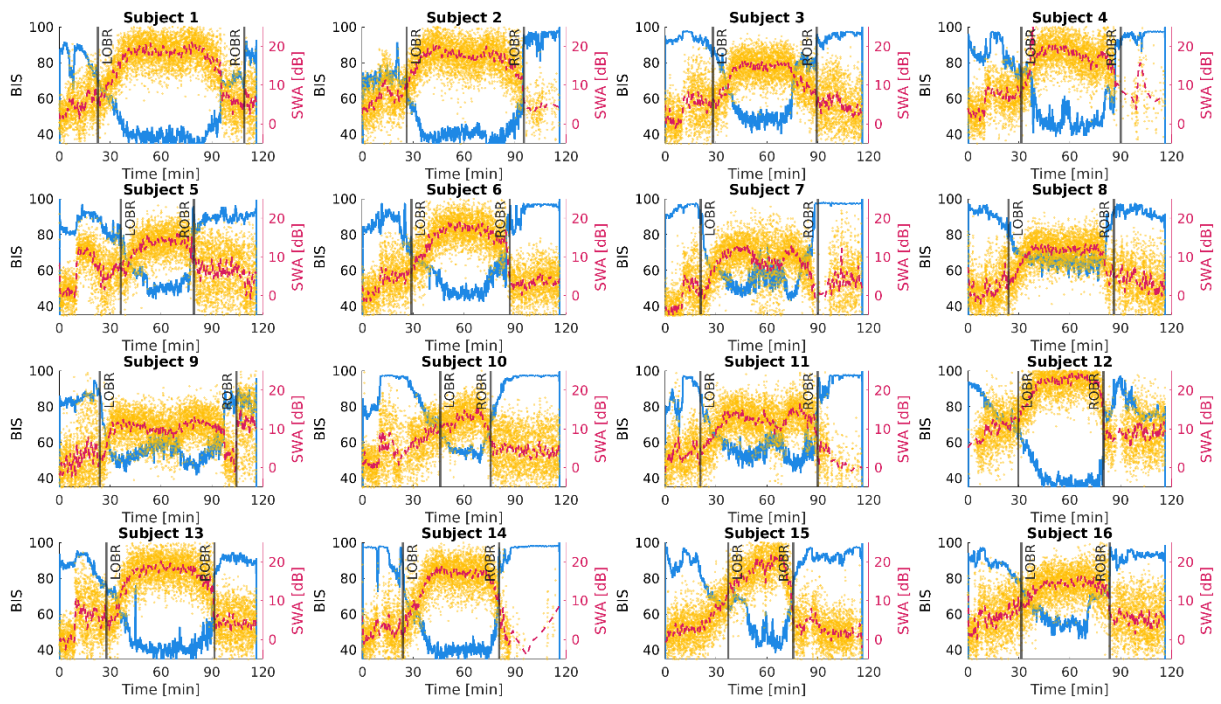


# 9 Appendices

## Appendix 1: Supplementary Figures to Chapter 2

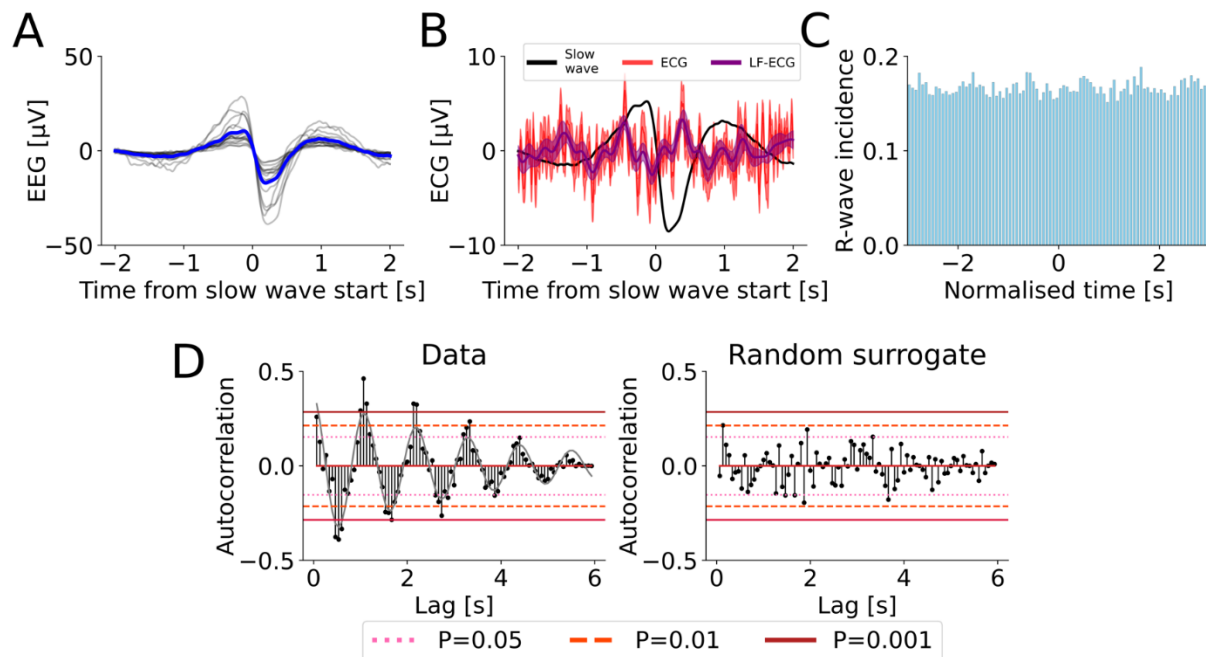


**Supplementary Figure 2.1:** Correlation between group-average local complexity and GABA<sub>A</sub> receptor density across experimental stages. A significant negative correlation is present during stages without behavioural responsiveness. Figure reproduced from Dr Di Zang with permission.

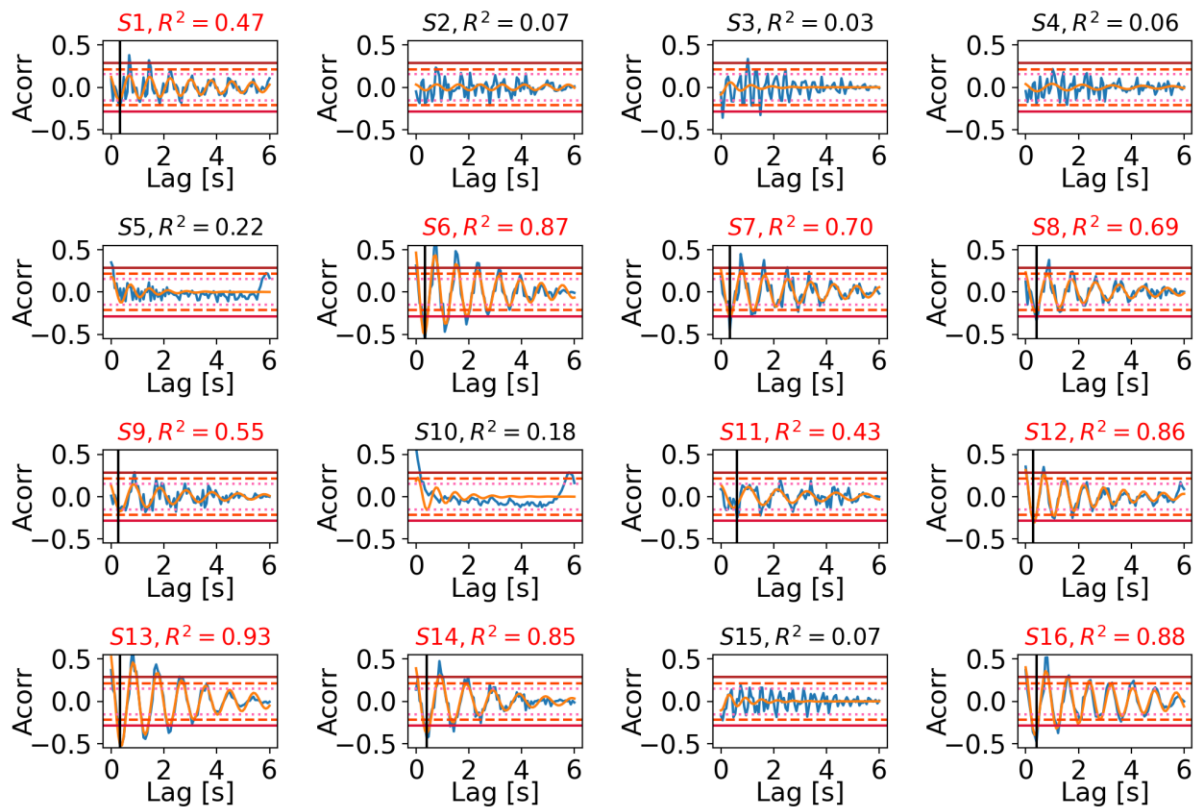


**Supplementary Figure 2.2:** BIS index values and slow-wave power throughout the experiment for each subject in the study.

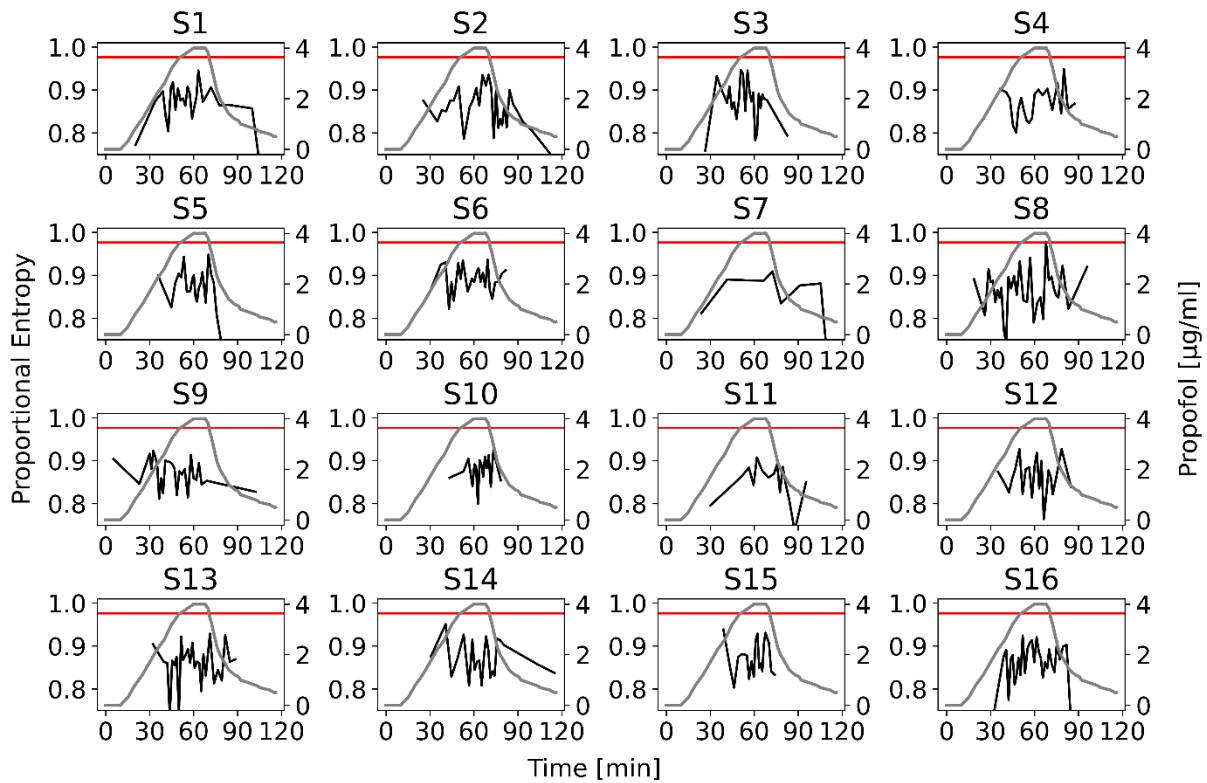
## Appendix 2: Supplementary Figures to Chapter 3



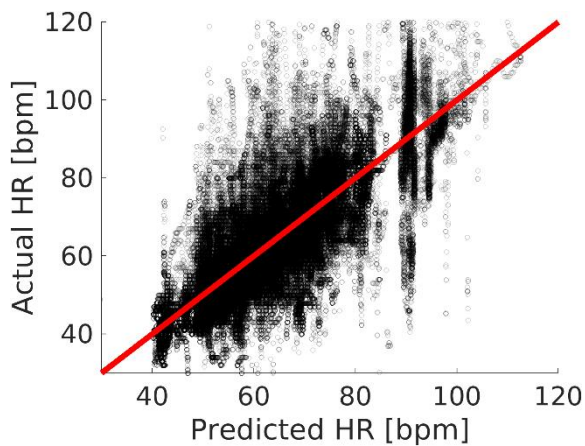
**Supplementary Figure 3.1:** Group-level cortico-cardiac coupling in healthy volunteers. **(A)** Mean slow wave detected (blue) with each subject mean in grey. **(B)** Group-average ECG (red – broadband, purple – 0.5Hz-1.5Hz only) time-locked to slow-wave (black) onset. The ongoing low-frequency ECG oscillation is present at the group-level. **(C)** Group-mean histogram of R-wave timings relative to slow-wave onset, with time for each subject adjusted for their mean heart rate. Individual heartbeats preferentially occur in phase with the slow wave. **(D)** Autocorrelation of (C) shows clear oscillatory structure (left). This is significant compared to P-values derived from N=1000 uniformly random surrogate timing distributions.



**Supplementary Figure 3.2:** Autocorrelation of RS histograms in each participant (blue) and a decaying sine fit (orange). 10 out of 16 participants showed a significant ongoing low-frequency ECG oscillation (red titles).

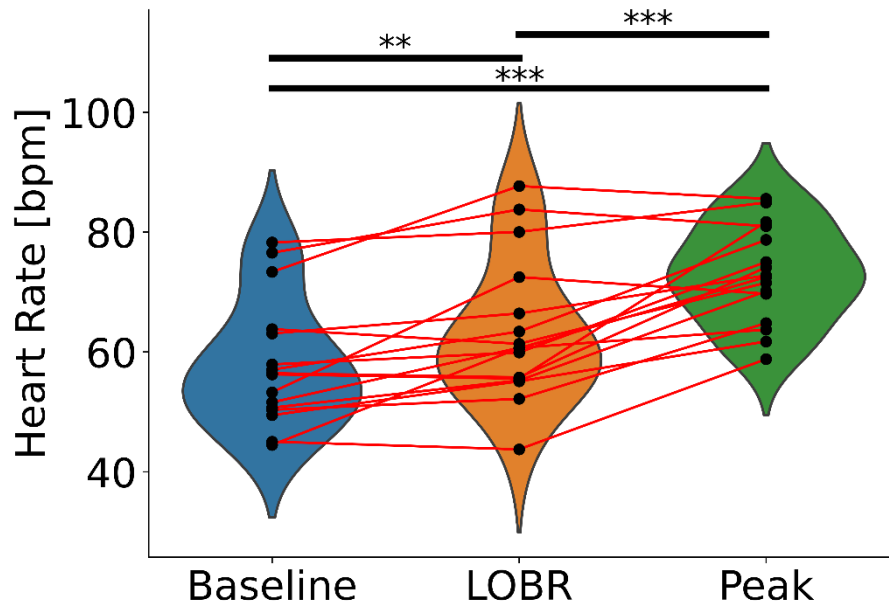


**Supplementary Figure 3.3:** Dose-dependence of cortico-cardiac coupling. Lower entropy means more significant coupling between slow-wave onset and the preceding heartbeat. No changes were observed between different propofol doses.



**Supplementary Figure 3.4:** Observed heart rate (HR) vs that predicted by a general linear model in an older, clinical population (see Main Text for model details).





**Supplementary Figure 3.5:** Heart rate in ultra-slow propofol infusion increases from baseline to loss of behavioural response to auditory and laser pain stimuli (LOBR) and peak anaesthesia. \*\* indicates Bonferroni-corrected paired t-test  $P < 0.01$ , \*\*\* indicates  $P < 0.001$ .

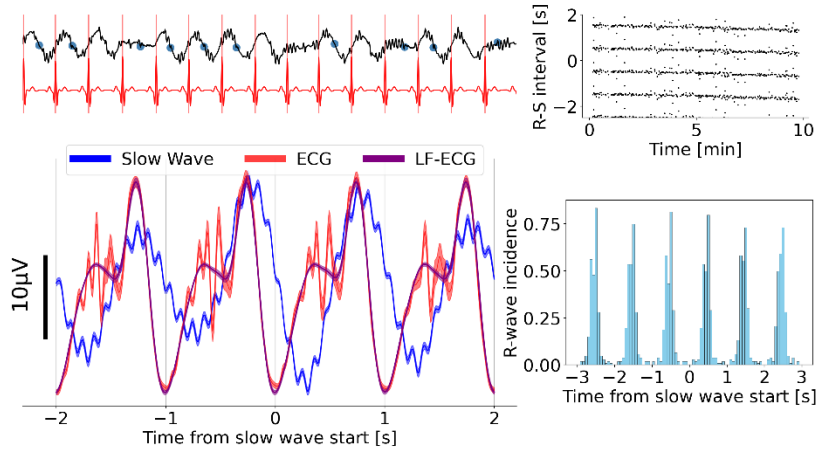
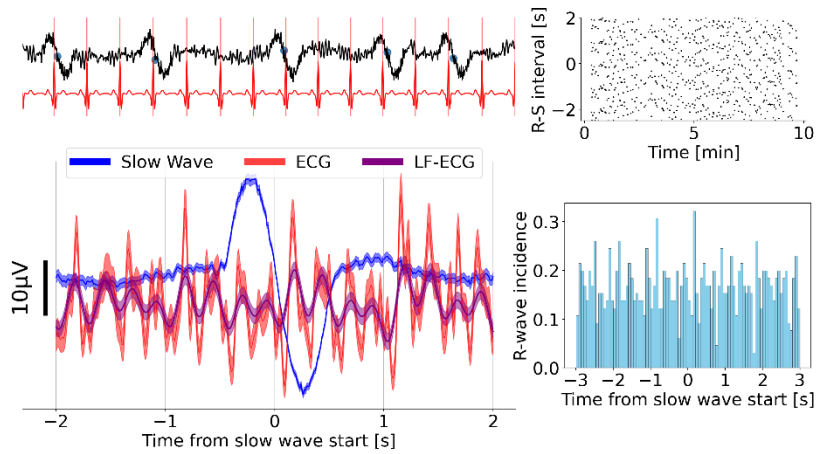
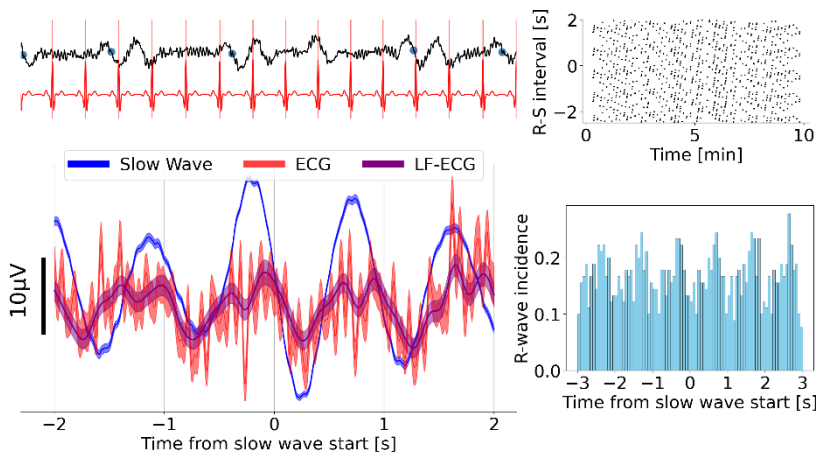
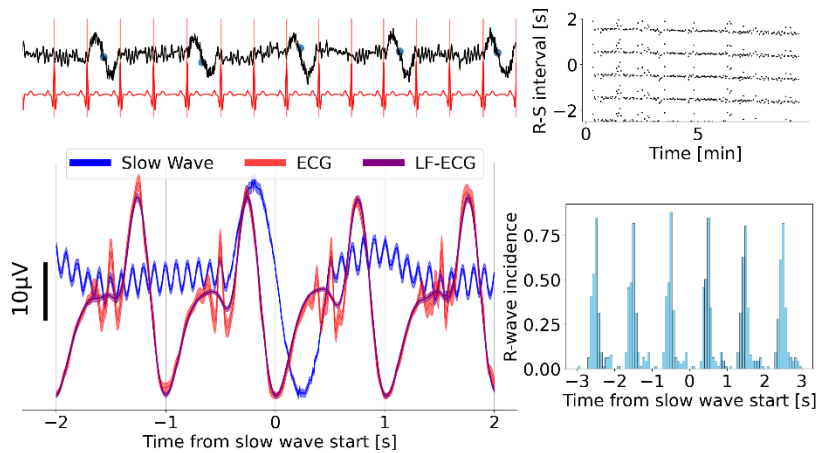
### 9.2.1 Understanding cortico-cardiac coupling

I performed extensive simulations to understand where the coupling may come from. Naively, one may wonder if two oscillations both around 1Hz (heartbeat and slow waves) trivially appear coupled because of their similar frequency. To study this, I simulated 10 minute EEG and ECG recordings with 100Hz sampling rate. The ECG was simulated with the neurokit2 module to have HR=60bpm (SD 1bpm). The EEG was simulated as the sum of aperiodic noise with spectral exponent -1.5 (amplitude 10 $\mu$ V), a bursty alpha oscillation (frequency 10Hz, probabilities to enter and exit burst 0.5, amplitude 5 $\mu$ V), and different types of slow waves.

First, slow waves were modelled as a bursty oscillation at 1Hz, perfectly coherent with the heart rate. Trivially, this causes high coupling (Supplementary Figure 3.6A, entropy=0.502). Next, slow waves were kept at 1Hz, but were inserted at random times. This destroys the coupling despite having the same frequency (Supplementary Figure 3.6B, entropy=0.982). Then, slow waves were again made a coherent oscillation, but this time at 1.1Hz. This also makes the coupling much weaker (Supplementary Figure 3.6C, entropy=0.981). Finally, the 1.1Hz slow waves were inserted every 3s. This recovers the coupling despite different frequencies of slow waves and heart rate (Supplementary Figure 3.6D, entropy=0.650).

In short, as the frequency of heart rate and slow waves is not exactly in an integer relationship, low entropy points to each slow wave being significantly coupled to a heartbeat.

At a high level, these simulations demonstrate the Main Text results show genuine coupling, and are not just methodologically trivial due to similar heart rate and slow wave frequencies.

**A****B****C****D**

**Supplementary Figure 3.6:** Explaining coupling between slow waves and R-waves.

**(A)** Two ongoing 1Hz oscillations with constant phase difference are trivially coupled.

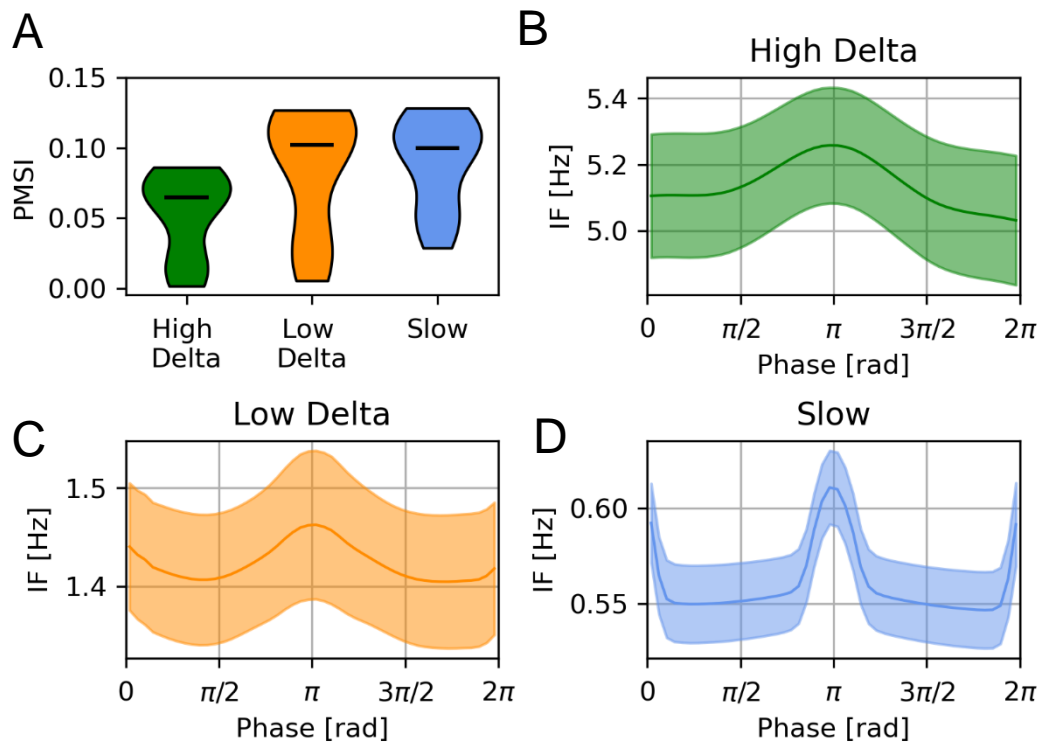
**(B)** Coupling is destroyed if slow waves occur at random times, even if both oscillations

are at 1Hz. **(C)** Coupling is also much weaker if frequencies do not match even slightly,

here 1Hz for heartbeats and 1.1Hz for ongoing slow waves. **(D)** Coupling is restored

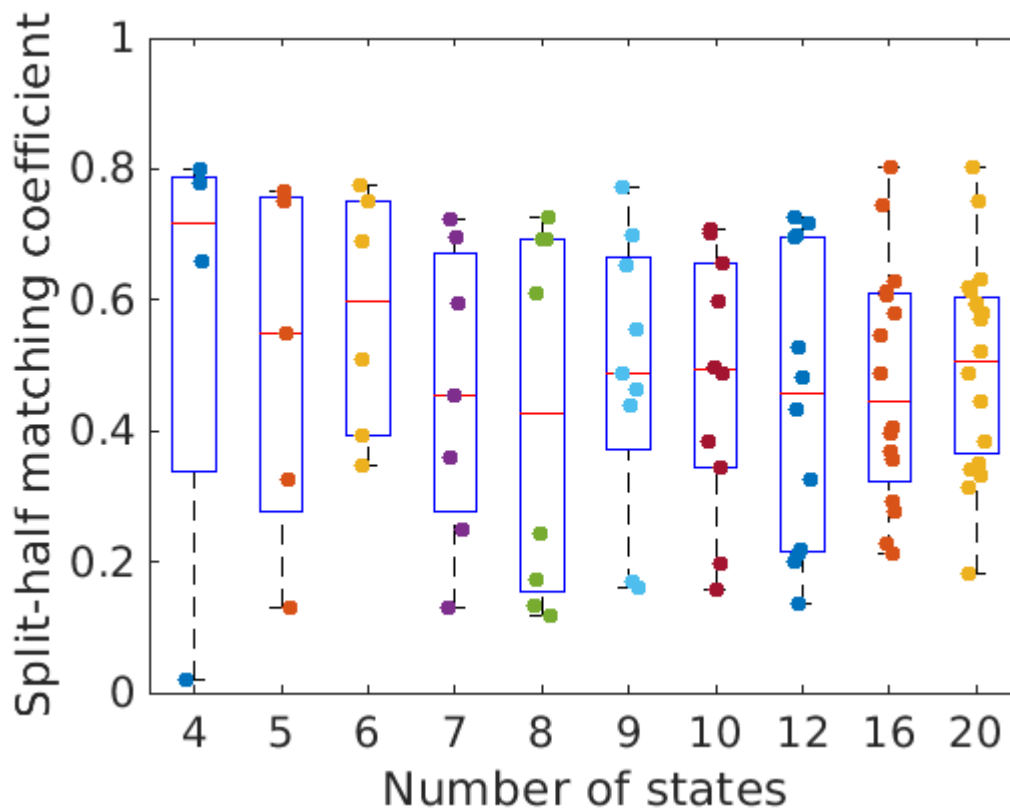
if each slow wave is related to individual heartbeats, even if their frequency is different.

## Appendix 3: Supplementary Figures to Chapter 4



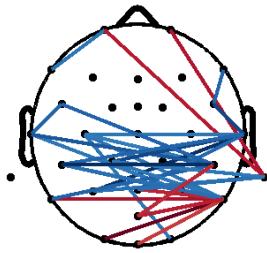
**Supplementary Figure 4.1:** Further waveform properties of itEMD modes in propofol data. **(A)** Pseudo mode-mixing index (PMSI) was low for all low-frequency modes ( $<0.15$ ), suggesting good decomposition performance. **(B) – (D)** Mean phase-aligned instantaneous frequency across all waves and subjects (mean  $\pm$  standard error across subjects shaded), All waves had slightly faster downward slopes around  $\pi$  phase, but this was most prominent for the slow mode.

## Appendix 4: Supplementary Figures to Chapter 5

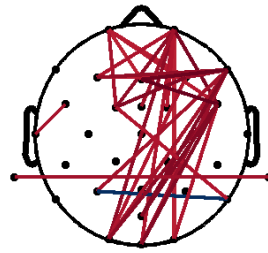


**Supplementary Figure 5.1:** Split-half validation across 4-20 HMM states. K=6 states have the largest proportion of well-matched states in both halves (Matching Coefficient > 50% without any very low matching coefficient states).

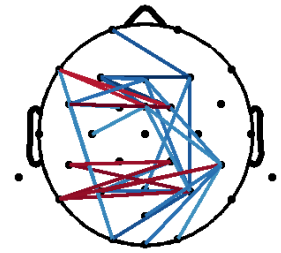
**State 1**



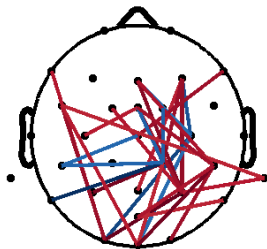
**State 2**



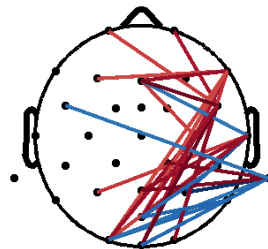
**State 3**



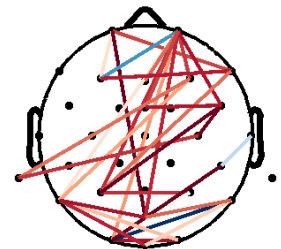
**State 4**



**State 5**

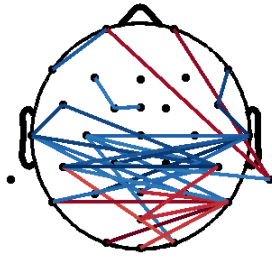


**State 6**

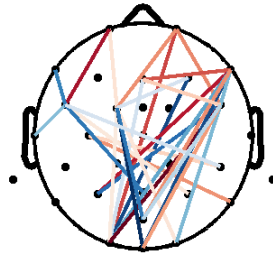


**Supplementary Figure 5.2:** Scalp connectivity maps (broadband coherence) in each state in the full 32-channel EEG HMM model.

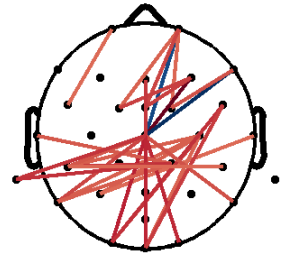
**State 1**



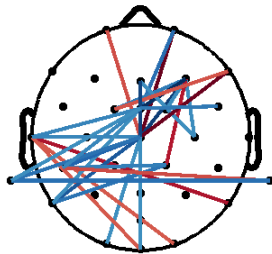
**State 2**



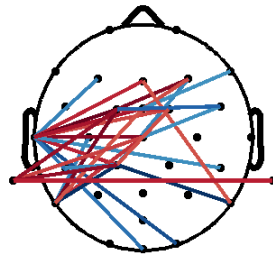
**State 3**



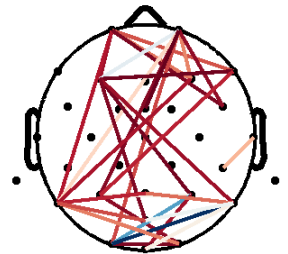
**State 4**



**State 5**

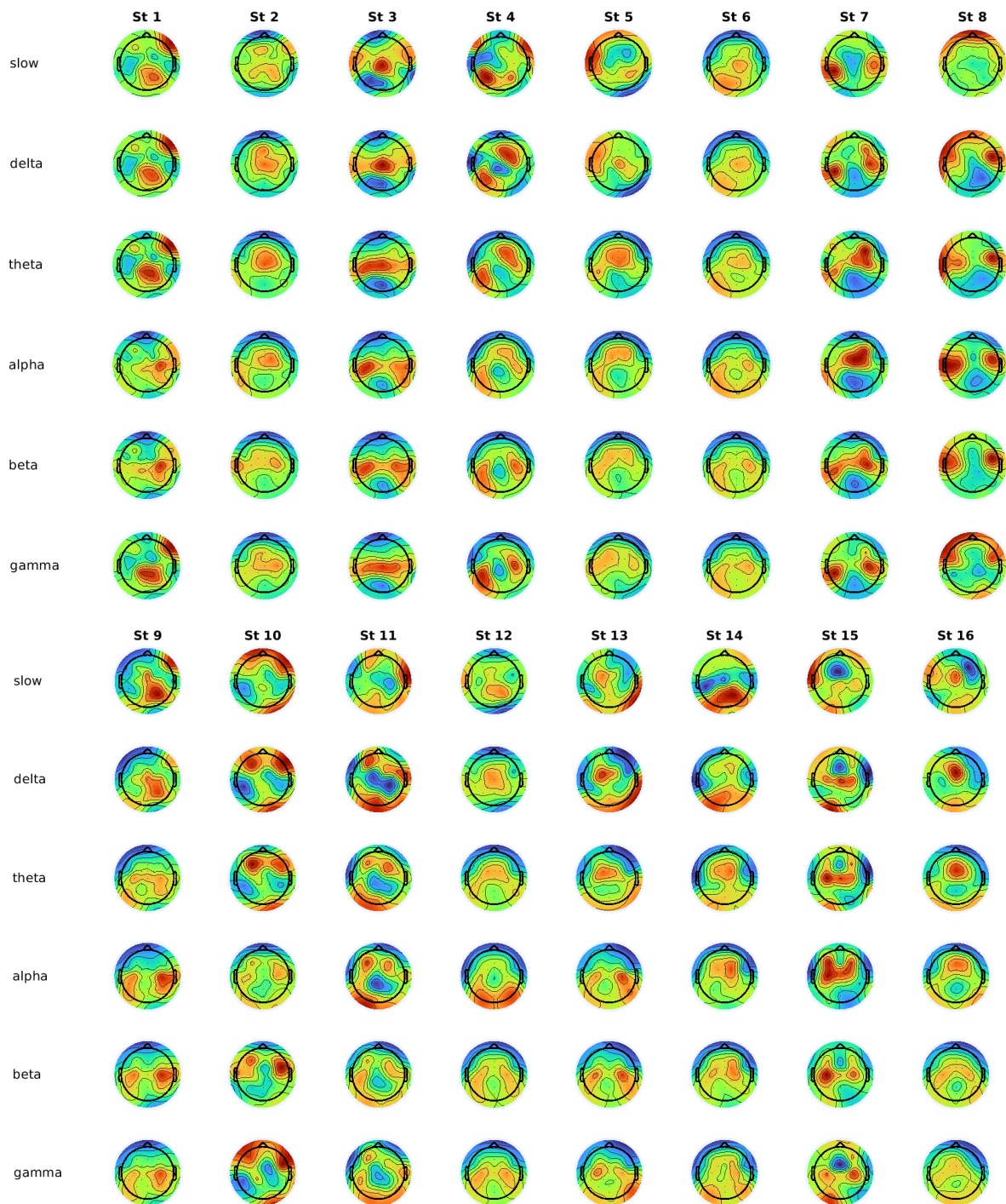


**State 6**

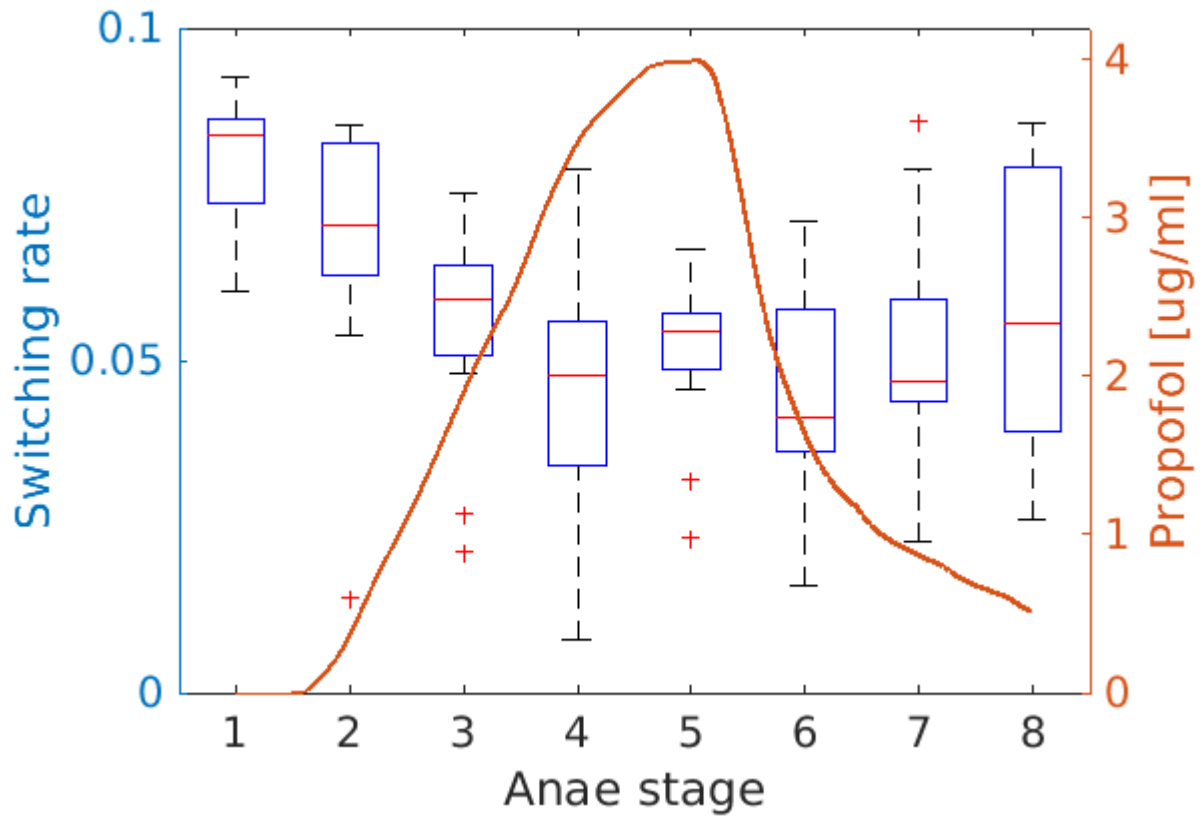


**Supplementary Figure 5.3:** Scalp connectivity maps (broadband coherence) in each state in the EXG-HMM (EEG + ECG) model.

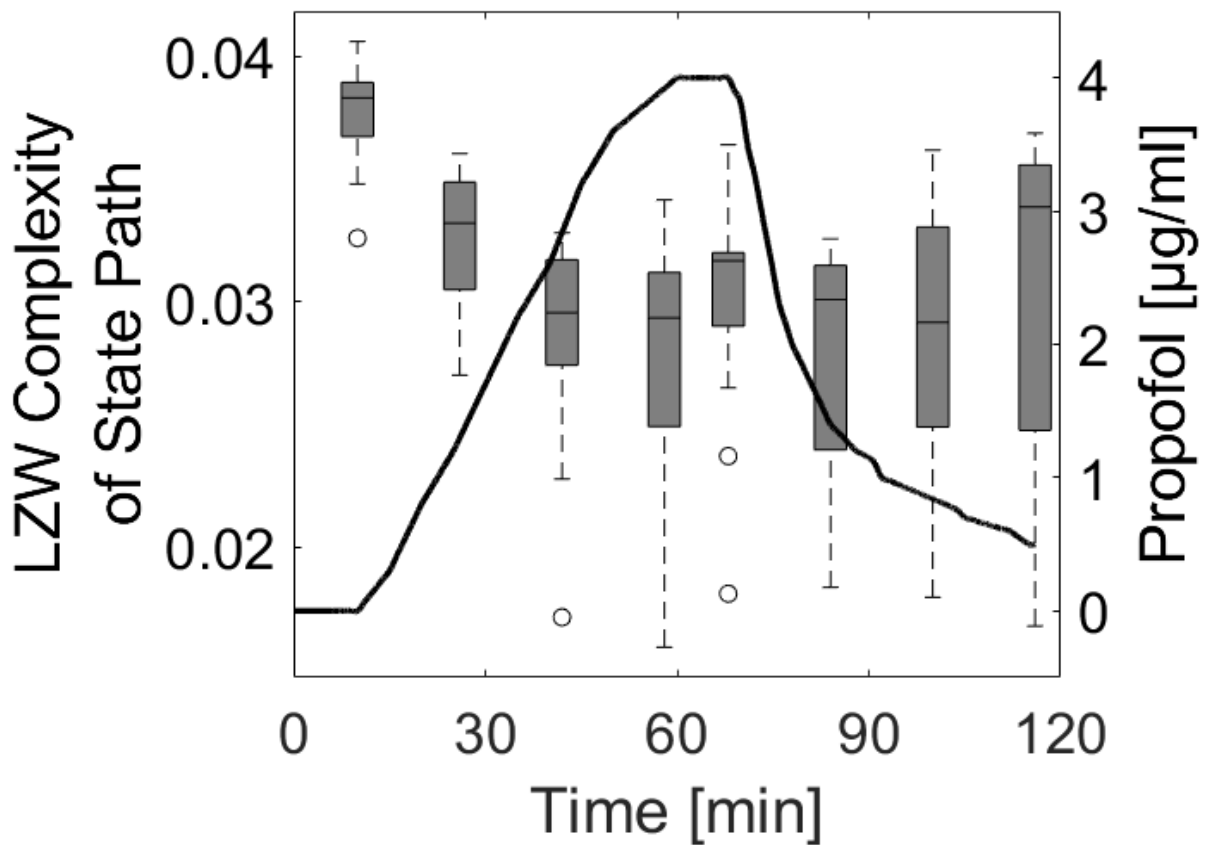




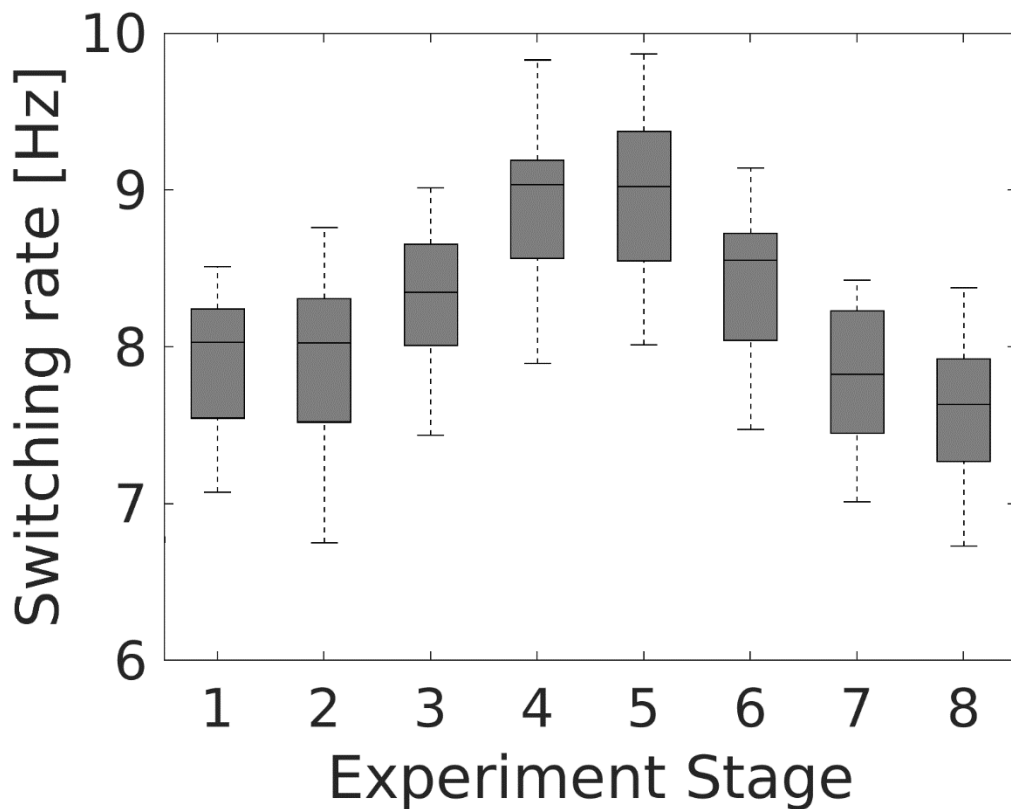
**Supplementary Figure 5.4:** Power topographical maps for each state in the K=16 state HMM model. States are qualitatively similar to the K=6 state model (e.g. artifact State 8, occipital alpha States 6 / 12, motor alpha/beta State 9, anterior alpha States 7/14).



**Supplementary Figure 5.5:** Switching rate in the K=16 state HMM run. Similarly to K=6 states (Figure 5.3B), switching rate (boxes) differs between experimental stages and follows the propofol concentration (orange; repeated measures ANOVA  $P < 0.01$ ).



**Supplementary Figure 5.6:** Lempel-Ziv-Welch complexity of the state switching paths across propofol concentrations. For this analysis, the Viterbi path derivative was binarized such that each state switch in the time-series represented a 1, 0 otherwise. There was a significant difference in this LZW Complexity between experimental stages (repeated measures ANOVA  $F=10.6$ ,  $P<0.001$ ). For more about LZW Complexity, see Chapter 2.

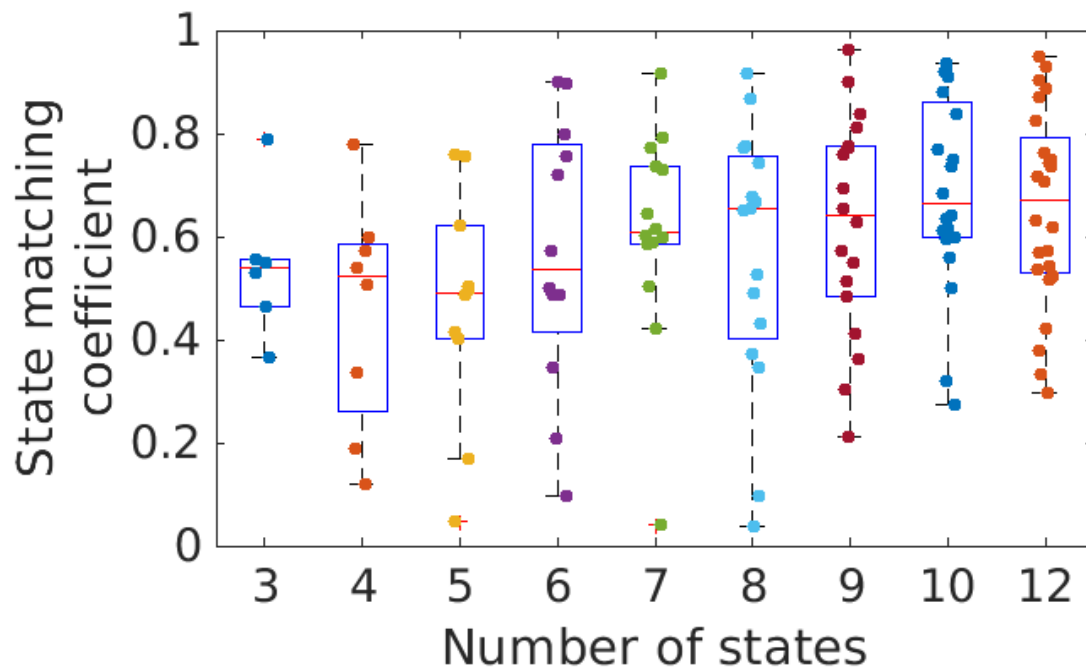


**Supplementary Figure 5.7:** Median switching rate across subjects for the N=31 low-density runs with 1 EEG channel (best channel for each column in the switching rate F-value matrix, c.f. Figure 5.9) and 1 ECG channel. The effect of propofol stage on switching rate was more significant with the ECG channel included (Wilcoxon  $P=0.0031$  vs single EEG channel only), but the effect direction was opposite (switching rate increased), likely due to the model being driven by the heart rate increase.

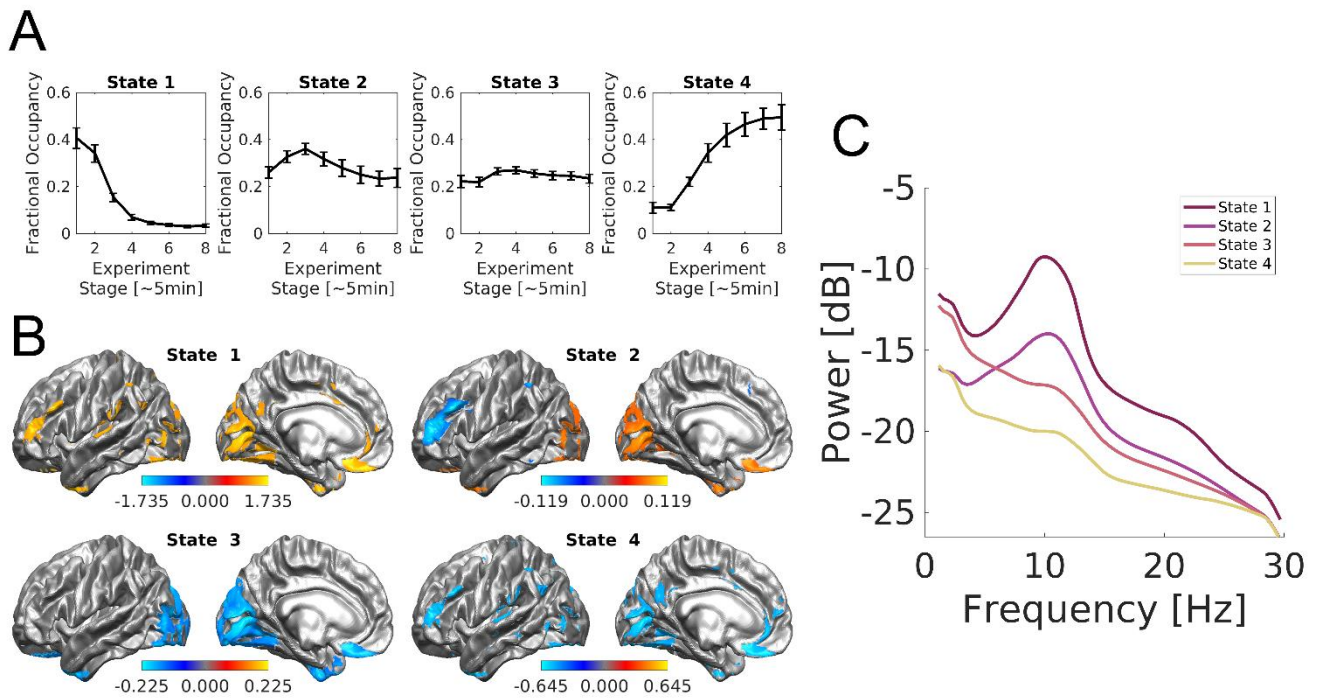
Result	Main Run	Re-run 1	Re-run 2	Re-run 3	Re-run 4	Re-run 5	Mean
Switching rate ANOVA F-value	10.1	6.2	7.4	5.5	8.9	8.5	7.77
FO ANOVA, propofol effect F-value	5.65	10.03	7.33	20.32	2.8	2.22	8.06
FO ANOVA, state effect F-value	5.76	8.33	0.89	11.45	0.6	21.03	8.01
FO ANOVA, propofol*state F-value	7.01	12.42	9.07	25.16	3.47	2.75	9.98
State 1 FO correlation with ESC	-0.27	-0.35	-0.33	-0.316	-0.33	-0.3	-0.32
State 3 FO correlation with ESC	0.22	0.33	0.21	0.35	0.24	0.17	0.25
State 5 FO correlation with ESC	-0.46	-0.41	-0.39	-0.48	-0.29	-0.5	-0.42
Time in State 2 until LOBR / $C_{LOBR}$ correlation	0.725	0.714	0.718	0.732	0.743	0.771	0.73
Time in State 5 until LOBR / $C_{LOBR}$ correlation	0.8	0.604	0.46	0.575	0.525	0.614	0.60
Time in State 2 until LOBR / $C_{SWAS}$ correlation	0.706	0.301	0.235	0.613	0.411	0.266	0.42

**Supplementary Table 5.1:** Results for K=6 states, re-run to validate against stochastic variability. All main results remain in the same direction, and except for one poor run (Run 5) and the last two correlations, results also remain significant after multiple comparisons correction (corrected  $P > 0.05$  in red).

## Appendix 5: Supplementary Figures to Chapter 6

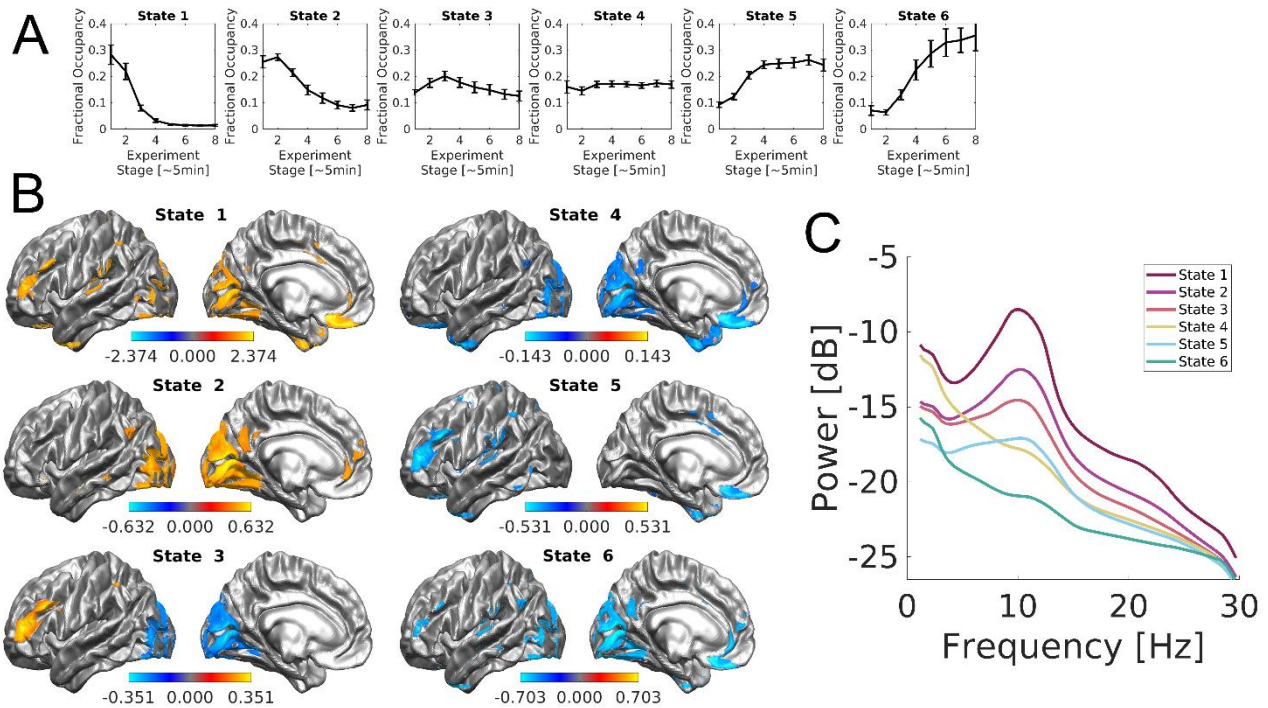


**Supplementary Figure 6.1:** Split-half validation across 3-12 HMM states.  $K=7$  states have the largest proportion of well-matched (Matching Coefficient  $> 50\%$ ) states in both halves. The only state not well-replicated was lowest-power State 7, which was most present in  $N=3$  subjects that happened to all be in the first half of the dataset.



**Supplementary Figure 6.2: (A) Fractional occupancies, (B) State maps and (C) Power spectra for  $K = 4$  HMM states. The main results from the Main Text (one high-power alpha state that gets suppressed by ketamine, one high-delta state, a medium-alpha state, one low-power state that subjects spend more time in under ketamine) holds across different state numbers.**

Correlation between fractional occupancies in State 1 / State 2 and disembodiment:  
Spearman  $\rho = -0.071$  ( $P=0.81$ ).



**Supplementary Figure 6.3: (A) Fractional occupancies, (B) State maps and (C) Power spectra for  $K = 6$  HMM states. The main results from the Main Text (one high-power alpha state that gets suppressed by ketamine, one high-delta state, several medium-alpha states, one low-power state that subjects spend more time in under ketamine) holds across different state numbers.**

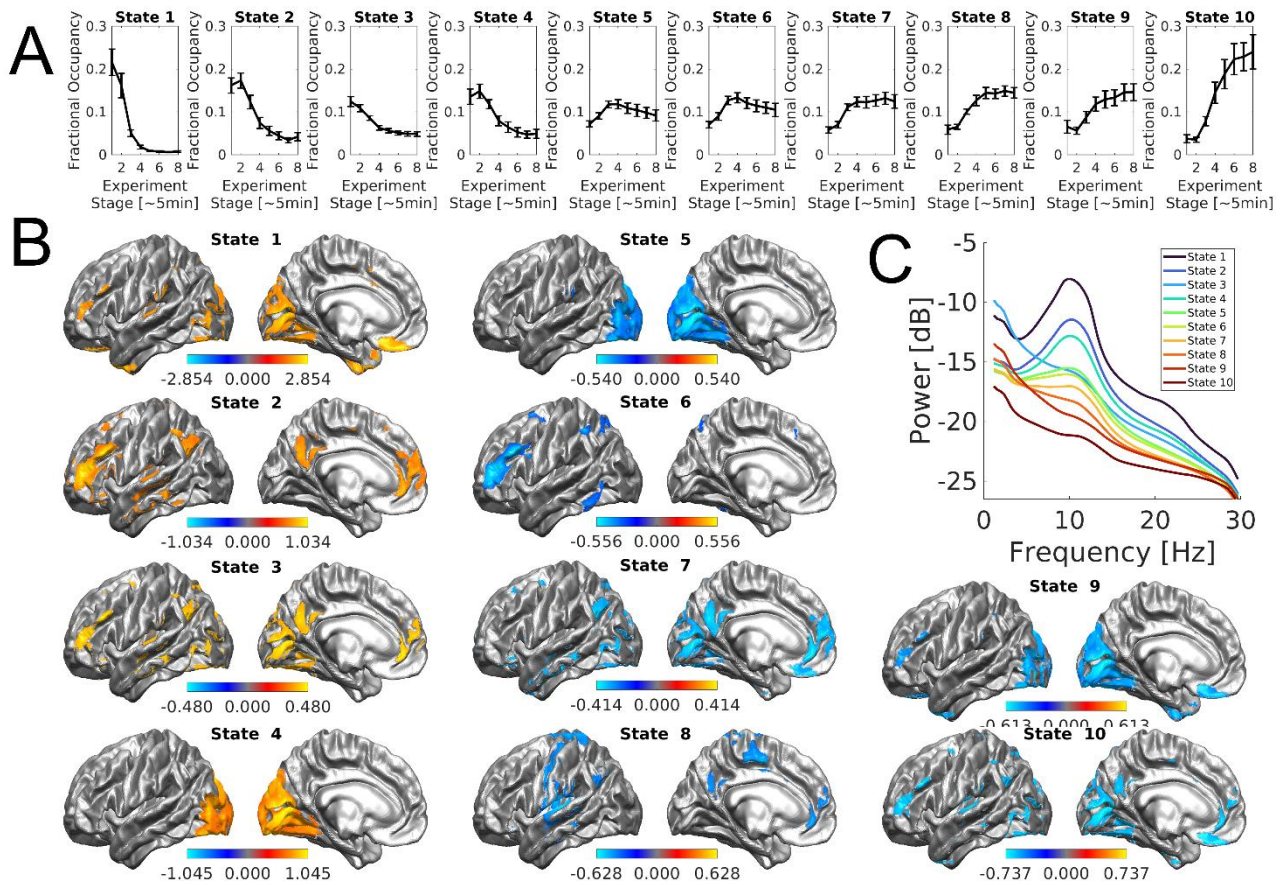
Correlation between fractional occupancies in State 1 / State 2 and disembodiment:  
Spearman  $\rho = -0.104$  ( $P=0.72$ ).

Same correlation for  $K = 7$  states but re-running due to stochastic state optimisation:

Run 1:  $-0.568$  ( $P=0.034$ ), Run 2:  $-0.260$  ( $P=0.37$ ),

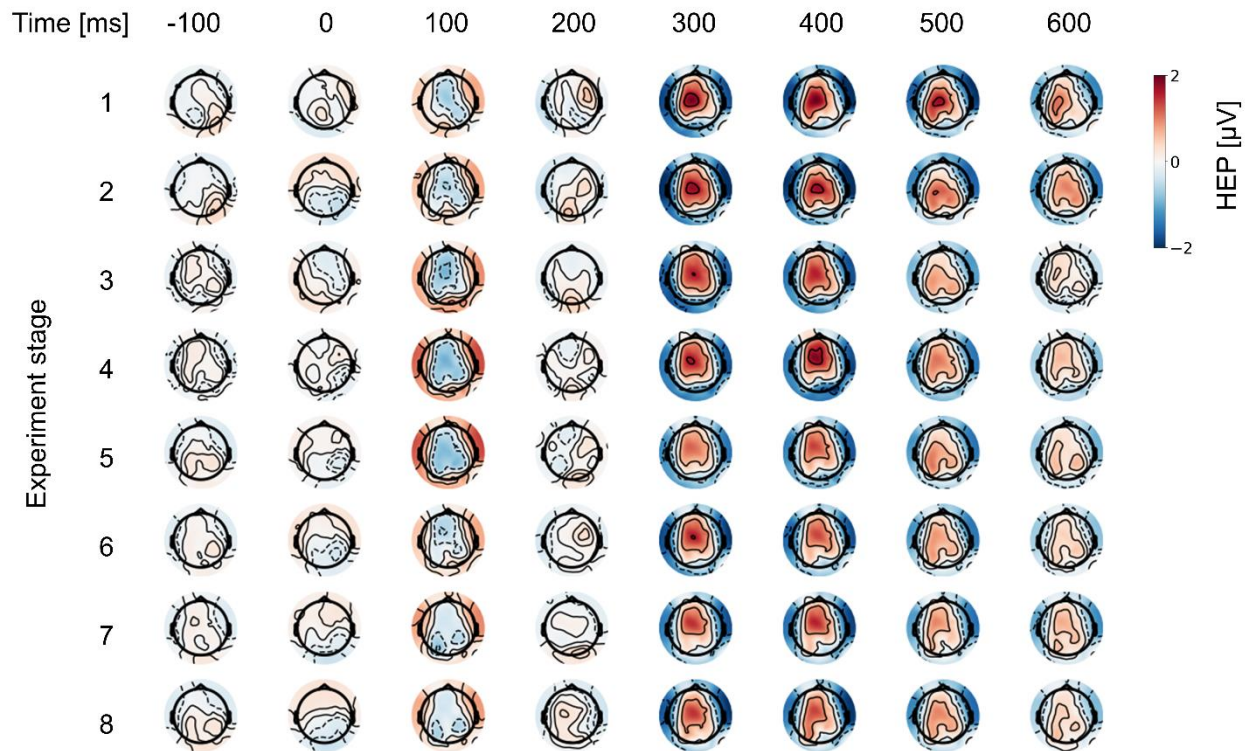
Run 3:  $-0.046$  ( $P=0.88$ ), Run 4:  $\rho = -0.617$  ( $P < 0.01$ ).



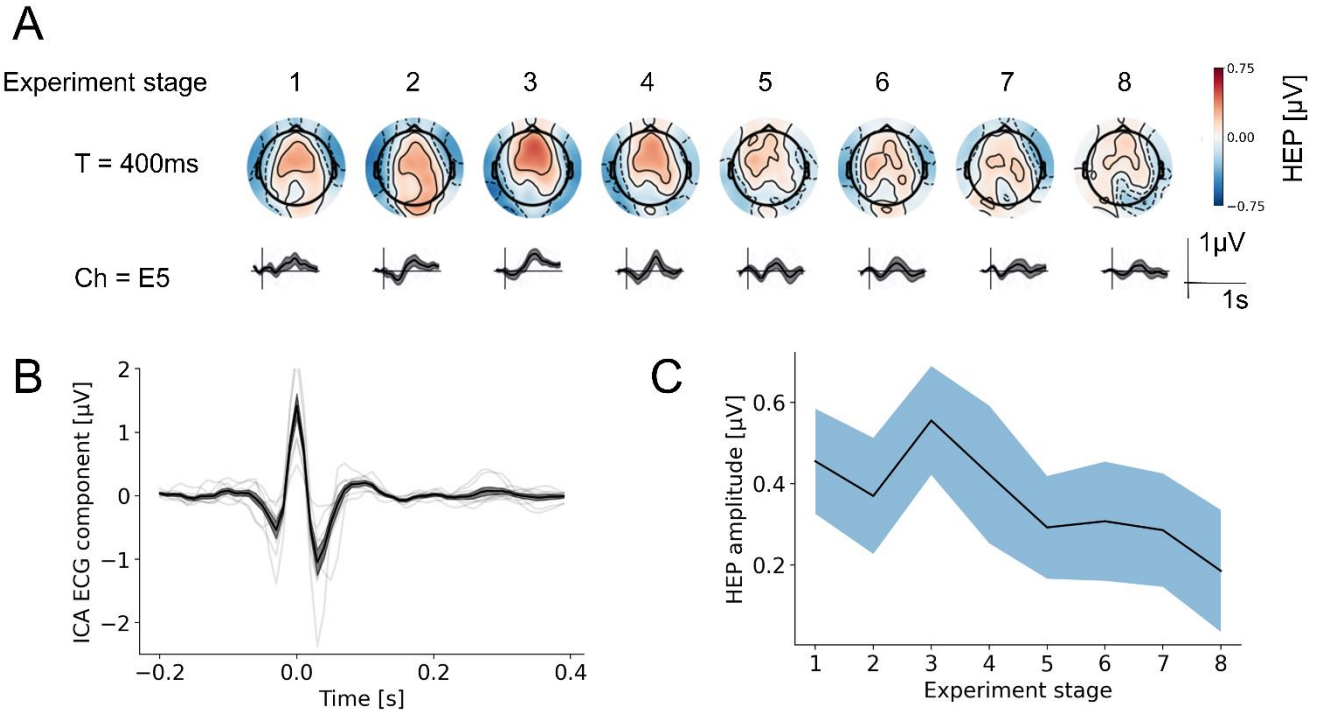


**Supplementary Figure 6.4: (A) Fractional occupancies, (B) State maps and (C) Power spectra for K = 10 HMM states. The main results from the Main Text (one high-power alpha state that gets suppressed by ketamine, one high-delta state, several medium-alpha states, one low-power state that subjects spend more time in under ketamine) holds across different state numbers.**

Correlation between fractional occupancies in State 1 / State 2 and disembodiment:  
Spearman  $\rho = -0.379$  ( $P=0.18$ ).

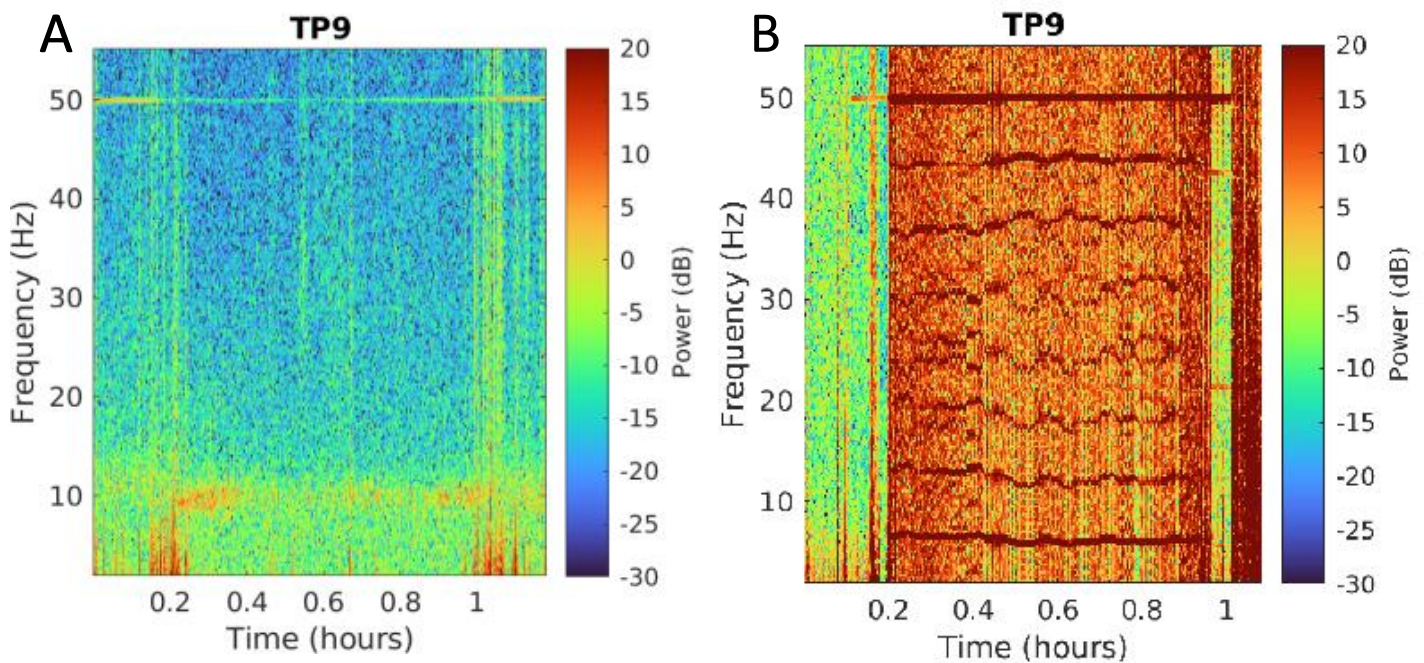


**Supplementary Figure 6.5:** Full spatiotemporal evolution of the heartbeat-evoked potential (HEP) case study. A consistent HEP around 300ms-500ms after an R-peak is seen, but its amplitude diminishes as the ketamine infusion progresses.



**Supplementary Figure 6.6:** Heartbeat-evoked potential (HEP) results for N=9 participants who showed at least a weak ECG ICA component. **(A)** Group-mean HEP topography across the experiment. **(B)** Group-level ICA component activity around detected R-peaks with a visible, ECG-like cardiac component (mean in black, standard error shaded, individual participants in grey lines). **(C)** Peak HEP amplitude across the experiment. There was a trend for a decrease in HEP amplitude, but the repeated-measures ANOVA was not significant ( $P>0.1$ ).

## Appendix 6: Supplementary Figures to Chapter 7



**Supplementary Figure 7.1:** Example individual spectrograms. **(A)** A relatively clean recording except for movement artifacts concentrated around the beginning and end of the infusion. **(B)** A bad recording. Clearly artifactual spectral bands are present, possibly due to coupling between a poorly connected electrode and patient headphones.

## Appendix 7: Questionnaires for the ketamine study

### 9.7.1 Set & Setting Questionnaire

Please rate your feelings right now.

Draw a vertical line through the horizontal line at a point corresponding to the intensity of your experience, from 'Not at all' to 'Extremely' (see the example below)

It is important that you make a mark on every line.

**YOUR PARTICIPANT NUMBER:**

**TODAY'S DATE:**

This is an example:

Not at all Extremely

---

|

I feel comfortable about the upcoming experience.

---

I feel anxious.

---

I have a good feeling about my relationship with the people who will be with me during my experience.

---

The setting feels good for my upcoming experience.

---

I feel well prepared for the upcoming experience.

---

I am in a good mood.

---

I have a good relationship with the main person who will look after me during the upcoming experience.

---

I have strong expectations for the upcoming experience.

---

I have a clear intention for the upcoming experience.

---

**Please check you have entered your participant number, date, and answered all questions.**

**Thank you very much for your help.**

## 9.7.2 Subjective noise &amp; light levels

Please indicate how you feel right now.

**YOUR PARTICIPANT NUMBER:**

**TODAY'S DATE:**

The room is noisy.	0 - Not at all 1 - A little bit 2 - Somewhat 3 - A lot 4 - Very much
The noise level in the room bothers me.	0 - Not at all 1 - A little bit 2 - Somewhat 3 - A lot 4 - Very much
The light in the room is bright.	0 - Not at all 1 - A little bit 2 - Somewhat 3 - A lot 4 - Very much
The light in the room bothers me.	0 - Not at all 1 - A little bit 2 - Somewhat 3 - A lot 4 - Very much

**Please check you have entered your participant number, date, and answered all questions.**

**Thank you very much for your help.**

### 9.7.3 5D-ASC questionnaire.

Please rate the experience you had during today's ketamine infusion.

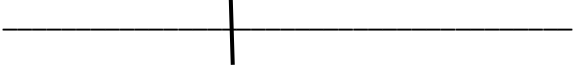
Draw a vertical line through the horizontal line at a point corresponding to the intensity of your experience, from 'Not at all' to 'Extremely' (see the example below). It is important that you make a mark on every line.

**YOUR PARTICIPANT NUMBER:**

**TODAY'S DATE:**

This is an example:

Not at all Extremely



I felt like a puppet

---

I had the feeling of being connected to a superior power

---

I enjoyed boundless pleasure

---

I saw regular patterns (in total darkness or with closed eyes)

---

Everything seemed to unify into a oneness

---

Noises seemed to influence what I saw

---

I saw colours before me (in total darkness or with closed eyes)

---

The shapes of things seemed to be changed by sounds or noises

---

It seemed to me as though I did not have a body any more

---

I had difficulty making even the smallest decision

---

Everyday things gained a special meaning

---

Things around me had a strange new meaning for me

---

I was afraid that the state I was in would last forever

---

I saw lights or flashes of lights (in total darkness or with closed eyes)

---

It seemed to me that my environment and I were one

---

I had difficulty in distinguishing important from unimportant things

---

I saw scenes rolling by (in total darkness or with my eyes closed)

---

I experienced a touch of eternity

---

Conflicts and contradictions seemed to dissolve

---

I was afraid without being able to say exactly why

---

I experienced everything terrifyingly distorted

---

I experienced my surroundings as strange and weird

---

I felt as though I was paralysed

---

I felt very profound

---

I experienced past, present and future as a oneness

---

Objects around me engaged me emotionally much more than usual

---

I felt threatened

---

I had the feeling of being outside my body

---

I felt as though I was floating

---

I felt isolated from everything and everyone

---

I was not able to complete a thought, my thought repeatedly became disconnected

---

I gained clarity into connections that puzzled me before

---

I could picture scenes from my past or fantasy extremely clearly

---

The colours of things seemed to be changed by sounds or noises

---

I had very original thoughts

---

I had the feeling that I no longer had a will of my own

---

I experienced a kind of awe

---

My imagination was extremely vivid

---

I experienced a profound peace in myself

---

I had the feeling something horrible would happen

---

I experienced an all-embracing love

---

My experience had religious aspects

---

I felt dissociated

---



Please circle the number which best describes how you felt at the PEAK EXPERIENCE

### 9.7.4 CADSS-6

**YOUR PARTICIPANT NUMBER:**

**TODAY'S DATE:**

<p>Did things seem to be moving in slow motion?</p>	<p>0 - Not at all 1 - Mild 2 - Moderate 3 - Severe 4 - Extreme</p>	<p>Things seemed slightly slowed down, but not very noticeable. Things were moving about twice as slow as normally. Things were moving so slowly that they are barely moving. Things were moving so slowly, I had the perception that everything had come to a stop, as if time was standing still.</p>
<p>Did things seem to be unreal to you, as if you were in a dream?</p>	<p>0 - Not at all 1 - Mild 2 - Moderate 3 - Severe 4 - Extreme</p>	<p>Things seemed a little unreal, but I was well aware of where I'm at. Things seemed dreamlike, although I knew I was awake. Things seemed very dreamlike, although I knew that I was there, I had the feeling like I might be asleep. I felt like nothing was real, like I should pinch myself to wake up, or ask someone if this is a dream.</p>
<p>Did you feel disconnected from your own body?</p>	<p>0 - Not at all 1 - Mild 2 - Moderate 3 - Severe 4 - Extreme</p>	<p>I felt a little bit disconnected from myself, but I was basically all here. I felt somewhat detached from my own body, but I was basically all together I felt detached from my own body, but not far removed from my body, and I felt as if it was me there. I felt like I was completely out of my body, as if I was looking at my own body from a long way off, as if there was another person there or no person there.</p>
<p>Did your sense of your own body feel changed: for instance, did your own body feel unusually large or unusually small?</p>	<p>0 - Not at all 1 - Mild 2 - Moderate 3 - Severe 4 - Extreme</p>	<p>I had a vague feeling that something about my body had changed, but I can't say exactly what it was. I felt like my body had increased or decreased in size slightly, or that it felt somewhat as if it was not my body I felt as if my body had increased to twice its normal size, or decreased to twice its normal size, or I very much felt as if this was not my body. I felt as if my body swelled up to at least ten times its normal size, or as if it was ten times as small, or as if my arms became like toothpicks</p>
<p>Did you space out, or in some other way lost track of what was going on during this experience?</p>	<p>0 - Not at all 1 - Mild 2 - Moderate 3 - Severe 4 - Extreme</p>	<p>I had some episodes of losing track of what is going on, but I followed everything for the most part I lost at least a minute of time or completely lost track of what was going on at some moments. I lost several segments of time of one minute or more. I lost large segments of time of at least 15 minutes or more.</p>
<p>Did you have gaps in your memory?</p>	<p>0 - Not at all 1 - Mild 2 - Moderate 3 - Severe 4 - Extreme</p>	<p>There were some then-recent things which I could not remember. There were a few gaps in my memory which lasted a few minutes. There were large gaps in my memory which lasted for more than a few minutes I couldn't piece together what was happening from one moment to the next due to large gaps in my memory.</p>

## 9.7.5 Open-ended questions

We would like to know more about the experience you had with today's ketamine infusion. Please answer the following questions in as much detail as you'd like to.

**YOUR PARTICIPANT NUMBER:**

**TODAY'S DATE:**

Do you think that this experience has affected your mood? If so, how?

Do you think that this experience has affected your perspective or outlook on life? If so, how?

Do you think that this experience has affected your ability to think about past experiences that you might find uncomfortable, or even traumatic? If so, how?

Anything else you'd like to share about the experience?

**Please check you have entered your participant number, date, and answered all questions. Thank you for your help.**

9.7.6 Demographic questionnaire.

**Please answer the following questions about yourself.**

<b>Your Participant Number</b>		<b>Today's date</b>	
Age	years		
Sex assigned at birth (Please circle)	Female Male Other Prefer not to say	Gender (Please circle)	Man Woman Non-binary Other Prefer not to say
<b>Ethnicity (Please circle)</b>	White – British White – Irish White – Any other  Mixed - White and Black Caribbean Mixed - White and Black African Mixed - White and Asian Mixed - Any other mixed background	Asian or Asian British – Indian  Asian or Asian British – Pakistani  Asian or Asian British – Bangladeshi  Asian or Asian British – Any other Asian background	Black or Black British – Caribbean Black or Black British – African Black or Black British – Any other Black background  Other Ethnic Groups – Chinese Other Ethnic Groups – Any other ethnic group  Prefer not to say
Height	m	Weight	kg
Medication taken			

**Please check you have entered your participant number, date, and answered all questions. Thank you for your help.**

# 10 References

1. Pandit JJ, Andrade J, Bogod DG, Hitchman JM, Jonker WR, Lucas N, Mackay JH, Nimmo AF, O'Connor K, O'Sullivan EP, Paul RG, Palmer JHMG, Plaat F, Radcliffe JJ, Sury MRJ, Torevell HE, Wang M, Hainsworth J, Cook TM, Royal College of Anaesthetists, Association of Anaesthetists of Great Britain and Ireland: 5th National Audit Project (NAP5) on accidental awareness during general anaesthesia: summary of main findings and risk factors. *Br J Anaesth* 2014; 113:549–59
2. Caton D: John Snow's Practice of Obstetric Anesthesia. *Anesthesiology* 2000; 92:247–247
3. Bergman NA: THE LEGACY OF JOHN SNOW. *Anesthesiology* 1958; 19:595–606
4. Oleckno WA: Remembering Dr. John Snow on the sesquicentennial of his death. *CMAJ* 2008; 178:1691–2
5. Dawson J, Jones M: The principles of anaesthesia. *Surgery (Oxford)* 2013; 31:67–71
6. Nightingale P: Accidental awareness during general anaesthesia in the United Kingdom and Ireland. *J R Coll Physicians Edinb* 2014; 44:289–90
7. Kane AD, Soar J, Armstrong RA, Kursumovic E, Davies MT, Oglesby FC, Cortes L, Taylor C, Moppett IK, Agarwal S, Cordingley J, Dorey J, Finney SJ, Kunst G, Lucas DN, Nickols G, Mouton R, Nolan JP, Patel B, Pappachan VJ, Plaat F, Scholefield BR, Smith JH, Varney L, Cook TM, Collaborators: Patient

- characteristics, anaesthetic workload and techniques in the UK: an analysis from the 7th National Audit Project (NAP7) activity survey. *Anaesthesia* n/a
8. Hirota K: Special cases: Ketamine, nitrous oxide and xenon. *Best Practice & Research Clinical Anaesthesiology* 2006; 20:69–79
  9. Aceto P, Perilli V, Lai C, Sacco T, Ancona P, Gasperin E, Sollazzi L: Update on post-traumatic stress syndrome after anesthesia. *Eur Rev Med Pharmacol Sci* 2013; 17:1730–7
  10. El-Gabalawy R, Sommer JL, Pietrzak R, Edmondson D, Sareen J, Avidan MS, Jacobsohn E: Post-traumatic stress in the postoperative period: current status and future directions. *Can J Anesth/J Can Anesth* 2019; 66:1385–95
  11. Hesse S, Kreuzer M, Hight D, Gaskell A, Devari P, Singh D, Taylor NB, Whalin MK, Lee S, Sleight JW, García PS: Association of electroencephalogram trajectories during emergence from anaesthesia with delirium in the postanaesthesia care unit: an early sign of postoperative complications. *British Journal of Anaesthesia* 2019; 122:622–34
  12. Vlisides P, Avidan M: Recent Advances in Preventing and Managing Postoperative Delirium. *F1000Res* 2019; 8:F1000 Faculty Rev-607
  13. Monk TG, Price CC: Postoperative cognitive disorders. *Curr Opin Crit Care* 2011; 17:10.1097/MCC.0b013e328348bece
  14. Negrini D, Wu A, Oba A, Harnke B, Ciancio N, Krause M, Clavijo C, Al-Musawi M, Linhares T, Fernandez-Bustamante A, Schmidt S: Incidence of Postoperative Cognitive Dysfunction Following Inhalational vs Total Intravenous General Anesthesia: A Systematic Review and Meta-Analysis. *Neuropsychiatr Dis Treat* 2022; 18:1455–67

15. Heurteaux C, Guy N, Laigle C, Blondeau N, Duprat F, Mazzuca M, Lang-Lazdunski L, Widmann C, Zanzouri M, Romey G: TREK-1, a K<sup>+</sup> channel involved in neuroprotection and general anesthesia. *The EMBO journal* 2004; 23:2684–95
16. Chen X, Shu S, Bayliss DA: HCN1 channel subunits are a molecular substrate for hypnotic actions of ketamine. *Journal of Neuroscience* 2009; 29:600–9
17. Bonin RP, Orser BA: CELLULAR AND MOLECULAR EFFECTS OF GENERAL ANESTHETICS IN THE BRAIN. *Neuroscientific Foundations of Anesthesiology* 2011:17
18. Moody OA, Zhang ER, Vincent KF, Kato R, Melonakos ED, Nehs CJ, Solt K: The Neural Circuits Underlying General Anesthesia and Sleep. *Anesthesia & Analgesia* 2021; 132:1254–64
19. Mashour GA, Hudetz AG: Bottom-Up and Top-Down Mechanisms of General Anesthetics Modulate Different Dimensions of Consciousness. *Front Neural Circuits* 2017; 11:44
20. Bonin RP, Orser BA: GABA<sub>A</sub> receptor subtypes underlying general anesthesia. *Pharmacology Biochemistry and behavior* 2008; 90:105–12
21. Vuyk J, Sitsen E, Reeker M: Intravenous anesthetics, *Miller's Anesthesia*, Edited by Miller RD. Elsevier/Saunders, Philadelphia, 2015
22. Al-Rifai Z, Mulvey D: Principles of total intravenous anaesthesia: basic pharmacokinetics and model descriptions. *Bja Education* 2016; 16:92–7
23. Sato M, Tanaka M, Umehara S, Nishikawa T: Baroreflex control of heart rate during and after propofol infusion in humans. *British Journal of Anaesthesia* 2005; 94:577–81

24. Jurd R, Arrasa M, Lambert S, Drexler B, Siegwart R, Crestani F, Zaugg M, Vogt KE, Ledermann B, Antkowiak B: General anesthetic actions in vivo strongly attenuated by a point mutation in the GABAA receptor  $\beta 3$  subunit. *The FASEB Journal* 2003; 17:250–2
25. Krasowski MD, Nishikawa K, Nikolaeva N, Lin A, Harrison NL: Methionine 286 in transmembrane domain 3 of the GABAA receptor  $\beta$  subunit controls a binding cavity for propofol and other alkylphenol general anesthetics. *Neuropharmacology* 2001; 41:952–64
26. Franks NP: Molecular targets underlying general anaesthesia. *British journal of pharmacology* 2006; 147:S72–81
27. Orser BA: Extrasynaptic GABAA Receptors Are Critical Targets for Sedative-Hypnotic Drugs. *Journal of Clinical Sleep Medicine* 2006; 02:S12–8
28. Hashemi M, Hutt A, Sleight J: Anesthetic action on extra-synaptic receptors: effects in neural population models of EEG activity. *Front Syst Neurosci* 2014; 8
29. Hemmings HC, Riegelhaupt PM, Kelz MB, Solt K, Eckenhoff RG, Orser BA, Goldstein PA: Towards a Comprehensive Understanding of Anesthetic Mechanisms of Action: A Decade of Discovery. *Trends in Pharmacological Sciences* 2019; 40:464–81
30. Xie G, Deschamps A, Backman SB, Fiset P, Chartrand D, Dagher A, Plourde G: Critical involvement of the thalamus and precuneus during restoration of consciousness with physostigmine in humans during propofol anaesthesia: a positron emission tomography study. *BJA: British Journal of Anaesthesia* 2011; 106:548–57

31. Ni Mhuirheartaigh R, Warnaby C, Rogers R, Jbabdi S, Tracey I: Slow-Wave Activity Saturation and Thalamocortical Isolation During Propofol Anesthesia in Humans. *Science Translational Medicine* 2013; 5:208ra148-208ra148
32. Luppi AH, Craig MM, Pappas I, Finoia P, Williams GB, Allanson J, Pickard JD, Owen AM, Naci L, Menon DK, Stamatakis EA: Consciousness-specific dynamic interactions of brain integration and functional diversity. *Nat Commun* 2019; 10:4616
33. Boveroux P, Vanhaudenhuyse A, Bruno M-A, Noirhomme Q, Lauwick S, Luxen A, Degueldre C, Plenevaux A, Schnakers C, Phillips C, Brichant J-F, Bonhomme V, Maquet P, Greicius MD, Laureys S, Boly M: Breakdown of within- and between-network Resting State Functional Magnetic Resonance Imaging Connectivity during Propofol-induced Loss of Consciousness. *Anesthesiology* 2010; 113:1038–53
34. Lee U, Ku S, Noh G, Baek S, Choi B, Mashour GA: Disruption of Frontal–Parietal Communication by Ketamine, Propofol, and Sevoflurane. *Anesthesiology* 2013; 118:1264–75
35. Paoletti P, Bellone C, Zhou Q: NMDA receptor subunit diversity: impact on receptor properties, synaptic plasticity and disease. *Nature Reviews Neuroscience* 2013; 14:383–400
36. Domino EF: Taming the ketamine tiger. 1965. *Anesthesiology* 2010; 113:678–84
37. Song JW, Shim JK, Song Y, Yang SY, Park SJ, Kwak YL: Effect of ketamine as an adjunct to intravenous patient-controlled analgesia, in patients at high risk of postoperative nausea and vomiting undergoing lumbar spinal surgery. *British journal of anaesthesia* 2013; 111:630–5



38. Annetta MG, Iemma D, Garisto C, Tafani C, Proietti R: Ketamine: New Indications for an Old Drug. *Current Drug Targets* 2005; 6:789–94
39. Sleight J, Harvey M, Voss L, Denny B: Ketamine – More mechanisms of action than just NMDA blockade. *Trends in Anaesthesia and Critical Care* 2014; 4:76–81
40. Zhou C, Douglas JE, Kumar NN, Shu S, Bayliss DA, Chen X: Forebrain HCN1 channels contribute to hypnotic actions of ketamine. *Anesthesiology* 2013; 118:785–95
41. Bonhomme V, Vanhaudenhuyse A, Demertzi A, Bruno M-A, Jaquet O, Bahri MA, Plenevaux A, Boly M, Boveroux P, Soddu A, Brichant JF, Maquet P, Laureys S: Resting-state Network-specific Breakdown of Functional Connectivity during Ketamine Alteration of Consciousness in Volunteers. *Anesthesiology* 2016; 125:873–88
42. Mashour GA: Network-level Mechanisms of Ketamine Anesthesia. *Anesthesiology* 2016; 125:830–1
43. Freye E, Levy JV: Mechanism of Action of Opioids and Clinical Effects, Opioids in Medicine: A Comprehensive Review on the Mode of Action and the Use of Analgesics in Different Clinical Pain States. Edited by Freye E, Levy JV. Dordrecht, Springer Netherlands, 2008, pp 85–187 doi:10.1007/978-1-4020-5947-6\_2
44. Egan TD: Are opioids indispensable for general anaesthesia? *British Journal of Anaesthesia* 2019; 122:e127–35
45. Egan TD, Minto CF: Pharmacodynamic drug interactions in anesthesia, *Anesthetic Pharmacology: Basic Principles and Clinical Practice*, 2nd edition.

Edited by Evers AS, Kharasch ED, Maze M. Cambridge, Cambridge University Press, 2011, pp 147–65 doi:10.1017/CBO9780511781933.012

46. Benyamin R, Trescot AM, Datta S, Buenaventura RM, Adlaka R, Sehgal N, Glaser SE, Vallejo R: Opioid complications and side effects. *Pain physician* 2008; 11:S105
47. Manzoni T: The cerebral ventricles, the animal spirits and the dawn of brain localization of function. *Arch Ital Biol* 1998; 136:103–52
48. Borck C: *Brainwaves: A Cultural History of Electroencephalography*. Taylor & Francis, 2018 doi:10.4324/9781315569840
49. Caton R: *The electric currents of the brain*. Taylor & Francis, 1970, pp 12–4
50. Berger H: Über das Elektrenkephalogramm des Menschen. *Archiv f Psychiatrie* 1929; 87:527–70
51. Adrian ED, Matthews BHC: The Berger rhythm: potential changes from the occipital lobes in man. *Brain: A Journal of Neurology* 1934; 57:355–85
52. GIBBS FA, GIBBS EL, LENNOX WG: EFFECT ON THE ELECTRO-ENCEPHALOGRAM OF CERTAIN DRUGS WHICH INFLUENCE NERVOUS ACTIVITY. *Archives of Internal Medicine* 1937; 60:154–66
53. Rosow C, Manberg PJ: Bispectral index monitoring. *Anesthesiology Clinics of North America* 2001; 19:947–66
54. Kreuer S, Wilhelm W: The narcotrend monitor. *Best Practice & Research Clinical Anaesthesiology* 2006; 20:111–9
55. Bein B: Entropy. *Best Practice & Research Clinical Anaesthesiology* 2006; 20:101–9

56. Millett D: Hans Berger: From Psychic Energy to the EEG. *Perspectives in Biology and Medicine* 2001; 44:522–42
57. Kaplan RM: The Mind Reader: the Forgotten Life of Hans Berger, Discoverer of the EEG. *Australas Psychiatry* 2011; 19:168–9
58. Bishop-Fitzpatrick L, Movaghar A, Greenberg JS, Page D, DaWalt LS, Brilliant MH, Mailick MR: Using machine learning to identify patterns of lifetime health problems in decedents with autism spectrum disorder. *Autism Research* 2018; 11:1120–8
59. Zeidman LA, Stone J, Kondziella D: New Revelations About Hans Berger, Father of the Electroencephalogram (EEG), and His Ties to the Third Reich. *J Child Neurol* 2014; 29:1002–10
60. Berger H: Über das Elektrenkephalogramm des Menschen. *Archiv f Psychiatrie* 1934; 101:452–69
61. Walter WG: THE LOCATION OF CEREBRAL TUMOURS BY ELECTRO-ENCEPHALOGRAPHY. *The Lancet* 1936; 228:305–8
62. In Memoriam Erna Leonhardt Gibbs 1906–1987. *American Journal of EEG Technology* 1987; 27:183–4
63. Bickford R: Automatic electroencephalographic control of general anesthesia 1950 doi:10.1016/0013-4694(50)90014-9
64. MAYO CW, BICKFORD RG, FAULCONER A Jr: ELECTROENCEPHALOGRAPHICALLY CONTROLLED ANESTHESIA IN ABDOMINAL SURGERY. *Journal of the American Medical Association* 1950; 144:1081–3
65. Hari R, Puce A: MEG-EEG primer. New York, NY, Oxford University Press, 2017

66. Pope KJ, Fitzgibbon SP, Lewis TW, Whitham EM, Willoughby JO: Relation of Gamma Oscillations in Scalp Recordings to Muscular Activity. *Brain Topogr* 2009; 22:13–7
67. Whitham EM, Pope KJ, Fitzgibbon SP, Lewis T, Clark CR, Loveless S, Broberg M, Wallace A, DeLosAngeles D, Lillie P, Hardy A, Fronsco R, Pulbrook A, Willoughby JO: Scalp electrical recording during paralysis: Quantitative evidence that EEG frequencies above 20Hz are contaminated by EMG. *Clinical Neurophysiology* 2007; 118:1877–88
68. Fitzgibbon SP, Powers DMW, Pope KJ, Clark CR: Removal of EEG noise and artifact using blind source separation. *J Clin Neurophysiol* 2007; 24:232–43
69. Fries P: A mechanism for cognitive dynamics: neuronal communication through neuronal coherence. *Trends in Cognitive Sciences* 2005; 9:474–80
70. Marchant N, Sanders R, Sleight J, Vanhaudenhuyse A, Bruno M-A, Brichant JF, Laureys S, Bonhomme V: How Electroencephalography Serves the Anesthesiologist. *Clin EEG Neurosci* 2014; 45:22–32
71. Hight DF, Kaiser HA, Sleight JW, Avidan MS: An updated introduction to electroencephalogram-based brain monitoring during intended general anesthesia. *Can J Anaesth* 2020; 67:1858–78
72. Tinker JH, Sharbrough FW, Michenfelder JD: Anterior shift of the dominant EEG rhythm during anesthesia in the Java monkey: correlation with anesthetic potency. *Anesthesiology* 1977; 46:252–9
73. Steriade M, Nuñez A, Amzica F: A novel slow (< 1 Hz) oscillation of neocortical neurons in vivo: depolarizing and hyperpolarizing components. *J Neurosci* 1993; 13:3252–65

74. Shanker A, Abel JH, Schamberg G, Brown EN: Etiology of Burst Suppression EEG Patterns. *Frontiers in Psychology* 2021; 12:2207
75. Ching S, Purdon PL, Vijayan S, Kopell NJ, Brown EN: A neurophysiological–metabolic model for burst suppression. *Proc Natl Acad Sci U S A* 2012; 109:3095–100
76. Lewis LD, Ching S, Weiner VS, Peterfreund RA, Eskandar EN, Cash SS, Brown EN, Purdon PL: Local cortical dynamics of burst suppression in the anaesthetized brain. *Brain* 2013; 136:2727–37
77. Ming Q, Liou J-Y, Yang F, Li J, Chu C, Zhou Q, Wu D, Xu S, Luo P, Liang J, Li D, Pryor KO, Lin W, Schwartz TH, Ma H: Isoflurane-Induced Burst Suppression Is a Thalamus-Modulated, Focal-Onset Rhythm With Persistent Local Asynchrony and Variable Propagation Patterns in Rats. *Front Syst Neurosci* 2021; 14
78. Soehle M, Dittmann A, Ellerkmann RK, Baumgarten G, Putensen C, Guenther U: Intraoperative burst suppression is associated with postoperative delirium following cardiac surgery: a prospective, observational study. *BMC Anesthesiol* 2015; 15:61
79. Hogan J, Sun H, Aboul Nour H, Jing J, Tabaeizadeh M, Shoukat M, Javed F, Kassa S, Edhi MM, Bordbar E, Gallagher J, Junior VM, Ghanta M, Shao Y-P, Akeju O, Cole AJ, Rosenthal ES, Zafar S, Westover MB: Burst Suppression: Causes and Effects on Mortality in Critical Illness. *Neurocrit Care* 2020 doi:10.1007/s12028-020-00932-4
80. Steriade M, McCormick DA, Sejnowski TJ: Thalamocortical oscillations in the sleeping and aroused brain. *Science* 1993; 262:679–85

81. Sanchez-Vives MV: Origin and dynamics of cortical slow oscillations. *Current Opinion in Physiology* 2020; 15:217–23
82. Sanchez-Vives MV, McCormick DA: Cellular and network mechanisms of rhythmic recurrent activity in neocortex. *Nat Neurosci* 2000; 3:1027–34
83. David F, Schmiedt JT, Taylor HL, Orban G, Giovanni GD, Uebele VN, Renger JJ, Lambert RC, Leresche N, Crunelli V: Essential Thalamic Contribution to Slow Waves of Natural Sleep. *J Neurosci* 2013; 33:19599–610
84. Neske GT: The Slow Oscillation in Cortical and Thalamic Networks: Mechanisms and Functions. *Front Neural Circuits* 2016; 9
85. Massimini M: The Sleep Slow Oscillation as a Traveling Wave. *Journal of Neuroscience* 2004; 24:6862–70
86. Murphy M, Bruno M-A, Riedner BA, Boveroux P, Noirhomme Q, Landsness EC, Brichant J-F, Phillips C, Massimini M, Laureys S, Tononi G, Boly M: Propofol Anesthesia and Sleep: A High-Density EEG Study. *Sleep* 2011; 34:283–91
87. Sleigh JW, Scheib CM, Sanders RD: General anaesthesia and electroencephalographic spindles. *Trends in Anaesthesia and Critical Care* 2011; 1:263–9
88. Avidan M, Sleigh J: Introduction to Electroencephalography. *Oxford Textbook of Neuroscience and Anaesthesiology* Oxford University Press <https://doi.org/10.1093/med/9780198746645001> 2019; 1
89. McMillan R, Muthukumaraswamy SD: The neurophysiology of ketamine: an integrative review. *Reviews in the Neurosciences* 2020; 31:457–503
90. Pavone KJ, Akeju O, Sampson AL, Ling K, Purdon PL, Brown EN: Nitrous oxide-induced slow and delta oscillations. *Clinical Neurophysiology* 2016; 127:556–64

91. Liley DTJ, Sinclair NC, Lipping T, Heyse B, Vereecke HEM, Struys MMRF: Propofol and Remifentanyl Differentially Modulate Frontal Electroencephalographic Activity: *Anesthesiology* 2010; 113:292–304
92. Frohlich J, Mediano PAM, Bavato F, Gharabaghi A: Down but not out: drugs that enhance delta oscillations but preserve consciousness 2023 doi:10.31234/osf.io/tj2sw
93. Frohlich J, Toker D, Monti MM: Consciousness among delta waves: a paradox? *Brain* 2021; 144:2257–77
94. Warnaby CE, Sleigh JW, Hight D, Jbabdi S, Tracey I: Investigation of Slow-wave Activity Saturation during Surgical Anesthesia Reveals a Signature of Neural Inertia in Humans. *Anesthesiology* 2017; 127:645–57
95. Sepúlveda PO, Tapia LF, Monsalves S: Neural inertia and differences between loss of and recovery from consciousness during total intravenous anaesthesia: a narrative review. *Anaesthesia* 2019; 74:801–9
96. Schuller PJ, Newell S, Strickland PA, Barry JJ: Response of bispectral index to neuromuscular block in awake volunteers†. *BJA: British Journal of Anaesthesia* 2015; 115:i95–103
97. Colombo MA, Napolitani M, Boly M, Gosseries O, Casarotto S, Rosanova M, Brichant J-F, Boveroux P, Rex S, Laureys S, Massimini M, Chiaregato A, Sarasso S: The spectral exponent of the resting EEG indexes the presence of consciousness during unresponsiveness induced by propofol, xenon, and ketamine. *NeuroImage* 2019; 189:631–44
98. Tononi G, Edelman GM: *Consciousness and Complexity* 1998; 282:7

99. Sarasso S, Boly M, Napolitani M, Gosseries O, Charland-Verville V, Casarotto S, Rosanova M, Casali AG, Brichant J-F, Boveroux P, Rex S, Tononi G, Laureys S, Massimini M: Consciousness and Complexity during Unresponsiveness Induced by Propofol, Xenon, and Ketamine. *Current Biology* 2015; 25:3099–105
100. Li D, Fabus MS, Sleigh JW: Brain Complexities and Anesthesia: Their Meaning and Measurement. *Anesthesiology* 2022; 137:290–302
101. Luppi AI, Vohryzek J, Kringelbach ML, Mediano PA, Craig MM, Adapa R, Carhart-Harris RL, Roseman L, Pappas I, Peattie AR: Distributed harmonic patterns of structure-function dependence orchestrate human consciousness. *Communications Biology* 2023; 6:117
102. Casali AG, Gosseries O, Rosanova M, Boly M, Sarasso S, Casali KR, Casarotto S, Bruno M-A, Laureys S, Tononi G, Massimini M: A theoretically based index of consciousness independent of sensory processing and behavior. *Sci Transl Med* 2013; 5:198ra105
103. Sleigh J, Pullon RM, Vlisides PE, Warnaby CE: Electroencephalographic slow wave dynamics and loss of behavioural responsiveness induced by ketamine in human volunteers. *British Journal of Anaesthesia* 2019; 123:592–600
104. McCracken C, Raisi-Estabragh Z, Veldsman M, Raman B, Dennis A, Husain M, Nichols TE, Petersen SE, Neubauer S: Multi-organ imaging demonstrates the heart-brain-liver axis in UK Biobank participants. *Nat Commun* 2022; 13:7839
105. Glick DB, Glick G, Stein EJ: The autonomic nervous system. *Basics of anesthesia* 2019; 6
106. Berthoud HR, Neuhuber WL: Functional and chemical anatomy of the afferent vagal system. *Auton Neurosci* 2000; 85:1–17



107. Tsakiris M, De Preester H: The interoceptive mind: From homeostasis to awareness. Oxford University Press, 2018
108. Candia-Rivera D: Brain-heart interactions in the neurobiology of consciousness. *Current Research in Neurobiology* 2022; 3:100050
109. Stankovski T, Petkoski S, Raeder J, Smith AF, McClintock PVE, Stefanovska A: Alterations in the coupling functions between cortical and cardio-respiratory oscillations due to anaesthesia with propofol and sevoflurane. *Philosophical Transactions of the Royal Society A: Mathematical, Physical and Engineering Sciences* 2016; 374:20150186
110. Greene AS, Horien C, Barson D, Scheinost D, Constable RT: Why is everyone talking about brain state? *Trends in Neurosciences* 2023; 0
111. Gaskell AL, Hight DF, Winders J, Tran G, Defresne A, Bonhomme V, Raz A, Sleight JW, Sanders RD: Frontal alpha-delta EEG does not preclude volitional response during anaesthesia: prospective cohort study of the isolated forearm technique. *BJA: British Journal of Anaesthesia* 2017; 119:664–73
112. Mashour GA, Avidan MS: Black swans: challenging the relationship of anaesthetic-induced unconsciousness and electroencephalographic oscillations in the frontal cortex. *British Journal of Anaesthesia* 2017; 119:563–5
113. Sanders RD, Gaskell A, Sleight J: Can use of frontal EEG monitoring increase intraoperative connected consciousness? *British Journal of Anaesthesia* 2018; 121:191–3
114. Sanders RD, Mostert N, Lindroth H, Tononi G, Sleight J: Is consciousness frontal? Two perioperative case reports that challenge that concept. *British Journal of Anaesthesia* 2018; 121:330–2

115. Boly M, Massimini M, Tsuchiya N, Postle BR, Koch C, Tononi G: Are the Neural Correlates of Consciousness in the Front or in the Back of the Cerebral Cortex? Clinical and Neuroimaging Evidence. *J Neurosci* 2017; 37:9603–13
116. Ihalainen R, Gosseries O, Steen FV de, Raimondo F, Panda R, Bonhomme V, Marinazzo D, Bowman H, Laureys S, Chennu S: How hot is the hot zone? Computational modelling clarifies the role of parietal and frontoparietal connectivity during anaesthetic-induced loss of consciousness. *NeuroImage* 2021; 231:117841
117. Stephen EP, Hotan GC, Pierce ET, Harrell PG, Walsh JL, Brown EN, Purdon PL: Broadband slow-wave modulation in posterior and anterior cortex tracks distinct states of propofol-induced unconsciousness. *Sci Rep* 2020; 10:13701
118. Rosanova M, Fecchio M, Casarotto S, Sarasso S, Casali AG, Pigorini A, Comanducci A, Seregini F, Devalle G, Citerio G, Bodart O, Boly M, Gosseries O, Laureys S, Massimini M: Sleep-like cortical OFF-periods disrupt causality and complexity in the brain of unresponsive wakefulness syndrome patients. *Nat Commun* 2018; 9:4427
119. Dasilva M, Camassa A, Navarro-Guzman A, Paziienti A, Perez-Mendez L, Zamora-López G, Mattia M, Sanchez-Vives MV: Modulation of cortical slow oscillations and complexity across anesthesia levels. *NeuroImage* 2021; 224:117415
120. Mensen A, Zhang Z, Qi M, Khatami R: The occurrence of individual slow waves in sleep is predicted by heart rate. *Scientific Reports* 2016; 6:29671
121. Amzica F, Steriade M: Electrophysiological correlates of sleep delta waves. *Electroencephalography and Clinical Neurophysiology* 1998; 107:69–83

122. Ujma PP, Simor P, Steiger A, Dresler M, Bódizs R: Individual slow-wave morphology is a marker of aging. *Neurobiology of Aging* 2019; 80:71–82
123. Siclari F, Bernardi G, Riedner BA, LaRocque JJ, Benca RM, Tononi G: Two Distinct Synchronization Processes in the Transition to Sleep: A High-Density Electroencephalographic Study. *Sleep* 2014; 37:1621–37
124. Bernardi G, Siclari F, Handjaras G, Riedner BA, Tononi G: Local and Widespread Slow Waves in Stable NREM Sleep: Evidence for Distinct Regulation Mechanisms. *Front Hum Neurosci* 2018; 12
125. Nghiem T-AE, Tort-Colet N, Górski T, Ferrari U, Moghimi-firoozabad S, Goldman JS, Teleńczuk B, Capone C, Bal T, Volo M di, Destexhe A: Cholinergic Switch between Two Types of Slow Waves in Cerebral Cortex. *Cereb Cortex* 2020; 30:3451–66
126. Vidaurre D, Quinn AJ, Baker AP, Dupret D, Tejero-Cantero A, Woolrich MW: Spectrally resolved fast transient brain states in electrophysiological data. *NeuroImage* 2016; 126:81–95
127. Vidaurre D, Hunt LT, Quinn AJ, Hunt BAE, Brookes MJ, Nobre AC, Woolrich MW: Spontaneous cortical activity transiently organises into frequency specific phase-coupling networks. *Nat Commun* 2018; 9:2987
128. Stevner ABA, Vidaurre D, Cabral J, Rapuano K, Nielsen SFV, Tagliazucchi E, Laufs H, Vuust P, Deco G, Woolrich MW, Van Someren E, Kringelbach ML: Discovery of key whole-brain transitions and dynamics during human wakefulness and non-REM sleep. *Nat Commun* 2019; 10:1035
129. Li D, Mashour GA: Cortical dynamics during psychedelic and anesthetized states induced by ketamine. *Neuroimage* 2019; 196:32–40

130. Luckenbaugh DA, Niciu MJ, Ionescu DF, Nolan NM, Richards EM, Brutsche NE, Guevara S, Zarate CA: Do the dissociative side effects of ketamine mediate its antidepressant effects? *Journal of Affective Disorders* 2014; 159:56–61
131. Mathai DS, Meyer MJ, Storch EA, Kosten TR: The relationship between subjective effects induced by a single dose of ketamine and treatment response in patients with major depressive disorder: A systematic review. *Journal of Affective Disorders* 2020; 264:123–9
132. Mathai DS, Nayak SM, Yaden DB, Garcia-Romeu A: Reconsidering “dissociation” as a predictor of antidepressant efficacy for esketamine. *Psychopharmacology* 2023 doi:10.1007/s00213-023-06324-8
133. Messina AG, Wang M, Ward MJ, Wilker CC, Smith BB, Vezina DP, Pace NL: Anaesthetic interventions for prevention of awareness during surgery. *Cochrane Database Syst Rev* 2016; 10:CD007272
134. Nimmo AF, Absalom AR, Bagshaw O, Biswas A, Cook TM, Costello A, Grimes S, Mulvey D, Shinde S, Whitehouse T, Wiles MD: Guidelines for the safe practice of total intravenous anaesthesia (TIVA). *Anaesthesia* 2019; 74:211–24
135. Coeckelenbergh S, Richebé P, Longrois D, Joosten A, De Hert S: Current trends in anesthetic depth and antinociception monitoring: an international survey. *J Clin Monit Comput* 2022; 36:1407–22
136. Holmgren J, Prisco L, Chiew M, Jbabdi S, Allen M, Sleight J, Tracey I, Warnaby CE: Auditory and pain processing is severely disrupted at slow wave activity saturation under general anaesthesia. *British Journal of Anaesthesia* 2019; 123:e514

137. Escallier KE, Nadelson MR, Zhou D, Avidan MS: Monitoring the brain: processed electroencephalogram and peri-operative outcomes. *Anaesthesia* 2014; 69:899–910
138. Connor CW: Open Reimplementation of the BIS Algorithms for Depth of Anesthesia. *Anesth Analg* 2022; 135:855–64
139. Obert DP, Schweizer C, Zinn S, Kratzer S, Hight D, Sleight J, Schneider G, García PS, Kreuzer M: The influence of age on EEG-based anaesthesia indices. *Journal of Clinical Anesthesia* 2021; 73:110325
140. Sanders RD, Tononi G, Laureys S, Sleight JW: Unresponsiveness ≠ Unconsciousness: *Anesthesiology* 2012; 116:946–59
141. Hajat Z, Ahmad N, Andrzejowski J: The role and limitations of EEG-based depth of anaesthesia monitoring in theatres and intensive care. *Anaesthesia* 2017; 72:38–47
142. Pandit JJ, Cook TM: I. National Institute for Clinical Excellence guidance on measuring depth of anaesthesia: limitations of EEG-based technology. *BJA: British Journal of Anaesthesia* 2013; 110:325–8
143. González J, Cavelli M, Tort AB, Tortero P, Rubido N: OFF-periods reduce the complexity of neocortical activity during sleep. *bioRxiv* 2021:2021.06.11.448131 doi:10.1101/2021.06.11.448131
144. Lempel A, Ziv J: On the Complexity of Finite Sequences. *IEEE Transactions on Information Theory* 1976; 22:75–81
145. Welch: A Technique for High-Performance Data Compression. *Computer* 1984; 17:8–19

146. Schartner M, Seth A, Noirhomme Q, Boly M, Bruno M-A, Laureys S, Barrett A: Complexity of Multi-Dimensional Spontaneous EEG Decreases during Propofol Induced General Anaesthesia. *PLOS ONE* 2015; 10:e0133532
147. Andrillon T, Poulsen AT, Hansen LK, Léger D, Kouider S: Neural Markers of Responsiveness to the Environment in Human Sleep. *J Neurosci* 2016; 36:6583–96
148. Halder S, Juel BE, Nilsen AS, Raghavan LV, Storm JF: Changes in measures of consciousness during anaesthesia of one hemisphere (Wada test). *NeuroImage* 2021; 226:117566
149. Boncompte G, Medel V, Cortínez LI, Ossandón T: Brain activity complexity has a nonlinear relation to the level of propofol sedation. *British Journal of Anaesthesia* 2021; 127:254–63
150. Fabus MS: Hysteron modeling of anaesthetic slow-wave power 2020
151. Rudolph U, Antkowiak B: Molecular and neuronal substrates for general anaesthetics. *Nat Rev Neurosci* 2004; 5:709–20
152. Braestrup C, Albrechtsen R, Squires RF: High densities of benzodiazepine receptors in human cortical areas. *Nature* 1977; 269:702–4
153. Enna SJ, Bennett Jr. JP, Bylund DB, Creese I, Burt DR, Charness ME, Yamamura HI, Simantov R, Snyder SH: Neurotransmitter receptor binding: regional distribution in human brain. *Journal of Neurochemistry* 1977; 28:233–6
154. Alkire MT, Haier RJ: Correlating in vivo anaesthetic effects with ex vivo receptor density data supports a GABAergic mechanism of action for propofol, but not for isoflurane† ‡. *BJA: British Journal of Anaesthesia* 2001; 86:618–26

155. Nørgaard M, Beliveau V, Ganz M, Svarer C, Pinborg LH, Keller SH, Jensen PS, Greve DN, Knudsen GM: A high-resolution in vivo atlas of the human brain's benzodiazepine binding site of GABAA receptors. *NeuroImage* 2021; 232:117878
156. Luppi AI, Mediano PAM, Rosas FE, Allanson J, Pickard JD, Williams GB, Craig MM, Finoia P, Peattie ARD, Coppola P, Owen A, Naci L, Menon DK, Bor D, Stamatakis EA: Paths to Oblivion: Common Neural Mechanisms of Anaesthesia and Disorders of Consciousness. *bioRxiv* 2021:2021.02.14.431140 doi:10.1101/2021.02.14.431140
157. Qin P, Wu X, Duncan NW, Bao W, Tang W, Zhang Z, Hu J, Jin Y, Wu X, Gao L, Lu L, Guan Y, Lane T, Huang Z, Bodien YG, Giacino JT, Mao Y, Northoff G: GABAA receptor deficits predict recovery in patients with disorders of consciousness: A preliminary multimodal [(11) C]Flumazenil PET and fMRI study. *Hum Brain Mapp* 2015; 36:3867–77
158. Scrivener CL, Reader AT: Variability of EEG electrode positions and their underlying brain regions: visualizing gel artifacts from a simultaneous EEG-fMRI dataset. *Brain Behav* 2022:e2476 doi:10.1002/brb3.2476
159. Ruffini G: An algorithmic information theory of consciousness. *Neuroscience of Consciousness* 2017; 2017:nix019
160. Ruffini G, Ibañez D, Kroupi E, Gagnon J-F, Montplaisir J, Postuma RB, Castellano M, Soria-Frisch A: Algorithmic Complexity of EEG for Prognosis of Neurodegeneration in Idiopathic Rapid Eye Movement Behavior Disorder (RBD). *Ann Biomed Eng* 2019; 47:282–96
161. Ruffini G: Lempel-Zip Complexity Reference. arXiv:170709848 [cs, math] 2017 at <<http://arxiv.org/abs/1707.09848>>

162. Jenkinson M, Beckmann CF, Behrens TEJ, Woolrich MW, Smith SM: FSL. *Neuroimage* 2012; 62:782–90
163. Connor CW: Open Reimplementation of the BIS Algorithms for Depth of Anesthesia. *Anesthesia & Analgesia* 2022; 135:855–64
164. Lustenberger C, Huber R: High Density Electroencephalography in Sleep Research: Potential, Problems, Future Perspective. *Frontiers in Neurology* 2012; 3
165. Hughes LM, Irwin MG, Nestor CC: Alternatives to remifentanyl for the analgesic component of total intravenous anaesthesia: a narrative review. *Anaesthesia* 2023; 78:620–5
166. Deco G, Cruzat J, Cabral J, Knudsen GM, Carhart-Harris RL, Whybrow PC, Logothetis NK, Kringelbach ML: Whole-Brain Multimodal Neuroimaging Model Using Serotonin Receptor Maps Explains Non-linear Functional Effects of LSD. *Current Biology* 2018; 28:3065-3074.e6
167. Afrasiabi M, Redinbaugh MJ, Phillips JM, Kambi NA, Mohanta S, Raz A, Haun AM, Saalman YB: Consciousness depends on integration between parietal cortex, striatum, and thalamus. *Cell Systems* 2021; 12:363-373.e11
168. Bayne T, Seth AK, Massimini M: Are There Islands of Awareness? *Trends in Neurosciences* 2020; 43:6–16
169. Cecconi B, Laureys S, Annen J: Islands of Awareness or Cortical Complexity? *Trends in Neurosciences* 2020; 43:545–6
170. Siclari F, Tononi G: Local aspects of sleep and wakefulness. *Current Opinion in Neurobiology* 2017; 44:222–7



171. Sarasso S, D'Ambrosio S, Fecchio M, Casarotto S, Viganò A, Landi C, Mattavelli G, Gosseries O, Quarenghi M, Laureys S, Devalle G, Rosanova M, Massimini M: Local sleep-like cortical reactivity in the awake brain after focal injury. *Brain* 2020; 143:3672–84
172. Baars BJ: Global workspace theory of consciousness: toward a cognitive neuroscience of human experience, *Progress in Brain Research*. Edited by Laureys S. Elsevier, 2005, pp 45–53
173. Ruffini G, Lopez-Sola E: AIT foundations of structured experience 2022 doi:10.31234/osf.io/k3q6r
174. Carhart-Harris RL, Friston KJ: REBUS and the Anarchic Brain: Toward a Unified Model of the Brain Action of Psychedelics. *Pharmacol Rev* Edited by Barker EL. 2019; 71:316–44
175. Aru J, Suzuki M, Larkum ME: Cellular Mechanisms of Conscious Processing. *Trends in Cognitive Sciences* 2020; 24:814–25
176. Bastos AM, Lundqvist M, Waite AS, Kopell N, Miller EK: Layer and rhythm specificity for predictive routing. *Proceedings of the National Academy of Sciences* 2020; 117:31459–69
177. Parr T, Pezzulo G, Friston KJ: *Active Inference: The Free Energy Principle in Mind, Brain, and Behavior*. Cambridge, MA, USA, MIT Press, 2022
178. Fabus MS, Woolrich MW, Tracey I, Warnaby CE: Dose-dependent spatiotemporal brain dynamics in propofol anaesthesia. in preparation
179. Frohlich J, Toker D, Monti MM: Consciousness among delta waves: a paradox? *Brain* 2021 doi:10.1093/brain/awab095

180. Aboy M, Hornero R, Abasolo D, Alvarez D: Interpretation of the Lempel-Ziv Complexity Measure in the Context of Biomedical Signal Analysis. *IEEE Transactions on Biomedical Engineering* 2006; 53:2282–8
181. Wang J, Noh G-J, Choi B-M, Ku S-W, Joo P, Jung W-S, Kim S, Lee H: Suppressed neural complexity during ketamine- and propofol-induced unconsciousness. *Neuroscience Letters* 2017; 653:320–5
182. Davies PA, Hanna MC, Hales TG, Kirkness EF: Insensitivity to anaesthetic agents conferred by a class of GABAA receptor subunit. *Nature* 1997; 385:820–3
183. Li D, Mashour GA: Cortical dynamics during psychedelic and anesthetized states induced by ketamine. *NeuroImage* 2019; 196:32–40
184. Thayer JF, Lane RD: Claude Bernard and the heart–brain connection: Further elaboration of a model of neurovisceral integration. *Neuroscience & Biobehavioral Reviews* 2009; 33:81–8
185. Tramèr MR, Moore RA, McQuay HJ: Propofol and bradycardia: causation, frequency and severity. *Br J Anaesth* 1997; 78:642–51
186. Wouters PF, Van de Velde M, Van Hemelrijck J: Cardiovascular Effects of Propofol. *Semin Cardiothorac Vasc Anesth* 1997; 1:121–31
187. Hug CC, McLeskey CH, Nahrwold ML, Roizen MF, Stanley TH, Thisted RA, Walawander CA, White PF, Apfelbaum JL, Grasela TH: Hemodynamic effects of propofol: data from over 25,000 patients. *Anesth Analg* 1993; 77:S21-9
188. McKeage K, Perry CM: Propofol. *CNS Drugs* 2003; 17:235–72
189. Fulton B, Sorkin EM: Propofol. *Drugs* 1995; 50:636–457

190. Kanaya N, Hirata N, Kurosawa S, Nakayama M, Namiki A: Differential effects of propofol and sevoflurane on heart rate variability. *Anesthesiology* 2003; 98:34–40
191. Wit F de, Vliet AL van, Wilde RB de, Jansen JR, Vuyk J, Aarts LP, Jonge E de, Veelo DP, Geerts BF: The effect of propofol on haemodynamics: cardiac output, venous return, mean systemic filling pressure, and vascular resistances. *Br J Anaesth* 2016; 116:784–9
192. Claeys MA, Gepts E, Camu F: Haemodynamic changes during anaesthesia induced and maintained with propofol. *Br J Anaesth* 1988; 60:3–9
193. Blake DW, Jover B, McGrath BP: Haemodynamic and heart rate reflex responses to propofol in the rabbit. Comparison with althesin. *Br J Anaesth* 1988; 61:194–9
194. Wang X, Huang Z-G, Gold A, Bouairi E, Evans C, Andresen MC, Mendelowitz D: Propofol Modulates  $\gamma$ -Aminobutyric Acid-mediated Inhibitory Neurotransmission to Cardiac Vagal Neurons in the Nucleus Ambiguus. *Anesthesiology* 2004; 100:1198–205
195. Mäenpää M, Penttilä J, Laitio T, Kaisti K, Kuusela T, Hinkka S, Scheinin H: The effects of surgical levels of sevoflurane and propofol anaesthesia on heart rate variability. *European Journal of Anaesthesiology | EJA* 2007; 24:626–33
196. Zambotti M de, Trinder J, Silvani A, Colrain IM, Baker FC: Dynamic coupling between the central and autonomic nervous systems during sleep: A review. *Neuroscience & Biobehavioral Reviews* 2018; 90:84–103
197. Azzalini D, Rebollo I, Tallon-Baudry C: Visceral Signals Shape Brain Dynamics and Cognition. *Trends in Cognitive Sciences* 2019; 23:488–509

198. Obert DP, Sepúlveda P, Kratzer S, Schneider G, Kreuzer M: The influence of induction speed on the frontal (processed) EEG. *Sci Rep* 2020; 10:19444
199. Gaskell A, Pullon R, Hight D, Termaat J, Mans G, Voss L, Kreuzer M, Schmid S, Kratzer S, Rodriguez A, Schneider G, Garcia P, Sleigh J: Modulation of frontal EEG alpha oscillations during maintenance and emergence phases of general anaesthesia to improve early neurocognitive recovery in older patients: protocol for a randomised controlled trial. *Trials* 2019; 20:146
200. Nunez PL: REST: A good idea but not the gold standard. *Clinical Neurophysiology* 2010; 121:2177–80
201. Hamilton P: Open source ECG analysis, *Computers in Cardiology*. 2002, pp 101–4 doi:10.1109/CIC.2002.1166717
202. Gomes P, Margaritoff P, Silva H: pyHRV: Development and evaluation of an open-source python toolbox for heart rate variability (HRV), *Proc. Int'l Conf. on Electrical, Electronic and Computing Engineering (IcETRAN)*. 2019, pp 822–8
203. Vallat R, Walker MP: An open-source, high-performance tool for automated sleep staging. *eLife* Edited by Peyrache A, Büchel C, Bagur S. 2021; 10:e70092
204. Galletly DC, Larsen PD: Cardioventilatory coupling during anaesthesia. *British Journal of Anaesthesia* 1997; 79:35–40
205. Galletly DC, Larsen PD: Relationship between cardioventilatory coupling and respiratory sinus arrhythmia. *Br J Anaesth* 1998; 80:164–8
206. Tzeng YC, Larsen PD, Galletly DC: Cardioventilatory Coupling in Resting Human Subjects. *Experimental Physiology* 2003; 88:775–82
207. Galletly D, Larsen P: Ventilatory frequency variability in spontaneously breathing anaesthetized subjects. *Br J Anaesth* 1999; 83:552–63

208. Stephan H, Sonntag H, Schenk HD, Kettler D, Khambatta HJ: Effects of propofol on cardiovascular dynamics, myocardial blood flow and myocardial metabolism in patients with coronary artery disease. *Br J Anaesth* 1986; 58:969–75
209. Grounds RM, Twigley A j., Carli F, Whitwam JG, Morgan M: The haemodynamic effects of intravenous induction. *Anaesthesia* 1985; 40:735–40
210. Daly WJ, Bondurant S: Effects of oxygen breathing on the heart rate, blood pressure, and cardiac index of normal men--resting, with reactive hyperemia, and after atropine. *J Clin Invest* 1962; 41:126–32
211. Parashar R, Amir M, Pakhare A, Rathi P, Chaudhary L: Age Related Changes in Autonomic Functions. *J Clin Diagn Res* 2016; 10:CC11–5
212. Stokes DN, Hutton P: Rate-dependent induction phenomena with propofol: implications for the relative potency of intravenous anesthetics. *Anesth Analg* 1991; 72:578–83
213. Galletly DC, Buckley DHF, Robinson BJ, Corfiatis T: Heart rate variability during propofol anaesthesia. *British Journal of Anaesthesia* 1994; 72:219–20
214. Deutschman CS, Harris AP, Fleisher LA: Changes in heart rate variability under propofol anesthesia: a possible explanation for propofol-induced bradycardia. *Anesth Analg* 1994; 79:373–7
215. Scheffer GJ, Ten Voorde BJ, Karemaker JM, Ros HH, Lange JJ de: Effects of thiopentone, etomidate and propofol on beat-to-beat cardiovascular signals in man. *Anaesthesia* 1993; 48:849–55
216. Paventi S, Santevecchi A, Ranieri R: Effects of sevoflurane versus propofol on QT interval. *Minerva Anesthesiol* 2001; 67:637–40

217. Tascanov MB, Tanriverdi Z, Gungoren F, Besli F, Bicer Yesilay A, Altiparmak HI, Bayram G, Demir K: The effect of propofol on frontal QRS-T angle in patients undergoing elective colonoscopy procedure. *Journal of Clinical Pharmacy and Therapeutics* 2020; 45:185–90
218. Puttick RM, Diedericks J, Sear JW, Glen JB, Foëx P, Ryder WA: Effect of graded infusion rates of propofol on regional and global left ventricular function in the dog. *Br J Anaesth* 1992; 69:375–81
219. Sprung J, Ogletree-Hughes ML, McConnell BK, Zakhary DR, Smolsky SM, Moravec CS: The effects of propofol on the contractility of failing and nonfailing human heart muscles. *Anesth Analg* 2001; 93:550–9
220. Moezzi N, Naddaf H, Avizeh R: Electrocardiographic Parameters in Healthy Dogs Anesthetized with Ketamine-propofol Combination and four Different Premedications. *IJAVA* 2014; 6:103–7
221. Lechinger J, Heib DPJ, Gruber W, Schabus M, Klimesch W: Heartbeat-related EEG amplitude and phase modulations from wakefulness to deep sleep: Interactions with sleep spindles and slow oscillations. *Psychophysiology* 2015; 52:1441–50
222. Pal D, Mashour GA: Consciousness, Anesthesia, and Acetylcholine. *Anesthesiology* 2021; 134:515–7
223. Benarroch EE: Interface between the Autonomic and Arousal Systems. *Autonomic Neuroscience: Basic and Clinical* 2015; 192:38
224. Naji M, Krishnan GP, McDevitt EA, Bazhenov M, Mednick SC: Timing between Cortical Slow Oscillations and Heart Rate Bursts during Sleep Predicts Temporal

- Processing Speed, but Not Offline Consolidation. *Journal of Cognitive Neuroscience* 2019; 31:1484–90
225. Glass L: Synchronization and rhythmic processes in physiology. *Nature* 2001; 410:277–84
226. Cole SR, Voytek B: Brain Oscillations and the Importance of Waveform Shape. *Trends in Cognitive Sciences* 2017; 21:137–49
227. Lo M-T, Novak V, Peng C-K, Liu Y, Hu K: Nonlinear phase interaction between nonstationary signals: A comparison study of methods based on Hilbert-Huang and Fourier transforms. *Phys Rev E Stat Nonlin Soft Matter Phys* 2009; 79:061924
228. Lozano-Soldevilla D, Huurne N ter, Oostenveld R: Neuronal Oscillations with Non-sinusoidal Morphology Produce Spurious Phase-to-Amplitude Coupling and Directionality. *Front Comput Neurosci* 2016; 10
229. Bartz S, Avarvand FS, Leicht G, Nolte G: Analyzing the waveshape of brain oscillations with bicoherence. *NeuroImage* 2019; 188:145–60
230. Belluscio MA, Mizuseki K, Schmidt R, Kempter R, Buzsáki G: Cross-Frequency Phase–Phase Coupling between Theta and Gamma Oscillations in the Hippocampus. *J Neurosci* 2012; 32:423–35
231. Cole SR, Meij R van der, Peterson EJ, Hemptinne C de, Starr PA, Voytek B: Nonsinusoidal Beta Oscillations Reflect Cortical Pathophysiology in Parkinson’s Disease. *J Neurosci* 2017; 37:4830–40
232. Pullon RM, McCabe S, Gaskell A, Sleight JW: Non-sinusoidal waves in the EEG and their simulated effect on anaesthetic quantitative EEG monitors. *J Clin Monit Comput* 2019; 33:1089–96

233. Huang NE, Shen Z, Long SR, Wu MC, Shih HH, Zheng Q, Yen N-C, Tung CC, Liu HH: The empirical mode decomposition and the Hilbert spectrum for nonlinear and non-stationary time series analysis. *Proceedings of the Royal Society of London Series A: Mathematical, Physical and Engineering Sciences* 1998; 454:903–95
234. Quinn AJ, Lopes-dos-Santos V, Huang N, Liang W-K, Juan C, Yeh J-R, Nobre AC, Dupret D, Woolrich MW: Within-cycle instantaneous frequency profiles report oscillatory waveform dynamics. *Journal of Neurophysiology* 2021; 0:0
235. Giehl J, Noury N, Siegel M: Dissociating harmonic and non-harmonic phase-amplitude coupling in the human brain. *NeuroImage* 2021; 227:117648
236. Yang Y, Deng J, Wu C: Analysis of Mode Mixing Phenomenon in the Empirical Mode Decomposition Method, 2009 Second International Symposium on Information Science and Engineering. Shanghai, China, IEEE, 2009, pp 553–6 doi:10.1109/ISISE.2009.19
237. Bueno-López M, Giraldo E, Molinas M, Fosso OB: The Mode Mixing Problem and its Influence in the Neural Activity Reconstruction. *IAENG International Journal of Computer Science* 2019; 46:11
238. Lundqvist M, Rose J, Herman P, Brincat SL, Buschman TJ, Miller EK: Gamma and Beta Bursts Underlie Working Memory. *Neuron* 2016; 90:152–64
239. Feingold J, Gibson DJ, DePasquale B, Graybiel AM: Bursts of beta oscillation differentiate postperformance activity in the striatum and motor cortex of monkeys performing movement tasks. *PNAS* 2015; 112:13687–92
240. Ede F van, Quinn AJ, Woolrich MW, Nobre AC: Neural Oscillations: Sustained Rhythms or Transient Burst-Events? *Trends in Neurosciences* 2018; 41:415–7



241. Wu Z, Huang NE: A study of the characteristics of white noise using the empirical mode decomposition method. *Proc R Soc Lond A* 2004; 460:1597–611
242. Flandrin P, Rilling G, Goncalves P: Empirical mode decomposition as a filter bank. *IEEE Signal Processing Letters* 2004; 11:112–4
243. Wu Z, Huang NE: Ensemble empirical mode decomposition: a noise-assisted data analysis method. *Adv Adapt Data Anal* 2009; 01:1–41
244. Deering R, Kaiser JF: The use of a masking signal to improve empirical mode decomposition, *Proceedings. (ICASSP '05). IEEE International Conference on Acoustics, Speech, and Signal Processing, 2005. 2005, p iv/485-iv/488 Vol. 4*
245. Wang Y-H, Hu K, Lo M-T: Uniform Phase Empirical Mode Decomposition: An Optimal Hybridization of Masking Signal and Ensemble Approaches. *IEEE Access* 2018; 6:34819–33
246. Wang H, Ji Y: A Revised Hilbert–Huang Transform and Its Application to Fault Diagnosis in a Rotor System. *Sensors* 2018; 18:4329
247. Yang Y, Deng J, Kang D: An improved empirical mode decomposition by using dyadic masking signals. *SIViP* 2015; 9:1259–63
248. Torres ME, Colominas MA, Schlotthauer G, Flandrin P: A complete ensemble empirical mode decomposition with adaptive noise, 2011 IEEE International Conference on Acoustics, Speech and Signal Processing (ICASSP). Prague, Czech Republic, IEEE, 2011, pp 4144–7 doi:10.1109/ICASSP.2011.5947265
249. Yeh J-R, Shieh J-S, Huang NE: Complementary ensemble empirical mode decomposition: a novel noise enhanced data analysis method. *Adv Adapt Data Anal* 2010; 02:135–56

250. Fosso OB, Molinas M: EMD Mode Mixing Separation of Signals with Close Spectral Proximity in Smart Grids, 2018 IEEE PES Innovative Smart Grid Technologies Conference Europe (ISGT-Europe). 2018, pp 1–6 doi:10.1109/ISGTEurope.2018.8571816
251. Rehman N, Mandic DP: Multivariate empirical mode decomposition. Proceedings of the Royal Society A: Mathematical, Physical and Engineering Sciences 2010; 466:1291–302
252. Huang W, Zeng J, Wang Z, Liang J: Partial noise assisted multivariate EMD: An improved noise assisted method for multivariate signals decomposition. Biomedical Signal Processing and Control 2017; 36:205–20
253. Li X, Li D, Liang Z, Voss LJ, Sleight JW: Analysis of depth of anesthesia with Hilbert–Huang spectral entropy. Clinical Neurophysiology 2008; 119:2465–75
254. Chen D, Li D, Xiong M, Bao H, Li X: GPGPU-Aided Ensemble Empirical-Mode Decomposition for EEG Analysis During Anesthesia. IEEE Transactions on Information Technology in Biomedicine 2010; 14:1417–27
255. Madanu R, Rahman F, Abbod MF, Fan S-Z, Shieh J-S: Depth of anesthesia prediction via EEG signals using convolutional neural network and ensemble empirical mode decomposition 2021 doi:10.3934/mbe.2021257
256. Wei Q, Liu Q, Fan S-Z, Lu C-W, Lin T-Y, Abbod MF, Shieh J-S: Analysis of EEG via Multivariate Empirical Mode Decomposition for Depth of Anesthesia Based on Sample Entropy. Entropy 2013; 15:3458–70
257. Huang J-R, Fan S-Z, Abbod MF, Jen K-K, Wu J-F, Shieh J-S: Application of Multivariate Empirical Mode Decomposition and Sample Entropy in EEG Signals

- via Artificial Neural Networks for Interpreting Depth of Anesthesia. *Entropy* 2013; 15:3325–39
258. Kortelainen J, Väyrynen E: Assessing EEG slow wave activity during anesthesia using Hilbert-Huang Transform, 2015 37th Annual International Conference of the IEEE Engineering in Medicine and Biology Society (EMBC). 2015, pp 117–20 doi:10.1109/EMBC.2015.7318314
259. Chen S-J, Peng C-J, Chen Y-C, Hwang Y-R, Lai Y-S, Fan S-Z, Jen K-K: Comparison of FFT and marginal spectra of EEG using empirical mode decomposition to monitor anesthesia. *Computer Methods and Programs in Biomedicine* 2016; 137:77–85
260. Sobolova G, Fabus MS, Fischer M, Drobny M, Drobna-Saniova B: Instantaneous EEG signal analysis based on empirical mode decomposition applied to burst-suppression in propofol anaesthesia. *General Reanimatology* 2021; 17
261. Fabus MS, Quinn AJ, Warnaby CE, Woolrich MW: Automatic decomposition of electrophysiological data into distinct nonsinusoidal oscillatory modes 2021; 126:pp 1670–84
262. Cole S, Voytek B: Cycle-by-cycle analysis of neural oscillations. *Journal of Neurophysiology* 2019; 122:849–61
263. Sherin B: Common sense clarified: The role of intuitive knowledge in physics problem solving. *J Res Sci Teach* 2006; 43:535–55
264. Boashash B: Estimating and interpreting the instantaneous frequency of a signal. I. Fundamentals. *Proceedings of the IEEE* 1992; 80:520–38
265. Huang NE, Wu Z, Long SR, Arnold KC, Chen X, Blank K: On instantaneous frequency. *Adv Adapt Data Anal* 2009; 01:177–229

266. Alabdulmohsin IM: Theorems and Methods on Partial Functional Iteration, Proceedings of the World Congress on Engineering 2009. 2009, p 7
267. Cranstoun SD, Ombao HC, Sachs R von, Wensheng Guo, Litt B: Time-frequency spectral estimation of multichannel EEG using the Auto-SLEX method. IEEE Trans Biomed Eng 2002; 49:988–96
268. Salmelin R, Hari R: Spatiotemporal characteristics of sensorimotor neuromagnetic rhythms related to thumb movement. Neuroscience 1994; 60:537–50
269. Sedgwick P: Multiple significance tests: the Bonferroni correction. BMJ 2012; 344:e509
270. Mizuseki K, Diba K, Pastalkova E, Teeters J, Sirota A, Buzsáki G: Neurosharing: large-scale data sets (spike, LFP) recorded from the hippocampal-entorhinal system in behaving rats. F1000Res 2014; 3
271. Mizuseki K, Sirota A, Pastalkova E, Diba K, Buzsáki G: Multiple single unit recordings from different rat hippocampal and entorhinal regions while the animals were performing multiple behavioral tasks. CRCNS.org 2013 at <<http://dx.doi.org/10.6080/K09G5JRZ>>
272. Shafto MA, Tyler LK, Dixon M, Taylor JR, Rowe JB, Cusack R, Calder AJ, Marslen-Wilson WD, Duncan J, Dalgleish T, Henson RN, Brayne C, Matthews FE, Cam-CAN: The Cambridge Centre for Ageing and Neuroscience (Cam-CAN) study protocol: a cross-sectional, lifespan, multidisciplinary examination of healthy cognitive ageing. BMC Neurology 2014; 14:204
273. Taylor JR, Williams N, Cusack R, Auer T, Shafto MA, Dixon M, Tyler LK, Cam-CAN, Henson RN: The Cambridge Centre for Ageing and Neuroscience (Cam-

- CAN) data repository: Structural and functional MRI, MEG, and cognitive data from a cross-sectional adult lifespan sample. *NeuroImage* 2017; 144:262–9
274. Steyn-Ross ML, Steyn-Ross DA, Sleight JW: Modelling general anaesthesia as a first-order phase transition in the cortex. *Progress in Biophysics and Molecular Biology* 2004; 85:369–85
275. Csercsa R, Dombovári B, Fabó D, Wittner L, Erőss L, Entz L, Sólyom A, Rásonyi G, Szűcs A, Kelemen A, Jakus R, Juhos V, Grand L, Magony A, Halász P, Freund TF, Maglóczy Z, Cash SS, Papp L, Karmos G, Halgren E, Ulbert I: Laminar analysis of slow wave activity in humans. *Brain* 2010; 133:2814–29
276. Kallionpää RE, Valli K, Scheinin A, Långsjö J, Maksimow A, Vahlberg T, Revonsuo A, Scheinin H, Mashour GA, Li D: Alpha band frontal connectivity is a state-specific electroencephalographic correlate of unresponsiveness during exposure to dexmedetomidine and propofol. *British Journal of Anaesthesia* 2020; 125:518–28
277. Blanca MJ, Alarcón R, Arnau J, Bono R, Bendayan R: Non-normal data: Is ANOVA still a valid option? *Psicothema* 2017; 29:552–7
278. Quinn AJ, Lopes-dos-Santos V, Dupret D, Nobre AC, Woolrich MW: EMD: Empirical Mode Decomposition and Hilbert-Huang Spectral Analyses in Python. *J Open Source Softw* 2021; 6:2977
279. Harris CR, Millman KJ, Walt SJ van der, Gommers R, Virtanen P, Cournapeau D, Wieser E, Taylor J, Berg S, Smith NJ, Kern R, Picus M, Hoyer S, Kerkwijk MH van, Brett M, Haldane A, Río JF del, Wiebe M, Peterson P, Gérard-Marchant P, Sheppard K, Reddy T, Weckesser W, Abbasi H, Gohlke C, Oliphant TE: Array programming with NumPy. *Nature* 2020; 585:357–62

280. Virtanen P, Gommers R, Oliphant TE, Haberland M, Reddy T, Cournapeau D, Burovski E, Peterson P, Weckesser W, Bright J, Walt SJ van der, Brett M, Wilson J, Millman KJ, Mayorov N, Nelson ARJ, Jones E, Kern R, Larson E, Carey CJ, Polat I, Feng Y, Moore EW, VanderPlas J, Laxalde D, Perktold J, Cimrman R, Henriksen I, Quintero EA, Harris CR, et al.: SciPy 1.0: fundamental algorithms for scientific computing in Python. *Nature Methods* 2020; 17:261–72
281. Reback J, jbrockmendel, McKinney W, Bossche JV den, Augspurger T, Cloud P, Hawkins S, gyoung, Roeschke M, Sinhrks, Klein A, Petersen T, Tratner J, She C, Ayd W, Hoefler P, Naveh S, Garcia M, Schendel J, Hayden A, Saxton D, Darbyshire JHM, Shadrach R, Gorelli ME, Li F, Zeitlin M, Jancauskas V, McMaster A, Battiston P, Seabold S: pandas-dev/pandas: Pandas 1.3.4 2021 doi:10.5281/zenodo.5574486
282. Vallat R: Pinguin: statistics in Python. *Journal of Open Source Software* 2018; 3:1026
283. Seabold S, Perktold J: Statsmodels: Econometric and Statistical Modeling with Python, *Proceedings of the Python in Science Conference* 2010. 2010, pp 92–6 doi:10.25080/Majora-92bf1922-011
284. Hunter JD: Matplotlib: A 2D Graphics Environment. *Computing in Science Engineering* 2007; 9:90–5
285. Donoghue T, Haller M, Peterson EJ, Varma P, Sebastian P, Gao R, Noto T, Lara AH, Wallis JD, Knight RT, Shestyuk A, Voytek B: Parameterizing neural power spectra into periodic and aperiodic components. *Nat Neurosci* 2020; 23:1655–65

286. Buzsáki G, Czopf J, Kondákor I, Kellényi L: Laminar distribution of hippocampal rhythmic slow activity (RSA) in the behaving rat: Current-source density analysis, effects of urethane and atropine. *Brain Research* 1986; 365:125–37
287. Buzsáki G, Rappelsberger P, Kellényi L: Depth profiles of hippocampal rhythmic slow activity ('theta rhythm') depend on behaviour. *Electroencephalogr Clin Neurophysiol* 1985; 61:77–88
288. Haegens S, Cousijn H, Wallis G, Harrison PJ, Nobre AC: Inter- and intra-individual variability in alpha peak frequency. *NeuroImage* 2014; 92:46–55
289. Klimesch W: EEG-alpha rhythms and memory processes. *International Journal of Psychophysiology* 1997; 26:319–40
290. Newson JJ, Thiagarajan TC: EEG Frequency Bands in Psychiatric Disorders: A Review of Resting State Studies. *Frontiers in Human Neuroscience* 2019; 12:521
291. Siapas AG, Lubenov EV, Wilson MA: Prefrontal Phase Locking to Hippocampal Theta Oscillations. *Neuron* 2005; 46:141–51
292. Gips B, Bahramisharif A, Lowet E, Roberts MJ, Weerd P de, Jensen O, Eerden J van der: Discovering recurring patterns in electrophysiological recordings. *Journal of Neuroscience Methods* 2017; 275:66–79
293. Jas M, Tour TD la, Simsekli U, Gramfort A: Learning the Morphology of Brain Signals Using Alpha-Stable Convolutional Sparse Coding, NIPS. 2017
294. Quinn AJ, Green GGR, Hymers M: Delineating between-subject heterogeneity in alpha networks with Spatio-Spectral Eigenmodes. *NeuroImage* 2021; 240:118330

295. Gerber EM, Sadeh B, Ward A, Knight RT, Deouell LY: Non-Sinusoidal Activity Can Produce Cross-Frequency Coupling in Cortical Signals in the Absence of Functional Interaction between Neural Sources. *PLOS ONE* 2016; 11:e0167351
296. Riedner BA, Vyazovskiy VV, Huber R, Massimini M, Esser S, Murphy M, Tononi G: Sleep Homeostasis and Cortical Synchronization: III. A High-Density EEG Study of Sleep Slow Waves in Humans. *Sleep* 2007; 30:1643–57
297. Litscher G, Schwarz G: Is there paradoxical arousal reaction in the EEG subdelta range in patients during anesthesia. *J Neurosurg Anesthesiol* 1999; 11:49–52
298. Fabus MS, Quinn AJ, Warnaby CE, Woolrich MW: Automatic decomposition of electrophysiological data into distinct non-sinusoidal oscillatory modes. *Journal of Neurophysiology* 2021 doi:10.1152/jn.00315.2021
299. García PS, Kreuzer M, Hight D, Sleight JW: Effects of noxious stimulation on the electroencephalogram during general anaesthesia: a narrative review and approach to analgesic titration. *British Journal of Anaesthesia* 2021; 126:445–57
300. Shih M-T, Doctor F, Fan S-Z, Jen K-K, Shieh J-S: Instantaneous 3D EEG Signal Analysis Based on Empirical Mode Decomposition and the Hilbert–Huang Transform Applied to Depth of Anaesthesia. *Entropy* 2015; 17:928–49
301. Martínez SA, Llera A, Horst G ter, Vidaurre D: Can fMRI functional connectivity index dynamic neural communication? *bioRxiv* 2021:2021.07. 27.453965
302. Mensen A, Riedner B, Tononi G: Optimizing detection and analysis of slow waves in sleep EEG. *Journal of Neuroscience Methods* 2016; 274:1–12
303. Oizumi M, Albantakis L, Tononi G: From the Phenomenology to the Mechanisms of Consciousness: Integrated Information Theory 3.0. *PLOS Computational Biology* 2014; 10:e1003588



304. Carhart-Harris RL: The entropic brain - revisited. *Neuropharmacology* 2018; 142:167–78
305. Dehaene S, Changeux J-P, Naccache L: *The Global Neuronal Workspace Model of Conscious Access: From Neuronal Architectures to Clinical Applications, Characterizing Consciousness: From Cognition to the Clinic?* Edited by Dehaene S, Christen Y. Berlin, Heidelberg, Springer, 2011, pp 55–84 doi:10.1007/978-3-642-18015-6\_4
306. Lee U, Mashour GA, Kim S, Noh G-J, Choi B-M: Propofol induction reduces the capacity for neural information integration: implications for the mechanism of consciousness and general anesthesia. *Conscious Cogn* 2009; 18:56–64
307. Luppi AI, Golkowski D, Ranft A, Ilg R, Jordan D, Menon DK, Stamatakis EA: Brain network integration dynamics are associated with loss and recovery of consciousness induced by sevoflurane. *Human Brain Mapping* 2021; 42:2802–22
308. Demertzi A, Tagliazucchi E, Dehaene S, Deco G, Barttfeld P, Raimondo F, Martial C, Fernández-Espejo D, Rohaut B, Voss HU, Schiff ND, Owen AM, Laureys S, Naccache L, Sitt JD: Human consciousness is supported by dynamic complex patterns of brain signal coordination. *Science Advances* 2019; 5:eaat7603
309. Huang Z, Zhang J, Wu J, Mashour GA, Hudetz AG: Temporal circuit of macroscale dynamic brain activity supports human consciousness. *Science Advances* 2020; 6:eaaz0087
310. Luppi AI, Mediano PAM, Rosas FE, Allanson J, Pickard JD, Williams GB, Craig MM, Finoia P, Peattie ARD, Coppola P, Owen AM, Naci L, Menon DK, Bor D, Stamatakis EA: Whole-brain modelling identifies distinct but convergent paths to

- unconsciousness in anaesthesia and disorders of consciousness. *Commun Biol* 2022; 5:1–15
311. Luppi AI, Vohryzek J, Kringelbach ML, Mediano PAM, Craig MM, Adapa R, Carhart-Harris RL, Roseman L, Pappas I, Peattie ARD, Manktelow AE, Sahakian BJ, Finoia P, Williams GB, Allanson J, Pickard JD, Menon DK, Atasoy S, Stamatakis EA: Distributed harmonic patterns of structure-function dependence orchestrate human consciousness. *Commun Biol* 2023; 6:1–19
312. Schartner MM, Carhart-Harris RL, Barrett AB, Seth AK, Muthukumaraswamy SD: Increased spontaneous MEG signal diversity for psychoactive doses of ketamine, LSD and psilocybin. *Sci Rep* 2017; 7:46421
313. Varley TF, Sporns O, Puce A, Beggs J: Differential effects of propofol and ketamine on critical brain dynamics. *PLOS Computational Biology* 2020; 16:e1008418
314. Varley TF, Denny V, Sporns O, Patania A: Topological analysis of differential effects of ketamine and propofol anaesthesia on brain dynamics. *Royal Society open science* 2021; 8:201971
315. Varley TF, Carhart-Harris R, Roseman L, Menon DK, Stamatakis EA: Serotonergic psychedelics LSD & psilocybin increase the fractal dimension of cortical brain activity in spatial and temporal domains. *NeuroImage* 2020; 220:117049
316. Vidaurre D, Smith SM, Woolrich MW: Brain network dynamics are hierarchically organized in time. *Proceedings of the National Academy of Sciences* 2017; 114:12827–32

317. Quinn AJ, Ede F van, Brookes MJ, Heideman SG, Nowak M, Seedat ZA, Vidaurre D, Zich C, Nobre AC, Woolrich MW: Unpacking Transient Event Dynamics in Electrophysiological Power Spectra. *Brain Topogr* 2019; 32:1020–34
318. Bai Y, He J, Xia X, Wang Y, Yang Y, Di H, Li X, Ziemann U: Spontaneous transient brain states in EEG source space in disorders of consciousness. *NeuroImage* 2021; 240:118407
319. Vidaurre D, Llera A, Smith SM, Woolrich MW: Behavioural relevance of spontaneous, transient brain network interactions in fMRI. *NeuroImage* 2021; 229:117713
320. Higgins C, Liu Y, Vidaurre D, Kurth-Nelson Z, Dolan R, Behrens T, Woolrich M: Replay bursts in humans coincide with activation of the default mode and parietal alpha networks. *Neuron* 2021; 109:882-893.e7
321. Khawaldeh S, Tinkhauser G, Torrecillos F, He S, Foltynie T, Limousin P, Zrinzo L, Oswal A, Quinn AJ, Vidaurre D, Tan H, Litvak V, Kühn A, Woolrich M, Brown P: Balance between competing spectral states in subthalamic nucleus is linked to motor impairment in Parkinson's disease. *Brain* 2022; 145:237–50
322. Charquero-Ballester M, Kleim B, Vidaurre D, Ruff C, Stark E, Tuulari JJ, McManners H, Bar-Haim Y, Bouquillon L, Moseley A, Williams SCR, Woolrich MW, Kringelbach ML, Ehlers A: Effective psychological therapy for PTSD changes the dynamics of specific large-scale brain networks. *Human Brain Mapping* 2022; 43:3207–20
323. Candia-Rivera D, Machado C: Changes in the heartbeat-evoked potential under ventricular fibrillation: a near-death case report

324. Seth AK: Interoceptive inference, emotion, and the embodied self. *Trends Cogn Sci* 2013; 17:565–73
325. Song J, Davey C, Poulsen C, Luu P, Turovets S, Anderson E, Li K, Tucker D: EEG source localization: Sensor density and head surface coverage. *Journal of Neuroscience Methods* 2015; 256:9–21
326. Soler A, Moctezuma LA, Giraldo E, Molinas M: Automated methodology for optimal selection of minimum electrode subsets for accurate EEG source estimation based on Genetic Algorithm optimization. *Sci Rep* 2022; 12:11221
327. Moctezuma LA, Molinas M: EEG channel-selection method for epileptic-seizure classification based on multi-objective optimization. *Frontiers in neuroscience* 2020; 14:593
328. Stenwig H, Soler A, Furuki J, Suzuki Y, Abe T, Molinas M: Automatic Sleep Stage Classification with Optimized Selection of EEG Channels. *bioRxiv* 2022:2022.06.14.496176
329. Van Essen DC, Smith SM, Barch DM, Behrens TEJ, Yacoub E, Ugurbil K: The WU-Minn Human Connectome Project: An Overview. *Neuroimage* 2013; 80:62–79
330. Rubinov M, Sporns O: Complex network measures of brain connectivity: Uses and interpretations. *NeuroImage* 2010; 52:1059–69
331. Mashour GA, Hudetz AG: Neural Correlates of Unconsciousness in Large-Scale Brain Networks. *Trends in Neurosciences* 2018; 41:150–60
332. Hudetz AG, Humphries CJ, Binder JR: Spin-glass model predicts metastable brain states that diminish in anesthesia. *Frontiers in systems neuroscience* 2014; 8:234

333. Hudetz AG, Liu X, Pillay S: Dynamic Repertoire of Intrinsic Brain States Is Reduced in Propofol-Induced Unconsciousness. *Brain Connectivity* 2015; 5:10–22
334. Wenzel M, Han S, Smith EH, Hoel E, Greger B, House PA, Yuste R: Reduced Repertoire of Cortical Microstates and Neuronal Ensembles in Medically Induced Loss of Consciousness. *Cell Systems* 2019; 8:467-474.e4
335. Purdon PL, Pierce ET, Mukamel EA, Prerau MJ, Walsh JL, Wong KFK, Salazar-Gomez AF, Harrell PG, Sampson AL, Cimenser A, Ching S, Kopell NJ, Tavares-Stoeckel C, Habeeb K, Merhar R, Brown EN: Electroencephalogram signatures of loss and recovery of consciousness from propofol. *PNAS* 2013; 110:E1142–51
336. Vijayan S, Ching S, Purdon PL, Brown EN, Kopell NJ: Thalamocortical Mechanisms for the Anteriorization of Alpha Rhythms during Propofol-Induced Unconsciousness. *J Neurosci* 2013; 33:11070–5
337. Zhang K, Shi W, Wang C, Li Y, Liu Z, Liu T, Li J, Yan X, Wang Q, Cao Z, Wang G: Reliability of EEG microstate analysis at different electrode densities during propofol-induced transitions of brain states. *NeuroImage* 2021; 231:117861
338. Lapointe AP, Li D, Hudetz AG, Vlisides PE: Microstate analyses as an indicator of anesthesia-induced unconsciousness. *Clinical Neurophysiology* 2023; 147:81–7
339. Shi W, Li Y, Liu Z, Li J, Wang Q, Yan X, Wang G: Non-Canonical Microstate Becomes Salient in High Density EEG During Propofol-Induced Altered States of Consciousness. *Int J Neur Syst* 2020; 30:2050005

340. Artoni F, Maillard J, Britz J, Seeber M, Lysakowski C, Bréchet L, Tramèr M, Michel C: EEG microstate dynamics indicate a U-shaped path to propofol-induced loss of consciousness 2021 doi:10.1101/2021.10.26.465841
341. Rukat T, Baker A, Quinn A, Woolrich M: Resting state brain networks from EEG: Hidden Markov states vs. classical microstates 2016 doi:10.48550/arXiv.1606.02344
342. Chavan M, Agarwala R, Uplane M: Suppression of noise in the ECG signal using digital IIR filter 2008
343. Park H-D, Blanke O: Heartbeat-evoked cortical responses: Underlying mechanisms, functional roles, and methodological considerations. *NeuroImage* 2019; 197:502–11
344. Coll M-P, Hobson H, Bird G, Murphy J: Systematic review and meta-analysis of the relationship between the heartbeat-evoked potential and interoception. *Neuroscience & Biobehavioral Reviews* 2021; 122:190–200
345. Martuzzi R, Ramani R, Qiu M, Shen X, Papademetris X, Constable RT: A whole-brain voxel based measure of intrinsic connectivity contrast reveals local changes in tissue connectivity with anesthetic without a priori assumptions on thresholds or regions of interest. *NeuroImage* 2011; 58:1044–50
346. Hudetz AG, Mashour GA: Disconnecting Consciousness: Is There a Common Anesthetic End Point? *Anesthesia & Analgesia* 2016; 123:1228–40
347. McLachlan G: Treatment resistant depression: what are the options? *BMJ* 2018; 363:k5354
348. Marwaha S, Palmer E, Suppes T, Cons E, Young AH, Upthegrove R: Novel and emerging treatments for major depression. *The Lancet* 2023; 401:141–53

349. Rotz R von, Schindowski EM, Jungwirth J, Schuldt A, Rieser NM, Zahoranszky K, Seifritz E, Nowak A, Nowak P, Jäncke L, Preller KH, Vollenweider FX: Single-dose psilocybin-assisted therapy in major depressive disorder: A placebo-controlled, double-blind, randomised clinical trial. *eClinicalMedicine* 2023; 56
350. Nagele P, Duma A, Kopec M, Gebara MA, Parsoei A, Walker M, Janski A, Panagopoulos VN, Cristancho P, Miller JP, Zorumski CF, Conway CR: Nitrous Oxide for Treatment-Resistant Major Depression: A Proof-of-Concept Trial. *Biological Psychiatry* 2015; 78:10–8
351. Mitchell JM, Bogenschutz M, Lilienstein A, Harrison C, Kleiman S, Parker-Guilbert K, Ot'abora G. M, Garas W, Paleos C, Gorman I, Nicholas C, Mithoefer M, Carlin S, Poulter B, Mithoefer A, Quevedo S, Wells G, Klaire SS, Kolk B van der, Tzarfaty K, Amiaz R, Worthy R, Shannon S, Woolley JD, Marta C, Gelfand Y, Hapke E, Amar S, Wallach Y, Brown R, et al.: MDMA-assisted therapy for severe PTSD: a randomized, double-blind, placebo-controlled phase 3 study. *Nat Med* 2021; 27:1025–33
352. DiVito AJ, Leger RF: Psychedelics as an emerging novel intervention in the treatment of substance use disorder: a review. *Mol Biol Rep* 2020; 47:9791–9
353. Aleksandrova LR, Phillips AG: Neuroplasticity as a convergent mechanism of ketamine and classical psychedelics. *Trends in Pharmacological Sciences* 2021; 42:929–42
354. Mickey BJ, White AT, Arp AM, Leonardi K, Torres MM, Larson AL, Odell DH, Whittingham SA, Beck MM, Jessop JE, Sakata DJ, Bushnell LA, Pierson MD, Solzbacher D, Kendrick EJ, Weeks HR, Light AR, Light KC, Tadler SC: Propofol

- for Treatment-Resistant Depression: A Pilot Study. *Int J Neuropsychopharmacol* 2018; 21:1079–89
355. Weeks HR, Tadler SC, Smith KW, Iacob E, Saccoman M, White AT, Landvatter JD, Chelune GJ, Suchy Y, Clark E, Cahalan MK, Bushnell L, Sakata D, Light AR, Light KC: Antidepressant and Neurocognitive Effects of Isoflurane Anesthesia versus Electroconvulsive Therapy in Refractory Depression. *PLoS One* 2013; 8:e69809
356. Zanos P, Thompson SM, Duman RS, Zarate CA, Gould TD: Convergent mechanisms underlying rapid antidepressant action. *CNS Drugs* 2018; 32:197–227
357. Wang J, Sun Y, Ai P, Cui V, Shi H, An D, Wu A, Wei C: The effect of intravenous ketamine on depressive symptoms after surgery: A systematic review. *J Clin Anesth* 2022; 77:110631
358. Guo J, Qiu D, Gu H, Wang X, Hashimoto K, Zhang G, Yang J: Efficacy and safety of perioperative application of ketamine on postoperative depression: A meta-analysis of randomized controlled studies. *Mol Psychiatry* 2023:1–11 doi:10.1038/s41380-023-01945-z
359. Berman RM, Cappiello A, Anand A, Oren DA, Heninger GR, Charney DS, Krystal JH: Antidepressant effects of ketamine in depressed patients. *Biol Psychiatry* 2000; 47:351–4
360. Corrigan A, Pickering G: Ketamine and depression: a narrative review. *Drug Des Devel Ther* 2019; 13:3051–67
361. Diamond PR, Farmery AD, Atkinson S, Haldar J, Williams N, Cowen PJ, Geddes JR, McShane R: Ketamine infusions for treatment resistant depression: a series



- of 28 patients treated weekly or twice weekly in an ECT clinic. *Journal of Psychopharmacology* 2014; 28:536–44
362. Tsai YC, Kuo H-C: Ketamine cystitis: Its urological impact and management. *Urological Science* 2015; 26:153–7
363. Bonnett CJ, Jain R, Ross CN, Wallington DA, Schock TR: Intramuscular ketamine to treat major depressive disorder: a case series of forty patients. *J Psychiatry Ment Heal* 2021; 6:1–4
364. Le TT, Cordero IP, Jawad MY, Swainson J, Di Vincenzo JD, Jaber S, Phan L, Lui LMW, Ho R, Rosenblat JD, McIntyre RS: The abuse liability of ketamine: A scoping review of preclinical and clinical studies. *Journal of Psychiatric Research* 2022; 151:476–96
365. McIntyre RS, Rosenblat JD, Nemeroff CB, Sanacora G, Murrough JW, Berk M, Brietzke E, Dodd S, Gorwood P, Ho R, Iosifescu DV, Lopez Jaramillo C, Kasper S, Kratiuk K, Lee JG, Lee Y, Lui LMW, Mansur RB, Papakostas GI, Subramaniapillai M, Thase M, Vieta E, Young AH, Zarate CA, Stahl S: Synthesizing the Evidence for Ketamine and Esketamine in Treatment-Resistant Depression: An International Expert Opinion on the Available Evidence and Implementation. *AJP* 2021; 178:383–99
366. Domino EF, Warner DS: Taming the Ketamine Tiger. *Anesthesiology* 2010; 113:678–84
367. Domino EF, Chodoff P, Corssen G: Pharmacologic effects of CI-581, a new dissociative anesthetic, in man. *Clinical Pharmacology & Therapeutics* 1965; 6:279–91

368. Denomme N: The Domino Effect: Ed Domino's early studies of Psychoactive Drugs. *J Psychoactive Drugs* 2018; 50:298–305
369. Moreau JJ: Du hachisch et de l'aliénation mentale : études psychologiques. Paris : Fortin, Masson, 1845 at <<http://archive.org/details/duhachischetdela00more>>
370. Dissociation and the dissociative disorders: DSM-V and beyond. New York, NY, US, Routledge/Taylor & Francis Group, 2009, pp xxxiv, 864
371. Krystal JH, Karper LP, Seibyl JP, Freeman GK, Delaney R, Bremner JD, Heninger GR, Bowers MB, Charney DS: Subanesthetic effects of the noncompetitive NMDA antagonist, ketamine, in humans. Psychotomimetic, perceptual, cognitive, and neuroendocrine responses. *Arch Gen Psychiatry* 1994; 51:199–214
372. Frohlich J, Van Horn JD: Reviewing the ketamine model for schizophrenia. *J Psychopharmacol* 2014; 28:287–302
373. Corlett PR, Honey GD, Fletcher PC: Prediction error, ketamine and psychosis: An updated model. *Journal of psychopharmacology* 2016; 30:1145–55
374. Kolp E, Friedman H, Krupitsky E, Jansen K, Sylvester M, Young M, Kolp A: Ketamine Psychedelic Psychotherapy: Focus on its Pharmacology, Phenomenology, and Clinical Applications. *International Journal of Transpersonal Studies* 2014; 33
375. Neehoff S, Glue P: Dissociation after ketamine dosing: Is the CADSS fit for purpose? *Journal of Affective Disorders* 2019; 244:239–40
376. Schalkwyk GI van, Wilkinson ST, Davidson L, Silverman WK, Sanacora G: Acute psychoactive effects of intravenous ketamine during treatment of mood disorders:

- Analysis of the Clinician Administered Dissociative State Scale. *Journal of Affective Disorders* 2018; 227:11–6
377. Bremner JD, Krystal JH, Putnam FW, Southwick SM, Marmar C, Charney DS, Mazure CM: Measurement of dissociative states with the Clinician-Administered Dissociative States Scale (CADSS). *Journal of Traumatic Stress* 1998; 11:125–36
378. Salle S de la, Choueiry J, Shah D, Bowers H, McIntosh J, Ilivitsky V, Knott V: Effects of Ketamine on Resting-State EEG Activity and Their Relationship to Perceptual/Dissociative Symptoms in Healthy Humans. *Frontiers in Pharmacology* 2016; 7:348
379. Vlisides PE, Bel-Bahar T, Lee U, Li D, Kim H, Janke E, Tarnal V, Pichurko AB, McKinney AM, Kunkler BS, Picton P, Mashour GA: Neurophysiologic Correlates of Ketamine Sedation and Anesthesia: A High-density Electroencephalography Study in Healthy Volunteers. *Anesthesiology* 2017; 127:58–69
380. Vlisides PE, Bel-Bahar T, Nelson A, Chilton K, Smith E, Janke E, Tarnal V, Picton P, Harris RE, Mashour GA: Subanaesthetic ketamine and altered states of consciousness in humans. *British Journal of Anaesthesia* 2018; 121:249–59
381. Farnes N, Juel BE, Nilsen AS, Romundstad LG, Storm JF: Increased signal diversity/complexity of spontaneous EEG, but not evoked EEG responses, in ketamine-induced psychedelic state in humans. *PLoS One* 2020; 15:e0242056
382. Li D, Vlisides PE, Mashour GA: Dynamic reconfiguration of frequency-specific cortical coactivation patterns during psychedelic and anesthetized states induced by ketamine. *NeuroImage* 2022; 249:118891

383. Salle S de la, Choueiry J, Shah D, Bowers H, McIntosh J, Ilivitsky V, Carroll B, Knott V: Resting-state functional EEG connectivity in salience and default mode networks and their relationship to dissociative symptoms during NMDA receptor antagonism. *Pharmacology Biochemistry and Behavior* 2021; 201:173092
384. Chamadia S, Gitlin J, Mekonnen J, Ethridge BR, Ibala R, Colon KM, Qu J, Akeju O: Ketamine induces EEG oscillations that may aid anesthetic state but not dissociation monitoring. *Clinical Neurophysiology* 2021; 132:3010–8
385. Molnar-Szakacs I, Uddin LQ: Anterior insula as a gatekeeper of executive control. *Neuroscience & Biobehavioral Reviews* 2022; 139:104736
386. Sleight J, Warnaby C, Tracey I: General anaesthesia as fragmentation of selfhood: insights from electroencephalography and neuroimaging. *Br J Anaesth* 2018; 121:233–40
387. Williams NR, Heifets BD, Blasey C, Sudheimer K, Pannu J, Pankow H, Hawkins J, Birnbaum J, Lyons DM, Rodriguez CI, Schatzberg AF: Opioid Receptor Antagonism Attenuates Antidepressant Effects of Ketamine. *Am J Psychiatry* 2018; 175:1205–15
388. Markello RD, Hansen JY, Liu Z-Q, Bazinet V, Shafiei G, Suárez LE, Blostein N, Seidlitz J, Baillet S, Satterthwaite TD, Chakravarty MM, Raznahan A, Misic B: neuromaps: structural and functional interpretation of brain maps. *Nat Methods* 2022; 19:1472–9
389. Studerus E, Gamma A, Vollenweider FX: Psychometric Evaluation of the Altered States of Consciousness Rating Scale (OAV). *PLOS ONE* 2010; 5:e12412

390. Delorme A, Makeig S: EEGLAB: an open source toolbox for analysis of single-trial EEG dynamics including independent component analysis. *Journal of Neuroscience Methods* 2004; 134:9–21
391. Artoni F, Menicucci D, Delorme A, Makeig S, Micera S: RELICA: a method for estimating the reliability of independent components. *Neuroimage* 2014; 103:391–400
392. Westner BU, Dalal SS, Gramfort A, Litvak V, Mosher JC, Oostenveld R, Schoffelen J-M: A unified view on beamformers for M/EEG source reconstruction. *NeuroImage* 2022; 246:118789
393. Thomas Yeo BT, Krienen FM, Sepulcre J, Sabuncu MR, Lashkari D, Hollinshead M, Roffman JL, Smoller JW, Zöllei L, Polimeni JR, Fischl B, Liu H, Buckner RL: The organization of the human cerebral cortex estimated by intrinsic functional connectivity. *J Neurophysiol* 2011; 106:1125–65
394. Colclough GL, Brookes MJ, Smith SM, Woolrich MW: A symmetric multivariate leakage correction for MEG connectomes. *NeuroImage* 2015; 117:439–48
395. Baker AP, Brookes MJ, Rezek IA, Smith SM, Behrens T, Probert Smith PJ, Woolrich M: Fast transient networks in spontaneous human brain activity. *eLife* Edited by Culham JC. 2014; 3:e01867
396. Andersen CM, Bro R: Variable selection in regression—a tutorial. *Journal of Chemometrics* 2010; 24:728–37
397. Burt JB, Helmer M, Shinn M, Anticevic A, Murray JD: Generative modeling of brain maps with spatial autocorrelation. *NeuroImage* 2020; 220:117038

398. Krigolson OE, Williams CC, Norton A, Hassall CD, Colino FL: Choosing MUSE: Validation of a Low-Cost, Portable EEG System for ERP Research. *Frontiers in Neuroscience* 2017; 11
399. Critchley HD, Harrison NA: Visceral Influences on Brain and Behavior. *Neuron* 2013; 77:624–38
400. Morgan HL, Turner DC, Corlett PR, Absalom AR, Adapa R, Arana FS, Pigott J, Gardner J, Everitt J, Haggard P, Fletcher PC: Exploring the Impact of Ketamine on the Experience of Illusory Body Ownership. *Biological Psychiatry* 2011; 69:35–41
401. Marguilho M, Figueiredo I, Castro-Rodrigues P: A unified model of ketamine's dissociative and psychedelic properties. *J Psychopharmacol* 2023; 37:14–32
402. Park H-D, Bernasconi F, Salomon R, Tallon-Baudry C, Spinelli L, Seeck M, Schaller K, Blanke O: Neural Sources and Underlying Mechanisms of Neural Responses to Heartbeats, and their Role in Bodily Self-consciousness: An Intracranial EEG Study. *Cereb Cortex* 2018; 28:2351–64
403. Schulz A, Köster S, Beutel ME, Schächinger H, Vögele C, Rost S, Rauh M, Michal M: Altered Patterns of Heartbeat-Evoked Potentials in Depersonalization/Derealization Disorder: Neurophysiological Evidence for Impaired Cortical Representation of Bodily Signals. *Psychosomatic Medicine* 2015; 77:506
404. Terhaar J, Viola FC, Bär K-J, Debener S: Heartbeat evoked potentials mirror altered body perception in depressed patients. *Clinical Neurophysiology* 2012; 123:1950–7

405. Weber LA, Diaconescu AO, Mathys C, Schmidt A, Kometer M, Vollenweider F, Stephan KE: Ketamine affects prediction errors about statistical regularities: a computational single-trial analysis of the mismatch negativity. *Journal of Neuroscience* 2020; 40:5658–68
406. Petzschner FH, Weber LA, Wellstein KV, Paolini G, Do CT, Stephan KE: Focus of attention modulates the heartbeat evoked potential. *NeuroImage* 2019; 186:595–606
407. Muthukumaraswamy S: High-frequency brain activity and muscle artifacts in MEG/EEG: A review and recommendations. *Frontiers in Human Neuroscience* 2013; 7
408. Klimesch W: Alpha-band oscillations, attention, and controlled access to stored information. *Trends in Cognitive Sciences* 2012; 16:606–17
409. Salami A, Andreu-Perez J, Gillmeister H: Symptoms of depersonalisation/derealisation disorder as measured by brain electrical activity: A systematic review. *Neuroscience & Biobehavioral Reviews* 2020; 118:524–37
410. Warnaby CE, Seretny M, Ní Mhuircheartaigh R, Rogers R, Jbabdi S, Sleigh J, Tracey I: Anesthesia-induced Suppression of Human Dorsal Anterior Insula Responsivity at Loss of Volitional Behavioral Response. *Anesthesiology* 2016; 124:766–78
411. Sen ZD, Scheer J, Danyeli LV, Colic L, Walter M: The effect of ketamine infusion on interoceptive accuracy in healthy adults, Kongress der Deutschen Gesellschaft für Psychiatrie und Psychotherapie, Psychosomatik und Nervenheilkunde e. V.(DGPPN 2018). 2018, p 220

412. Ho JT, Preller KH, Lenggenger B: Neuropharmacological modulation of the aberrant bodily self through psychedelics. *Neuroscience & Biobehavioral Reviews* 2020; 108:526–41
413. Letheby C, Gerrans P: Self unbound: ego dissolution in psychedelic experience. *Neuroscience of Consciousness* 2017; 2017:nix016
414. Dai R, Larkin TE, Huang Z, Tarnal V, Picton P, Vlisides PE, Janke E, McKinney A, Hudetz AG, Harris RE, Mashour GA: Classical and non-classical psychedelic drugs induce common network changes in human cortex. *NeuroImage* 2023; 273:120097
415. Csernansky JG, Bardgett ME: Limbic-cortical neuronal damage and the pathophysiology of schizophrenia. *Schizophr Bull* 1998; 24:231–48
416. Duncan GE, Moy SS, Knapp DJ, Mueller RA, Breese GR: Metabolic mapping of the rat brain after subanesthetic doses of ketamine: potential relevance to schizophrenia. *Brain Research* 1998; 787:181–90
417. Silberbauer LR, Spurny B, Handschuh P, Klöbl M, Bednarik P, Reiter B, Ritter V, Trost P, Konadu ME, Windpassinger M, Stimpfl T, Bogner W, Lanzenberger R, Spies M: Effect of Ketamine on Limbic GABA and Glutamate: A Human In Vivo Multivoxel Magnetic Resonance Spectroscopy Study. *Frontiers in Psychiatry* 2020; 11
418. Vasavada MM, Loureiro J, Kubicki A, Sahib A, Wade B, Helleman G, Espinoza RT, Congdon E, Narr KL, Leaver AM: Effects of Serial Ketamine Infusions on Corticolimbic Functional Connectivity in Major Depression. *Biological Psychiatry: Cognitive Neuroscience and Neuroimaging* 2021; 6:735–44



419. Forsyth A, McMillan R, Campbell D, Malpas G, Maxwell E, Sleigh J, Dukart J, Hipp J, Muthukumaraswamy SD: Modulation of simultaneously collected hemodynamic and electrophysiological functional connectivity by ketamine and midazolam. *Human Brain Mapping* 2020; 41:1472–94
420. Kotoula V, Webster T, Stone J, Mehta MA: Resting-state connectivity studies as a marker of the acute and delayed effects of subanaesthetic ketamine administration in healthy and depressed individuals: A systematic review. *Brain and Neuroscience Advances* 2021; 5:23982128211055424
421. Muthukumaraswamy SD, Shaw AD, Jackson LE, Hall J, Moran R, Saxena N: Evidence that Subanesthetic Doses of Ketamine Cause Sustained Disruptions of NMDA and AMPA-Mediated Frontoparietal Connectivity in Humans. *J Neurosci* 2015; 35:11694–706
422. Mueller F, Musso F, London M, Boer P de, Zacharias N, Winterer G: Pharmacological fMRI: Effects of subanesthetic ketamine on resting-state functional connectivity in the default mode network, salience network, dorsal attention network and executive control network. *Neuroimage Clin* 2018; 19:745–57
423. Pinault D: N-Methyl d-Aspartate Receptor Antagonists Ketamine and MK-801 Induce Wake-Related Aberrant  $\gamma$  Oscillations in the Rat Neocortex. *Biological Psychiatry* 2008; 63:730–5
424. Tian F, Lewis LD, Zhou DW, Balanza GA, Paulk AC, Zelmann R, Peled N, Soper D, Santa Cruz Mercado LA, Peterfreund RA, Aglio LS, Eskandar EN, Cosgrove GR, Williams ZM, Richardson RM, Brown EN, Akeju O, Cash SS, Purdon PL: Characterizing brain dynamics during ketamine-induced dissociation and

- subsequent interactions with propofol using human intracranial neurophysiology. *Nat Commun* 2023; 14:1748
425. Kohrs R, Durieux ME: Ketamine: Teaching an Old Drug New Tricks. *Anesthesia & Analgesia* 1998; 87:1186–93
426. Xu W, Li H, Wang L, Zhang J, Liu C, Wan X, Liu X, Hu Y, Fang Q, Xiao Y, Bu Q, Wang H, Tian J, Zhao Y, Cen X: Endocannabinoid signaling regulates the reinforcing and psychostimulant effects of ketamine in mice. *Nat Commun* 2020; 11:5962
427. Farahmandfar M, Akbarabadi A, Bakhtazad A, Zarrindast M-R: Recovery from ketamine-induced amnesia by blockade of GABA-A receptor in the medial prefrontal cortex of mice. *Neuroscience* 2017; 344:48–55
428. Zhang B, Yang X, Ye L, Liu R, Ye B, Du W, Shen F, Li Q, Guo F, Liu J, Guo F, Li Y, Xu Z, Liu Z: Ketamine activated glutamatergic neurotransmission by GABAergic disinhibition in the medial prefrontal cortex. *Neuropharmacology* 2021; 194:108382
429. Gupta A, Devi LA, Gomes I: Potentiation of  $\mu$ -opioid receptor-mediated signaling by ketamine. *Journal of Neurochemistry* 2011; 119:294–302
430. Nugent AC, Ballard ED, Gould TD, Park LT, Moaddel R, Brutsche NE, Zarate CA: Ketamine has distinct electrophysiological and behavioral effects in depressed and healthy subjects. *Mol Psychiatry* 2019; 24:1040–52
431. Ballard ED, Zarate CA: The role of dissociation in ketamine's antidepressant effects. *Nat Commun* 2020; 11:6431

432. Liechti ME, Dolder PC, Schmid Y: Alterations of consciousness and mystical-type experiences after acute LSD in humans. *Psychopharmacology* 2017; 234:1499–510
433. Tagliazucchi E, Zamberlan F, Cavanna F, Fuente L de la, Romero C, Sanz Perl Y, Pallavicini C: Baseline Power of Theta Oscillations Predicts Mystical-Type Experiences Induced by DMT in a Natural Setting. *Frontiers in Psychiatry* 2021; 12
434. Lahogue C, Pinault D: Frontoparietal anodal tDCS reduces ketamine-induced oscillopathies. *Translational Neuroscience* 2021; 12:282–96
435. Lewis SR, Pritchard MW, Fawcett LJ, Punjasawadwong Y: Bispectral index for improving intraoperative awareness and early postoperative recovery in adults. *Cochrane Database Syst Rev* 2019; 2019:CD003843
436. Niciu MJ, Shovestul BJ, Jaso BA, Farmer C, Luckenbaugh DA, Brutsche NE, Park LT, Ballard ED, Zarate CA: Features of dissociation differentially predict antidepressant response to ketamine in treatment-resistant depression. *Journal of Affective Disorders* 2018; 232:310–5
437. Włodarczyk A, Cubała WJ, Gałuszko-Węgielnik M, Szarmach J: Dissociative symptoms with intravenous ketamine in treatment-resistant depression exploratory observational study. *Medicine (Baltimore)* 2021; 100:e26769
438. Acevedo-Diaz EE, Cavanaugh GW, Greenstein D, Kraus C, Kadriu B, Park L, Zarate CA: Can 'floating' predict treatment response to ketamine? Data from three randomized trials of individuals with treatment-resistant depression. *Journal of Psychiatric Research* 2020; 130:280–5

439. Lii TR, Smith AE, Flohr JR, Okada RL, Nyongesa CA, Cianfichi LJ, Hack LM, Schatzberg AF, Heifets BD: Trial of Ketamine Masked by Surgical Anesthesia in Depressed Patients 2023;p 2023.04.28.23289210 doi:10.1101/2023.04.28.23289210
440. Clutterbuck J: Mind Monitor. Available: <https://mind-monitor.com/>.
441. Haijen ECHM, Kaelen M, Roseman L, Timmermann C, Kettner H, Russ S, Nutt D, Daws RE, Hampshire ADG, Lorenz R, Carhart-Harris RL: Predicting Responses to Psychedelics: A Prospective Study. *Frontiers in Pharmacology* 2018; 9:897
442. Murphy E, King EA: Testing the accuracy of smartphones and sound level meter applications for measuring environmental noise. *Applied Acoustics* 2016; 106:16–22
443. Rodrigues NB, McIntyre RS, Lipsitz O, Lee Y, Cha DS, Shekotikhina M, Vinberg M, Gill H, Subramaniapillai M, Kratiuk K, Lin K, Ho R, Mansur RB, Rosenblat JD: A simplified 6-Item clinician administered dissociative symptom scale (CADSS-6) for monitoring dissociative effects of sub-anesthetic ketamine infusions. *J Affect Disord* 2021; 282:160–4
444. Gotlib IH: EEG alpha asymmetry, depression, and cognitive functioning. *Cognition & Emotion* 1998; 12:449–78
445. Derntl B, Hornung J, Sen ZD, Colic L, Li M, Walter M: Interaction of Sex and Age on the Dissociative Effects of Ketamine Action in Young Healthy Participants. *Front Neurosci* 2019; 13:616
446. Pope D: Decibel levels and noise generators on four medical/surgical nursing units. *Journal of Clinical Nursing* 2010; 19:2463–70

447. He C, Chen Y-Y, Phang C-R, Stevenson C, Chen I-P, Jung T-P, Ko L-W: Diversity and Suitability of the State-of-the-Art Wearable and Wireless EEG Systems Review. *IEEE Journal of Biomedical and Health Informatics* 2023:1–14 doi:10.1109/JBHI.2023.3239053
448. Salle S de la, Phillips JL, Blier P, Knott V: Electrophysiological correlates and predictors of the antidepressant response to repeated ketamine infusions in treatment-resistant depression. *Prog Neuropsychopharmacol Biol Psychiatry* 2022; 115:110507
449. Van Der Vinne N, Vollebregt MA, Van Putten MJ, Arns M: Frontal alpha asymmetry as a diagnostic marker in depression: Fact or fiction? A meta-analysis. *Neuroimage: clinical* 2017; 16:79–87
450. Piazza GG, Iskandar G, Hennessy V, Zhao H, Walsh K, McDonnell J, Terhune DB, Das RK, Kamboj SK: Pharmacological modelling of dissociation and psychosis: an evaluation of the Clinician Administered Dissociative States Scale and Psychotomimetic States Inventory during nitrous oxide ('laughing gas')-induced anomalous states. *Psychopharmacology* 2022; 239:2317–29
451. Olofsen E, Kamp J, Henthorn TK, Velzen M van, Niesters M, Sarton E, Dahan A: Ketamine Psychedelic and Antinociceptive Effects Are Connected. *Anesthesiology* 2022; 136:792–801
452. Fabus MS, Woolrich MW, Warnaby CW, Quinn AJ: Understanding Harmonic Structures Through Instantaneous Frequency. *IEEE Open J Signal Process* 2022; 3:320–34

453. Vesuna S, Kauvar IV, Richman E, Gore F, Oskotsky T, Sava-Segal C, Luo L, Malenka RC, Henderson JM, Nuyujukian P, Parvizi J, Deisseroth K: Deep posteromedial cortical rhythm in dissociation. *Nature* 2020; 586:87–94
454. Artoni F, Maillard J, Britz J, Seeber M, Lysakowski C, Bréchet L, Tramèr MR, Michel CM: EEG microstate dynamics indicate a U-shaped path to propofol-induced loss of consciousness. *NeuroImage* 2022; 256:119156
455. Liu Z, Si L, Xu W, Zhang K, Wang Q, Chen B, Wang G: Characteristics of EEG Microstate Sequences During Propofol-Induced Alterations of Brain Consciousness States. *IEEE Transactions on Neural Systems and Rehabilitation Engineering* 2022; 30:1631–41
456. Gohil C, Roberts E, Timms R, Skates A, Higgins C, Quinn A, Pervaiz U, Amersfoort J van, Notin P, Gal Y, Adaszewski S, Woolrich M: Mixtures of large-scale dynamic functional brain network modes. *NeuroImage* 2022; 263:119595
457. Sleight JW: Depth of anesthesia: perhaps the patient isn't a submarine. *The Journal of the American Society of Anesthesiologists* 2011; 115:1149–50
458. Perouansky M, Sleight JW: A Crack at MAC. *Anesthesiology* 2021; 134:835–7
459. Whitlock EL, Villafranca AJ, Lin N, Palanca BJ, Jacobsohn E, Finkel KJ, Zhang L, Burnside BA, Kaiser HA, Evers AS, Avidan MS: Relationship between bispectral index values and volatile anesthetic concentrations during the maintenance phase of anesthesia in the B-Unaware trial. *Anesthesiology* 2011; 115:1209–18
460. Hight D, Kreuzer M, Ugen G, Schuller P, Stüber F, Sleight J, Kaiser HA: Five commercial 'depth of anaesthesia' monitors provide discordant clinical recommendations in response to identical emergence-like EEG signals. *British Journal of Anaesthesia* 2023; 130:536–45

461. Kee C-Y, Ponnambalam SG, Loo C-K: Multi-objective genetic algorithm as channel selection method for P300 and motor imagery data set. *Neurocomputing* 2015; 161:120–31
462. Allen M, Tsakiris M: The body as first prior: Interoceptive predictive processing and the primacy. *The interoceptive mind: From homeostasis to awareness* 2018; 27
463. Babo-Rebelo M, Tallon-Baudry C: Interoceptive signals, brain dynamics, and subjectivity. *The interoceptive mind: From homeostasis to awareness* 2018; 46
464. Ngo H-VV, Martinetz T, Born J, Mölle M: Auditory Closed-Loop Stimulation of the Sleep Slow Oscillation Enhances Memory. *Neuron* 2013; 78:545–53
465. Candia-Rivera D, Machado C: The differences of heartbeat-evoked responses and EEG non-locked to heartbeats may shed light in identifying disorders of consciousness. 2021 doi:10.13140/RG.2.2.36025.90722
466. Tumati S, Paulus MP, Northoff G: Out-of-step: Brain-heart desynchronization in anxiety disorders. *Molecular Psychiatry* 2021; 26:1726–37
467. Parviainen T, Lyyra P, Nokia MS: Cardiorespiratory rhythms, brain oscillatory activity and cognition: review of evidence and proposal for significance. *Neuroscience & Biobehavioral Reviews* 2022; 142:104908
468. Russel B: *Autobiography of Bertrand Russel*. Allen and Unwin, 1967

## IUCUNDI ACTI LABORES